UNIVERSITÀ
DEGLI STUDI
FIRENZE

DOTTORATO DI RICERCA IN
SCIENZE DELLA TERRA

CICLO XXVI

COORDINATORE Prof. LORENZO ROOK

Geochemical investigation on marine sediments, on volcanoes and on diapirs mud Basin of Paola (Calabria, Italy)

Settore Scientifico Disciplinare GEO/08

Dottorando
Dott.ssa Rashed Heba
hebarashed

Tutore
Prof. Vaselli Orlando

Co-Tutori
Dott.ssa Rovere Marzia
Marzia Rovere
Dr. Gamberi Fabiano

Dott.ssa Pecchioni Elena

Coordinatore
Prof. Lorenzo Rook

Anni 2011/2016

Contents Pages

Abstract

The study area is located along the Paola Ridge, a NNW–SSE 60-km-long anticline that confines the Paola Basin westward (north-western Calabrian margin) and the Tyrrhenian Sea to southeastern (Fig.1). The Paola Ridge has recently been re-interpreted as due to a mobile mud belt, consisting of the diapirs (D1, D2 and D3) and the mud volcanoes (MMV and RMV), connected to a set of NW-SE to NNW-SSE trending extensional faults. With the aim of proving this latter interpretation, the MVP11 oceanographic cruise was carried out in August-September 2011 on board the research vessel CNR Urania. During the cruise, multi-beam bathymetric data, CHIRP profiles, gravity cores and box-cores were collected mainly to define the sedimentological features, the petrographical, mineralogical and geochemical composition of the cored sediments. Paola Ridge is characterized by the presence of cold seeps and thus of past and/or present gas emission at the seabed as recovered by mineralogical and geochemical analyses of the related mineralization. Petrographical, mineralogical, chemical and isotopic data obtained from the cored sediments and the rock sample allowed to define the depths of the biogeochemical zones and the geochemical processes mainly affecting the depositional environment into which the marine sediments were deposited. The mud volcanoes are sites of vigorous venting at the seafloor and are characterized by a high backscatter signature and the presence of rare to almost absent pockmarks. Several sites were sampled over the mud volcanoes, iron oxy-hydroxide crusts were found at the seafloor. XRD analyses showed that they were always consisting of FeOOH. Pyrite crusts and pavements were collected at depth of 10 to 50 cm below the seafloor. They showed a mineralogical composition consisting of pyrite and /or sphalerite, quartz and scarce feldspars. Sulfur isotopes (expressed as δ^{34}S ‰V-CDT) were measured in a few samples showing that S can be sourced from ^{32}S-depleted H_2S from the water column. Tubular authigenic carbonates were found at depth of 5-6 m below the seafloor. They were consisting of siderite, quartzes and few phyllosilicates. Stable isotope (C and O, expressed as δ^{13}C ‰ V-PDB and δ^{18}O ‰ V-PBD, respectively) measurements in siderite showed peculiar enrichment in the heavier isotopes, which were hypothesized to be compatible only with the presence of methane in the deepest part of the system. Mudflows are areas where gas

discharges are not vigorously venting at the seafloor, likely because they are trapped 2-3 m below it. They share similar characteristics with other sites where mud volcanoes occur. On the contrary, mud diapirs are characterized by low backscatter with abundant pockmarks and dissected by normal faults. Here, organogenic carbonate crusts were found, with a mineralogical composition mainly consisting of calcite, aragonite and dolomite, few phyllosilicates, feldspar and pyroxene. The associated macro-fauna showed the presence of bivalve assemblages, that are symbionts of sulfur oxidizing bacteria and usually live in extreme environments, like cold seeps. Stable isotope (C and O) analysis performed on the organogenic carbonates showed extremely depleted δ^{13}C values (as low as -41.50 ‰V-PDB) and slightly enriched δ^{18}O values (between 0.40 and 5.50 ‰ V-PDB). Such values are compatible with authigenic carbonates precipitated due to AOM (Anaerobic Oxidation of Methane) in the SRZ (Sulfate Reduction Zone). A second cruise (MarBeep 2014) was conducted on board the CNR R/V Urania aimed at the identification of the deeper morphology and structure of the mud volcanoes and mud diapir plumbing systems. Water and gas samples at the sea surface from rosette and drilled core were collected, respectively. Autighenic carbonates and sulfides were also found whose mineralogical and geochemical features confirmed what previously assessed from the samples collected from the first cruise.

Trace element and rare earth element (REE) compositions of different carbonate and non carbonate phases are used in this study to indicate source fluid characteristics and redox conditions. Flat REE pattern and the absence of Ce anomaly in the organogenic carbonates suggest that these carbonates incorporated high amounts of organic matter and precipitated within highly alkaline pore water under sub-oxic conditions. The siderite REE pattern showed consistent LREE fractionation, MREE enrichment and positive Gd and La anomalies, suggesting non-marine origin close to the exchange equilibrium of adsorbed/dissolved REE under prolonged reducing conditions.

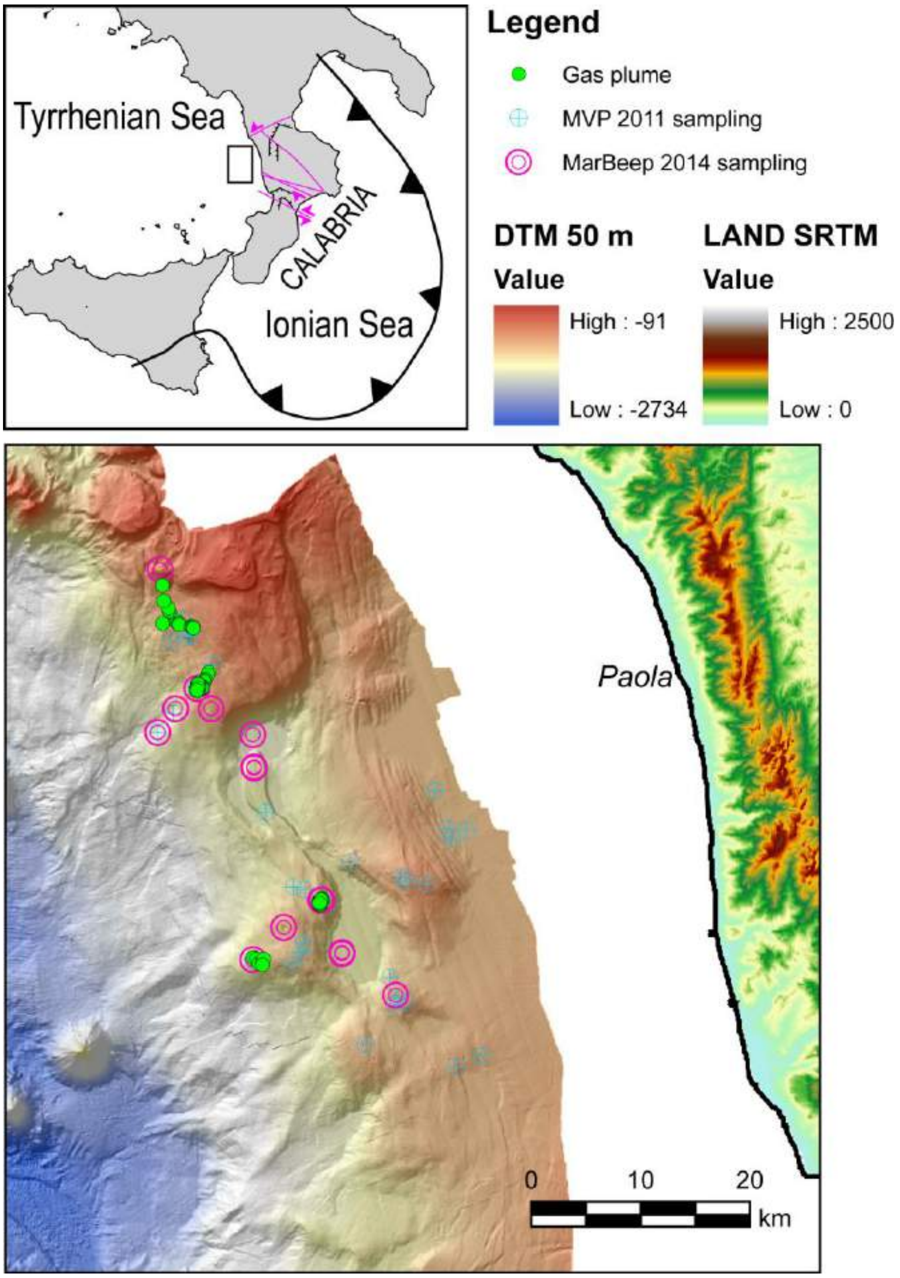

Figure 1 – Bathymetry of the study area in the southern Tyrrhenian Sea. Sampling stations and venting sites (gas plumes) are shown in the map (see legend).

Introduction

Surface emission of fluids are well known processes occurring on both subaerial and submarine environments and formed on either the top of mud diapir or along fault systems. Cold seeps in marine environments are common phenomena found in several continental margins worldwide as either fossil or active manifestations, where shallow to deep fluids can escape to the sea bottom without an appreciable temperature rise (Judd and Hovland, 2007; Tribovillard et al., 2013 and reference therein). There are sites that are mostly CH_4-dominated although higher derivatives or even oil seeps from the subsurface are released. High-resolution seafloor mapping in fluid-rich structures have recently been reported in the Central Mediterranean area: in the Adriatic Sea (Geletti et al., 2008), in the eastern Sardinia continental slope (Dalla Valle and Gamberi, 2011) and in the Malta plateau (Savini et al., 2009). Cold seeps represent hotspots for increased biological activity, where chemosynthetic communities operated by consortia of anaerobic methane oxidizing archaea and sulfate reducing bacteria occur (Paull et al., 2005; Boetius et al., 200). These biomediated reactions such as methane oxidation and sulfate reduction, increase carbonate alkalinity in the form of dissolved inorganic carbon, which can lead to the precipitation of isotopically depleted carbonates in the sulfate reduction zone and at the sulfate/methane transition zone (Ritger et al, 1987; Paull et al, 1992; Bohrmann et al, 1998; Aloisi et al, 2000; Niemann et al, 2005; Campbell et al, 2010; Bayon et al, 2013). Deeper in the sub-seafloor, >10 m below the seafloor, always in the sulfate depleted sediments (Borowski et al, 1999; D'Hondt et al, 2002; Leloup et al, 2007), siderites can form through methanogenesis and/or gas hydrate formation/decomposition (Matsumoto, 1989; Coleman, 1993) and have a different isotopic signature when compared to other carbonate mineral phases, such as dolomite and aragonite, siderite being usually ^{13}C- and ^{18}O-enriched (Matsumoto, 1989; Rodriguez et al, 2000).

In the western part of Central Mediterranean Sea, the Tyrrhenian Sea, little evidence of past and present fluid circulation has found, except for the Paola Ridge, along the NW Calabrian margin (SE Tyrrhenian sea). This area was described as characterized by intense fluid seepage, gas venting and precipitation of methane-related authigenic carbonates (Gamberi and Rovere, 2010; Rovere et al., 2014, 2015). New high-resolution data and seafloor sampling campaigns were carried out in 2011 and 2014, have revealed that cold seeps are present in the Paola Ridge, at 500-1000 m water depth. They are represented by mud volcanoes and mud diapirs, which are characterized by the presence of pockmarks on top of them.

In the study area, the mud volcanoes are sites of vigorous venting at the seafloor where precipitation of siderite and iron sulfides occur. Authigenic calcite/aragonite deposition associated with macrofauna bivalve assemblages on pockmarks-punctuated mud diapirs was also recognized (Gamberi and Rovere 2010).

Calcite/aragonite authigenic products precipitated from the seeping fluids were geochemically and isotopically characterized in previous studies (e.g. Rongemaille et al. 2011; Peckmann et al., 2001; Magalhàes et al., 2012; Cangemi et al.,2010). On the contrary, the presence of authigenic siderite at seepage sites is less documented (Fritz et al., 1971; Curtis et al., 1972; Mozley and Wersin, 1992; Rongemaille et al., 2011). Siderite nodules were recorded from modern setting associated with methane seepage (Niger delta; Rongemaille et al., 2011) or methane hydrate decomposition (Black Outer Ridge; Matsumoto, 1989), with highly ferruginous, low sulfate and anoxic lake water (Wittkop et al., 2014).

This study was aimed to define the mineralogical, geochemical and isotopic features of the authigenic products as well as unraveling the past and/or present gas emission at the seabed in the Paola Ridge. The fluid source(s) in the Paola Ridge was/were inferred from the composition of stable of carbon and oxygen isotopes and rare earth elements REE of carbonates. In fact, REE composition of carbonates is commonly investigated to reconstruct seawater chemistry and the possible presence of fluid mixing processes in both recent (e.g. Himmler et al.,2010; Hu et al., 2014) and ancient (e.g. Nothdurft et al., 2004; Feng et al., 2009; Franchi et al., 2015) settings. Furthermore, it was explored if variations of the REE pattern of the seawater with respect to the standard composition (e.g. Zhong and Mucci, 1995; Zhang and Nozaki, 1998) were possibly related to either mixing with methane-rich/hydrothermal fluids (e.g., Kamber et al., 2004; Feng et al., 2009) or modification of the pore water redox conditions (Kim et al., 2012; Hu et al., 2014). By coupling REE compositions and $\delta^{13}C$ (‰ V-PDB) and $\delta^{18}O$ (‰ V-PDB) values, new and useful insights on the source of the seeping fluids and redox conditions during the deposition of the carbonates at Paola Ridge were achieved. The results allowed to constrain the geochemical processes involved in the formation and early diagenesis of authigenic minerals precipitated at sites of fluids venting in the southern Tyrrhenian Sea.

CHAPTER 1: General geological setting

1.1- Tectonic evolution of the Mediterranean region in the last 30 Ma

During the Late Mesozoic and Cenozoic, the Mediterranean region experienced complex subduction and associated collisions, resulting in the formation of mountain belts and the opening of back-arc basins (Dilek et al., 2006). During the Late Jurassic-Early Cretaceous, the plate convergence between Africa and Europe was initiated by a sinistral strike-slip related to the progressive opening of the Atlantic Ocean. During the Cenozoic (Oligo-Miocene), the progressive closure of the Tethys Ocean formed the Alpine orogenic belt, presently exposed in the Alps, northwestern Corsica, Calabria and the Betics (Stampfli and Borel, 2002).

The geological evolution of the western and central Mediterranean region in the last 30 Ma thus took place within the context of the slow, almost N-S directed, persisting convergence (0.5-1 cm/year) between Africa and Eurasia (Dewey et al., 1989; De Mets et al., 1990; Goes et al., 2004), during two stages of trench migration and back- arc opening, which consumed the westernmost extension of the Tethys Ocean and small oceanic basins formed, including the Tyrrhenian Sea in which our study area is located (Krijgsman et al., 2002, Fig. 1.1). In the first stage, during the Oligocene-Miocene, the Corsica-Sardinia block rotated anticlockwise to its present position (Vigliotti and Langenheim, 1995), opening the Liguro-Provençal basin (Fig. 1.2). In the mean time, the Calabrian Arc separated from the Corsica-Sardinia block and migrated rapidly, at a rate of up to 6-8 cm/year, to its present position (Goes et al., 2004), colliding with Apulia and Africa to form the Apenninic and Maghrebian orogenic belts (Fig. 1.3). This movement was due to the hypothesized subduction roll-back of the Ionian oceanic slab, which is generally considered to be the cause of the opening of the Tyrrhenian back-arc basin that had been occurring since 9 Ma ago (Malinverno and Ryan, 1986; Knott and Turco, 1991; Doglioni et al., 1999; Rosenbaum et al., 2002; Faccenna et al., 2004; Rosenbaum and Lister, 2004).

Therefore, the Mediterranean region is presently characterized by intense seismicity along the plate boundaries, the mountain belts and active volcanism related to subduction and intra-plate systems. Nevertheless, it also hosts mud volcanoes in a different variety of settings, modern and fossil, subaerial and submarine, tectonically passive and active (Kopf, 2002; Jean & Chaumillon 1997). The western and central Mediterranean Sea nowadays consists of 5 basins: the Alboran Sea, the Algerian-Provençal Basin, the Valencia Trough, the Ligurian Sea and the Tyrrhenian Sea (Fig. 1.4). These basins show different types of crust: from transitional to continental and oceanic, calc-alkaline volcanism and shallow and intermediate depth earthquakes (Fig. 1.6, Horvath et al., 1981).

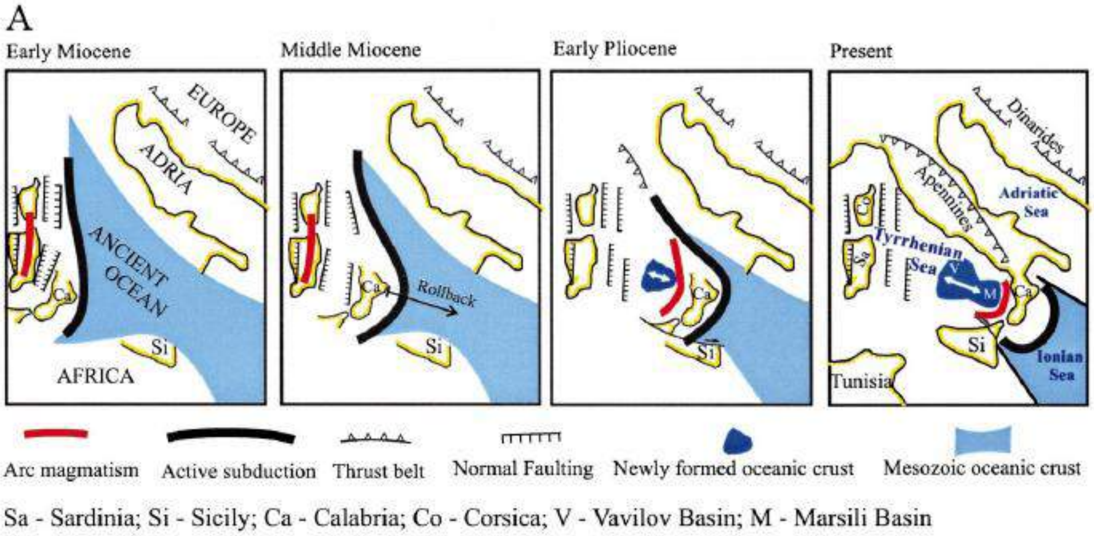

Figure 1.1 - The tectonic evolution of the central Mediterranean during the past 10-20 Myr is dominated by the eastward migration of the Apennine-Calabrian subduction zone. This eastward motion does not correlate to the regional convergence between Africa and Europe, which is approximately N-S and 5-6 times slower. The motion is interpreted to be a result of slab rollback, the process in which descending slabs retreat laterally under their own weight. When a retreating slab rolls back faster than the convergence rate, it pulls on the edge of the overriding plate, rifting it from the rest of the plate and eventually forming a backarc basin with new oceanic floor (the Tyrrhenian basin). From Gvirtzman and Nur, 2001.

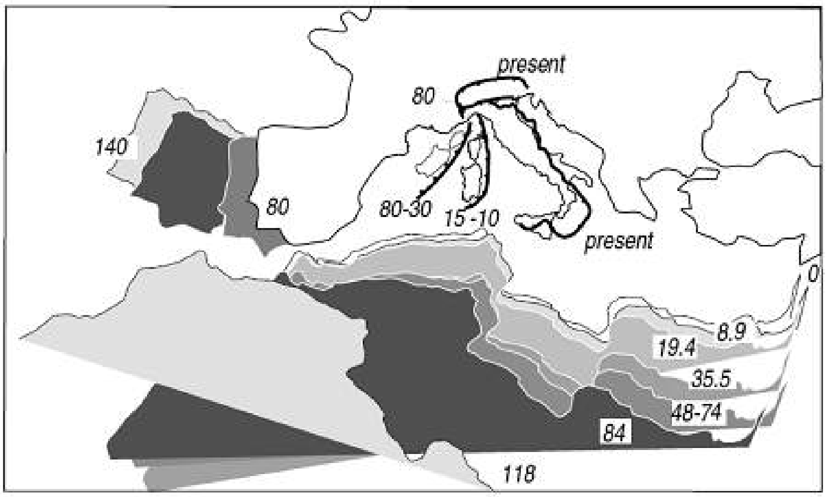

Figure 1.2 – African motion with respect to fixed Eurasia as calculated by Dewey et al (1989) and motion of Iberia. The orientation of the Central Mediterranean trench is also shown. Numbers are Myr, from Faccenna et al., 2001.

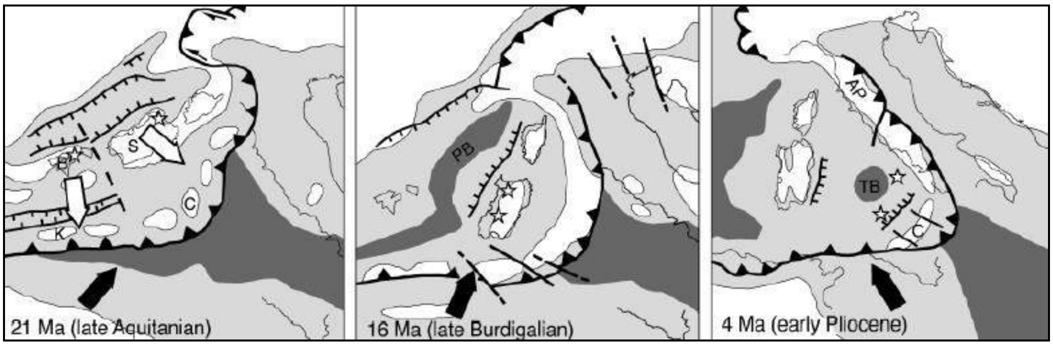

Figure 1.3- Schematic maps showing the paleotectonic evolution of the Western Mediterranean during the Neogene time (modified after Bonardi et al., 2001 and Roca, 2001). Only active tectonic elements. White: exposed land; light gray: epicontinental sea; darker gray: oceanic crust. Black arrows indicate the direction of Africa's motion with respect to Europe (from Mazzoli and Helman, 1994). White arrows indicate upper-plate direction of extension. Stars indicate subduction-related magmatism. AP, Apennines; B, Balearic block; C, Calabria-Peloritani terrane; K, Kabilies; PB, Provençal Basin, S, Sardinia; TB, Tyrrhenian Basin.

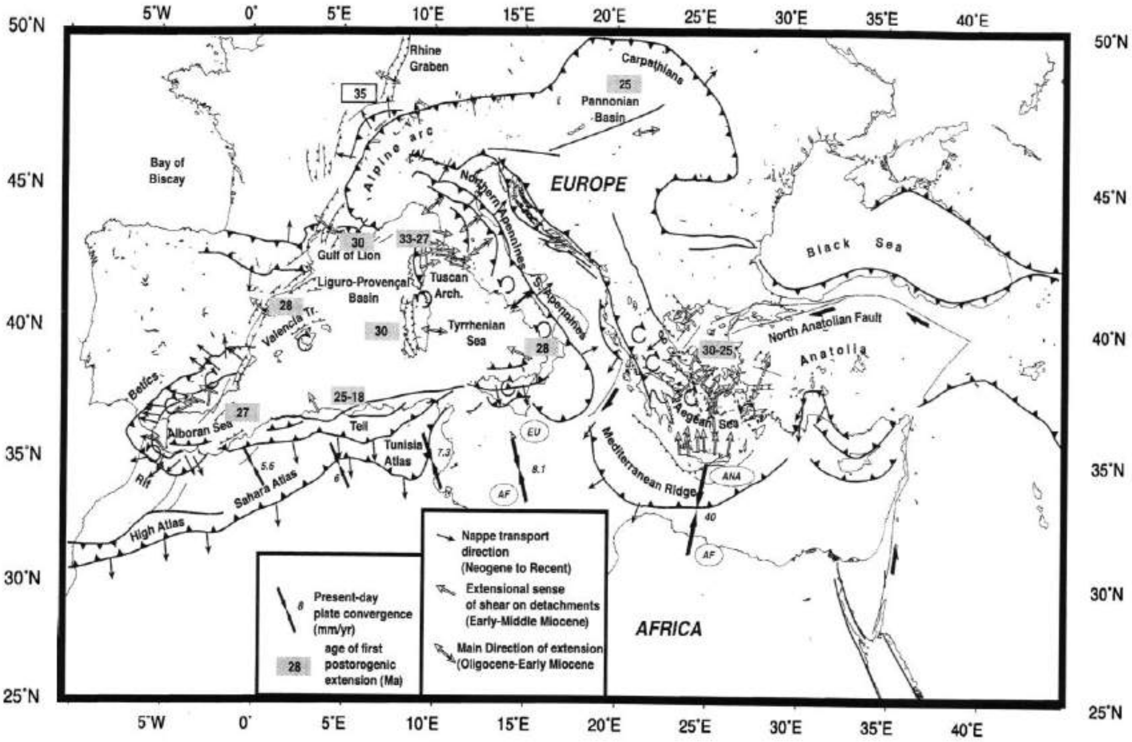

Figure 1.4 - Map of the Mediterranean region showing the major basins and surrounding mountain belts (Jolivet and Faccenna, 2000).

1.2 – The Tyrrhenian Sea

The Tyrrhenian Sea is a Neogene back-arc basin formed since Tortonian within the frame of the Europe-Africa convergence, and it was opened as a result of a southeastward roll-back of the northwesterly subducting Ionian oceanic slab (Malinverno and Ryan, 1986; Kastens et al., 1988; Kastens et al., 1990; Sartori, 1990; Jolivet, 1991). It is surrounded by the continental masses of Corsica-Sardinia to the west, Sicily to the south and the peninsular Italy to the east (Fig. 1.5). The opening of the Tyrrhenian Sea occurred in two stages: an early (9-5 Ma) opening of the northern Tyrrhenian Sea, which was characterized by a thinning and rifting of continental crust (Vavilov Basin), and a late (5-0 Ma) opening of the southern Tyrrhenian which was due to the emplacement of a thin oceanic type crust in the Marsili Basin during the Pleistocene (Kastens et al., 1988; Sartori et al., 2004, Fig. 1.6). This favored the formation of elongated peripheric basins, the peri-Tyrrhenian basins, the Paola, Gioia and Cefalù basins, which are characterized by Plio-Quaternary sedimentary infilling up to 5-km-thick (Fabbri et al., 1981; Trincardi et al., 1995, Pepe et al., 2010; Fig. 1.7).

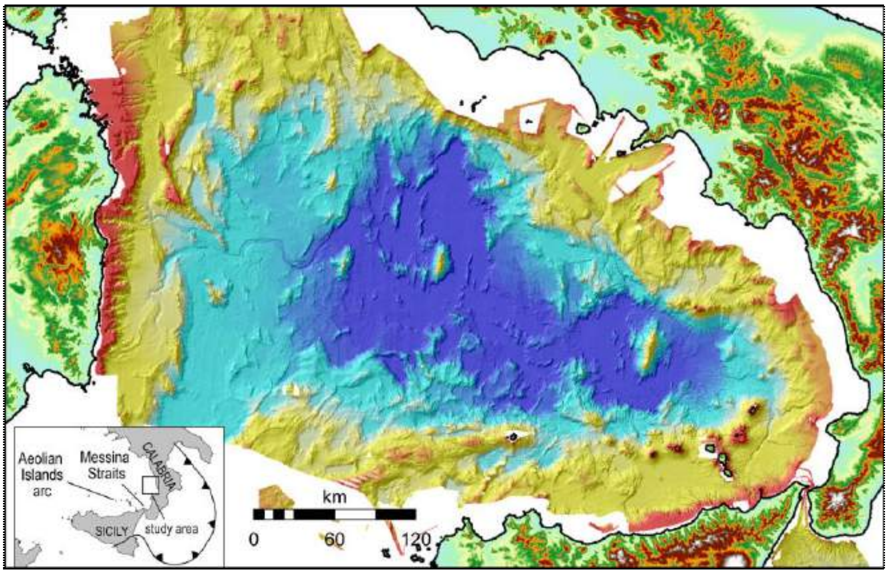

Figure 1.5 - Bathymetric map of the Tyrrhenian sea. Courtesy of Marzia Rovere.

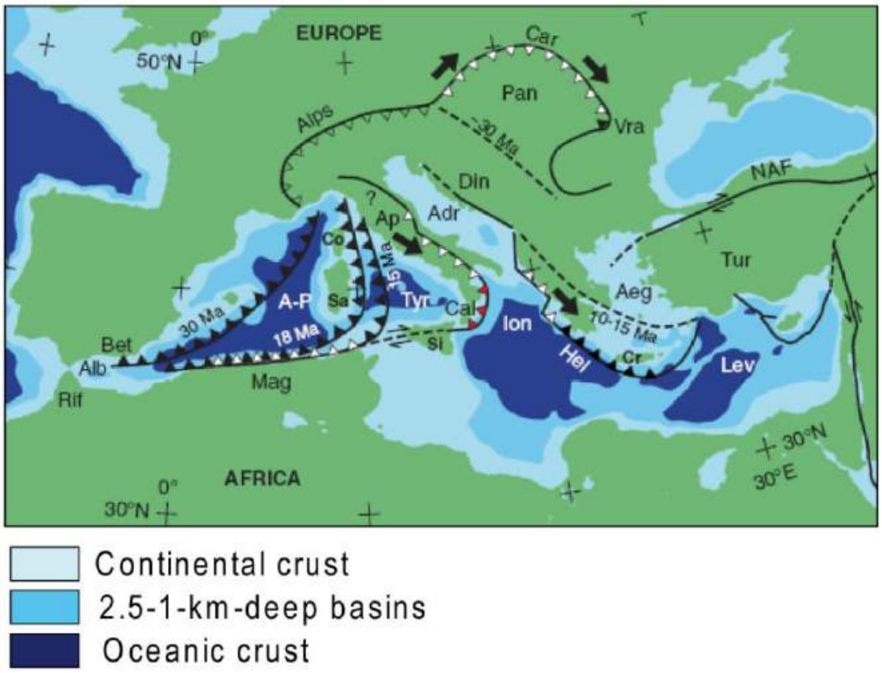

Figure 1.6 – Types of crust in the Mediterranean Sea. Adjusted from Wortel and Spakman, 2000.

Figure 1.7 - Tectonic setting of the Tyrrhenian Sea, showing the main structural features (Rosenbaum et al., 2004).

During the Quaternary, intense volcanic activity, mostly calcalkaline to high-potassic in composition, affected the southern portion generating the volcanic arc of the Aeolian Islands (Barberi et al., 1973; Fig. 1.8). The composition of the Aeolian volcanic rocks is varied and spreads over four typical magmatic series of orogenic setting: island-arc tholeiites, calc-alkaline, high-K calc-alkaline, and shoshonitic (Francalanci et al., 2012). It is therefore characterized by the presence of both IAB (Island Arc Basalts) and OIB (Oceanic Island Basalts) type magmas (Trua et al., 2004). There are 3 sectors of the Aeolian Arc whose volcanism activated at different times (Fig. 1.9):

- A western sector, which extends from the Glauco seamount to the Alicudi and Filicudi islands. In this sector the volcanism developed between 3.04 and 1.3 Myr (Beccaluva et al., 1982, 1985; Santo and Clark, 1994).
- A central sector, which includes Salina, Lipari and Volcano, where the volcanism started at 0.4 Myr (Beccaluva et al., 1985).
- An eastern sector, which extends from Panarea and Stromboli islands to the Alcione and Palinuro seamounts, where the volcanism started at about 0.8 Myr and it is still active at Stromboli (De Astis et al., 2003).

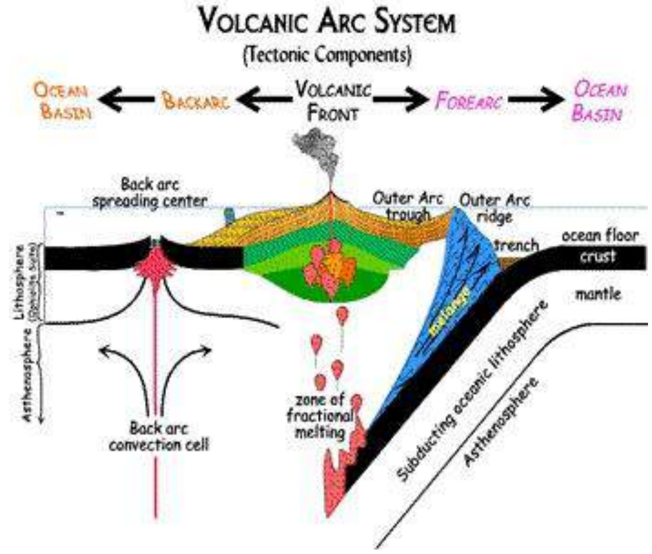

Figure 1.8 – Concept of formation of a volcanic arc system. From http://earthquake.usgs.gov/learning/glossary.php?term=forearc

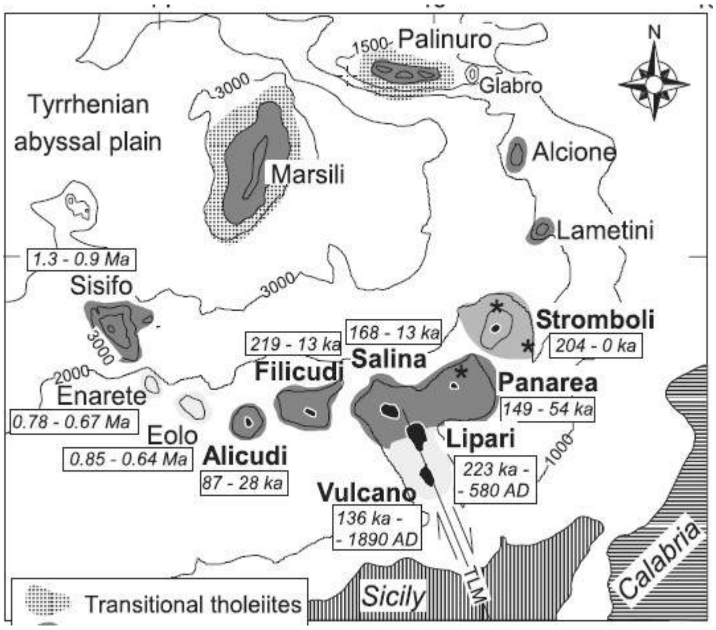

Figure 1.9 - General map of the Aeolian island arc (in black) and relevant seamounts for this study. (Francalanci et al., 2007).

The Tyrrhenian Sea shows high Bouguer anomaly (>250 mGal) and heat flow values (Cella et al., 1998; Zito et al., 2003), indicating shallow upper mantle and thin crust, the highest values being recorded in the eastern part of the basin. Close to the Vavilov and Marsili basins, the Moho is very shallow (about 15-20 km deep) and the crust thickness is less than 10 km (Nicolich, 1989; Nicolich and Dal Piaz, 1991). The central and southern Tyrrhenian region is the most thinned and deepest part (> 3,500 m) and is also the area where the highest heat flow values occur (Zito et al., 2003). The recent volcanism brought to the formation of different submarine volcanoes, among them: the Gortani Ridge (~ 4 Ma old; Beccaluva et al., 1990; Serri et al., 2001); the Magnaghi Seamount (2.7–3.0 Ma, Selli et al., 1977); the Vavilov volcano (2.4-0.1 Ma, Robin et al., 1987); the Marsili volcano (0.7–0.1 Ma; Faggion et al., 1995; Selli et al., 1977).

1.3 - On land geology of the Calabrian Arc

The study area is located about 15 nautical miles off the western coast of northern Calabria at the rear of the Calabrian Arc. The Calabrian Arc (CA) is a prominent arc-shaped structure belonging to the Apennine-Maghrebian orogenic belt (Ghisetti and Vezzani, 1982; Ghisetti et al., 1991; Tortorici et al., 1995; Federico et al., 2004).

The Calabrian Arc is characterized by:

1- series of thrust nappes composed of tectonic units deriving from the deformation of different palaeogeographic domains;

2- Palaeozoic crystalline rocks, which were interpreted as basement belonging to the African continental margin (Grandjacquet and Mascle, 1978) or as part of the European paleo-margin (Bouillin et al., 1986; Dewey et al., 1989);

3- Ophiolite-bearing units of the Neo-Tethys domains.

The Neogene and Quaternary geodynamic evolution of the Calabrian Arc is related to its southeastward migration (Mazzoli and Helman, 1994) due to, as previously mentioned, the subduction roll-back of the Ionian oceanic lithosphere. During the Late Pliocene-Early Quaternary, the Calabria Arc was dissected by longitudinal and transversal normal faults, these faults ranging from 10 to 45 km in length, that caused the fragmentation of the arc into structural highs, both parallel and orthogonal to the Tyrrhenian margin (Ghisetti, 1979; Van Dijk et al., 2000; Guarnieri, 2006, Fig.1.10).

1.4- The study area

The study area is located within the Paola Basin in the southeastern margin of the Tyrrhenian Sea, along a 60-km-long and NNW-SSE oriented anticline, called the Paola Ridge. The study area is bounded by a calc-alkaline volcanic complex (Alcione and Lametini) to the west, while to the east it is bordered by a system of normal faults that separate it from the Coastal Range in Calabria (Fig. 1.11).

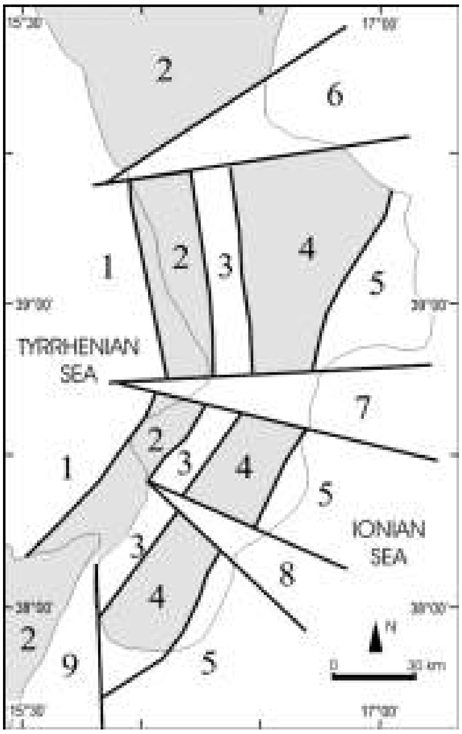

Figure 1.10- Tectonic pattern of the Calabria Arc. Black lines indicate the main faults. Key: (1) Paola and Gioia peri-Tyrrhenian basins; (2) Pollino Massif, Coastal Chain, Capo Vaticano and Mt. Peloritani highs; (3) Crati and Mesima basins; (4) Sila, Serre and Aspromonte highs; (5) Crotone-Capo Spartivento peri-Ionian basins; (6) Sibari basin; (7) Catanzaro basin; (8) Siderno basin; (9) Messina basin (Tansi et al., 2007).

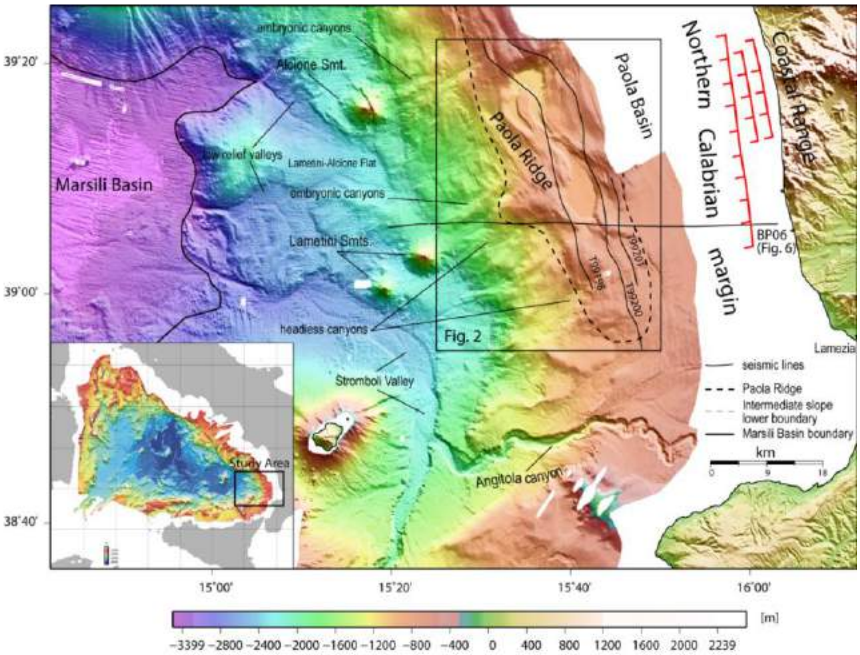

Figure 1.11- Bathymetry of the southeastern Tyrrhenian Sea, Paola Basin. The study area is enclosed in the black-lined rectangle. From Gamberi and Rovere (2010).

The main basin fill is likely related to turbiditic currents (Trincardi et al., 1995), but these turbiditic deposits pinch-out in correspondence of the Paola Ridge, which represents a topographic high and a geographical barrier for terrigeneous fluxes (Rovere et al., 2014). The Miocene and Messinian (marginal evaporites) are represented by few hundred meters of sediments visible in the deep penetration seismic data. In the Pliocene, basin subsidence accumulated more than 1.5 mm/year of terrigenous deposits. In the upper Pliocene-Pleistocene a gradual decrease in the sedimentation rate slowed down to 0.5 mm/year (Sartori, 1982).

The Paola Ridge has been interpreted to be the result of an episode of contraction occurred in the early Pleistocene (Argnani and Trincardi, 1988, Fig. 1.12).

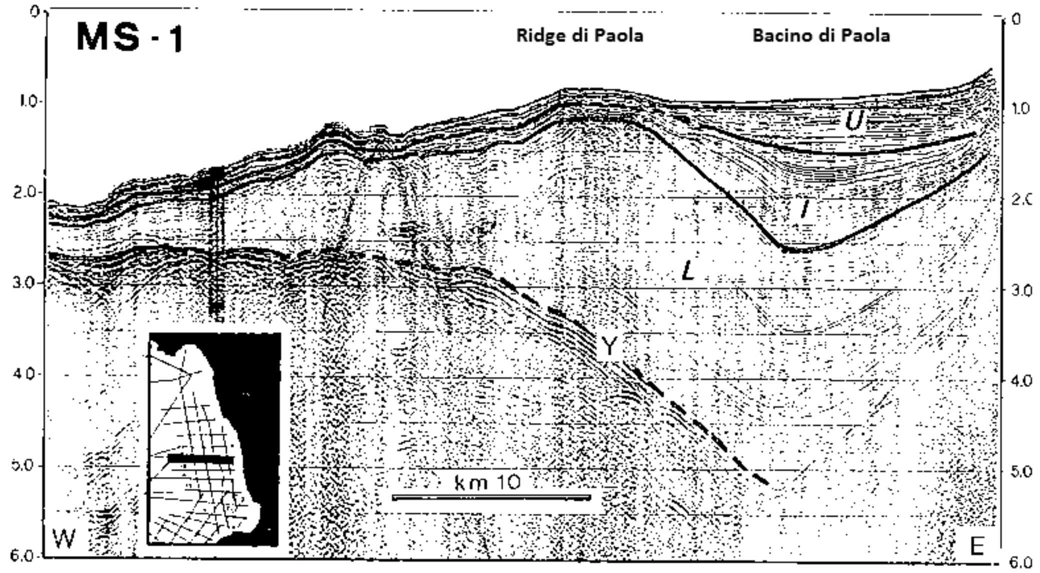

Figure 1.12- Seismic profile (MS-1) of the Paola basin, illustrating the ridge and the sequence of filling divided into units lower (L: lower, I: intermediate, U: upper). Y marks the Messinian unconformity. From Argnani and Trincardi (1993).

More recently, according to Gamberi and Rovere (2010), the Paola Ridge can be interpreted as due to a mobile mud belt, connected to a set of extensional faults trending NW- SE to NNW- SSE. The authors also demonstrated that the ridge hosts cold seep structures (Rovere et al., 2014).

1.5- Mud volcanism and diapirism

Mud volcanoes are defined as geological structures formed by fluids (fluid flow structures), gases and clay material extruded from deep sediment layers to the surface or seafloor (Dimitrov, 2002; Chen et al., 2014; Jerosch et al., 2007; Higgins and Saunders, 1974; Barber et al., 1986; Kopf et al., 1998). The extruded material forms typical morphological structures, largely varying in both shape and size (very large structures reach 10 km in diameter and a few hundred meters in height), known as “mud diapirs” and “mud pies” (Kopf, 2002; Fig. 1.13). The shapes and sizes of mud volcanoes depend on the degree of pore-fluid pressures, the frequency and character of their activity and the viscosity of the outflowing mud (Dimitrov, 2002). The mud volcanoes can be originated by a thick sequence of marine clays characterized by high sedimentation rates, sediment over-pressure, e presence of faults and salt diapirs and they are accompanied by fluid emission (gas, brines, gas hydrate water, or, rarely, oil). The term mud volcano is used to describe a more or less violent eruption.

The main components that contribute to mud volcanoes formation are: mud breccia, water and gas. The relative quantities and the exact qualitative properties of these components are relatively variable, depending on local geology and processes (Tinivella and Giustiniani, 2012), and they are characterized by complete absence of solid rock fragments. The mud breccia is basically composed of clasts in a clay mineral-rich matrix and is what makes up most mud volcanic features. The discharging gases that play a significant role in the formation of mud volcanoes are mainly from source rocks and muddy sediments and are composed dominantly of methane (about 70-99%) and related hydrocarbons (e.g. Bonini et al., 2013) although quite often carbon dioxide, nitrogen, hydrogen sulfide, argon and helium occur (Tinivella and Giustiniani, 2012; Dimitrov, 2002).

The surface expressions of mud volcanoes are highly variable and primarily depend on the fluid content and the extruded material (Brown, 1990). The morphology of the edifice is largely controlled by the viscosity of the mud. Muds with low fluid contents and low porosities (<50%) tend to form mud domes or ridges, whereas more cohesive muds with intermediate fluid content can give rise to mud volcanoes with large diameters (1–2 km) and elevation above the seafloor (<50 m), eventually high-porosity muds create mud pies (Lance et al., 1998) on the seafloor.

The geographical distribution of mud volcanoes is strongly controlled by the geological settings in which they occur (Fig. 1.14). Mud volcanoes are irregularly clustered forming belts, and more than half of the total number of mud volcanoes is located along the Alpine-Himalayas Active Belt where there are about 650 terrestrial and 470 offshore mud volcanoes, from the Mediterranean area up to the forelands of, e.g. Eastern Carpathians (Romania), Kerch and Taman Peninsulas (Arhangelski, 1932; Gubkin and Feodorov, 1940), Great Caucasus (Gubkin and Feodorov, 1940), the Black Sea (Ivanov et al., 1996), Southern Caspian Sea (Jakubov et al., 1971; Guliyev and Feizullayev, 1997; Ginsburg and Soloviev, 1994), Gorgon Plain (Iran), Makran coast (Pakistan; Higgins and Saunders, 1974), Southern Himalayas (India and China).

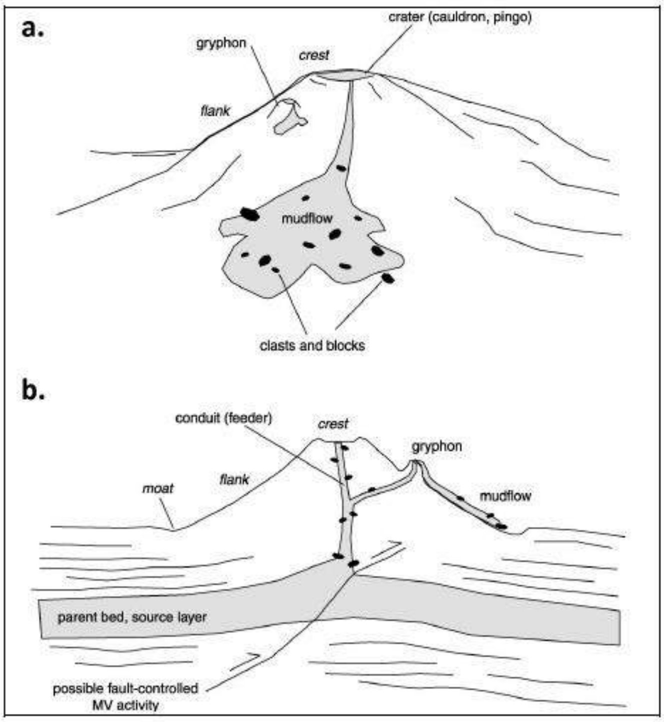

Figure 1.13 - Schematic diagrams of (a) cone-shaped and (b) pie-shaped mud feature. The gryphon is a small steep-sided cone shorter than 3 m, formed off the crest or at the flank of a mud volcano. The crater is a circular depression in the summit area, the mud flows occur when the mud travels very fast down from a slope (from Kopf, 2002).

The Pacific Ocean mud-volcano belts are situated along the eastern and western edges of the ocean. The latter contains the great majority of mud volcanoes, e.g. Nankai Trough (Kobayashi et al., 1992; Morita et al., 2004). At least 150 terrestrial and an unknown, though large, number of submarine mud volcanoes (Dimitrov, 2002) are present. Contrarily, the Atlantic Ocean mud-volcano belts are mainly located in the western and eastern middle parts of the ocean and the Southern Caribbean Sea (Higgins and Saunders, 1974), e.g. Barbados (Brown and Westbrook, 1988; Sumner and Westbrook, 2001) and Gulf of Cádiz accretionary wedges (León et al., 2007; Somoza et al., 2003).

Most mud volcanoes occur in accretionary wedges, and this is also the case of Mediterranean region, where they are predominantly located in the Mediterranean Ridge (Limonov et al., 1996; Camerlenghi et al., 1995; Robertson, 1996; Kopf et al., 1998, 2000) and adjacent land areas, such as Sicily, Albania and Southern, Central and Northern Apennines (Martinelli, 1998). Notwithstanding, others occur in extensional provinces (Fig. 1.15), such as in the Black Sea (Krastel et al., 2003; Limonov et al., 1997) and the southeastern Tyrrhenian Sea (Gamberi and Rovere, 2010).

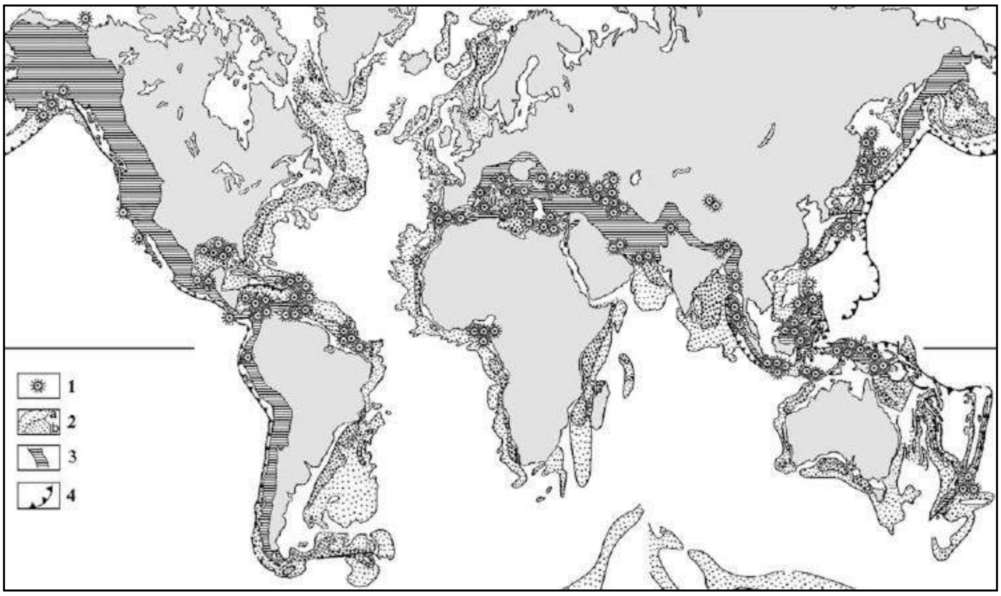

Figure 1.14- World geographical distribution of mud volcanoes. 1—single mud volcanoes, separated mud volcano areas and mud volcano belts; 2—sediment thickness in the areas out of the continental shelve; 3 -Active compressional areas; 4 Subduction zones (from Dimitrov, 2002).

In Italy there is a rich historical literature about mud volcanoes. They were already described by Pliny the Older (in his Naturalis Historia, AD 77), Spallanzani (1795) and Stoppani (1908). When the Italian mud volcanoes (e.g. Bonini, 2012) are compared to those from other parts of the world, the former are relatively smaller and less spectacular. They do not exhibit the periodic explosive activity and they are rather characterized by continuous, relatively quiescent expulsion of gas, water and mud.

Mud volcanoes are clustered in three main geographical portions of Italy, as follows: i) northern (where the largest mud volcanoes occur) and ii) central Italy and Sicily; there are also a few in southern Italy, and offshore in the Italian Adriatic Sea (Martinelli and Judd, 2004; Fig. 1.16).

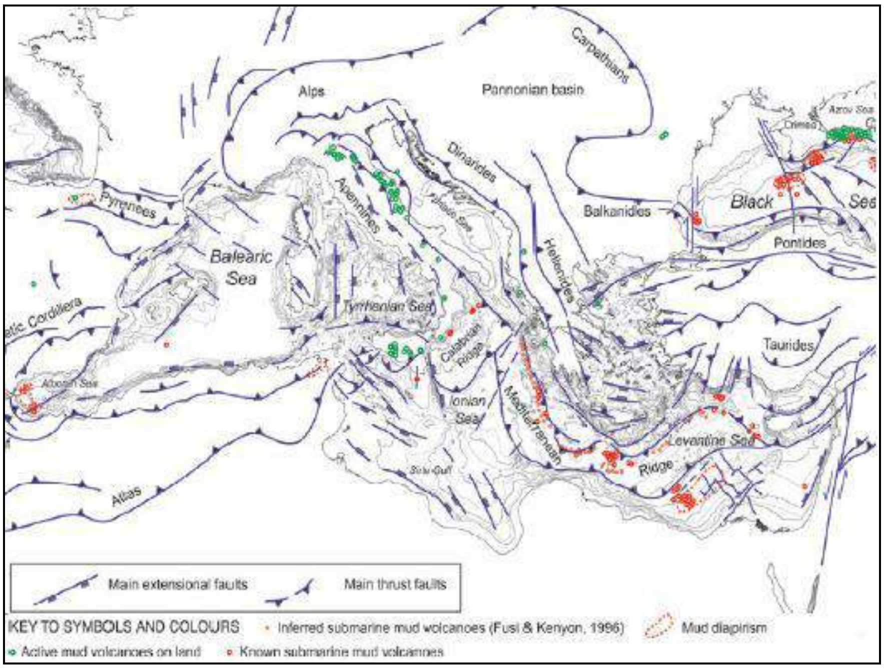

Figure 1.15- Distribution of mud volcanoes in the Mediterranean region. From Camerlenghi and Pini (2009).

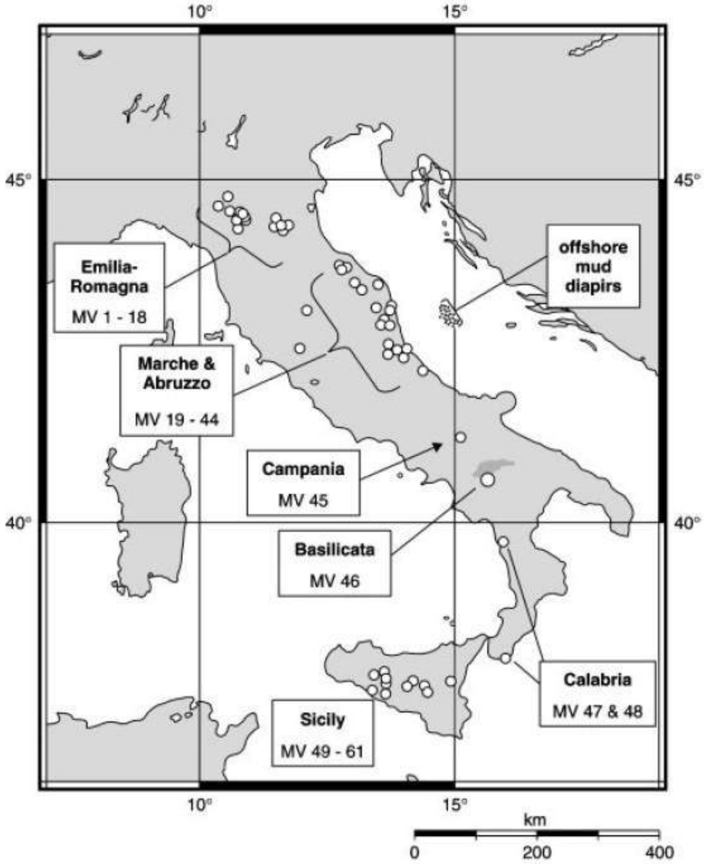

Figure 1.16 - The geographical distribution of mud volcanoes in Italy from Martinelli and Judd (2004).

Commonly or occasionally, all mud volcanoes can be associated with diapirs. Mud diapirs is an intrusive structure characterized by a slowly upward migrating mass of clay-rich sediment and fluid discharge (Kopf, 2002). A mud volcano usually occurs above the diapir, as a result of fluid migration directly along the body of the mud diaper or through faults (fractures) connected to the mud diapirs (Milkov, 2000; Kopf, 2002). Mud diapirs are driven by buoyancy forces due to the bulk density contrast between an overpressured muddy mass and an overburden of greater density (Brown,1990).

1.6- Cold seeps

Mud volcanoes and diapirs belong to a broader classification of seafloor structures, commonly known as cold seeps, because the fluids involved in the plumbing system are not as hot (max. temperature: 60 °C) as those gas discharges found in hydrothermal venting systems (up to 400 °C). They represent geological features generated by venting of fluids on the seabed. They have been known since about 25 years, and were identified in the Atlantic Ocean, the eastern and western Pacific Ocean and the Mediterranean Sea on both passive and active margins, at depths ranging between 50 and 5,000 m water depth (Whiticar and Werner 1981; Hovland and Judd 1988; Sassen et al. 1993; Aharon, 1994; Barry et al. 1996; Suess et al. 1998; Coleman and Ballard, 2001). Depending on the area and on the fluid seep activities and dynamics, cold seeps can be associated with positive sedimentary outbuilding (such as mud domes and volcanoes, carbonate mounds) or with small depressions (pockmarks), which are easily recognizable on the seafloor (Behrens, 1988; Bryant, Hovland & Judd, 1988; Kaluza & Doyle, 1996; Neurauter & Bryant, 1990; Neurauter&Roberts, 1994; Roberts, Aharon, Carney, Larkin, & Sassen, 1990).

Therefore, from now onwards, in this work the term “cold seeps” is used to indicate a wider range of seafloor structures where a series of sedimentary processes and bio-mediated reactions occur, producing a series of products, including carbonates, sulfides, oxides and where chemosynthetic benthic communities reside. Fluid seepage is in fact normally accompanied by extensive chemosynthetic life, such as microbial mats, tubeworms, chemotrophic bivalves (MacDonald et al., 1989; Fisher, 1990; Sibuet and Olu, 1998; Childress et al., 1986; Olu et al., 2004) and specific authigenic mineralization (predominantly carbonate minerals and sulfides) (Roberts and Aharon, 1993; Morse, 1994; Aloisi et al., 2000; Thiel et al., 2001; Peckmann et al., 2001). These habitats show peculiar anoxic environments. Below the top few millimeters of the surface sediment the presence of sulfides and authigenic carbonates and gas hydrates (Zemskaja et al., 2010) is indeed a typical feature of these zones. Seeps are related to geological processes such as tectonically induced high-fluid pressures, petroleum or natural gas escape, artesian flow or significant erosion processes and slides (Sibuet and Olu, 1998). Most of the fluids emitted from cold seeps are methane, carbon dioxide and hydrogen sulfide.

Small depressions (namely pockmarks, e.g. Mazurenko et al., 2003) represent seafloor features associated with fluid venting, mostly occurring on top of mud volcanoes and diapirs.

Pockmarks are depressions on the seabed and can be formed from gas and ground water seepage. They occur in areas of fluid discharges and require fine-grained sediments to sustain their structure and long existence (Hovland et al., 1984; Hovland and Judd, 1988; Hovland et al., 2002; Dimitrov and Woodside, 2003).

The density of pockmarks can vary as a consequence of underlying geology, fluid flux and nature of the seabed sediments. The shape of pockmark is often circular although, where bottom tidal currents are present, they can be elongated as their diameters can vary in the range of 10 to several hundred meters (Ondreas et al., 2005). Pockmarks can be grouped into six morphological classes (Hovland et al., 2002), as follows:

1. Unit pockmark is a small depression, whose diameter ranges from 1 to 10 m and it can be up to 0.5 m deep, likely representing a one- time expulsion event;
2. Normal pockmark is a circular depression with a diameter from 10 m up to 700 m, with a depth varying from 1 m to 45 m;
3. Elongated pockmark is a depression with one axis longer than the other. It occurs on slopes and areas of seafloor influenced by strong bottom currents;
4. Eyed pockmark contains an acoustically high-reflective area (seafloor backscatter) in its central part that is believed to be due to three possible causes: coarse material remaining after the erosive process, biological activity (skeleton remains, dead and living shells, etc) and authigenic carbonate precipitation;

Strings of pockmarks consist of unit pockmarks or small normal pockmarks arranged in curvilinear chains or strings that can be kilometers in length. They are suspected to be a result of fluid focusing along near-vertical faults, flexures or weakness zones in the upper sedimentary layer.

1.6.1- The anaerobic oxidation of methane (AOM) and the sulfate reduction zone

Anaerobic oxidation of methane (AOM) plays a major role in the sub-seafloor methane flux and in marine sediments. The main sources for methane production in ocean sediments are thermogenic methane formation and microbial methane formation in past and present. Also methane hydrates at the seafloor are releasing methane to the seawater and consequently to the atmosphere. Methane can be degraded by means of microbial oxidation under both aerobic and anaerobic conditions (Fig.1.17).

Recent studies revealed that methane diffusing upwards from deep sites of sediments often disappears before any contact with oxygen and microorganisms (methanotrophs) are thought to consume methane in such anoxic zones. However, the microorganisms responsible for this process have been isolated only very recently (Boetius, 2000). AOM was first discovered in anoxic marine sediments. It was shown that methane from deeper sediments was disappearing in the same zone, similarly to sulfate, in absence of oxygen. In such anoxic zones, sulfate is the only electron acceptor that can account for methane oxidation. AOM is catalyzed by methanotrophic archaea that form aggregates with sulfate reducing bacteria.

During AOM, methane is oxidized with concurrent sulfate reduction (SR) according to the following reaction:

$$\mathbf{CH_4+SO_4^{-2} \rightarrow HCO_3^{-}+HS^{-}+H_2O}$$

In marine sediments, AOM focuses in a region of sulfate and methane depletion, known as the sulfate-methane transition zone (SMTZ). AOM plays a major role in the sub-seafloor methane flux and in marine sediments and methane is the main energy source for the cold seep community.

1.6.2- Authigenic carbonates at seep sites

Authigenic carbonate precipitation is a widely observed process at several continental margins hosting cold seeps worldwide. The precipitation of authigenic carbonates is indeed associated with the seepage of methane-rich fluids. These carbonates are resulting from anaerobic oxidation of methane (AOM) in the sulfate reduction zone (SRZ) (Kulm et al., 1986; Hovland et al., 1987; Boetiuse et al., 2000; Greinert et al., 2001). AOM and the production of bicarbonate lead to an increase in alkalinity of pore waters and consequently leading to the precipitation of authigenic carbonate minerals and pyrite (Fig.1.18).

These deposits of carbonate build up can occur in varying sizes and shapes, from centimeter to meter dimensions, in the form of chimneys, crusts, solid pipes, cemented slabs or pavements, and irregular mounds. These carbonates are referred to as methane-derived authigenic carbonates (MDAC). All cold seep carbonates are characterized by very depleted ^{13}C carbon isotopic values (down to -62‰ V-PDB), which indicate that they are methane-derived products. Authigenic carbonates represent reliable archives of the history of seep activity. Furthermore, mineralogy, geochemical and isotopic compositions of carbonates provide information about the composition, temperature and origin of fluids from which they have precipitated.

The mineralogy of carbonates is influenced by multiple factors such as temperature, Ca^{+2}, Mg^{+2} and Fe^{+2} concentrations, complex-forming anions such as PO_4^{-3} and SO_4^{-2} and microbial metabolism (Burton, 1993; Burton and Walter, 1987; Morse et al., 1997; Savard et al., 1996), consequently the different carbonate minerals record distinct formation environments.

This bicarbonate is mostly precipitated as calcium carbonate in the aragonite crystal form, following this reaction:

$$\mathbf{HCO_3^- + OH^- + Ca^{+2} \rightarrow CaCO_3}$$

Aragonite precipitation is favored with respect to that of calcite in environments characterized by high sulfate concentration with high alkalinity concentrations, at relatively elevated temperatures and in oxic environment (Aloisi et al., 2000; Burton, 1993; Naehr et al., 2000) and for low phosphate and organic matter concentration (Burton and Walter, 1990). Consequently, aragonite is preferentially formed in more open systems, such as the sedimentary environments at or close to the seafloor. The precipitation of aragonite instead of calcite is favored in seawater, as a result of the inhibiting effect of the hydrated Mg ions on the calcite structure. These environmental conditions are met when intense methane flux moves the SMTZ to very close to the seafloor.

With regard to the occurrences of dolomite, commonly observed in organic carbon-rich marine sediments (e.g., Murata et al., 1969; Burns and Baker, 1987; Pisciotto and Mahoney, 1981; Kelts and McKenzie, 1984), several studies showed that the formation of dolomite is considered to have occurred in situ under the influence of oxidation processes of organic material by sulfate (Magalhàes et al., 2012 and reference therein). Magnesium in seawater, which is supersaturated for dolomite, tends to form the $MgSO_4^0$ ion-complex even at very low SO_4^{2-}concentrations (Baker and Kastner, 1981). Therefore, SO_4^{2-} is an effective inhibitor for dolomite precipitation, even at concentrations, less than 5% of its value in seawater. At methane seeps, where there is an efficient system of migration of sulfate-deficient and methane enriched deep fluids, the SMTZ will be pulled upwards and AOM-SR contributes to higher HCO_3^-over-saturation and the seawater sulfate will be consumed. As a result, the amount of $MgSO_4^0$ decreases and free Mg ion increases, the Mg/Ca ratio increases, these factors enhancing the dolomite precipitation (Baker and Kastner, 1981).

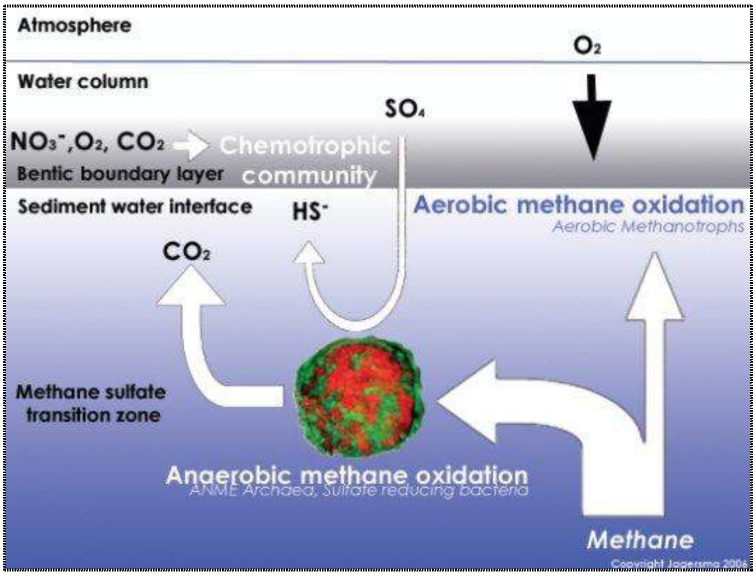

Figure 1.17 - Illustration of methane oxidation. Anaerobic methane oxidation is visualized by the red and green consortium, respectively, ANME archaea and sulfate reducing bacteria. From https://www.wageningenur.nl/en/show/Anaerobic-oxidation-of-methane.htm.

In marine environments, siderite ($FeCO_3$) is difficult to be found with respect to iron sulfides because it is not stable thermodynamically in presence of even low dissolved sulfide activities and because H_2S effectively scavenges Fe^{2+}, forming pyrite and other sulfide minerals, thereby significantly decreasing the concentrations of Fe^{2+} pore-water (Postma 1982).

Therefore, siderite formation is enhanced when: dissolved sulfide is absent, presence of high Fe pore-water concentrations and carbonate alkalinity (Mozley and Burns, 1993). Of these factors, the Fe content in pore-water is the most important in promoting the precipitation of siderite. Siderite forms in two distinct geochemical environments: one under slightly reducing conditions of the suboxic zone, and the other under strongly reduction conditions of the methanogenic zone. Suboxic conditions are available in marine environments when they are characterized by relative low concentrations of organic matter and low sedimentation rates (Berner, 1981; Coleman, 1985).

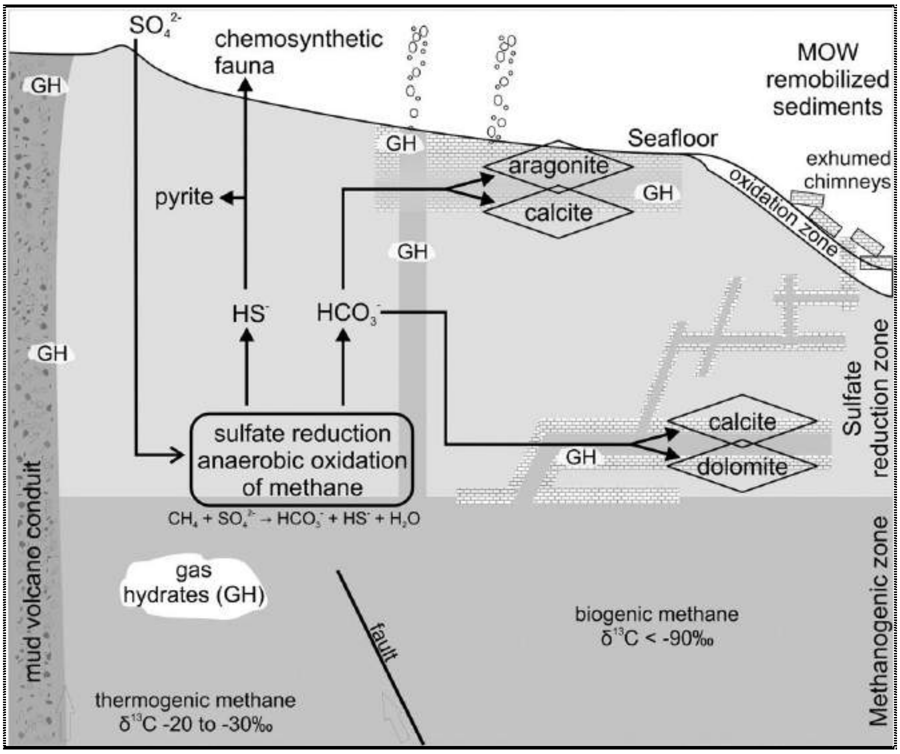

Figure.1.18- Schematic model for the formation of the methane-derived authigenic carbonates in the Gulf of Cadiz. The aragonite-dominated carbonates are formed at or close to the seawater interface whereas dolomite-dominated carbonates are formed within the sedimentary column along and around the fluid conduits (Magalhaes et al., 2012).

Siderite can also be formed in near-shore and intertidal sediments that are subject to alternating anoxic and oxic conditions (Coleman, 1985) whereas metanogenic zones are favored in environments characterized by low sulfate concentrations, high sedimentation rates and high organic carbon content (Coleman, 1985; Mozley and Carothers, 1992). The precipitation of siderite in the methanogenesis zone was noted in a variety of continental and marine sediments (Pye et al., 1990; Moore et al., 1992; Thyne and Gwinn, 1994).

1.6.3- Sulfides at seep sites

Other authigenic minerals are also found in cold seep environments and provide diagnostic information on the chemistry of the diagenetic fluids. Iron sulfides are important minerals that form in association with both organoclastic and methanotrophic sulfate reduction, or as a result of the hydrogen sulfide produced by these processes (Schulz and Zabel, 2006). The mineral pyrite is a common and widespread authigenic constituent of marine sediments where is found with organic matter and demonstrating that these minerals are by products of sulfate reduction and methane oxidation. Thus, pyrite formation involves several reaction steps: hydrogen sulfide (H_2S), produced during processes mediated by sulfate-reducing bacteria, reacts with iron to form amorphous iron sulfides and transformation of amorphous FeS to pyrite (Schulz and Zabel, 2006).

$$FeS + H_2S \rightarrow FeS_2 + H_2$$

Pyrite and iron sulfide play a central role in the sulfur and iron cycles of marine sediments (Berner, 1984; Luther et al., 1986; 1991; Jørgensen and Bak, 1991; Canfield and Teske, 1996; Berner and Petsch, 1998). FeS and FeS_2 may be buried in the sediment or oxidized by oxygen after transport by bioturbation to the sediment surface (Ferdelman et al., 1997), and they may also be oxidized within the anoxic sediment where NO_3^-, Fe(III) oxides or MnO_2 are available as potential electron acceptors.

1.6.4- Oxides at seep sites

Solid phase ferric iron is present in various iron-bearing minerals and amorphous phases of marine sediments. In oxic marine sediments, secondary Fe phases (formed by weathering of Fe-bearing primary minerals) occur predominantly as Fe

(III) oxides, hydroxides and oxy-hydroxides, (iron phases collectively hereafter referred to as iron oxy-hydroxide). Among iron oxides FeOOH and hematite are the most abundant and are mostly associated with each other.

Iron oxides/oxy-hydroxides have a high affinity for the adsorption and reduction reactivity. For example, reactive iron oxides is important significance of a large number of dissolved species, particularly phosphorus, arsenic and heavy metals through surface adsorption and incorporation.

CHAPTER 2: Materials and methods

In order to understand the mechanisms of formation and evolution of the mud volcanoes and mud diapirs and to reconstruct the marine environments in the studied portion of the Paola Basin, geophysical and geological data together with lithological, sedimentological, mineralogical and chemical and isotopic analyses were performed. The next chapter provide a summary of the techniques used during the two cruises (MVP11 and MarBeep14). Laboratory facilities at the departments of Earth Sciences of Florence and Physics and Earth Sciences of Parma, CNR-IGG (National Council of Reasearch–Institute of Geosciences and Earth Resources, CRIST (Center of Crystallography) and MEMA (Center of Electron Microscopy and Micro-Analysis) of Florence, ACME (Vancouver, Canada)and ISO analytical Limited (U.K.) is described.

2.1- The oceanographic cruises

2.1.1 – The MVP11

The MVP11 oceanographic cruise was carried out in August-September 2011 on board of the R/V CNR Urania (Fig. 2.1). The aim of the cruise was to verify the presence of cold seeps in the study area (Paola Basin). Bathymetric data, seismic (CHIRP, Compressed High Intensity Radar Pulse) profiles, gravity coring and box coring samples were acquired (Table 2.1). During the cruise, the bathymetric measurements were carried out with the multi-beamecho-sounder Kongsberg EM710 (frequency 70-100 kHz) for depths between 300 and 1,300 m while the shallow seismic data were collected using a CHIRP modulated (3-7 kHz) system.

The positioning system was represented by a DGPS Ominstar code L1 connected directly to Seatex Sea Path 200 by Kongsberg and a Seatex MRU5 (Kongsberg) attitude sensory. In addition, 36 gravity coring, 28 box cores, 3 dredges, 8 rosette and Grab were collected (Fig.2.2).

Figure 2.1-The research oceanographic vessel Urania is equipped with a precise positioning system consisting of a DGPS, Kongsberg EM710 and EM302 multi-beam systems, sub-bottom seismic profiler (CHIRP) and is suitable for the collection of samples from the seabed.

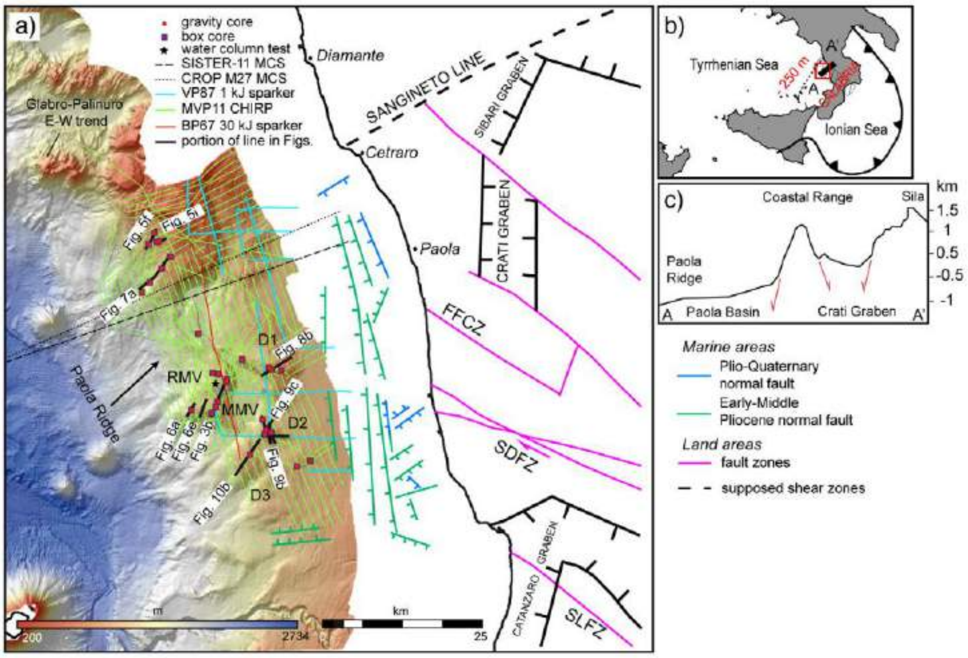

Figure 2.2-Sampling sites in the Paola Basin during the MVP11 cruise. D1-D3= diapirs; RMV= Richthofen mud volcano; MMV= Mojsisovics mud volcano; R1MV= new mud volcano (after Rovere et al., 2014).

Sampling station	Type	Depth	Structure
MVP11-GC01	gravity core	727	RMV
MVP11-GC02	gravity core	727	RMV
MVP11-GC03	gravity core	726	RMV
MVP11-GC04	gravity core	808	RMV
MVP11-GC05	gravity core	728	MMV
MVP11-GC06	gravity core	729	MMV
MVP11-GC07	gravity core	709	MMV
MVP11-GC08	gravity core	760	RMV mudflow
MVP11-GC09	gravity core	728	RMV
MVP11-GC10	gravity core	860	RMV mudflow
MVP11-GC11	gravity core	922	Propeller ridge
MVP11-GC12	gravity core	1055	R1MV mudflow
MVP11-GC13	gravity core	717	R1MV
MVP11-GC14	gravity core	530	D1
MVP11-GC15	gravity core	557	D1
MVP11-GC16	gravity core	521	D1 fault scarp
MVP11-GC17	gravity core	728	RMV
MVP11-GC18	gravity core	750	D1
MVP11-GC19	gravity core	731	D2
MVP11-GC20	gravity core	653	D2 fault scarp
MVP11-GC21	gravity core	634	D2
MVP11-GC22	gravity core	677	D3
MVP11-GC23	gravity core	680	D1
MVP11-GC24	gravity core	679	D1
MVP11-GC25	gravity core	694	D2 fault scarp
MVP11-GC26	gravity core	576	R1MV
MVP11-GC27	gravity core	570	R1MV
MVP11-GC28	gravity core	552	R1MV
MVP11-GC29	gravity core	707	R1MV mudflow
MVP11-GC30	gravity core	957	R1MV mudflow
MVP11-GC31	gravity core	617	R1MV
MVP11-BC01	box core	727	RMV
MVP11-BC02	box core	726	RMV
MVP11-BC03	box core	808	RMV
MVP11-BC04	box core	728	RMV
MVP11-BC05	box core	709	RMV
MVP11-BC06	box core	760	RMV
MVP11-BC07	box core	728	RMV
MVP11-BC08	box core	860	RMV mudflow
MVP11-BC09	box core	922	Propeller central rridge
MVP11-BC10	box core	1055	R1MV mudflow
MVP11-BC11	box core	530	D1
MVP11-BC12	box core	557	D1
MVP11-BC13	box core	521	D1
MVP11-BC14	box core	731	D2
MVP11-BC17	box core	634	D2
MVP11-BC18	box core	677	D3
MVP11-BC21	box core	694	D2
MVP11-BC22	box core	694	D2
MVP11-BC23	box core	576	R1MV
MVP11-BC24	box core	570	R1MV
MVP11-BC25	box core	552	R1MV
MVP11-BC26	box core	707	R1MV mudflow
MVP11-BC27	box core	957	R1MV mudflow
MVP11-BC28	box core	617	R1MV

Table 2.1: Location of the coring and box coring sites collected in the study area (Paola Basin) during the cruise MVP11.Depths are in meters.

2.1.2 – The MarBeep14

The MarBeep14 oceanographic cruise was conducted in June 2014 and was extended around the submarine volcano Palinuro and in the Gioia Basin (northern Sicily). During the cruise geophysical and geological surveys were performed (Fig. 2.3); furthermore, overall 16 gravity cores and 17 box cores were collected specifically in the study area (Table 2.2). The main activities and aims of the campaign were, as follows:

- bathymetric surveys and water column acoustics, with multi-beam systems Kongsberg EM710 1° x 1°(71-97 kHz) e EM302 1° x 2° (30 kHz), to identify areas of emission of fluids at the seabed, characterized by the presence of mineralization in the seafloor and sub-seafloor gas plumes in the water column;
- single channel seismic sub-bottom data were collected through CHIRP Benthos-CHIRPIII DSP-664 technology to investigate the first 50 m of the sub-seafloor Stratification;
- high resolution multi channel seismic reflection profiles, acquired with a mini GI-Gun Sercel and a 300-m-long digital multi channel streamer GeoEl (96 channels and 3.125m sections), to identify seepage system and pockmarks, transparent facies related to the presence of gas, bright reflections, normal faults associated to rising fluids;
- collection of sediment samples through gravity coring and box coring for sedimentological, geochemical, isotopic analyses and biodiversity analyses of the benthic components;
- water samples were collected by using a device for the collection of samples at different depths (Rosette). Occasionally, gas-saturated sediments were observed and the released gas was sampled when spontaneous bubbling from the box and gravity cores was evident. Two gas samples were collected at the sea surface above the R1MV structure (MB14_BC05) and the RMV structure (MB14_BC09). The main components and the $^{13}C/^{12}C$ isotopic ratios in CO_2 were analyzed in laboratory.

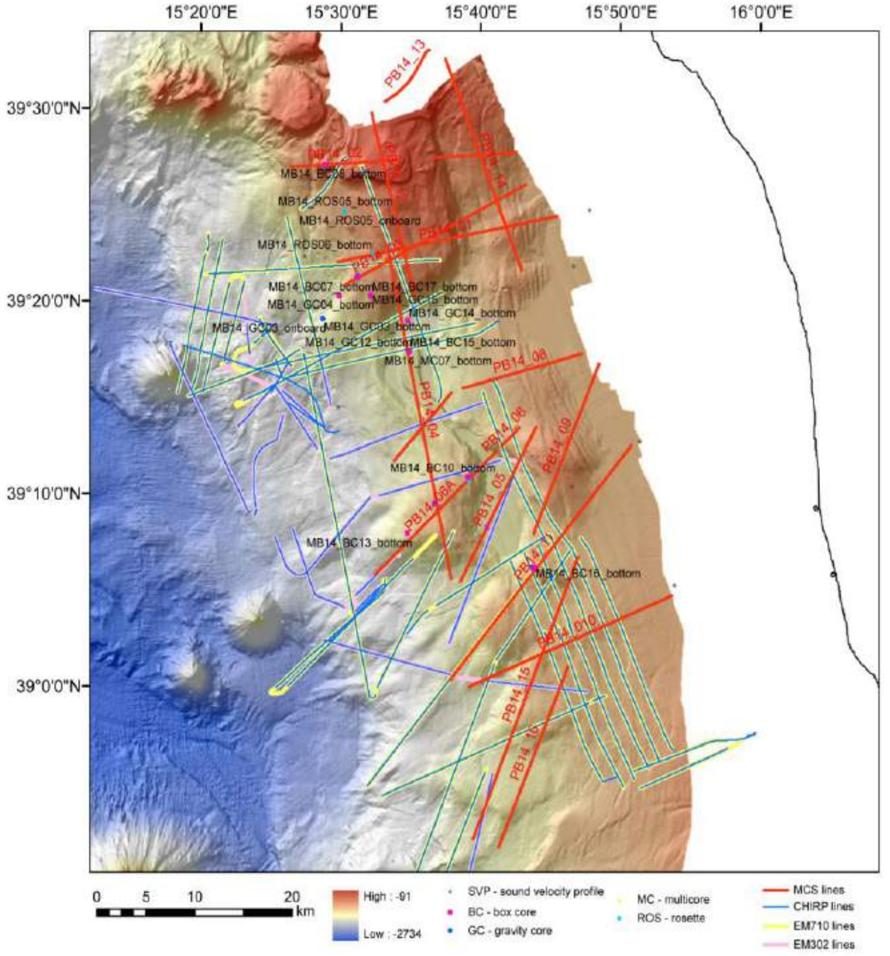

Figure 2.3-Map of coring sites and geophysical profiles acquired during the campaign MarBeep in the study area (Paola Basin).

Sampling station	Type	Depth	Structure
MB14_GC01	gravity core	710	R1MV
MB14_GC02	gravity core	700	R1MV
MB14_GC03	gravity core	1070	R1MV mudflow
MB14_GC04	gravity core	963	R1MV mudflow
MB14_GC05	gravity core	381	Mound
MB14_GC06	gravity core	725	RMV
MB14_GC07	gravity core	771	MMV
MB14_GC08	gravity core	926	South Propeller basin
MB14_GC09	gravity core	726	RMV
MB14_GC10	gravity core	870	RMV mudflow
MB14_GC11	gravity core	657	D2 fault
MB14_GC12	gravity core	942	Propeller Ridge
MB14_GC13	gravity core	711	R1MV
MB14_GC14	gravity core	1091	North Propeller basin
MB14_GC15	gravity core	652	R1MV
MB14_GC16	gravity core	778	Acquarone Ridge, pockmark
MB14_BC05	box core	710	R1MV
MB14_BC06	box core	716	R1MV
MB14_BC07	box core	968	R1MV mudflow
MB14_BC08	box core	390	Mound
MB14_BC09	box core	725	RMV
MB14_BC10	box core	725	RMV
MB14_BC11	box core	766	MMV
MB14_BC12	box core	938	south Propeller basin
MB14_BC13	box core	870	RMV mudflow
MB14_BC14	box core	661	D2
MB14_BC15	box core	947	Propeller Ridge
MB14_BC16	box core	1090	North Propeller basin
MB14_BC17	box core	652	R1MV

Table 2.2: Description of the coring sites, which were collectedin the Basin of Paola during the cruise MarBeep 14. Depths are in meters.

2.1.3- Physical Methods used during the oceanographic cruises

Hereafter, a short review of the sampling and acquisition methodologies that were used during the cruises is reported.

MULTIBEAM

A multi-beam echo-sounder is a device typically used for hydrographic surveys to determine the water depth and the nature of the seabed (reflectivity or seafloor back-scatter) in terms of estimated grain size, hard or soft seafloor etc. Most modern systems work by transmitting a broad acoustic fan shaped pulse from a specially designed transducer across the full swath across track with a narrow along track then forming multiple receive beams (beam-forming) that are much narrower in the across track (Fig.2.4). From this narrow beam, a two-way travel time of the acoustic pulse is then established utilizing a bottom detection algorithm. If the speed of the sound in water is known for the full water column profile, the depth and position of the return signal can be determined from the receive angle and the two-way travel time.

In order to determine the transmit and receive angle of each beam, a multi-beam echo-sounder requires accurate measurements of the motion of the sonar relative to a cartesian coordinate system. The measured values are typically heave, pitch, roll, yaw, and heading. The multi-beamecho-sounder is positioned below the bottom of the boat (hull-mounted) and measures the depth of the seafloor during the navigation.

CHIRP

The CHIRP (Compressed High Intensity Radar Pulse) system is a seismic reflection instrument that uses sound to determine the layering of the sedimentary strata on and below the sea floor. The produced frequencies of the sound are between 500 Hz and 12 kHz. The CHIRP has two advantages since it allows to: i) get excellent penetration (> 50 m into the seabed) and ii) perform a high resolution (vertical resolution < 0.5 m),when compared to other seismic reflection tools designed for similar purposes. First, it produces a sound (the CHIRP) that is composed by a range of frequencies. This is beneficial because the lower the frequencies the better the penetration, although higher frequencies give improved resolution. Second, the sound it makes can be repeated almost identically every time (Fig.2.5). This allows special processing called “match filtering” to reduce the noise contribution to the signal. The term CHIRP is used interchangeably with sweep signal. The software SWANPRO2.2 allows both the acquisition of the data and the display of the acquired profiles. The program may change the frequency of the pulse sent to improve the resolution, decreasing the depth of investigation, or to increase the depth at the expenses of the resolution. The CHIRP is connected with the DGPS system on board.

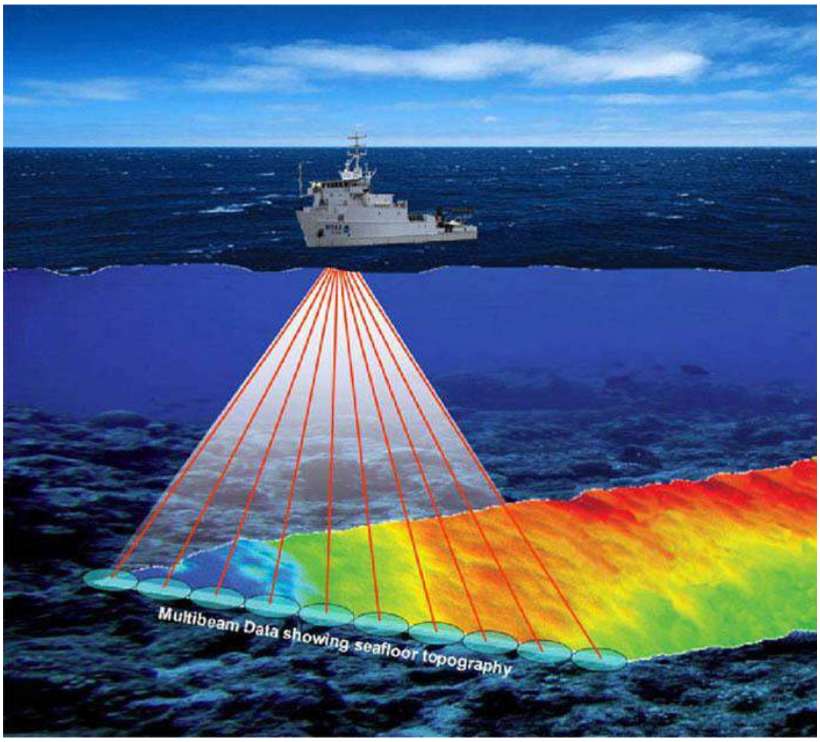

Figure 2.4 – Representation of a ship using multi-beam echo-sounder to map a swath of seafloor. **Credit:** Fisheries and Oceans Canada http://www.charts.gc.ca/about-apropos/hwd-cfn-eng.asp.

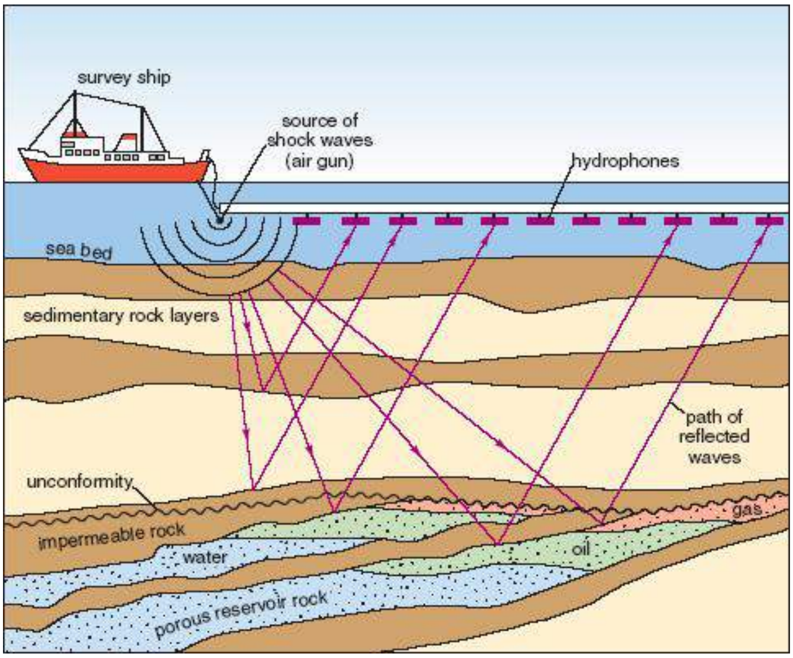

Figure 2.5 – Representation of a ship using a seismic reflection method to investigate the sub-seafloor.**Credit:**http://www.epa.gov/esd/cmb/GeophysicsWebsite/pages/reference/methods/Marine_ Geophysical_Methods/Marine _Seismic_Methods.htm.

GRAVITY CORER

The Gravity Corer is a simple and reliable instrument for collecting sediment cores from coastal and deepwater sites for sample analysis. The corer uses the pull of gravity to penetrate the seabed with its carbon steel core barrel, which can collect samples of up to 12 m in length (Fig.2.6).

The entire corer is made of carbon steel and is fitted with stabilizing fins to ensure that the corer penetrates the seabed in a straight line (Fig.2.7). The standard lead weights supplied at the coring head reach 1,2 T to allow the penetration in the sediment. A replaceable core liner is housed within the carbon steel barrel to ensure that it is simple to remove the collected sample. The barrel is fitted with a sharpened replaceable carbon steel core cutter to ensure minimal disturbance. Sample losses on retrieval are minimized by using a core catcher fitted inside the end of the barrel.

A hand-gear system, prepared in advance and at the desired height, operated by a weight, allows the free gravity fall in the last few meters from the seabed. The cores are then cut in 1m-long sections and stored in refrigerator at -5/6°C.

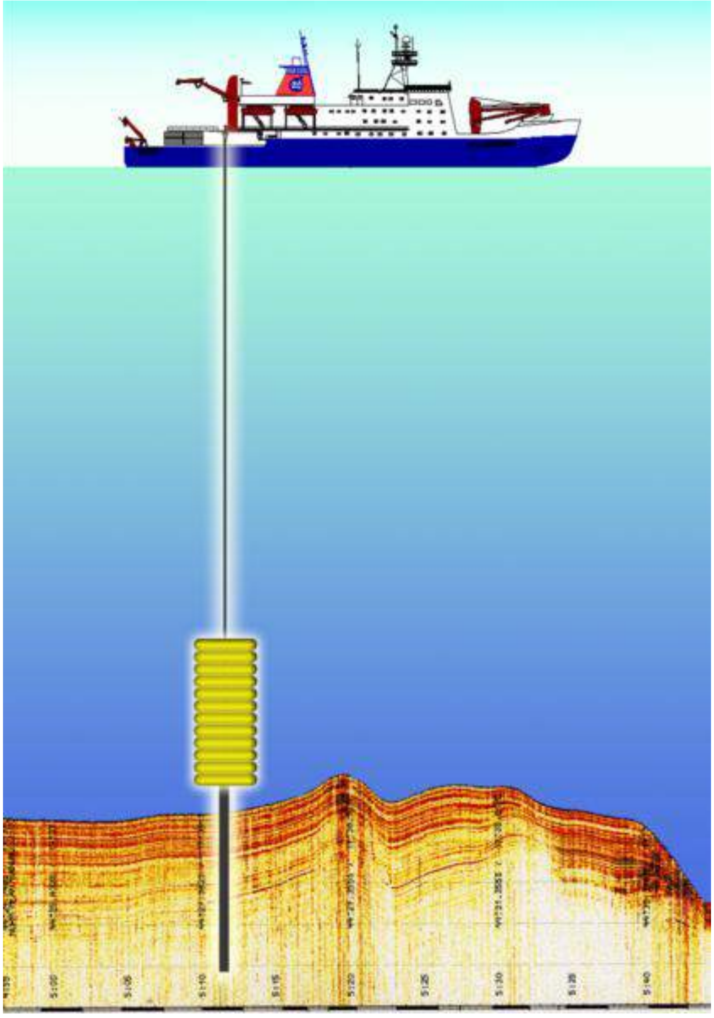

Figure 2.6 – Use ofthe gravity corer at sea. Cartoon from http://commons.wikimedia.org/wiki/File:Gravity corer_hg.png.

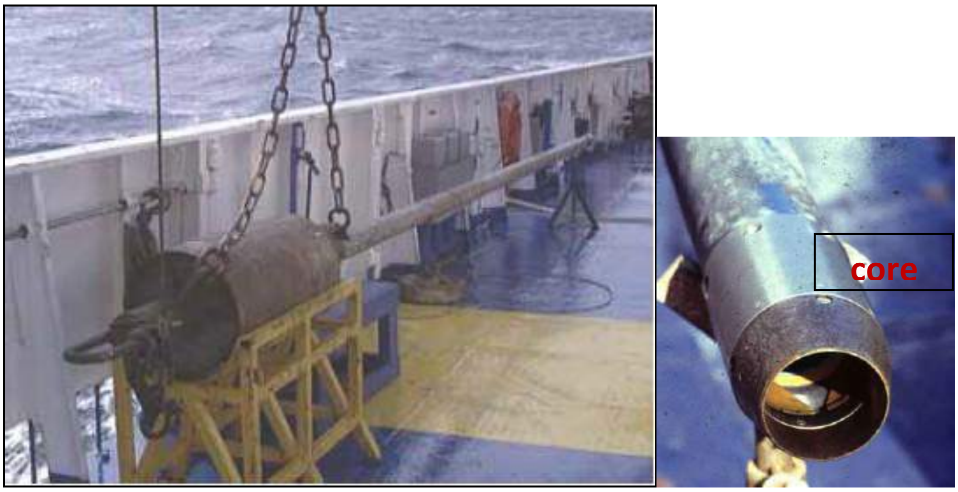

Figure 2.7-The gravity used on board the R/V Urania and its core catcher.

BOX CORER

The box corer allows to obtain larger volumes of almost undisturbed sediment with a penetration depth of about 50 cm. It consists of a hollow open metal cylinder-open at both ends. The tool, once attached to a very heavy hammer, is lowered from the ship (Fig.2.8). When the tool touches the ground seafloor sediments and seawater enters the cylinder, then a blade system closes the base of the cylinder, allowing the recovery of the sediment (Fig.2.9). This system can also be used for the virtual sampling of the water-sediment interface.

Figure 2.8-Recovery phase of the box corer once it is retrieved on the back deck of the ship

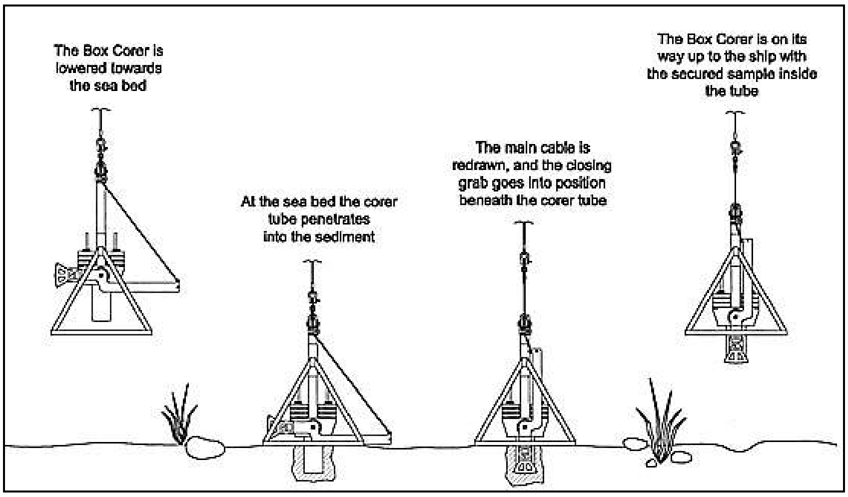

Figure 2.9–Sketch representing the functionality of the box corer. Credit: http://www.kcdenmark.dk/products/sediment-samplers/box-corer/box-corer-1000-cm%C2%B2.aspx.

THE DREDGING TECHNIQUE

The dredge is a large metal cylinder with open ends (the lower one with a mesh). It is lowered to the bottom and pulled for some distance until it is full of the rocks and sediments. It allows to sample large amounts of (fine to coarse) sediments and it is mainly used to tear hard material from the bottom.

Figure 2.10 -The dredging system.

ROSETTE

The rosette is a tool that allows to sample seawater. It is composed of 24 Niskin bottles with capacity of 10 L (Fig.2.11). The water samplers are fully made of PVC and its interior is totally free from metal parts. Top-and bottom plates are held together with a seawater resistant rubber string, and a drop messenger releases the closing mechanism at the required depth with a command passed through the drop cable. The cable is indeed attached to a weight (called "messenger") that slides along the cable and tapping on the rod triggers the closure of the bottle. The samples are then stored at -20°C. During the MVP11 cruise one station was collected for further analyses.

Figure 2.11 - Rosette system of the R/V Urania equipped with twenty-four 10 L Niskin bottles.

2.2-Materials

The samples (represented by both consolidated and unconsolidated rocks and sediments; Table2.3) analyzed for this study were obtained from cores and box cores collected during the two cruises MVP11 and MarBeep14 and can be grouped, as

follows:

1- limestone crusts sampled in the pockmarks along faults that cut the mud diapirs, these are located at a depth to 1-3 m below the seabed;

2- carbonates of tubular shape, likely precipitated in burrows excavated by crustaceans, these were retrieved from the core catcher of stations performed over mud volcanoes and their down-slope mudflows at 5-6 meters below the seabed;

3- iron oxy-hydroxide crusts found in the box cores stations on top of the mud volcanoes structures. Here, persistent and consistent gas emissions were noticed in the water column multi-beam records. These can be found a few centimeters below the seabed;

4- flat crusts of pyrite and sulfur retrieved in the upper section of the cores and in the box cores performed on top of the mud volcanoes. These can also be found

some meters below the seabed in the sedimentary succession, depending on the degree of gas
expulsion in the water column during the recovery of the gravity corer;

5- cohesive mud samples collected along the cores performed on the mud volcanoes structures.

All the samples were first dried in an oven(at 40 °C), and powdered using a planetary agate mille device to perform the mineralogical and geochemical analyses.

Samples	Position	Structure	Description
Sulfides			
Cal-L	BC25 1-25cm bsf	R1MV	Pyrite lining burrow 
Cal-Q	BC25 1-50cm bsf	R1MV	Pyrite and sulfur lining burrow 
Cal-S	GC29 II 29cm bsf	R1MVmudflow	Pyrite burrow 
Cal-Z	GC29 II 70cm bsf	R1MVmudflow	Pyrite 
Cal-W	GC29 II 83cm-4m bsf	R1MVmudflow	Pyritic sand 
Cal-X	GC29 I 74cm-5m bsf	R1MVmudflow	Pyriticsand 
Cal-Q1	BC25 1-50cm bsf	R1MV	Sulfur 
Cal-D	BC02 1-50cm bsf	RMV	Pyrite flat crusts 
Cal-K	BC01 1-50cm bsf	RMV	Pyrite pellets 
Cal-O	BC01 1-50 cm	RMV	Cemented pyrite sand 
Cal-MB1	MB14_GC09 core cather ~5.37 m bsf	RMV	Cemented dark grey slab 
Cal-MB2	MB14_GC06 core catcher	RMV	Pyrite crusts

	~5 m bsf		
Cal-MB3	MB14_BC10 1-50 cm	RMV	Pyrite and sulfur lining burrow 
Fe-oxyhydroxides			
Cal-T	GC26 coring head	R1MV	Fe-oxides 
Cal-P	BC04 1-50 cm bsf	RMV	Fe oxy-hydroxides 
Cal-F	BC04 1-50cm bsf	RMV	Fe-oxy-hydroxides 
Cal-Y	GC29 I 95cm-5m bsf	R1MVmudflow	Fe-oxides 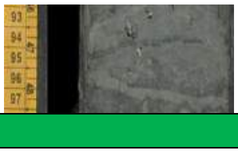
Siderite			
Cal-I	GC26 ~5m bsf	R1MV	Tubular authigenic carbonates 
Cal-G	GC12 ~6 m bsf	R1MVmudflow	Tubular authigenic carbonates 
Cal-M	GC10 5m bsf	RMVmudflow	Tubular authigenic carbonates 
Cal-E	GC17few cm bsf	RMV	Tubular authigenic carbonates 
Cal-R	GC17few cm bsf	RMV	Tubular authigenic carbonates 

Cal-A	GC17~ 6 cm bsf	RMV	Tubular authigenic carbonates 
Cal-V	GC36 ~ 6m bsf	R1MV	Tubular authigenic carbonates 
Cal-U	GC29 IV 86 cm ~2m bsf	R1MVmudflow	Tubular authigenic carbonates 
Cal-EE	GC03 III 26cm ~1.30m bsf	RMV	Tubular authigenic carbonates 
Cal-RR	GC03 IV ~35cm bsf	RMV	Tubular authigenic carbonates 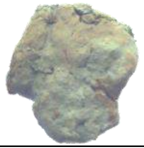
Cal-MB4	MB14_GC03 core catcher 6.20 m bsf	R1MV mudflow	Limestone burrow 
Limestones			
Cal-N	GC16 core ~10 cm bsf	D1 (fault)	Limestone crust 
Cal-C	GC16 core ~10cm bsf	D1 (fault)	Limestone crust 
Cal-B	GC20 core 40cm-1m bsf	D2 (fault)	Limestone crust with lucinids 
Cal-H	BC21 1-50 cm bsf	D2 (fault)	Light-grey cemented crust of bioclastic limestone 

Cal-CC	GC21 III 73cm ~2m bsf	D2 (fault)	Limestone pavement crust 
Cal-NN	GC21 III 82cm ~2.3m bsf	D2 (fault)	Limestone pavement crust
Cal-BB	GC21 III 99cm ~2.5m bsf	D2 (fault)	Limestone pavement crust
Cal-HH	GC21 II 52cm ~3m bsf	D2 (fault)	Limestone burrow 
Cal-AA	GC25 I 95cm	D2 (fault)	Dark-grey limestone crust with lucinids 
Mud			
Cal-1	GC17IV 77 cm	RMV	Fractured mud contains Fe-oxides
Cal-2	GC17III 65 cm	RMV	Vuggy mud containingwater
Cal-3	GC07II 21 cm	RMV	Fractured grey/brown mud
Cal-4	GC28IV 90 cm	R1MV	Homogeneous cohesive mud contains carbonate minerals
Cal-5	GC0**7** V 88 cm	RMV	Fractured mud
Cal-6	GC17I 18 cm	RMV	Silty mud with nodules andcarbonate minerals
Cal-7	GC17 core 50 cm	RMV	Brownish mud containing siderite
Cal-8	GC17 core 11 cm	RMV	Brownish mud with pyrite
Cal-9	GC08 V 60 cm	RMV	Bioturbated grey mudcontainingcarbonate minerals
Cal-10	GC08I 67 cm	RMV	Fractured mud containingcarbonate minerals
Cal-11	GC07I 85 cm	RMV	Consolidated slightly fractured mud containing Fe-oxides
Cal-12	GC28II 88 cm	R1MV	Fractured grey mud containing Fe-oxides
Cal-13	GC07IV 83 cm	RMV	Fractured mud

Cal-14	GC28II 25 cm	R1MV	Sand slightly cemented with pyrite
Cal-15	GC08II 56 cm	RMV	Fractured mud containing carbonate minerals
Cal-16	GC08V 24 cm	RMV	Mud containing carbonate minerals
Cal-17	GC20IV 22 cm	D2	Organogenic mud with high organic and water content
Cal-18	GC28II 55 cm	R1MV	Cohesive grey mud with sulfur
Cal-19	GC17II 41 cm	RMV	Slightly fractured mud
Cal-20	GC28IV 35 cm	R1MV	Vuggy mud
Cal-21	GC28IV 82 cm	R1MV	cohesive mud with pyrite mineralizations inside
Cal-22	GC17V 19 cm	RMV	Vuggy brownish mud containingFe-oxides
Cal-23	GC17 I 70 cm	RMV	High water content mud
Cal-24	GC07VI 52 cm	RMV	Cohesive mud
Cal-25	GC07I 10 cm	RMV	Fractured grayish mud
Cal-26	GC07 III 86 cm	RMV	Fractured grey/green mud
Cal-27	GC15 I 42 cm	D1	Cohesive mud
Cal-28	GC03 II 18 cm	RMV	Tefra layer
Cal-29	GC21 III 67 cm	D2	Mud with bioturbation above the carbonates
Cal-30	GC15 I 44-45 cm	D1	Tefra layer
Cal-31	GC03 IV 40-41 cm	RMV	Cohesive mud below the limestone crust
Cal-32	GC21 II 66 cm	D2	Cohesive mud below carbonates

Table 2.3: Background information, stratigraphic position and selected pictures of the studied samples.

2.3.Analytical methods

All the samples were petrographically, mineralogically and geochemically characterized by applying the following techniques: (PLM) optical petrography; XRD (X-ray diffractometry); SEM (Scanning Electron Microscopy)-EDS (Energy Dispersive

System) for morphological and semi-quantitative chemical analysis; EMPA (Electron Micro-Probe Analysis) for quantitative punctual chemical analysis of minerals; XRF (X-ray fluorescence) for bulk main chemistry; Gravimetry for LOI (Loss On Ignition), Titration for Ferrous Iron, ICP-AES (Inductively Coupled Plasma-Atomic Emission Spectrometry) and ICP-MS-bulk (Inductively Coupled Plasma-Mass Spectrometry) for trace element chemistry. For selected samples, stable isotopic analyses (carbon, oxygen and sulfur)were carried out by EBGMS (Electron Bombardment of Gas Mass-Spectrometry). In addition, IC (Ion Chromatography) and GC (Gas Chromatography) were used for the analyses of the main components in the liquid and gas phase, respectively.

2.3.1 Optical Microscopy in transmitted light (PLM)

Polished 30 µm thick thin sections were observed in transmitted light (PLM) – cross-polarized light (XPL) and in plane-polarized light (PPL) - in order to determine the petrographic and textural-structural features. The petrographic investigations were carried out on thin sections at the Department of Earth Sciences (University of Florence) using a microscope ZEISS Axio Skope.A1, equipped with a video camera (resolution 5 Megapixel), provide with an Axio Vision image analysis (Fig.3.12).

2.3.2 X-Ray diffractometry (XRD)

The X-rays are electromagnetic radiation of high energy (>1 keV), characterized by a shorter wavelength than that of visible light, between about 1nm and 0.001 nm.

The powder X- ray diffractometry is a technique that is based on X-ray diffraction by the lattice planes of the analyzed substance, allowing qualitative mineralogical analyses and the semi-quantitative analyses of the clay fraction (<4µm; at a content> 5% of the total mass inside). The powdered sample is manually mounted on a plate (plexiglass, glass or other suitable material) and placed in the sample holder of the instrument. The sample, hit by a radiation with monochromatic wavelength (λ), diffracts at a certain angle (θ). The X-ray diffraction can therefore be assimilated to a sort of "reflection" by the lattice planes of a crystal affected by X-rays. The X-raydiffraction is obtained from a crystal lattice when it is satisfied the Bragg's equation (Klug and Alexander, 1969):

Bragg's equation: $n\lambda = 2d \sin\theta$

λ: is the wavelength of the X-ray; θ: is the angle of diffraction; d: is interplanar distance

The XRD analyses were performed at the laboratories of the Department of Earth Sciences (University of Florence) using an X-ray Philips PW 1050/37 diffractometer (Fig.2.13), with the X'Pert PRO Philips acquisition system, operating at 40 kV-20 mA, with a Cu anode, graphite monochromator at an interval 2θ of 5-70° and 2-32° for the clay analysis (limit of detection 4%). The instrument was used for the mineralogical semi-quantitative characterization of the studied samples and according to the amount of phyllosilicates, the clay fraction was specifically separated and analyzed. The semi-quantitative evaluation was obtained from the elongation of the peaks of the mineral phases both on the bulk sample and on the clay fraction.

The analysis of the clay fraction was carried out according to the following methodology proposed by Cipriani :

The clay fraction < 4 mµ was obtained following the method by Cipriani (1958): few grams (1.5 g) of powdered samples were placed in about 50 mL of deionized water, dispersed by ultrasonic treatment and centrifuged to wash. After repeating these steps (at least 4 times), the wet sediment was transferred to sedimentation cylinders at which water (100 mL) was added and allowed to settle for one hour to separate the < 4µm clay fraction. Once discharged the surnatant, few mL of deionized water were added to the separated solid fraction and agitated with a glass rod. About 3-5 mL of the water-sediment suspension was placed on the plexiglass plates and left to dry before diffrattometric analyses. The clay minerals were recognized and semi-quantitatively estimated after 4 steps, as follows:

1- on the dry sample without any furthertreatment;

2- on the dry sample ontosprayed ethylene glycol was added;

3- on the dry sample after heating in a ventilated stove at 450 °C for an hour and a half;

4- on the 450 °C sample after heating in a ventilated stove at 600 °C for an hour and a half.

These treatments lead to the displacement or disappearance of the basal reflections to some clay minerals, allowing their identification. As previously mentioned, the semi-quantitative evaluation was obtained from the elongation of the peaks, on the clay fraction, after the 4-steps treatment (dry sample, glycolates, heated at 450 °C and 600 °C) (Cipriani,1958; Banchelli et al., 1997).

The quantitative analysis was evaluated by Maud v2.2 program (Material Analysis Using Diffraction). It is a general diffraction/reflectivity analysis program mainly based on the Rietveld method.

Figure 2.12 – The Zeiss Microscope Axio Scope at the Department of Earth Sciences (University of Florence).

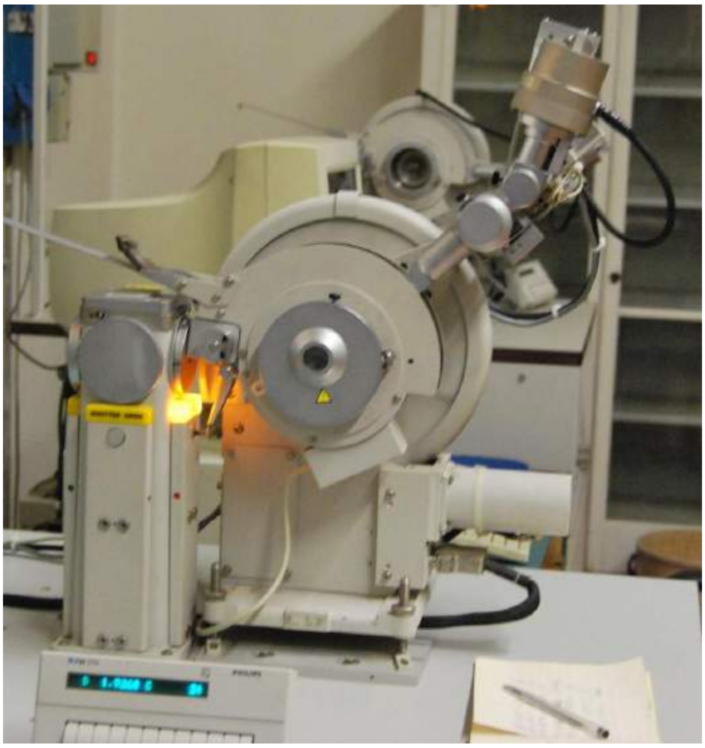

Figure 2.13–The PHILIPS PW 1050/37diffractometer at the Department of Earth Sciences (University of Florence).

2.3.3 The scanning electron microscope (SEM-EDS)

Morphological and morphometrical images with high resolution and micro-chemical analyses were obtained by using a ZEISS EVO MA15 Scanning Electron Microscope (Fig.2.14) with microanalysis (EDS) OXFORD INCA 250 at the M.E.M.A (Interdepartmental Centre for Electron Microscopy and Microanalysis- University of Florence). In the scanning electron microscope, equipped with an energy dispersive spectrometry (SEM-EDS), a "probe" consisting of a very thin electron beam with energy up to 30 keV is focused on the sample surface via a microscope and is induced to exert a scan in the form of a succession of parallel lines. The micro-chemical analyses were carried out on thin not covered sections and rock and mineral fragments after carbon coating. The semi-quantitative chemical analysis (microanalysis) by SEM-EDS was performed by measuring the energy and the intensity distribution of X-rays generated by the electron beam on the sample using the EDS detector.

2.3.4 The electron microprobe (EMP) analysis

The electron microprobe is an analytical method that used for determining the element of solid sample. Through the utilization of a Wavelength Dispersive System (WDS) it is possible to obtain quantitative punctual chemical analyses (for elements with Z>8) of minerals (e.g. silicates, phosphates, carbonates, oxides), after the calibration via suitable standards. Besides, it is possible to perform back-scattered and secondary electrons images and acquire maps of different elements, dosed with either WDS or Energy Dispersive Spectrometry (EDS) techniques. It is possible to acquire EDS spectra in few seconds, just to get a semi-quantitative or quantitative (in this case a standardization is compulsory) analysis of the investigated solid. The samples to be analyzed must be polished and metalized by the application of a thin layer of graphite. The chemical analyses were carried out on thin sections of rock samples at the CNR-IGG of Florence using an Electron Microprobe JEOL JXA-8600 (Fig.2.15), is equipped with four Wavelength Dispersive Spectrometers, each one containing two analyzing crystals and an Energy Dispersive Spectrometer.

Figure 2.14 -Scanning Electron Microscope ZEISS EVO MA15 with microanalysis EDS OXFORD INCA 250http://www.mema.unifi.it/CMpro-v-p-18.html.

Figure 2.15 - Electron Microprobe JEOL-JXA 8600 at the CNR-IGG of Florence.

2.3.5 The Dietrich-Fruhling Calcimeter

The calcimetric analysis was used to determine the amount of $CaCO_3$ occurring in the sediment samples. This analysis was carried out on selected mud samples by using a Dietrich-Fruhling Calcimetr (Fig.2.16), which is based on the quantity of carbon dioxide developed by a chemical reaction between a specific quantity of the sample (defined according to environmental temperature and pressure conditions (measured during the analysis with a high-precision barometer and Hg-thermometer with a precision of 0.1 °C, respectively) and a solution of HCl and water with 2:3 ratio, according to the following chemical reaction:

$$CaCO_3 + 2HCl \rightarrow Ca^{2+} + 2Cl^- + CO_2 + H_2O$$

The powdered and weighed sample is placed at the bottom of a 250 mL conical flask along with a 12 mL tube containing 10 mL of diluted HCl. Once the flask was connected to the calcimeter, the HCl solution is let reacting with the sample and CO_2 is formed. As the reaction is exothermic the CO_2 flux passes through a serpentine cooled with water. CO_2 then lowers the water contained in a 150 mL burette, causing a slight depression on the vial positioned on a rod opposite the lowering pipe level to equal the same level of that contained in the graduated tube. A few minutes are then waited until the stabilization of the meniscus level and scan the volume of CO_2 are achieved.

The amount of $CaCO_3$ is then calculated according to the following formula:

$$\frac{V+Y}{2}$$

$Y = 0.014 * v + 4.64$

V: volume of CO_2 developed; Y: correction to be done by considering the absorption of carbon dioxide from the solution of hydrochloric acid. The amount of sample to be weighed and the correction (Y) are listed in two tables with which the calcimetry is equipped.

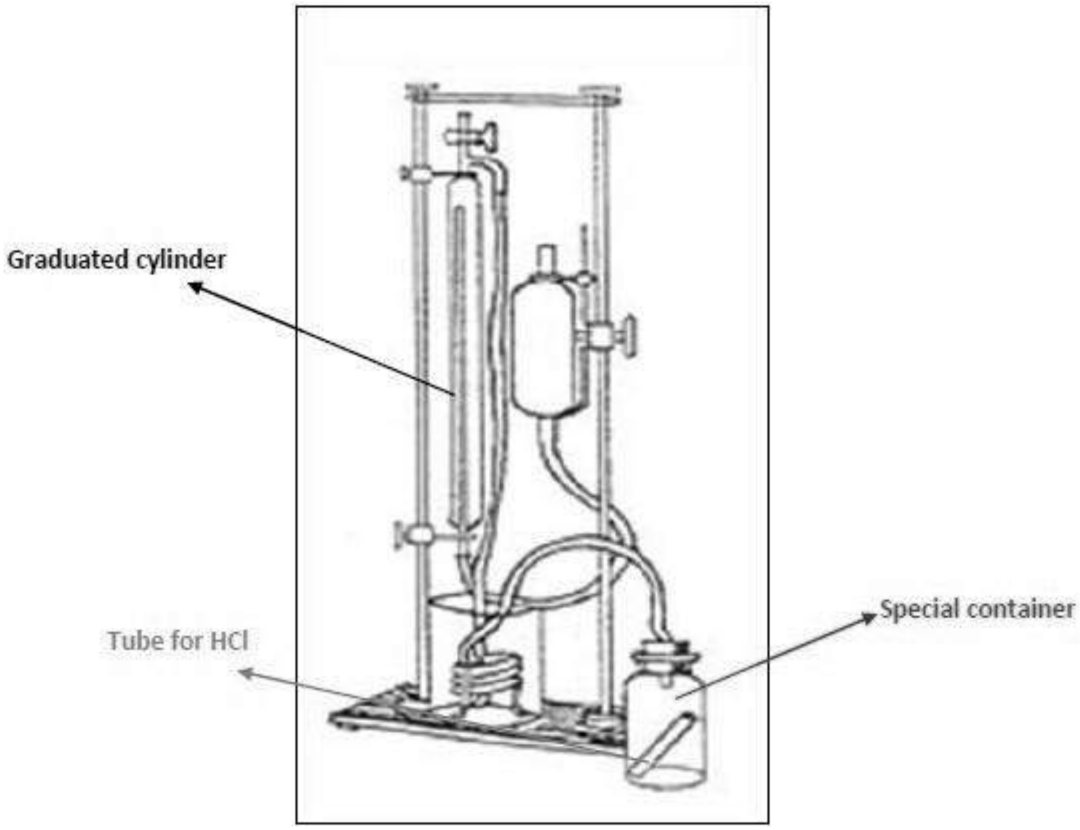

Figure 2.16– Schematic representation of the Dietrich-Fruhling Calcimeter.

2.3.6 X-Ray Fluorescence (XRF), LOI and Ferrous Iron (FeO)

The chemical composition of the studied samples was performed by using the X-ray Fluorescence (XRF) on pressed powder pellets with a Rigaku II wavelength dispersive spectrometer with a Rh anode (Fig.2.17). The main composition was acquired with a ZSX Rigaku Software Package version 3.50 and quantified with the SQX semi-quantitative elemental analysis routine by the fundamental parameter (FP) method without the use of reference standard samples. In the quantifying process, a sensitivity library (Rigaku analytical system) was used and has the FP sensitivities for every element. Pure metals and reagents were used for the calibration.

Total volatile components (e.g. H_2O^+ and CO_2) were determined as Loss On Ignition (L.O.I.), which was determined by gravimetry. About 0.5 g of powdered samples were weighed into quartz-fiber crucibles and then heated by using a CEM microwave oven. The samples were stored for 2h at the temperature of 950 °C. Samples, previously dried at 110 °C, were used for this measurement. To calculate the loss of weight (in %), the following formula was used:

$$L.O.I = \frac{\underline{W_b - W_c}}{W_a} * 100$$

W_a: weight of powder, in grams;

W_b: weight of the crucible containing the dry powder, in grams;

W_c: weight of the crucible containing the ignited dry powder, in grams.

The concentration of FeO was calculated by volumetric titration with Potassium dichromate (N: 0.400) ($K_2Cr_2O_7$) on a quantity of powdered sample (up to 0.5 g), transferred to a 10 mL Pt capsule and solubilized by 10 mL of H_2SO_4 and 5 mL of HF (Shapiro and Brannock, 1962) under a Bunsen burner. Natrium-diphenylamine-sulfonate (solubilized in H_2SO_4) was used as indicator. To compute the amount of FeO (in % by weight), the below-reported formula was applied.

0.4*mL of titration solution

2.3.7 Inductively Coupled Plasma (Mass) Spectrometry (ICP-AES and MS)

Selected trace elements were determined by ICP-AES and ICP-MS (Ba, Be, Co, Cs, Ga, Hf, Nb, Rb, Sn, Sr, Ta, Th, U, V, W, Zr, Y, La, Ce, Pr, Nd, Sm, Eu, Gd, Tb, Dy, Ho, Er, Tm, Yb, Lu, Mo, Cu, Pb, Zn, Ag, Ni, As, Au, Cd, Sb, Bi, Hg, Ti and Se) at the ACME Laboratories resolution (Canada).

Inductively Coupled Plasma (ICP): is a widely used plasma sourced method for the measurement of trace metals concentration. ICP is a technique that uses a plasma source coupled with a quadrupole mass spectrometer (ICP-MS) or with an optical detector (photomultiplier) in the case of the ICP-AES. The powdered samples, weighed (about 0.2 g) in PTFE tubes, were dissolved with the three-acid (HCl-HF-HNO_3) dissolution method, in a microwave oven. From each sample, an aliquot of approximately 5mL was transferred to 10 mL tubes and placed in an automatic sampler. About 0.5 mL of each sample were convoyed to the plasma torch by a pump via a 70 cm long capillary tube. The basic principle of this instrumentation is that to provide a stream of argon, which transports the vaporized sample in an plasma torch, where temperatures of 6000-8000 °C are achieved and where ionization and atomization of the various analytics occur. The resulting plasma is aspirated and transported to the detector. In the case of an ICP-MS is a quadrupole to detect the various elements as a function of the mass/charge ratio. This implies that for each element an appropriate isotope was selected in order to determine the quantitative analysis, according to the respective natural isotopic abundance. Internal and international standards were used to define the accuracy and precision of the analysis. In the ICP-AES the spectral composition of the light emitted from the source through a monochromator (diffraction grating) is analyzed, which splits the incoming light in the spectra that are intercepted by a photomultiplier. The plasma is produced by the interaction of an intense magnetic field (produced by radio frequency - RF - passing through a copper coil). In the center of this coil is placed the torch that consists of 3 concentric quartz tubes through which the Ar gas streams pass. The plasma is induced by the flow of Ar.

The ICP-MS technique is commonly used for the chemical analyses of liquid samples, for solutes between the mass of Lithium up to that of Uranium. In addition the simultaneous determination of several elements provides the consequent advantage of reducing considerably the time of analysis. The purpose of a mass spectrometer is to carry out the separation of various analytes according to the mass (m) / charge (z) ratio of the ions under vacuum conditions.

The instrumentation used is an Agilent Technologies 7500ce ICP-MS mass spectrometer (Fig.2.18) with plasma source with collision cell, Shield Torch and ISIS system, and an ASX520 automatic sample.

Figure 2.17 - Fluorescence spectrometer of dispersive X-ray wavelength http ://www.crist.unifi.it/CMpro-v-p-16.html.

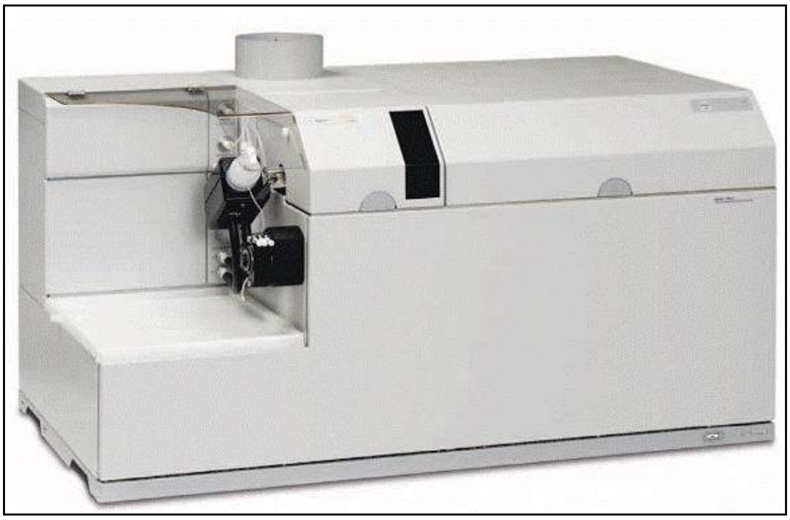

Figure 2.18 Agilent 7500ce ICP-MS.

2.3.8 Electron bombardment of gas mass spectrometry (EBGMS)

Stable isotopes (C and O) measurements on carbonate minerals were carried out on selected samples. The preparation of the samples for the isotopic analysis was carried out on the powdered muds at the Department of Earth Sciences of Florence. Prior the analysis the powdered samples were ignited under vacuum at 550 °C for removing the presence of organic matter. Then, the samples were transferred in 25 mL flasks equipped with a glass tap and let reacting with 4 mL of 100% anhydrous phosphoric acid at 25 °C after degassing H_3PO_4 under vacuum. The samples were successively placed into a thermostatic bath at the temperature of 25 °C±0.1 for at least 8h ($CaCO_3$ samples). Once the samples were removed from the bath they were connected to the extraction and purification isotopic line (Fig.2.19). The following steps were then carried out, as follows: 1-) extraction: turn on the display pressures Multi Gauge, open the valve of connection to the pump, place the trap of nitrogen (liquid at -195°C) for the condensation of CO_2 and H_2O, open the sample holder taps to transfer the released gas to the liquid-N_2 trap and wait 5 minutes for homogenizing the temperature. While opening the sample valves for about 10 seconds each, in the cryogenic trap the formation of a white halo (condensed CO_2 and H_2O) can be seen. Wait until complete the condensation has occurred, then close the samples (ca. 10minutes);

2-) purification of CO_2: the liquid nitrogen trap was then replaced with a trap of nitrogen and trichloroethylene (in equilibrium solid-liquid at -54 °C) to release of CO_2 by keeping condensed H_2O, close the valve of connection to the pump, place N_2 liquid traps below the sample holders, close the sample holders except the one corresponding to the sample where CO_2 is being collected, open the taps corresponding to the sample holder and open the valve of connection to the pump, wait for the stabilization of pressure then close them. After that transfer CO_2 to the N_2 trap where the sample holder was placed. For the samples containing calcite-dolomite-siderite, a selective separation was carried out to obtain the isotopic analysis of each carbonate phase. The isotopic analyses were carried out on powdered sample (<200 mesh) at the Department of Physical and Earth Sciences of Parma. These samples were let reacting, under vacuum, with 100% phosphoric acid at 25 °C and 50 °C for different time intervals: 1-) extraction of CO_2 from calcite, after a 2h reaction with phosphoric acid at 25 °C; 2-) removal of CO_2 from residual calcite after 24h; 3-) extraction of CO_2 from dolomite, after a 72h reaction with phosphoric acid at 50 °C and 4-) extraction of CO_2 from siderite, after 30 days reaction with phosphoric acid at 25 °C (Al-Aasm et al., 1990).

The carbon and oxygen isotopes in CO_2 were analyzed using a Finnigan Delta S mass spectrometer(Fig.2.20). The $\delta^{13}C$ and $\delta^{18}O$ values are reported in per mill (‰) relative to the V-PDB (Vienna Pee Dee Belemnite) standard with precision ±0.3 ‰.

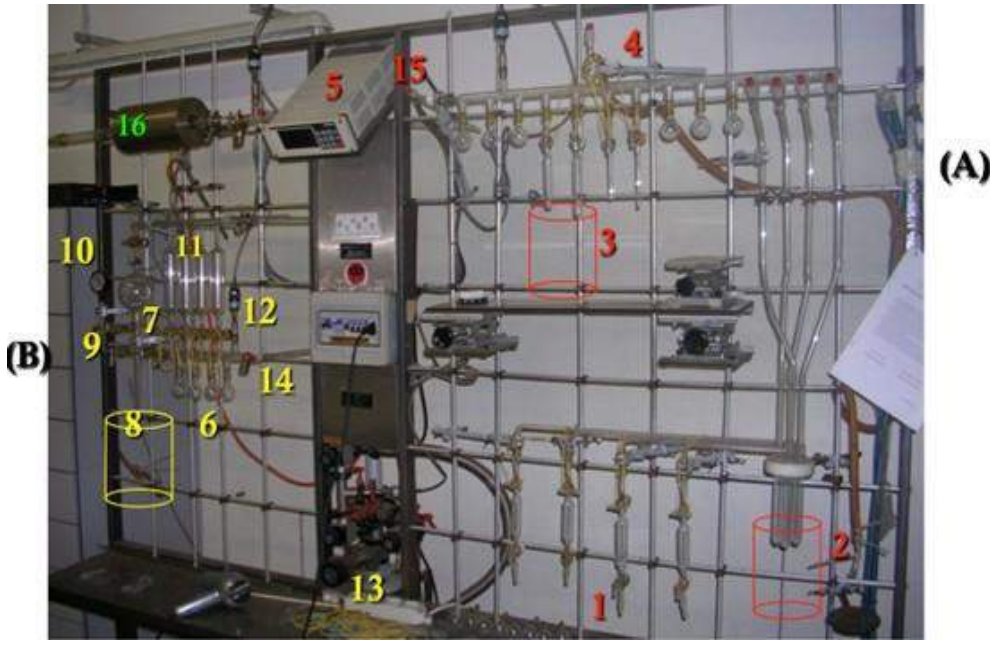

Figure 2.19 -line of purification and extraction for isotopic analyses of water (oxygen and hydrogen), gas (carbon to CO_2) and solids (carbon and oxygen in carbonates): A) purification and extraction zone of gas; B) zone preparation of water. 1) sample connections; 2) trap of N_2 liquid; 3) fitting sample holder with 2nd trap; 4) pressure valve control; 5) display pressures; 6) sample connection; 7) expansion CO_2 flask; 8) liquid-N_2 vial; 9) connection to the CO_2 cylinder; 10) barometer; 11) lung expansion; 12) pressure control valve ; 13) fitting pumps; 14,15)valve of connection to the pump; 16) oven.

Figure 2.20 -Finnigan Delta S mass spectrometer supplied at the University of Parma.

2.3.9 Elemental analyses-Isotope Ratio Mass-Spectrometry (EA-IRMS)

The isotopic analyses of sulfur in sulfide minerals were measured at the ISO Analytical Ltd.(U.K.) and measured by elemental analyzer isotope ratio mass spectrometry using a Roboprep-CN linked to a 20-20 mass spectrometer (Fig.2.21), Europe scientific, Crewe, UK. The isotopic analysis of sulfur requires the production of sulfur dioxide. To prepare sulfur dioxide through combustion of sulfides with cuprous oxide (Cu_2O) the method by Robinson and Kusakabe (1975) was followed: sulfide samples are mixed with an excess of Cu_2O and ground to grain size at about 150 µm in a small agate mortar. The sample plus Cu_2O are then transferred to a small ceramic boat that was pre-heated to remove sulfur contamination. The ceramic cell is then placed into a quartz tube, which is sealed at one end, together with a magnetic pusher. The quartz tube is then connected to a vacuum line and evacuated. The resulting SO_2 peak enters the ion source of the IRMS, where it was ionized and accelerated. Gas species of different mass were separated in a magnetic field and simultaneously measured by a Faraday cup universal collector array. The isotopic analysis was based on monitoring of m/z 48, 49 and 50 of SO^+ produced from SO_2 in the ion source. The $\delta^{34}S$ values are expressed in per mill (‰) relative to the V-CDT(Vienna Canyon Diablo Troilite).

The reference material used for analysis was IA-R061 (Iso-Analytical working standard barium sulphate, $\delta^{34}S$ V-CDT= +20.33‰).

IA-R025 (Iso-Analytical working standard barium sulfate, $\delta^{34}S$ V-CDT= +8.53‰), IA-R026 (Iso-Analytical working standard silver sulfide, $\delta^{34}S$ V-CDT= +3.96‰) and IA-R061 were used for calibration and correction of the ^{18}O contribution to the SO^+ ion beam. Working standards are traceable to NBS-127 (barium sulfate, $\delta^{34}S$ V-CDT= +20.3‰), IAEA-SO-5 (barium sulfate, $\delta^{34}S$ V-CDT = +0.5 ‰) and IAEA-S-1 (silver sulfide, $\delta^{34}S$V-CDT = -0.3 ‰). Test samples of IA-R061 and IAEA-SO-5 were also measured as quality control check samples during analysis of our samples.

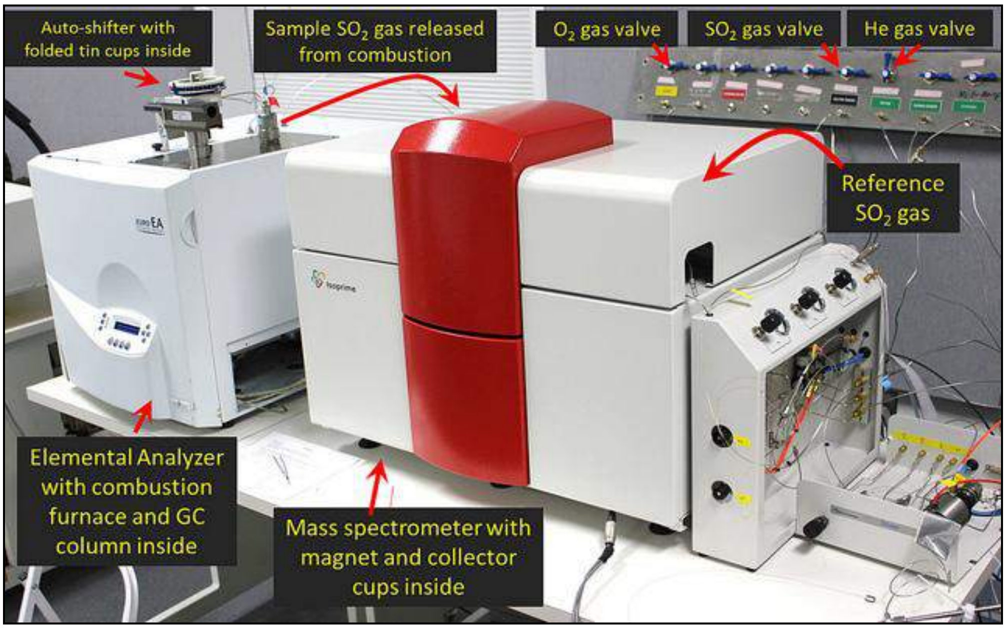

Figure 2.21- EA-IRMS Elemental Analyzer-IosPrime Isotope ratio Mass Spectrometer.

2.3.10 Ion chromatography

The chromatography is a separation technique of the components of homogeneous mixture, which is based on the distribution of its components between a mobile and a stationary phase. The ion exchange chromatography, or simply ion chromatography (IC), is the type of chromatography that is based on the principle of attraction between the oppositely charged ions. The chromatographic technique is used for the determination of cation (Na^+, K^+, Ca^{2+}, Mg^{2+} and NH_4^+) and anion (Cl^-, SO_4^{2-}, NO_3^-, Br^- and F^-). The sample is placed in the meter circuit by means of a syringe and then enters inside the chromatographic separation column filled with an ion exchange resin (Fig.2.22). The chemical analyses of waters were carried out at the Department of Earth Sciences of the University of Florence using Metrohm 861 and 761 ion chromatographers, respectively.

2.3.11 Acidimetric titration for bicarbonate

The volumetric titration is the determination of the concentration of certain species by measuring the volume of a solution of known concentration (standard solution or titration) required for reacting the solution quantitatively with the test substance. Through this technique the alkalinity can be measured, corresponding to the concentration of the bicarbonates. The concentration of bicarbonates in the samples is obtained by using a titration automatic Metrohm 794 Basic Titration equipped with a combined glass electrode and calomel electrode for the pH measurement, an automatic burette for the addition of the titration and a magnetic stirrer to homogenize the sample (Fig.2.23). The titration is 0.01M HCl.

During the volumetric titration, the titration curve acidimetric is obtained (Fig.2.24), in which it is interested to obtain the inflection point or "equivalence point", in which there is complete neutralization of the analyte by titrating agent (acid). The inflection point, corresponding to pH ~ 4.3, indicates the appearance in solution of bicarbonates or from the complete transformation of bicarbonate (HCO^-_3) into carbonic acid (H_2CO_3). The concentration of the bicarbonates (in mmol / L) is obtained by the formula:

$$\text{mL}_{\text{titration solution}}*0.01(\text{HCl in mol/L})/\text{mL sample}*100$$

The number of mL of titration solution is read in acidimetric curve at the inflection. The analytical errors for IC and titration were ≤ 5%.

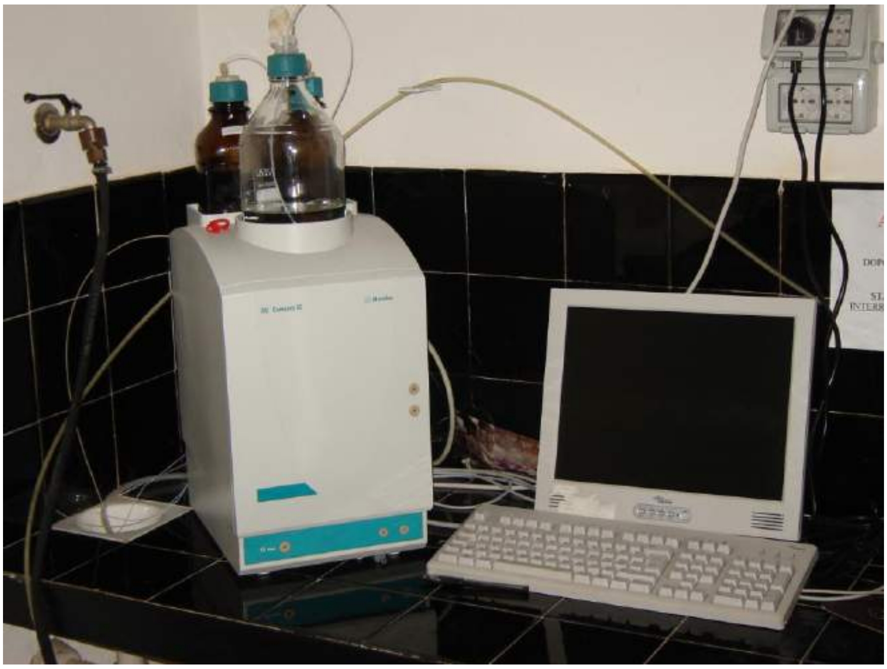

Figure 2.22- Metrohm 761 ion chromatographers for anions.

Figure 2.23- Metrohm 794 Basic Titration for bicarbonates.

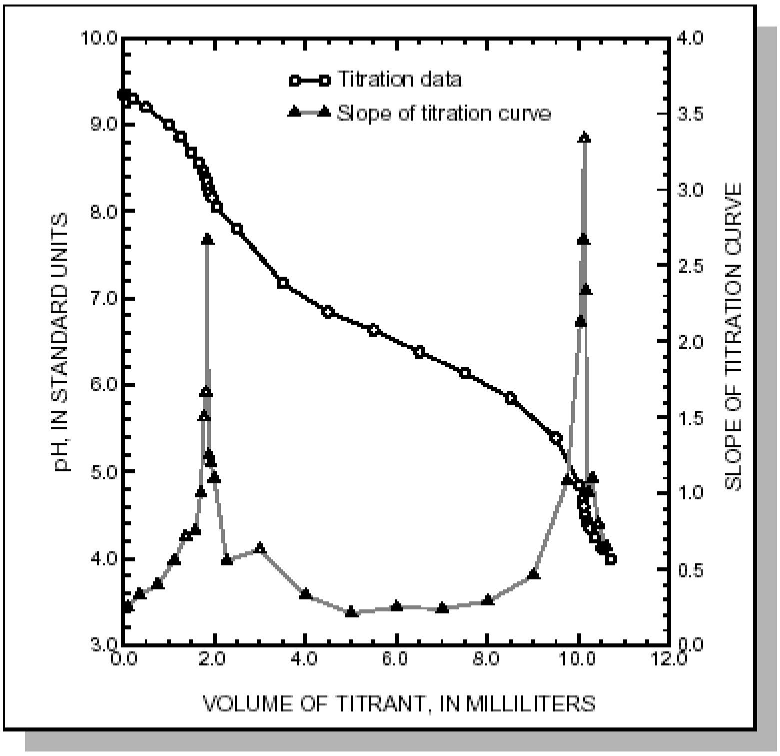

Figure 2.24 – The titration curve.

2.3.12 Gas chromatography

The composition of the main inorganic compounds (CO_2, N_2, Ar, CH_4, O_2 and Ne) were analyzed by gas-chromatography (GC) using a Shimadzu 15A equipped with a 9 m long 5A-molecular sieve column and Thermal Conductivity Detector (TCD) (Fig.2.25). The analyses of CH_4 was carried out by using a Shimadzu 14A gas chromatograph equipped with a Flame Ionization Detector (FID) and a 10 m long stainless steel column packed with Chromosorb PAW 80/100 mesh coated with 23% SP 1700 (Fig.2.26). The isotopic composition ($\delta^{13}C$ and $\delta^{18}O$-CO_2‰ vs. V-PDB) was analyzed using a Finnigan Delta S mass spectrometer, after the two-step extraction and purification procedure of the gas mixtures. Standards used for estimation of external precision were Carrara and San Vincenzo marbles (internal), NBS18 and NBS19 (international). The analytical uncertainty and the reproducibility were ±0.05‰ and ±0.1‰, respectively.

Figure 2.25- Shimadzu 15A gas-chromatography (GC).

Figure 2.26- Shimadzu 14A gas-chromatograph (GC).

CHAPTER3: Sample Description and Results

3.1- Seismic and morphobathymetric data

The morphological and structural interpretation of the study area, investigated during the first campaign (August-September 2011), was made possible by integrating several geophysical data (seismic CHIRP, multibeam bathymetry and reflectivity of the seabed). A summarizing map with the morphological interpretation is given in Fig. 3.1.

3.1.1- The Propeller Basin

The multibeam bathymetric data showed the presence of a NNW-SSE-oriented narrow basin that dissects the Paola Ridge (Fig.3.2). Owing to its peculiar shape, this basin was termed as Propeller Basin (PB). The basin can be divided into two sectors: i) the southern sector, which is characterized by a flat central area and ii) the northern sector, whose bottom is interrupted by a central 50 m-high narrow ridge that gives to the basin a horseshoe shape (Rovere and Gamberi, 2010). The PB is surrounded by elongated bathymetric reliefs, which represent the culminations of the Paola Ridge (D1-D3 and RMV and MMV in Fig. 3.2).

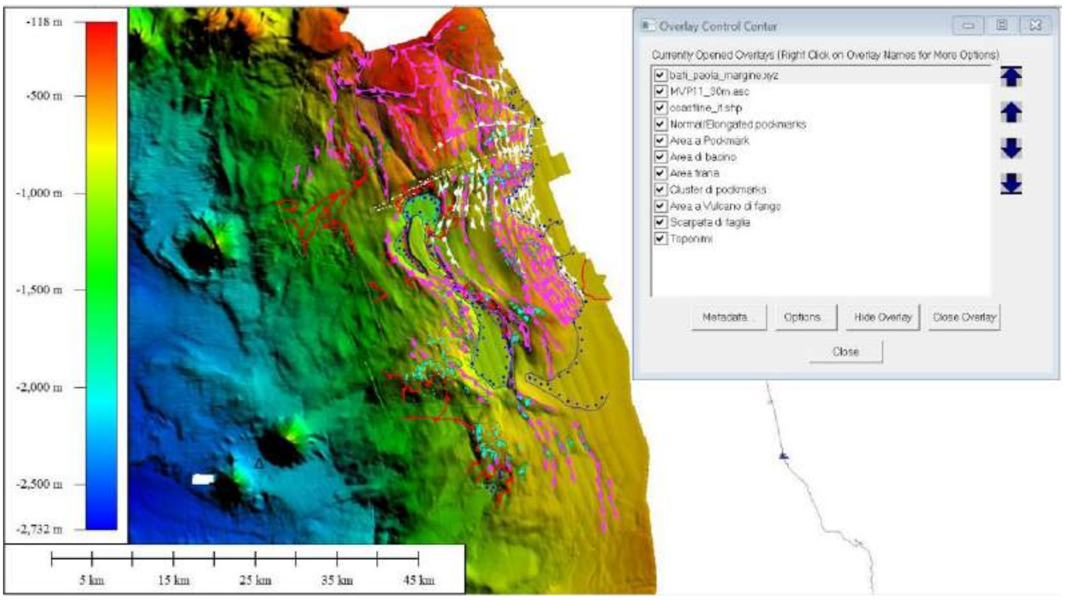

Currently Opened Overlays (Right Click on Overlay Names for More Options)

☑ bati_paola_margine.xyz
☑ MVP11_30m.asc
☑ coastline_it.shp
☑ Normal/Elongated pockmarks
☑ Area a Pockmark
☑ Area di bacino
☑ Area frana
☑ Cluster di pockmarks
☑ Area a Vulcano di fango
☑ Scarpata di taglia
☑ Toponimi

Figure 3.1-Morphological and structural interpretation of the study area (from Funari2011). Faults confining the major structures are outlined in magenta, pockmarks are depicted in cyan, crater-like structures in yellow, headwalls of shallow seated slides from the slopes of the mud volcanoes in red. The dotted blue lines encircle the principal basins of the area.

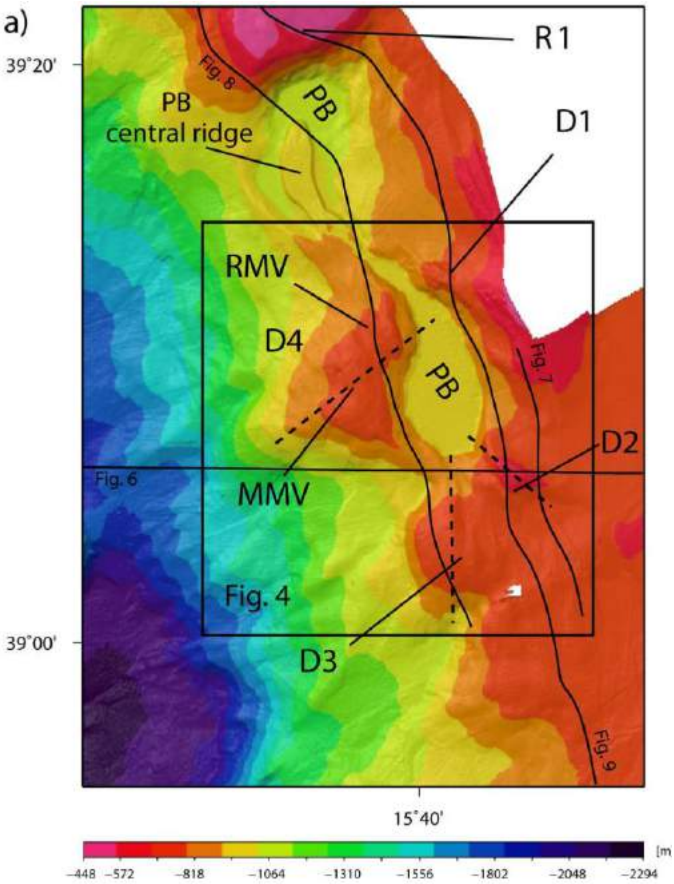

Figure 3.2-Multibeam bathymetry of the study area. PB= Propeller Basin; R1= Ridge 1; D1-D4= Diapirs 1-4; RMV= Richthofen mud volcano; MMV= Mojsisovics mud volcano.D4 represents the structure formed by MMV and RMV. From Rovere and Gamberi (2010).

3.1.2- Mud Volcanoes

RMV and MMV mud volcanoes

The RMV and MMV were interpreted as mud volcanoes (Richthofen and Mojsisovics mud volcanoes) (Rovere and Gamberi, 2010; Fig.3.2), which are connected by a common area of high backscatter comprised between -20 and +5 dB (Fig. 3.3). Pockmarks (diameter < 100 m) are rare on the MMV, and almost absent on top of the RMV.

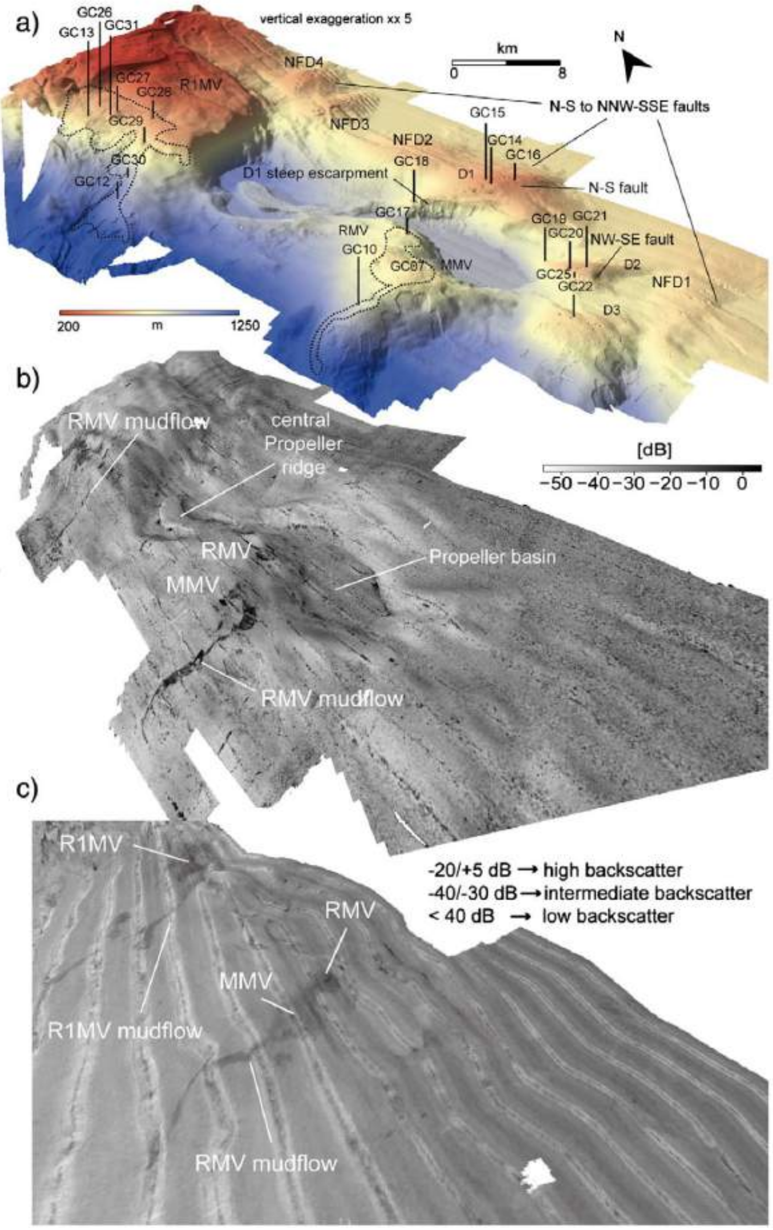

Figure 3.3-a) Kongsberg EM710 bathymetry and b) Kongsberg EM710; c) Simrad EM12 backscatter draped over the bathymetry of the study area (from Rovere et al., 2014).

It was observed a concentration of pockmarks at the base of the southern slope of MMV, in coincidence with the headwalls of shallow-seated slides. A 500-m-wide crater is present at the top of RMV (Fig.3.4a). A CHIRP profile crossing the two mud volcanoes showeda deep acoustic transparent zone, which interrupts the sub-bottom reflections of the structures flanks. The transparent *facies* is overlain by a few reflections in the MMV, whereas it reaches the seafloor at the top of the RMV (Fig.3.4b). Several corer were sampled over the highest backscatter area on top of the RMV structure (GC01-02-03-09-17 in Fig.3.4a) in addition to the box cores (BC01- 02- 04). In addition, the sampling in the MMV summit, where the seafloor backscatter is high, registered gas expulsion during core recovery (GC05, GC06 and GC07). The box corer performed on the MMV registered a lower degree of oxidization at the water-sediment interface with respect to the RMV. During core recovery, all the gravity corer were observed to strongly degas when close to the sea surface. A comparison of gravity corer and box corer taken in the same stations showed that the top section of the gravity cores was thrown out from the coring head, before reaching the sea surface. It was evidenced the presence of gas within the sediment through a strong H_2S smelling.

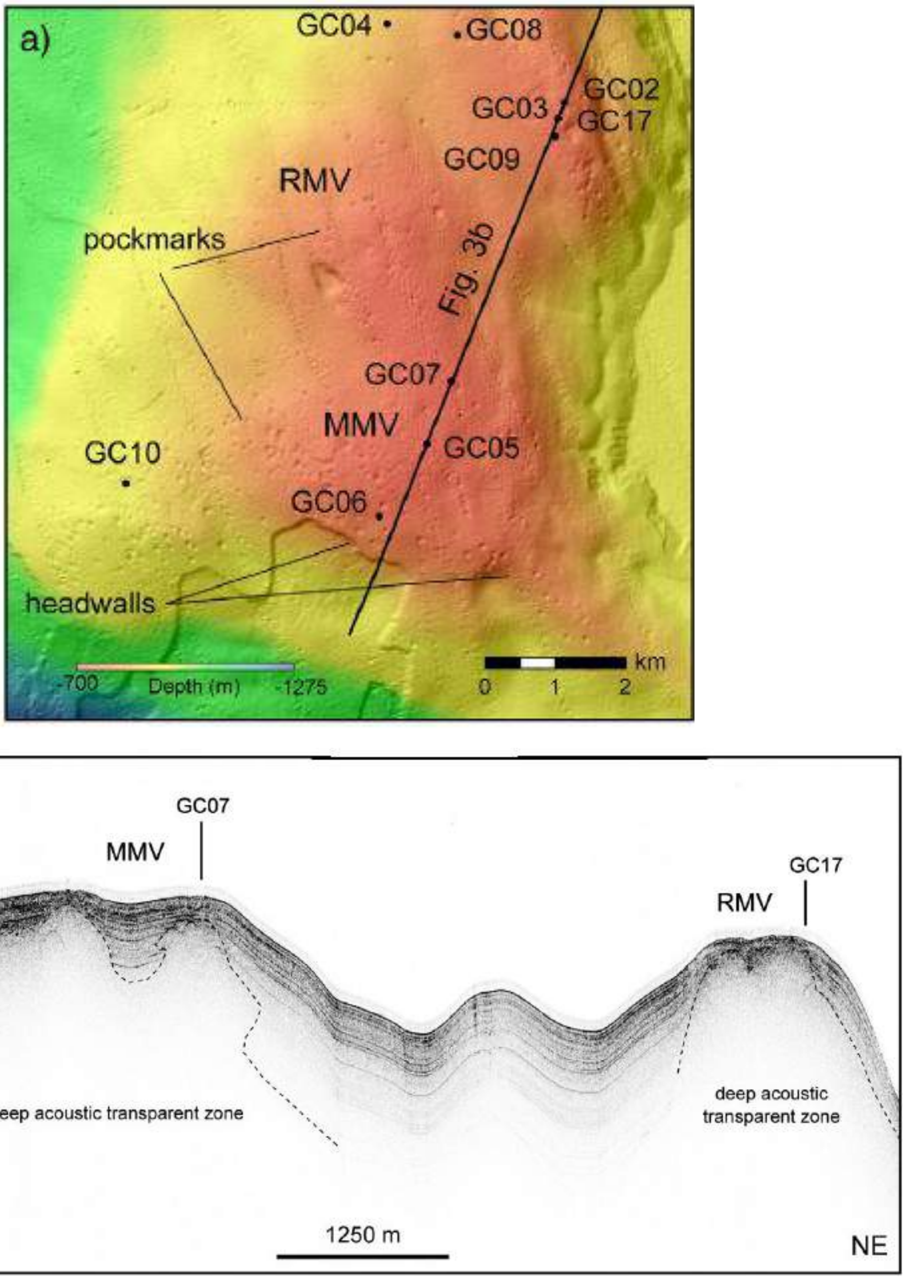

Figure 3.4-a) Close inset of the 20-m-resolution DTM and b) CHIRP profile over the MMV and RMV mud volcanoes where the core GC17 was collected on top of the RMV (Rovere et al.,2014).

R1MV mud volcano

During the MVP11 cruise a further mud volcano (termed R1MV) was recognized (Rovere et al., 2014). The R1MV is a flat-topped structure and constraints PB to the NE along a very steep escarpmentand rises about 500 m above the adjacent seafloor (Fig.3.2). High backscatter of the seafloor was only occurring in the western slope of R1MV (Fig.3.3). Pockmark fields are almost absent on the R1MV, with the exception of a 100-m-wide depression. The CHIRP profiles showed a transparent thin drape at the seafloor (Fig.3.5 b,c). Several cores (GC13-26-27-28-31, Fig.3.5a) and box cores (BC23-24-25-28) were collected in this area. During core recovery, mud was expelled from the coring head in several test sites and a strong H_2S odour was smelt when the cores were taken onboard.

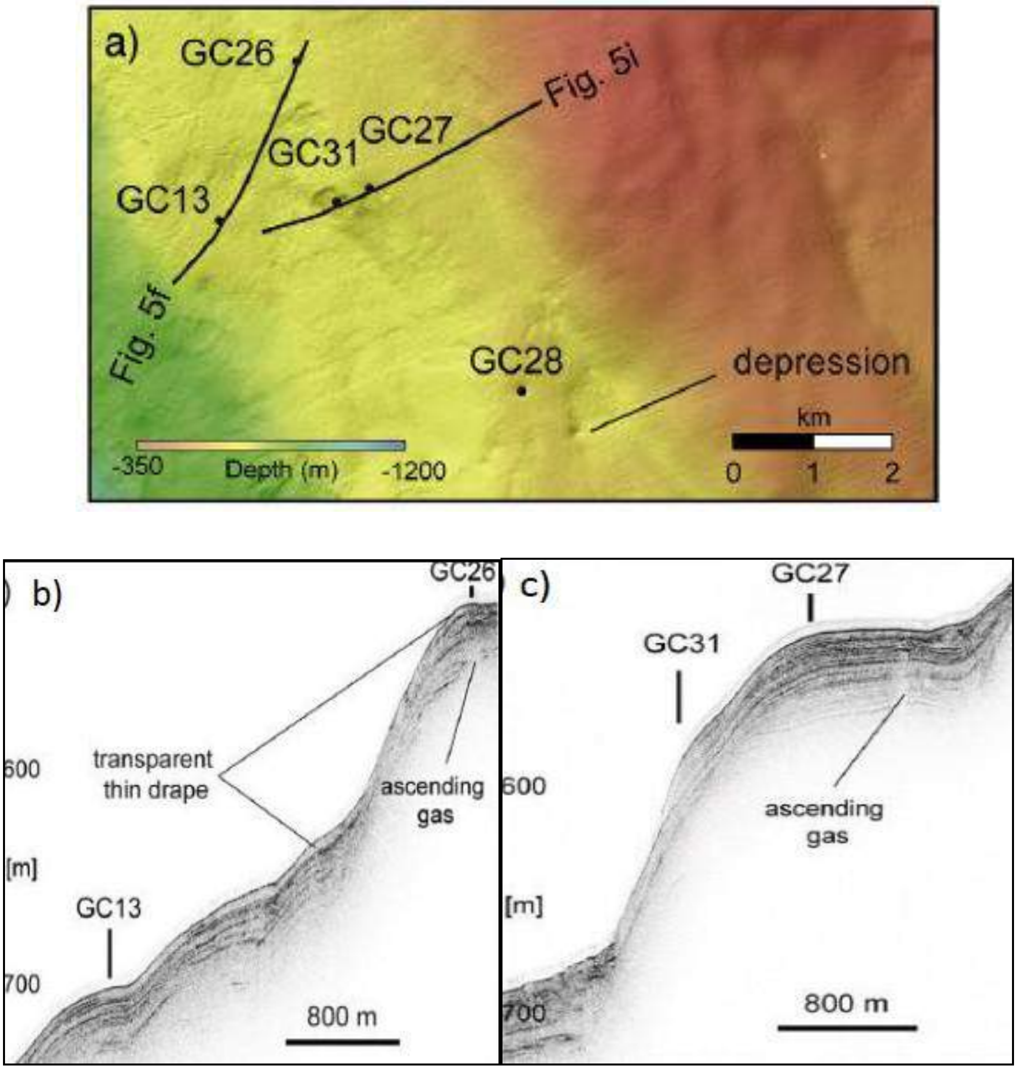

Figure 3.5-a) Close inset of the 20-m-resolution DTM over the mud volcano R1MV, b) CHIRP profile over cores GC26 and GC13 and c) CHIR profile over cores GC27 and GC31.

3.1.3- Mudflows

Two narrow bands of intermediate-to-high backscatter (-40/-30 dB) extended down slope from the RMV and the R1MV (Fig.3.3c). All the coring stations along the mudflow were not associated with degassing in the water column and the expulsion of the coring head did not occur in any of them. In some stations gas started to be slowly expelled only after the cores were retrieved on deck, the sediment cores "self-extruded" during the core opening operations and sectioning and for several days afterwards, during their storage in the fridge cell at -20 °C, other stations were not associated with gas expansion. In the distal portion of the RMV mudflow a CHIRP profile shows a transparent *facies* close to the seafloor (Fig.3.6 a,b), where the core GC10 and the Box core BC08 were collected (Fig.3.6a). Sulfides were not found in the core and box corer. Tubular authigenic carbonates (siderite) were averagely found 5 m below the seafloor. No corer were available along the proximal part of the RMV mudflow, where the backscatter intensity was lower and comprised between -16 and -15 dB. A CHIRP profile showed that several transparent bodies of comparable thickness (less than 1 m) were present at the seafloor.

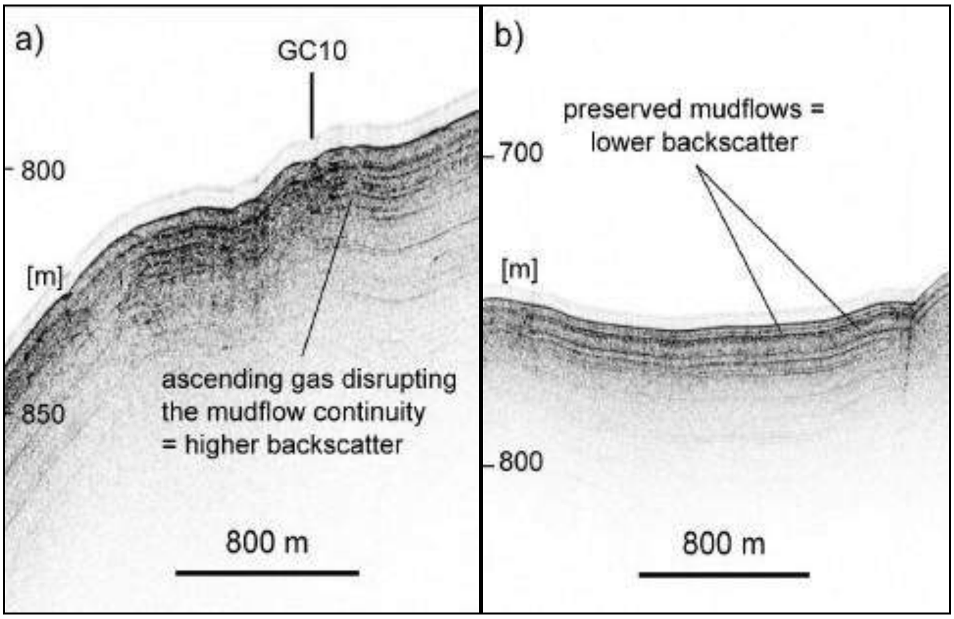

Figure 3.6-a) CHIRP profile showing the seismic *facies* of the distal part of the RMV mudflow and b)CHIRP profile of the proximal part of the mudflow.

In the distal portion of the R1MV mudflow, CHIRP data showed possible evidence of gas ascending towards the seafloor (Fig.3.7). Here, the backscatter was about -13 dB. The proximal part of the R1MV mudflow displayed intermediate backscatter values (-16/-15 dB) and preserved sedimentary bodies, which were visible in the CHIRP profiles. Several corer were collected on the R1MV mudflow (GC12, GC29 and GC30) and associated box cores (BC10-BC26-BC27). Tubular authigenic carbonates (siderite) were found approximately 6 m below the seafloor in the GC12 core catcher. Several pyrite crusts were found in the lower section of the GC29 core catcher.

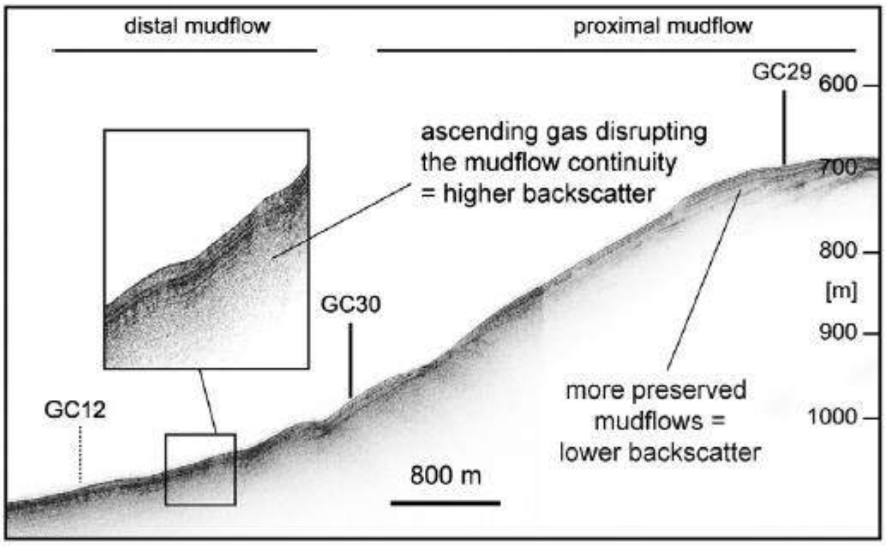

Figure 3.7-CHIRP profile showing the seismic *facies* of the R1MV mudflow and the cores were collected on the R1MV.

3.1.4- Mud diapirs

D1 mud diapir

D1 is the easternmost structure of the Paola Ridge (Fig.3.2). It consists of a NW-SE elongated structure for about 9 km, with a relief of 300 m (Rovere and Gamberi, 2010). The D1 is characterized by both low backscatter and the presence of normal pockmarks. In the crest of D1, normal pockmarks, with diameters of tens meters, were aligned along the same trend of the structure. They are from 20 to 150 m wide and 1 to 10 m deep (Fig.3.8a). N-S-elongated pockmarks were also recognized (Fig.3.8a). Pockmarks are also present in the northwestern portion of the structure, where a steep escarpment, probably corresponding with a normal fault, is visible (Fig.3.8a,b). The CHIRP profile also allowed to observe that the eastern flank of D1 was affected by a set of NNW-SSE trending normal faults (Fig.3.8b). Several corer (GC14, GC15, GC16 and GC18) and box corer (BC11-12-13) were collected at D1 (Fig.3.8a). Limestone crusts with benthic organisms (serpulidae) and iron oxy-hydroxides coating were found in the core catcher about 10 cm below the seafloor. About 2 m below the seafloor, fragments of chemosynthetic (sulfate-oxidizing bacteria) bivalves (lucinids) and decapod crustaceans (Calliax lobata) were found.

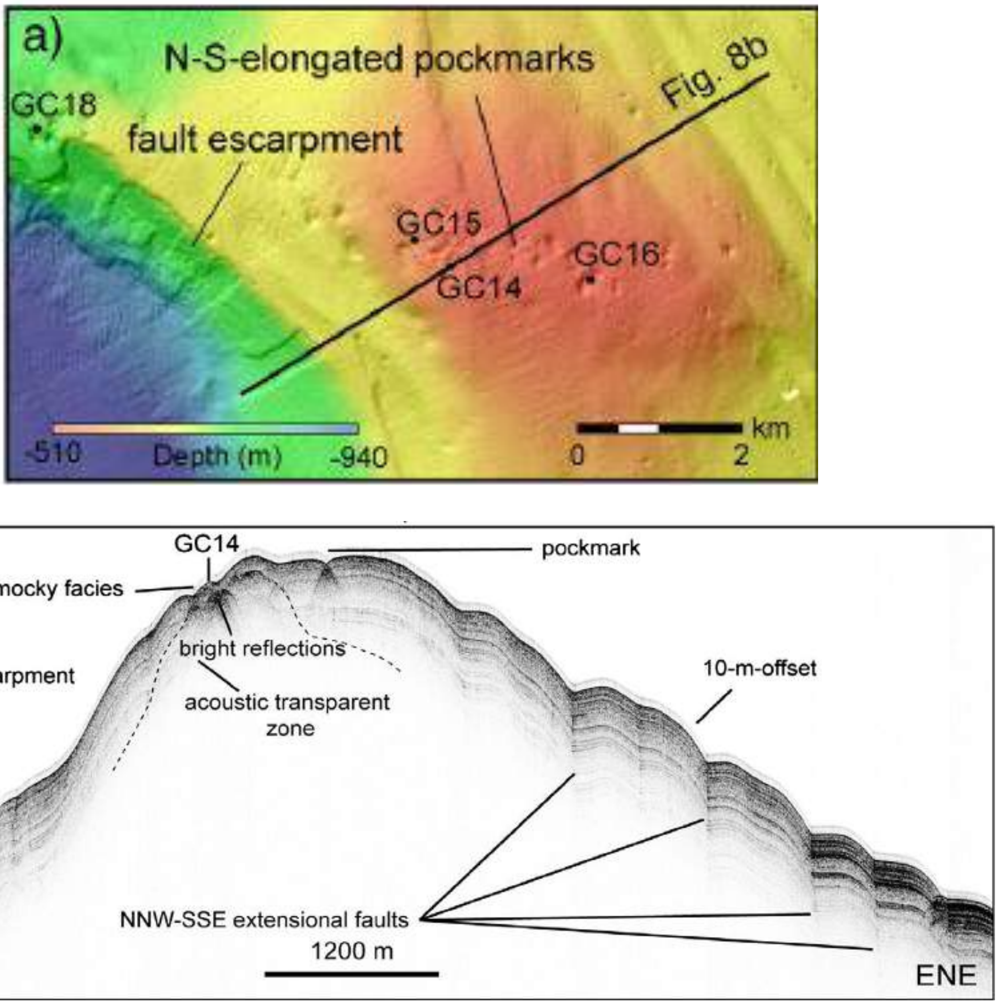

Figure 3.8-a) Close inset of the 20-m-resolution DTM b) CHIRP profile over D1 where the core GC14 was collected on the central axial portion of the diapir D1 on the floor of a large pockmark field.

D2 mud diapir

The D2 mud diapir is elongated for 6 km in a NW-SE direction and has an average relief of 300m. It is composed of two ridges separated by a saddle (Fig.3.9a). The pockmarks were aligned along the major axis of the structure. They are 20 to 50 m wide and 0.5 to 1 m deep, prevailing in its northern edge (Fig.3.9a), where in the central part of the structure, 100 m wide and 5 m deep pockmarks were coalescing along N-S to NWN-ESE trending normal faults to form elongated depressions. The CHIRP profile evidenced a hummocky *facies* at the seafloor underlain by a deeper wider area showing an acoustic transparent *facies* (Fig.3.9b). Several corer (GC19, GC 20, GC 21,GC 25) and box corer (BC14-15-17-21-22) were collected in D1 (Fig.3.9a).

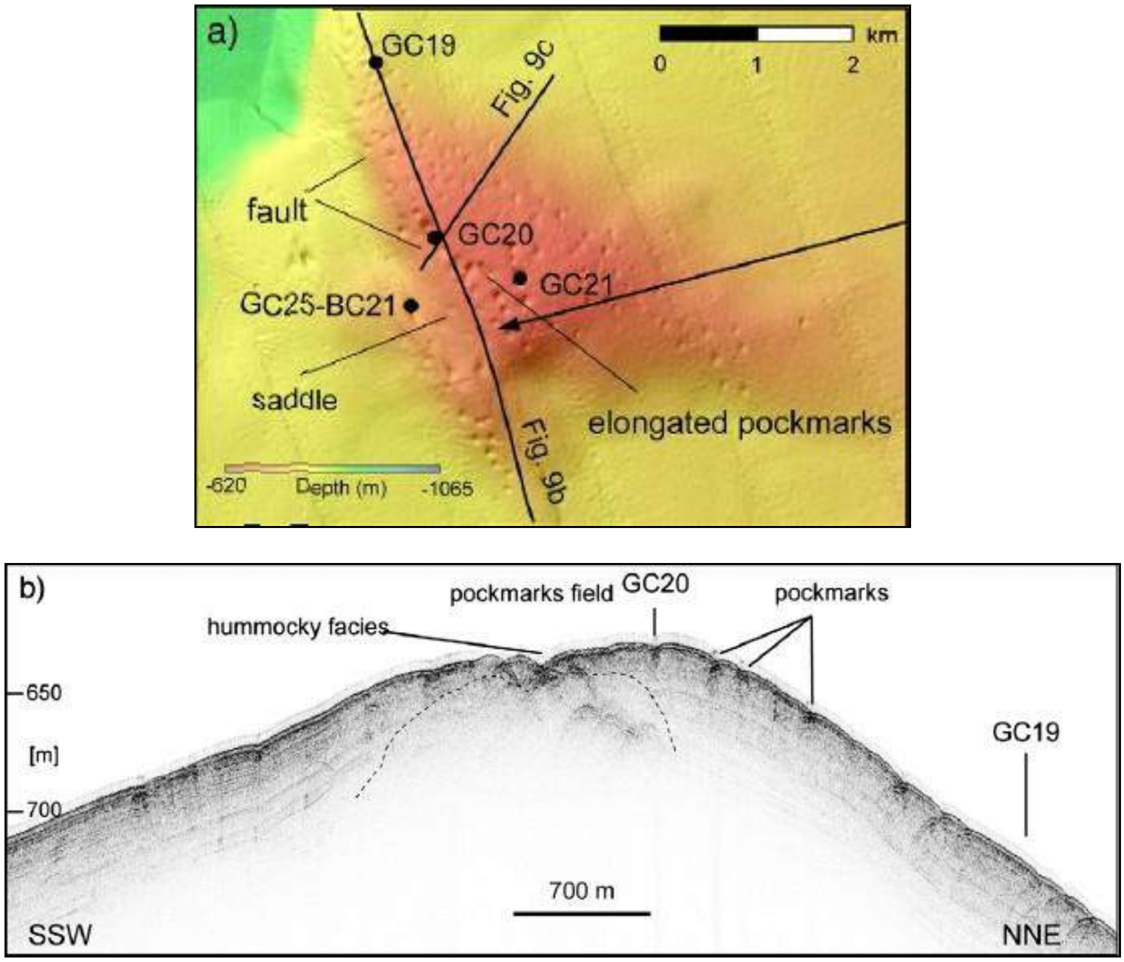

Figure 3.9-a) Close inset of the 20-m-resolution DTM, b) CHIRP profile over D2 where the core GC19 was collected in the northern termination of the diapir D2 and GC20 collected on top of D2.

D3 mud diapir

The D3 mud diapir has a circular dome shape, with a radius of 7 km and a relief of 200 m (Fig.3.2) and was punctuated by pockmarks concentrated in its western flank, towards the slope (Fig.3.10a). Some of the pockmarks had dimensions in the order of 100 m in diameter and 10m in depth. The CHIRP profile over D3 showed a hummocky *facies* in coincidence with the pockmark field (Fig.3.10b).Several corer (GC22-23-24; Fig.3.10) and associated box corer (BC18-19-20) were collected on top of the diapir D3.

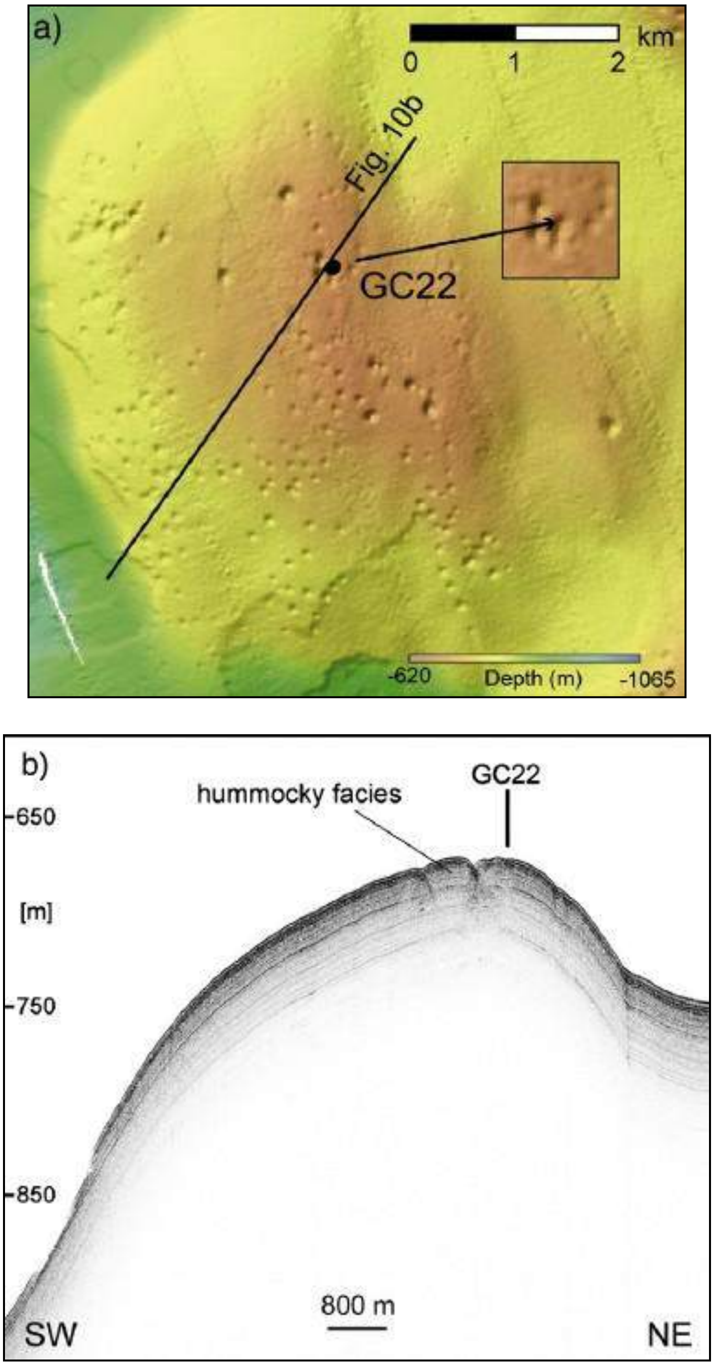

Figure 3.10-a) Close inset of the 20-m-resolution DTM and b) CHIRP profile over D3 where the core GC22 was collected (top of D3).

3.2-Description of sediment cores

In this section the petrographic and mineralogical features of the studied sediment cores from cruise MVP11 are described, along with the presence of organic matter and/or bioturbation. For each core the sampling depth and sites are listed in Table 3.1. The cores were opened in the Laboratory of Sedimentology (CNR-ISMAR), one or several for each different structure (e.g. GC07 for MMV, GC19 for D2, etc.). The physical and lithological features of all cores were described. In addition, for some of them the profiles of the magnetic susceptibility were also reported.

Sampling station	Type	Depth	Structure
MVP11-GC01	gravity core	727	RMV
MVP11-GC02	gravity core	727	RMV
MVP11-GC03	gravity core	726	RMV
MVP11-GC04	gravity core	808	RMV
MVP11-GC05	gravity core	728	MMV
MVP11-GC06	gravity core	729	MMV
MVP11-GC07	gravity core	709	MMV
MVP11-GC08	gravity core	760	RMV mudflow
MVP11-GC09	gravity core	728	RMV
MVP11-GC10	gravity core	860	RMV mudflow
MVP11-GC11	gravity core	922	Propeller ridge
MVP11-GC12	gravity core	1055	R1MV mudflow
MVP11-GC13	gravity core	717	R1MV
MVP11-GC14	gravity core	530	D1
MVP11-GC15	gravity core	557	D1
MVP11-GC16	gravity core	521	D1 fault scarp
MVP11-GC17	gravity core	728	RMV
MVP11-GC18	gravity core	750	D1
MVP11-GC19	gravity core	731	D2
MVP11-GC20	gravity core	653	D2 fault scarp
MVP11-GC21	gravity core	634	D2
MVP11-GC22	gravity core	677	D3
MVP11-GC23	gravity core	680	D1
MVP11-GC24	gravity core	679	D1
MVP11-GC25	gravity core	694	D2 fault scarp
MVP11-GC26	gravity core	576	R1MV
MVP11-GC27	gravity core	570	R1MV
MVP11-GC28	gravity core	552	R1MV
MVP11-GC29	gravity core	707	R1MV mudflow
MVP11-GC30	gravity core	957	R1MV mudflow
MVP11-GC31	gravity core	617	R1MV

Table 3.1-The coring sites during sampling operations. GC= Core gravity, RMV= Richtofen mudvolcano, MMV= Mojsisovics mud volcano, D1-D3= Diapirs, R1MV= new mud volcano.

Core gravity MVP11_GC01(Fig.3.11)

LONG-WGS84	LAT-WGS84	DEPTH (m)	RECOVERY (m)	SITE
15.647000	39.176686	727	1m	RICHTHOFEN mud volcano (RMV)

<u>Description of the core</u>: the GC01 core was performed on the higher backscatter spot on top of RMV.

Degassing in the water column during coring operations and mud expulsion and H_2S smelling when the core was retrieved on the deck were observed. Only 1 m of sediment against the 6-m-long liner was preserved, the content of the liner was completely disrupted by the gas emitted in the water column during the recovery of the coring device. In the core catcher of GC01, a few pumice fragments (0.2 to 1 cm in diameter) intercalated with sulfides and oxy-hydroxides were found.

Figure 3.11–The gravity core GC01.

Core gravity MVP11_GC02 (Fig.3.12)

LONG-WGS84	LAT-WGS84	DEPTH (m)	RECOVERY (m)	SITE
15.647020	39.176722	727	**3.54**	RICHTHOFEN mud volcano (RMV)

<u>Description of the core:</u> the GC02 core was collected in the same station of GC01. The top section of the core was expelled when the coring device reached the sea-surface, all the remaining deeper sections were deformed and intercalated with reddish brown layers. Expansion cracks were present through the core and the bottom section was represented by completely fluidized mud.

<u>Box corer associated</u>: MVP11_BC01(Fig. 3.13).

Figure 3.12–The gravity core GC02.

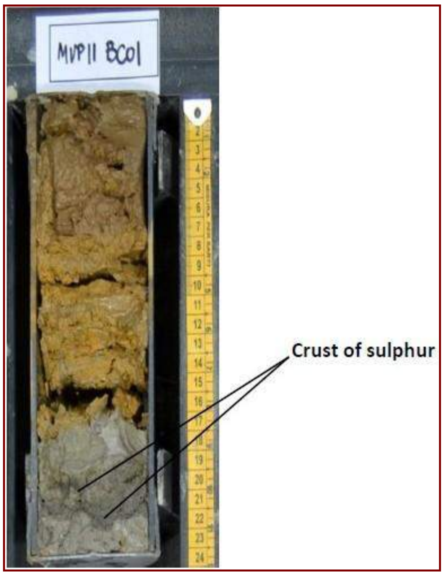

Figure 3.13–The Box core BC01.

<u>Description of the Box Core:</u> the BC01 box core was recovered in the same station of GC01 and GC02. It contained Fe-oxy-hydroxides in the first few centimeters and sulfides down to 20 cm b.s.f. (Fig. 3.13). Two samples were collected from the BC01: small pyritized burrows represented by the sample Cal-K and small pavements

made of Pyrite-Marcasite or Sphalerite (sample Cal-O), as resulting by XRD analysis. The Fe oxy-hydroxides also contained fresh trails of organisms slightly oxidized.

Core gravity MVP11_GC03 (Fig.3.14)

LONG-WGS84	LAT-WGS84	DEPTH (m)	RECOVERY (m)	SITE
15.648154	39.178721	723	3.96-m-long	RICHTHOFEN mud volcano (RMV)

Description of the core: the GC03 core was collected 250 m northward of the GC02 station. Degassing in the water column, mud expulsion from the coring head and H_2S smelling were observed. With respect to GC02, the GC03 core was poorer in water, but it showed the same expansion cracks and intercalated deformed layers in the oxidized sediments. At about 35 cm a limestone burrow consisting of siderite was present (sample Cal-RR), it was associated with fragments of Pteropodes and micas, at 1.30 m b.s.f., another limestone burrow made of siderite (sample Cal-EE) was found. The bottom of the core hosted a light yellow tephra. In the core catcher, fresh sulfides and native sulfur fragments were present, they appeared as both consolidated and unconsolidated. In addition to the siderite samples (samples Cal-EE and Cal-RR), several mud samples (samples Cal-28, Cal-31 and Cal-33) were collected from different depths in the core section (Fig. 3.14).

Box corer associated: MVP11_BC02 (Fig. 3.15).

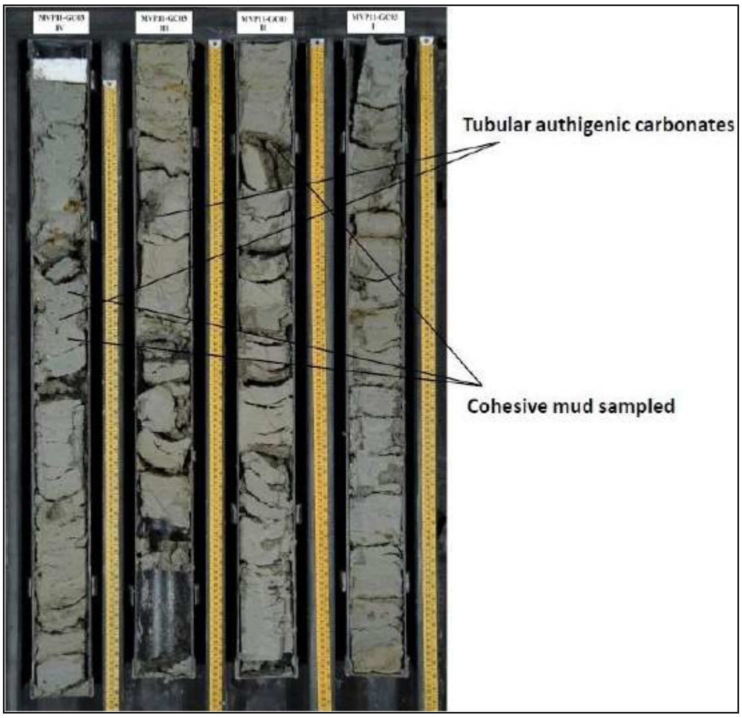

Figure 3.14–The gravity core GC03.

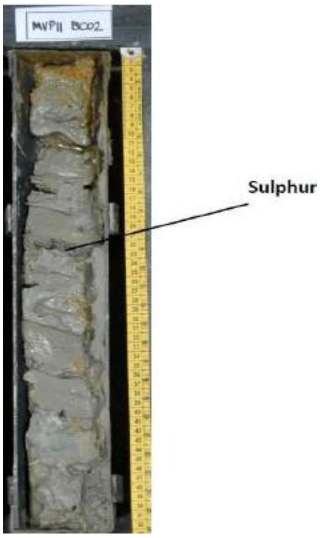

Figure 3.15–The Box core BC02.

<u>Description of the Box Core</u>: the BC02 box core was fully recovered (50 cm) and contained at the top a very thin layer of Fe-oxy-hydroxides and oxidized mud and sulfides in the form of flat crusts and pavements, possibly because the upper part of the sediment section was partly lost in the sea due to gas expansion (gas was still present in the sediment when the box corer was retrieved on board). Most samples were comprised of grey water-rich mud. The sample Cal-D was collected from the BC02.

Core gravity MVP11_GC04 **(Fig.3.16)**

LONG-WGS84	LAT-WGS84	DEPTH (m)	RECOVERY (m)	SITE
15.619020	39.188884	808	4 m	RICHTHOFEN mud volcano (RMV)

Description of the core: this core was collected from the low backscatter of the RMV structure. The core was relatively different with respect to the previous ones since no significant degassing and H_2S odor were recognized while retrieving the core on the deck. There was no evidence of the presence of a well-developed hemipelagic mud cap on the top of the core. Only 2 cm of reddish brown mud was present at the top of the core, but it was not thick and water-rich. The deeper sediment was comprised of consolidated mud with clear evidence of bioturbation, especially in the first 20 cm b.s.f., small expansion holes present along the section of the core could tentatively be ascribed to gas expansion.

Box core associated: MVP11_BC03 (Fig.3.17).

Description of the Box Core: the BC03 box core recovered 24 cm of red laminated mud. Several pumices were also found in the box corer.

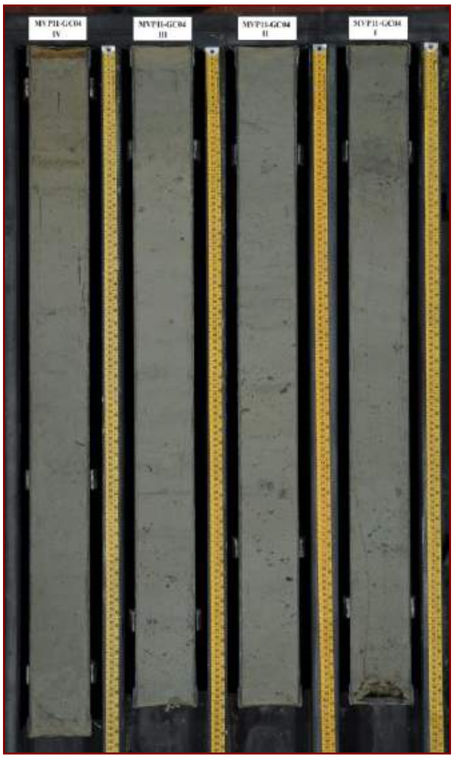

Figure 3.16–The gravity core GC04.

Figure 3.17–The Box Core BC03.

Core gravity MVP11_GC05 (Fig.3.18)

LONG-WGS84	LAT-WGS84	DEPTH (m)	RECOVERY (m)	SITE
15.625064	39.135206	728	3.35 m	MOJSISOVICS mud volcano (MMV)

Description of the core: the GC05 core was collected in the high backscatter on top of the MMV mud volcano. Degassing in the water column, mud expulsion from the coring head and H_2S smelling were recorded. The top section was characterized by highly fluidized and very rich in water mud. The core was completely deformed and the tephra layers were not clearly visible within the succession. Expansion cracks were present within all the grey mud. The bottom section appeared to be rich in water. The susceptibility profile does not indicate the presence of tephra or turbiditic layers, probably due to the deformation caused by the expansion of gas within the sediment.

Box corer associated: MVP11_BC04 (Fig.3.19).

Figure 3.18–The gravity core GC05.

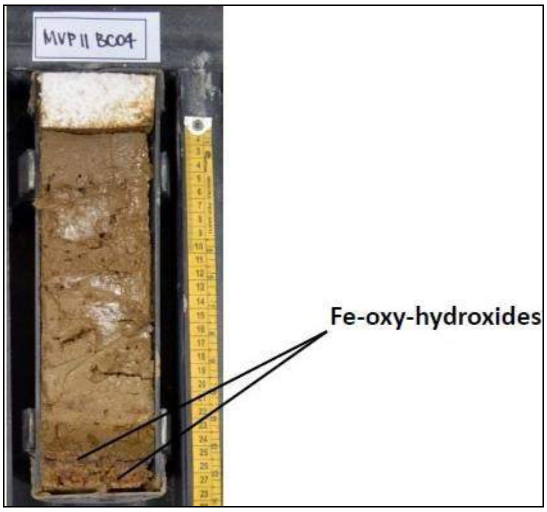

Figure 3.19-The Box Core BC04.

Description of the Box Core: the BC04 core was 27-cm-long and was almost completely consisting of highly oxidized mud. At the bottom of the liner 2-cm-thick Fe-oxy-hydroxide crusts were present (Fig. 3.19). Two samples were collected from BC04 (samples Cal-P and Cal-F).

Core gravity MVP11_GC06 **(Fig.3.20)**

LONG-WGS84	LAT-WGS84	DEPTH (m)	RECOVERY (m)	SITE
15.617170	39.125866	729	4 m	MOJSISOVICS mud volcano (MMV)

Description of the core: the GC06 core was collected in the low backscatter on the southern flank of MMV. No degassing and smelling were observed. The top section was brown-grey mud. The core liner contained light grey mud with intense bioturbation and several elongated features, possibly between 52 and 60 cm b.s.f. A thick dark grey tephra layer was observed at 2.78 m b.s.f., just below it, at 2.91 m b.s.f., tiny pumice fragments were found.

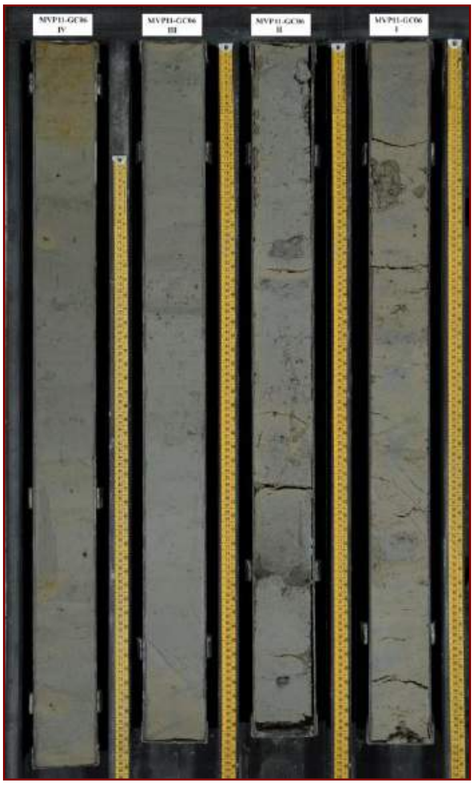

Figure 3.20 –The gravity core GC06.

Core gravity MVP11_GC07 (Fig.3.21)

LONG-WGS84	LAT-WGS84	DEPTH (m)	RECOVERY (m)	SITE
15.629398	39.143197	709	5.72+ extruded top	MOJSISOVICS mud Volcano (MMV)

Description of the core: the GC07 core was collected in the high backscatter on the top of MMV. The core started to degas once retrieved on the deck, although the lack of a preserved hemiplegic mud cap was indicative of expulsion of the upper section in the water, similarly to what occurred with other cores collected on top of the RMV mud volcano. Expansion cracks were present within the sediment, even though the first 67 cm b.s.f., appeared to be less deformed and chaoticized with respect to the mid sections. At 4 m b.s.f., a yellow tephra layer was observed, though deformed; however, the susceptibility profile did not record it. Between the V and the VI sections of the core, some limestone fragments were found. At 3.30 m b.s.f., a grey-brown volcanic ash layer made of pumices was occurring. A fragment of authigenic limestone was found in the core catcher, but not analyzed. Several samples (samples Cal-03, Cal-05, Cal-13, Cal-24, Cal-25 and Cal-26) were collected in the core at different depths (Fig. 3.21).

Box corer associated: MVP11_BC05 (Fig.3.22).

Description of the box corer: the box core BC05 penetrated for 26 cm down into the sub-seafloor and recovered a reddish laminated brown mud. The bottom of the liner hosted a 1-cm-thick layer of orange-brown mud.

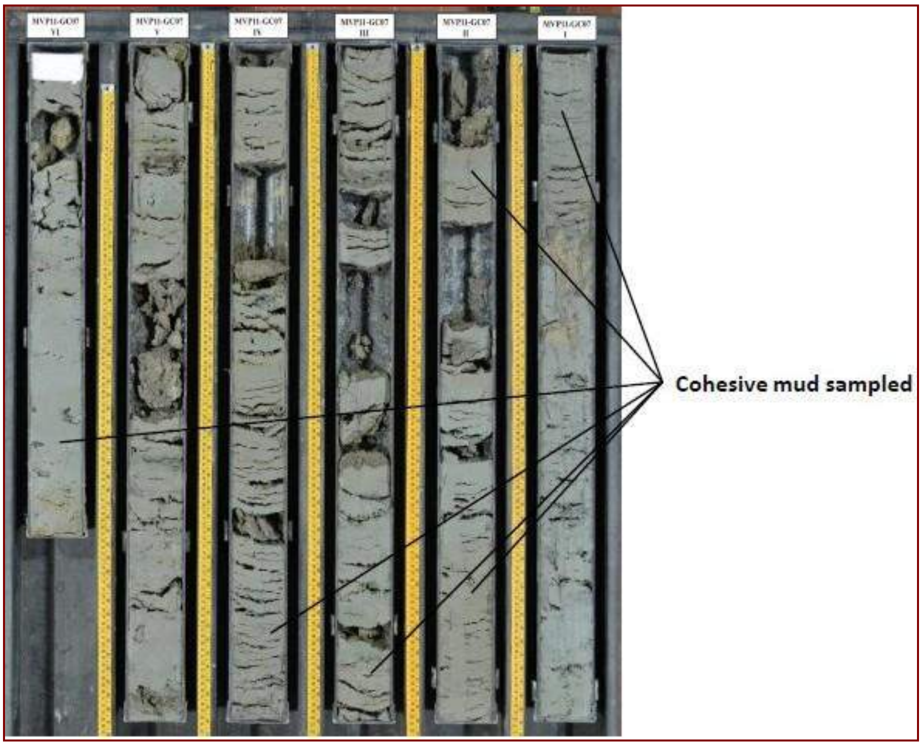

Figure 3.21-The gravity core GC07.

Figure 3.22–TheBox core BC05.

Core gravity MVP11_GC08 **(Fig.3.23)**

LONG-WGS84	LAT-WGS84	DEPTH (m)	RECOVERY (m)	SITE
15.630492	39.187372	760	5.12	RICHTHOFEN mud volcano (RMV)

Description of the core: the GC08 core was collected in the high backscatter spot on the northern flank of RMV. Degassing was observed only after the core was retrieved on the deck and H_2S smelling was felt. GC08 is the first core that showed a perfectly preserved highly oxidized upper stratified section down to 50 cm b.s.f. The presence of Fe-related minerals was also evidenced in the susceptibility profile. Expansions cracks started to be present only at 3.12 m b.s.f., gas was trapped well down into the sediment and this may be the cause why the core was not observed to degas in the water column during the recovery, but just a few minutes after it was on board. Yellow and green layers were present, where tephra layers possibly underwent chemical reactions due to the presence of fluids and related bacteria. One thin yellow tephra was possibly present at 2.94 m b.s.f. Several samples of mud (samplesCal-09, Cal-10, Cal-15 and Cal-16) were collected in the core (Fig. 3.23).

Box corer associated: MVP11_BC06 (Fig.3.24).

Description of the box corer: the BC06 box core was collected in the same station and contained 24 cm of brown laminated mud with oxy-hydroxide crusts at the bottom.

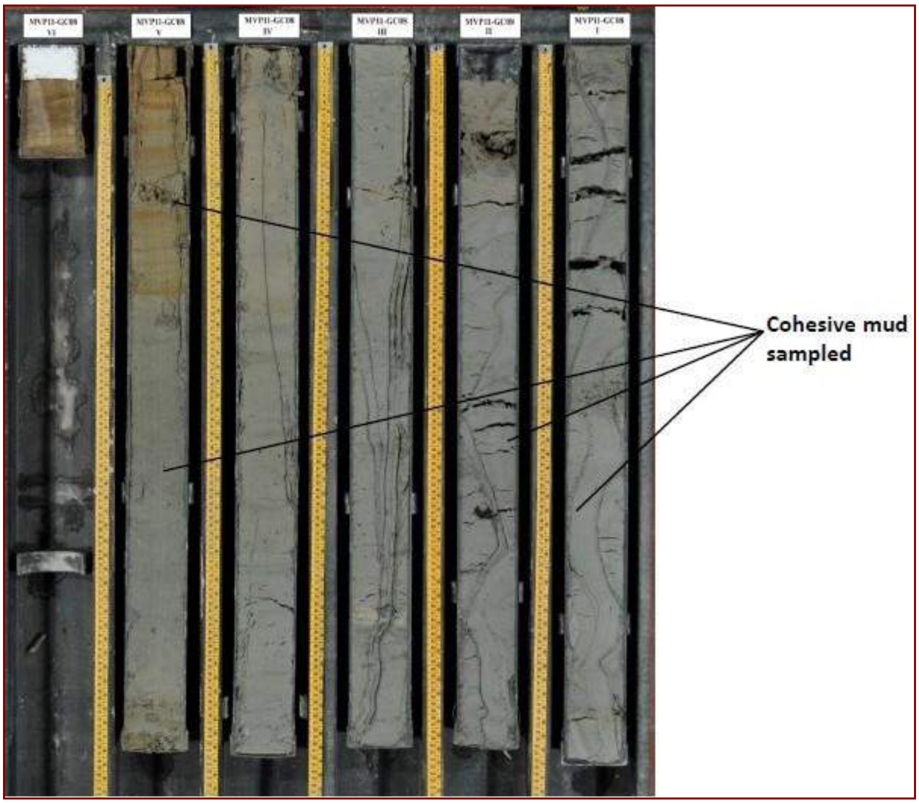

Figure 3.23–The gravity core GC08.

Figure 3.24–The Box core BC06.

Core gravity MVP11_GC09 **(Fig.3.25)**

LONG-WGS84	**LAT-WGS84**	**DEPTH (m)**	**RECOVERY (m)**	**SITE**
15.646652	39.174399	728	3.80	RICHTHOFEN mud volcano (RMV)

Description of the core: the GC09 was collected in the high backscatter area on the top of RMV, where all the geophysical and geological evidences suggested that seafloor venting was occurring on top of this structure. Degassing in the water column, mud expulsion from the coring head and H_2S smelling were noticed similarly to what recorded at the GC01 and GC02 stations and, though at a minor extent, in the GC03 station. The upper section was missing and the sediment was deformed. Expansion cracks were visible throughout the core, which was consisting of completely fluidized mud in the bottom part. A yellow tephra layer was visible at 2 m b.s.f., but no corresponding high signal was present in the susceptibility profile, similarly to what observed for the GC07 profile.

Box corer associated : Box core BC07 (Fig.3.26).

Description of the box core: the BC07 box core recovered only 20 cm of sediment with a lower 10-cm-thick layer of highly oxidized mud of orange color. Evidence of bioturbation was present in the upper part of the sediment.

Figure 3.25–The gravity core GC09.

Figure 3.26–The Box core BC07.

Core gravity MVP11_GC10 (Fig.3.27)

LONG-WGS84	LAT-WGS84	DEPTH (m)	RECOVERY (m)	SITE
15.575511	39.130375	860	5.0	RMV mudflow

Description of the core: the GC10 core was collected on the distal part of the RMV mudflow where the backscatter was comprised between -40 and -30 dB. Degassing occurred after its retrieval on the deck. The GC10 core showed an upper undisturbed and brown oxidized part (down to 50 cm b.s.f.), similar to the GC08 core as also testified by a similar susceptibility profile, and a lower part where gas was expelled leaving expansion cracks within the core liner. Expansion cracks were actually visible only down to 2.0 m b.s.f. Tephra layers showed alterations and unusual green and red colors. In the bottom part of the core, a yellow tephra was present at 4.82 m b.s.f. and possibly correlated to the layers recorded in the GC03, GC07, GC09 cores. It is to mention that no strong signal was present in the susceptibility profile. Tubular authigenic carbonate (siderite) was collected in the core catcher (sample Cal-M).

Box corer associated: Box core BC08 (Fig.3.28).

Description of box core: the BC08 box core sediment penetration was 26-cm-thick and wascomprised of brown laminated mud, reddish mud was apparent in the lower part of the liner.

Figure 3.27–The gravity core GC10.

Figure 3.28-The Box core BC08.

Core gravity MVP11_GC11 (Fig.3.29)

LONG-WGS84	LAT-WGS84	DEPTH (m)	RECOVERY (m)	SITE
15.590249	39.250499	922	5.70 m of sediment	Propeller Ridge (PB)

<u>Description of the core:</u> the GC11 core was relatively different from those collected on the RMV and MMV structures, no degassing and no smelling were observed. The mud was highly cohesive and the opening of the core was difficult due to the dryness of the mud. Bioturbation was present. Turbiditic and tephra layers were

observed. The bottom of the core hosted several tephra or turbiditic layers, as was also shown by the susceptibility profile.

<u>Box corer associated</u>: MVP11_BC09 (Fig.3.30).

<u>Description of the core:</u> the BC09 box core showed 23 cm of light brown mud; oxidized levels were not present.

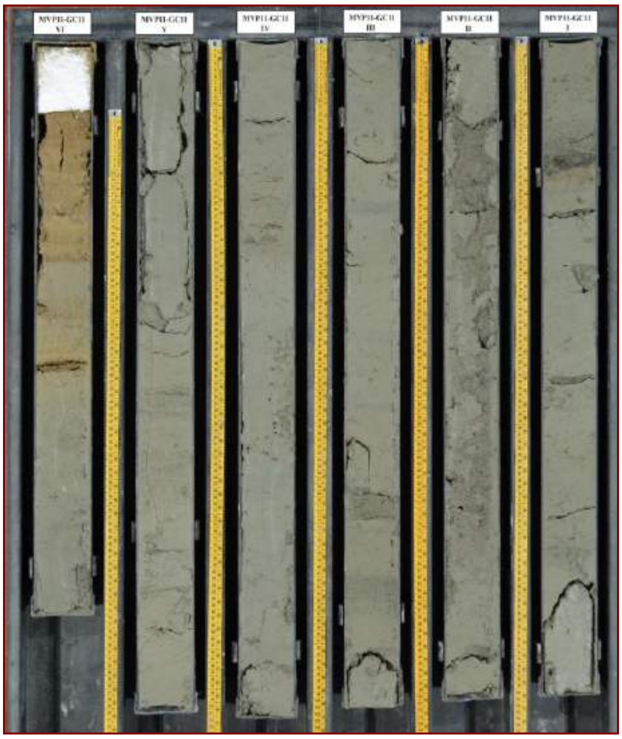

Figure 3.29–The gravity core GC11.

Figure 3.30–The Box core BC09.

Core gravity MVP11_GC12 (Fig.3.31)

LONG-WGS84	LAT-WGS84	DEPTH (m)	RECOVERY (m)	SITE
15.476268	39.316441	1055	5.85	R1MV mudflow

Description of the core: the GC12 was collected in the distal part of the R1MV mudflow. Quick degassing after retrieval on the deck was observed. The GC12 showed an upper, undisturbed and strong oxidized part and a lower part where gas was expelled leaving cracks within the core liner. Tephra layers and very thin fine sandy turbidites were intercalated within the cohesive grey mud. They appeared to be strongly oxidized; towards the bottom of the recovered sections the tephra layers had less chemical alteration and showed their normal light yellow/grey colors. Tubular authigenic carbonate (siderite) was collected from the core catcher GC12 (sample Cal-G).

Box corer associated: MVP11_BC10 (Fig.3.32).

Description of the core: the BC10 core was collected in the same station and showed strong bioturbation along the sedimentary column.

Figure 3.31–The gravity core GC12.

Figure 3.32–The Box core BC10.

Core gravity MVP11_GC13 (Fig.3.33)

LONG-WGS84	LAT-WGS84	DEPTH (m)	RECOVERY (m)	SITE
15.490881	39.391800	717	5.86	R1MV mud volcano

Figure 3.33-The gravity core GC13.

<u>Description of the core:</u> the GC13 core was collected on the high backscatter seafloor of the mud volcano R1MV. Degassing apparently occurred only after it was retrieved on the deck, H_2S smelling was felt, even if the brown mud cap was absent, suggesting gas expulsion of the upper section in the water column, even if it was not possible to observe it while on board. The upper section was including apparently undisturbed grey cohesive mud, whereas the typical upper hemipelagic soft brown mud was missing. Expansion cracks started at 1.20 m b.s.f., were wide spread and levels of oxidations on the sediment were very frequent. The susceptibility profile was very low, in analogy with what observed in most cores on top of RMV where the sediment was completely deformed. No tephra layers were apparently preserved.

<u>Box corer associated:</u> no box corer were available at this station.

Core gravity MVP11_GC14 (Fig.3.34)

LONG-WGS84	LAT-WGS84	DEPTH (m)	RECOVERY (m)	SITE
15.738252	39.193349	530	4.90	D1 Pockmark

<u>Description of the core:</u> the GC14 core was collected on the central axial portion of the diapir D1 on the floor of a large pockmark field. When the core was completely retrieved on board the deck of the ship, no degassing and no smelling were

observed. Bioturbated sediments, bearing no evidence of gas and topped by brown soft hemipelagic mud characterized the GC14 core. Fragments of coral stems were found in the core sections at 2.95 m b.s.f. Bioturbation was diffuse. The presence of green layers indicative of chemical alteration on the sediment was present. The susceptibility profile suggested the presence of volcanic layers in the upper and bottom parts of the core.

Box corer associated: MVP11_BC11 (Fig. 3.35).

Description of the core: the BC11 box core showed remnants of macrofossils, indicative of normal pelagic conditions. Pumice fragments were diffuse and were better noticed after sewing.

Figure 3.34-The gravity core GC14.

Figure 3.35-The Box Core BC11.

Core gravity MVP11_GC15 **(Fig.3.36)**

LONG-WGS84	**LAT-WGS84**	**DEPTH (m)**	**RECOVERY (m)**	**SITE**
15.733077	39.196390	557	5.27	D1 Pockmark

Description of the core: the GC15 core was located 560 m northwest the GC14 core on top of D1. The core was almost identical of GC14. The bioturbation was more intense, shell fragments were diffuse and fragments of decapodan crustaceans were present starting from 2.0 m b.s.f. Green layers indicative of chemical alteration on the sediment were present. Two samples (Cal-27 and Cal-30) were collected in the coring sample (Fig. 3.36).

Box corer associated: MVP11_BC12 (Fig.3.37).

Description of the core: the BC12 box core showed soft brown hemipelagic mud with no signs of deformation or evident bioturbation.

Figure 3.36–The gravity core GC15.

Figure 3.37-The Box Core BC12.

Core gravity MVP11_GC16

LONG-WGS84	**LAT-WGS84**	**DEPTH (m)**	**RECOVERY (m)**	**SITE**
15.758275	39.191809	521	None	D1 Pockmark

Description of the core: The GC16 core was collected 1.7 km away from that of GC14 along what appeared to be a NNW-SSE oriented normal fault that dissected the diapir D1 in its eastern part. The core was collected at 521 m water depth but the corer device could not penetrate below a hard substrate consisting of authigenic limestones developed on the seafloor. The limestone crusts consisted of laminated bioclastic and foraminifera-rich packstones. Benthic organisms (*Serpulidae*) were encrustation some portions of the authigenic limestones (sample Cal-C). A thin superficial coating of red Fe-iron oxy-hydroxides was recognized in some portions of the carbonate crusts and coral stems (*Madrepora oculata*) were present within the crust (sample Cal-N).

Box corer associated: MVP11_BC13 (Fig. 3.38).

Figure 3.38- The Box Core BC13.

Description of the core: From the BC13 box core only 20 cm of light brown mud intercalated with a surface of oxidation in the mid section of the liner was recovered. Macrofossils typical of seamounts were found, among them *Cuspidaria cuspidate* and *Madrepora sp.*

Core gravity MVP11_GC17 **(Fig.3.39)**

LONG-WGS84	LAT-WGS84	DEPTH(m)	RECOVERY (m)	SITE
15.646991	39.176665	728	6.00	RICHTHOFEN mud volcano RMV

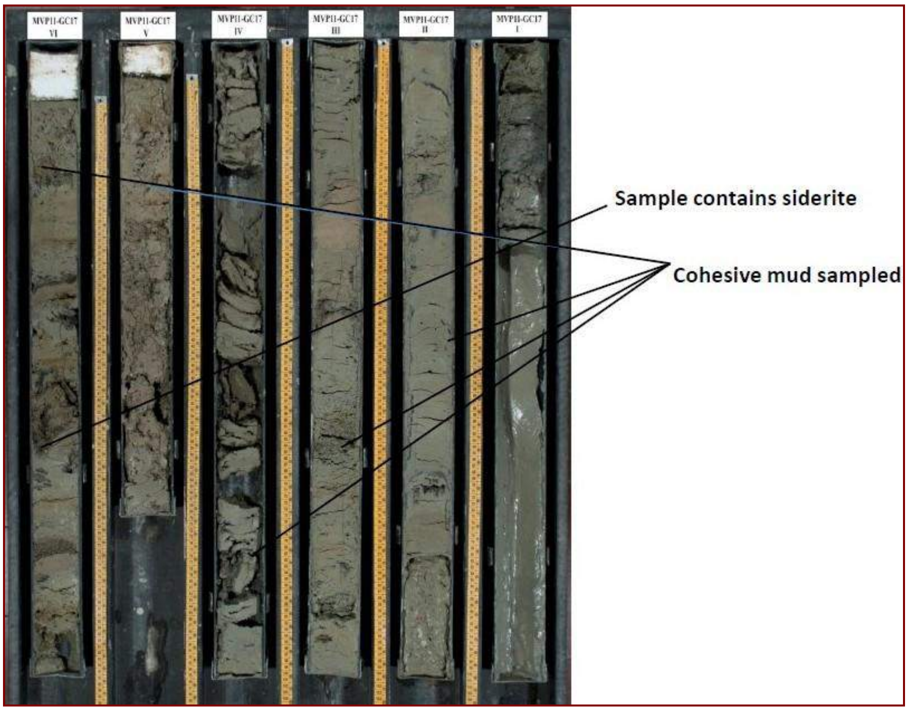

Figure 3.39-The gravity core GC17.

Description of the core: The GC17 core was collected at the same station of GC01 and GC02. Degassing in the water column, mud expulsion from the coring head and H_2S smelling were observed. The core was very similar to GC01 and GC02 with expansion cracks throughout the recovered sections and fluidized sediment in the bottom part. Limestone burrows consisting of siderite (represented by samples Cal-A, Cal-E and Cal-R) and several mud samples (Cal-01, Cal02, Cal-06-Cal-07, Cal-08, Cal-19, Cal-22 and Cal-23) were collected in the GC17 core. Coarse-grained sulfides and consolidated Fe-oxy-hydroxides were recovered.

Box corer associated: MVP11_BC01 (Fig.3.12).

Core gravity MVP11_GC18 (Fig.3.40)

LONG-WGS84	LAT-WGS84	DEPTH (m)	RECOVERY (m)	SITE
15.679025	39.209072	750	4.97	D1 pockmark

Figure 3.40–The gravity core GC18.

Description of the core: The GC18 core was collected on the northwestern of the fault escarpment confining the D1 structure to the south. Bioturbation was diffuse. A fragment of *Acharax sp.* with decapodan crustaceans was found at 2.88 m b.s.f., deeper in the section (3.90 m b.s.f.) and an almost entirely preserved echinoid carapax was present. Traces of Echinoderms were evident in several cores in the mud diapirs.

Box corer associated: No box corer are available at this station.

Core gravity MVP11_GC19 **(Fig.3.41)**

LONG-WGS84	LAT-WGS84	DEPTH(m)	RECOVERY (m)	SITE
15.719679	39.114999	731	5.76	D2 pockmark

Description of the core: The GC19 core was collected in the northern termination of the diapir D2 structure, in the lower flank of the edifice. The GC19 core was characterized by highly bioturbated sediments. This core was similar to those of GC14 and GC15, with an upper light brown mud followed by grey bioturbated mud downward. Vestiments from worms and pteropodes were present in the upper part of the core. At 2m b.s.f., a very coarse grained tephra layer was visible. The susceptibility profile showed high values. Other tephra layers were likely correlated to those found in the GC14 core.

Box corer associated: MVP11_BC14 (Fig.3.43).

Description of the box core: The BC14 box core recovered 17 cm of mud where biotubationsigns were present. Worms in their living position were found in the box corer and outside the box corer.

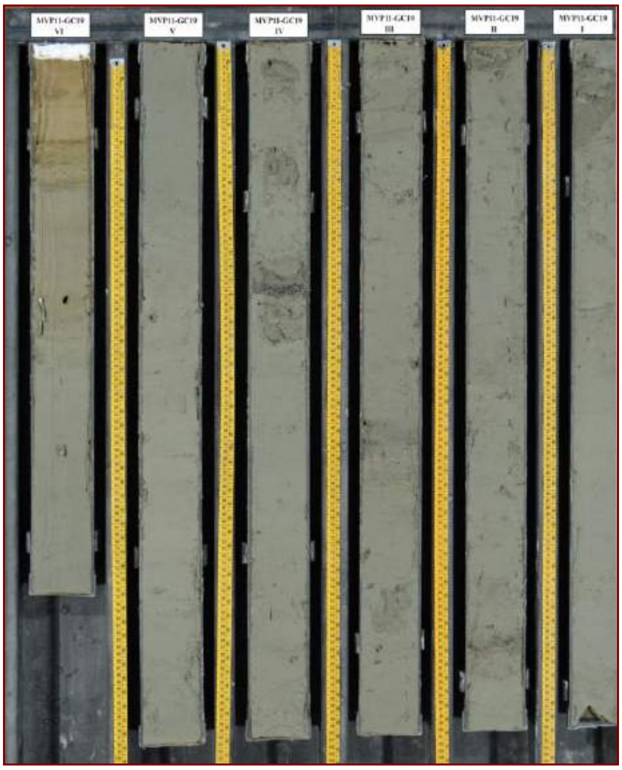

Figure 3.42- The gravity core GC19.

Figure 3.43–The box core BC14.

Core gravity MVP11_GC20 (Fig.3.44)

LONG-WGS84	LAT-WGS84	DEPTH (m)	RECOVERY (m)	SITE
15.726634	39.098514	653	60 cm	D2 pockmark

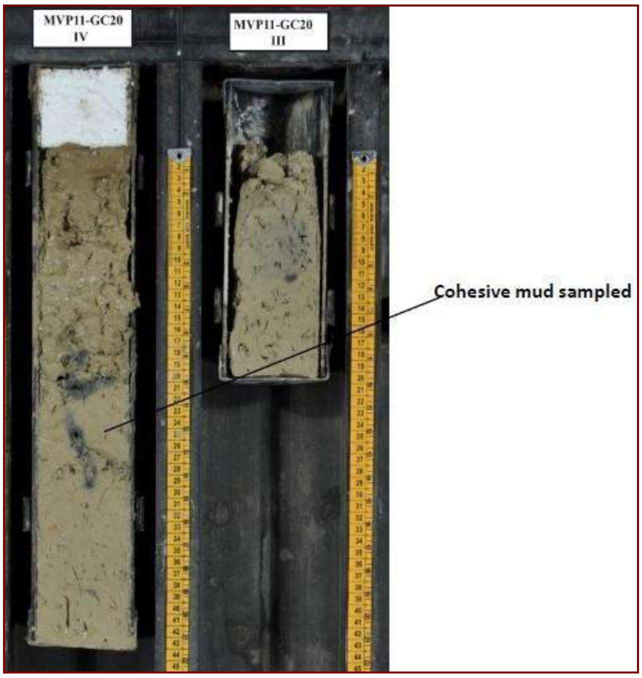

Figure 3.44-The gravity core GC20.

<u>Description of the core:</u> the core GC20 was collected in the area with the largest pockmarks concentration along the NW-SE fault, which dissects the diapir structure D2. On top of the D2 structure, the CHIRP profile showed a hummocky *facies* at the seafloor underlain by a deeper wider area showing an acoustic transparent *facies*. The core catcher was halted against a hard substrate made of carbonates and bivalves' shells. Similarly to the other cores collected in the diapirs, no degassing and smelling were noticed observed during the operations. In the core station, authigenic limestones and a fauna associationcomprising an extraordinary abundance of fragments of decapod crustaceans (*Calliax lobata*) and loose and disarticulated shells of *Lucinoma borealis* and *Acharaxsp.* were sampled below about 60 cm of red highly bioturbated mud. Trace fossils were evident in some carbonates, probably corresponding to the burrows of the decapods crustaceans. Samples of carbonate (Cal-B) and mud (Cal-17) were collected from the GC20 and analyzed via XRD.

<u>Box corer associated:</u> MVP11_BC15

Description of the box corer: The BC15 box core collected an extraordinary abundance of disarticulated lucinids shells and fragments of *Calliax lobata* and corals *Isidella*.

Core gravity MVP11_GC21 **(Fig.3.45)**

LONG-WGS84	LAT-WGS84	DEPTH (m)	RECOVERY (m)	SITE
15.736875	39.094501	634	4.43	D2 pockmark

Description of the core: A grey bioturbated mud with biogenic fragments was found below 40 cm of brown mud. Several fragments of *Acharax sp.* were found disseminated in the core section from 1 to 3.8 m b.s.f., above and below the pavement crust. Several samples of limestone crust (samples Cal-CC, Cal-BB, Cal-NN, Cal-HH) and other mud samples (samples Cal-29 and Cal-32) were collected from the GC21 core. Stable isotopic analysis was performed on a few samples of limestone crusts.

Box corer associated: MVP11_BC17

Description of the box corer: The BC17 box core (Fig.3.46) recovered 17 cm of mud.

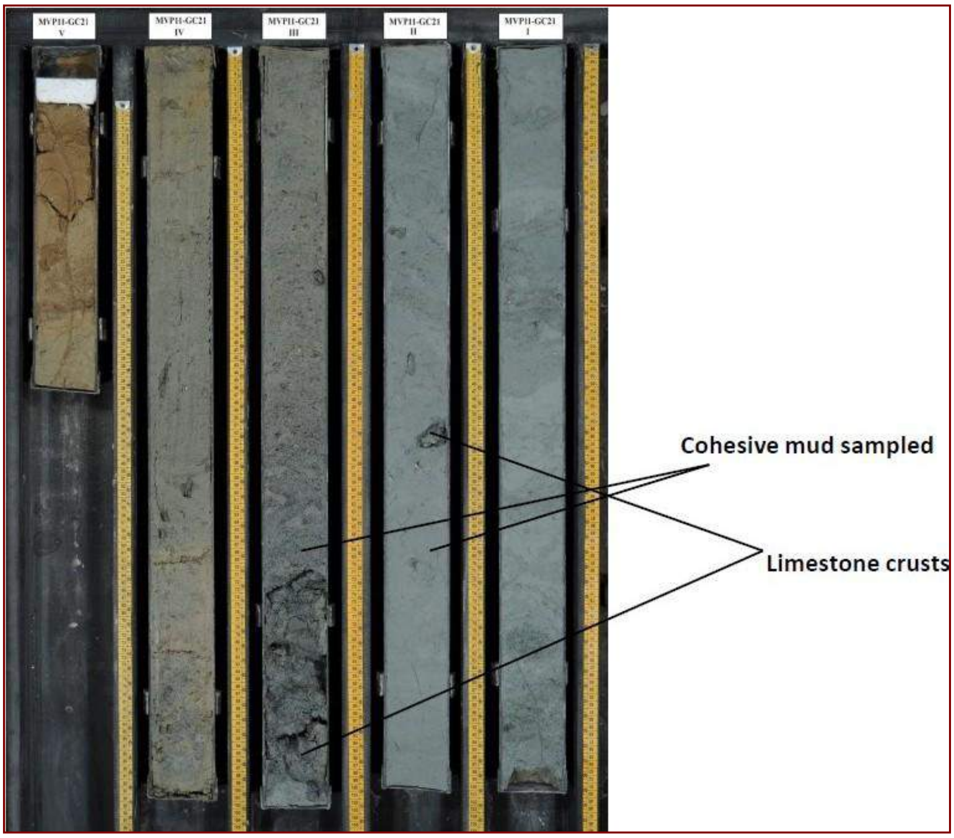

Figure 3.45–The gravity core GC21.

Figure 3.46–The Box core BC17.

Core gravity MVP11_GC22 **(Fig.3.47)**

LONG-WGS84	**LAT-WGS84**	**DEPTH (m)**	**RECOVERY (m)**	**SITE**
15.693392	39.059755	677	5 m	D3 pockmark

<u>Description of the core:</u> the core GC22 was collected on top of the diapirD3, in the centre of a 100 m-wide pockmark. A sedimentary succession consisting of bioturbated mud was found, although, further down, vertically elongated or circular

traces were present. No sulfate-related fauna assemblages were observed and only few shell fragments were found within the core. Susceptibility profile showed two peaks that were hardly observed in the sediment.

<u>Box corer associated:</u> MVP11_BC18 (Fig.3.48).

Figure 3.47-The gravity core GC22.

Figure 3.48–The Box core BC18.

Description of the box core: The BC18 box core was collected in the same station of the GC22 core and soft brown hemipelagic mud was recovered.

Core gravity MVP11_GC23(Fig.3.49)

LONG-WGS84	LAT-WGS84	DEPTH (m)	RECOVERY (m)	SITE
15.787976	39.040585	680	5.79	D3 pockmark

Description of the core: The GC23 core was similar to the other cores collected in the pockmark fields. No degassing and no smelling were recognized. The core was represented by grey mud, highly bioturbated with the presence of evident biogenic fragments. The typical soft brown mud cap was not present. No gas emission in the water column was observed during the recovering of the core.

Box corer associated: MVP11_BC19 (Fig.3.50).

Description of the box core: The BC19 box core was 29-cm-thick and had a 10-cm-thick soft brown hemipelagic mud in the upper part; a brown-grey laminated mud was present underneath.

Figure 3.49–The gravity core GC23.

Figure 3.50–The Box core BC19.

Core gravity MVP11_GC24 **(Fig.3.51)**

LONG-WGS84	LAT-WGS84	DEPTH (m)	RECOVERY (m)	SITE
15.815189	39.049236	679	5.80	D3 Fault scarp

Description of the core: the GC24 core was collected 2.5km eastward of the GC23 core. It was similar to GC23; the upper soft brown hemipelagic mud was missing, likely because it was trapped in the core head. A sedimentary sequence of bioturbated mud was present below it. When compared to GC23, this core had less evidence of bioturbation. Some tephra layers were recognized by the susceptibility profile, although yellow and coarse-grained layers found in other cores were not present.

Box corer associated: MVP11_BC20 (Fig.3.52).

Description of the box core: The BC20 core was made of light brown laminate mud.

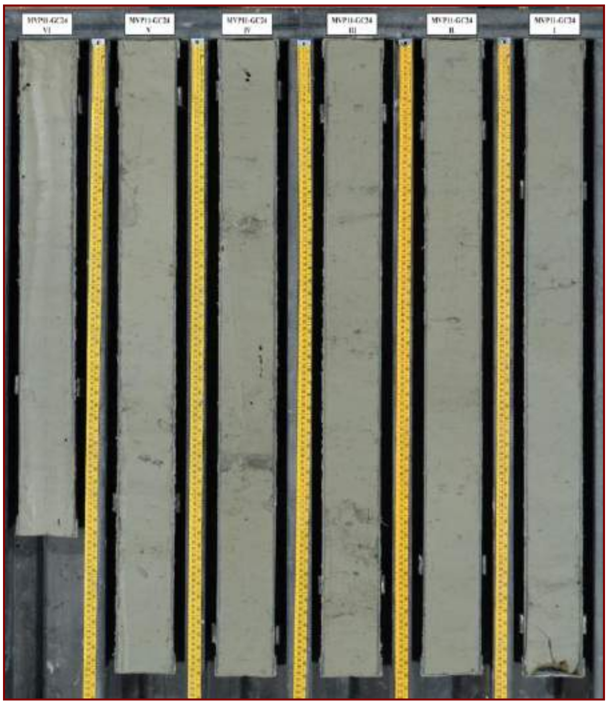

Figure 3.51–The gravity core GC24.

Figure 3.52–The box core BC20.

Core gravity MVP11_GC25 (Fig.3.53)

LONG-WGS84	LAT-WGS84	DEPTH(m)	RECOVERY (m)	SITE
15.723919	39.091773	694	1 m	D2 Fault scarp

Description of the core: The GC25 core was halted by authigenic carbonates cementing disarticulated lucinid shells after having penetrated 1 m of organic-rich mud. Limestone crusts with Lucinids were sampled at 95 cm b.s.f., (sample Cal-AA).

Box corer associated: MVP11_BC21 (Fig. 3.54) and MVP11_BC22 (Fig. 3.55).

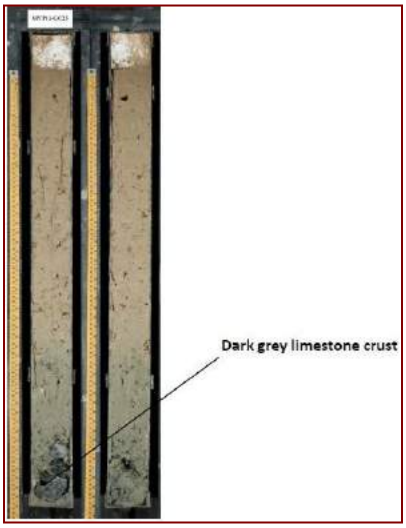

Figure 3.53–The gravity core GC25.

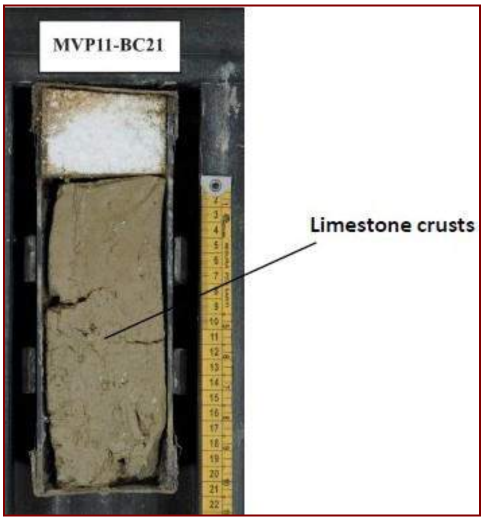

Figure 3.54-The Box core BC21.

Description of the core: The BC21 box core was collected in the same station of GC25 (Fig. 3.54), and retrieved living individuals of *Calliax lobata*, organogenic limestones with a vuggy and spongy fabric (sample Cal-H) and loose and disarticulated shells of lucinids.

Figure 3.55- The Box core BC22.

While the BC22 box core was collected in the same station of GC25, it retrieved only 20 cm of brown mud (Fig.3.55). Serpulids encrusted pumices were found, suggesting that part of the slightly cemented sediment was exposed to the seawater. Pteropodes were found.

Core gravity MVP11_GC26 **(Fig.3.56)**

LONG-WGS84	LAT-WGS84	DEPTH (m)	RECOVERY (m)	SITE
15.502335	39.409688	576	5.79	R1MV mud volcano

Description of the core: Gas bubbles were observed at the sea surface during coring operations. Mud was expelled from the coring head when reached the sea surface and H_2S smelling was clearly recognized once the coring barrel was retrieved on board. The core showed expansion cracks throughout the core. Strong evidence of chemical alterations and oxidations was present. In the IV section there was a level at 33 cm of yellow tephra. Several carbonate burrows made of Siderite were collected from the core catcher of GC26 (sample Cal-I) and Fe-oxy-hydroxide crusts (sample Cal-T) (Fig.3.56).

Box corer associated: MVP11_BC23 (Fig.3.57).

Description of the box core: The BC23 box core only recovered 20 cm of brown mud with Fe-oxy-hydroxide crusts.

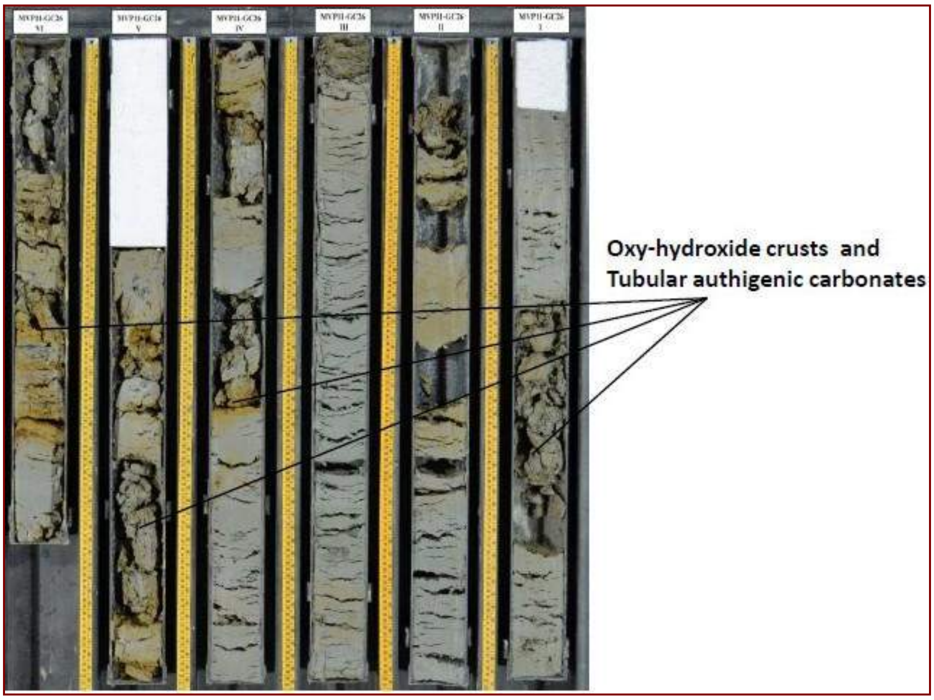

Figure 3.56–The gravity core GC26.

Figure 3.57-The Box Core BC23.

Core gravity MVP11_GC27 (Fig.3.58)

LONG-WGS84	LAT-WGS84	DEPTH(m)	RECOVERY (m)	SITE
15.512230	39.396533	570	5.78	R1MV mud volcano

<u>Description of the core:</u> No degassing and H_2S smelling were recorded during the operations. The core did not present the upper soft brown hemipelagic mud because it was trapped in the coring head. The core was relatively different from the other ones. It did not show any evidence related to the presence of fluids, no

tephra layers were visible and even the susceptibility profile was low. Bioturbation was diffuse through the entire section of the core. The core did not have the upper soft brown hemipelagic mud because it was trapped in the coring head, so the actual depths of the layers were not preserved in the core.

Box corer associated: MVP11_BC24 (Fig.3.59).

Figure 3.58–The gravity core GC27.

Figure 3.59-The Box core BC24.

Description of the box core: the BC24 box core showed bioturbated hemipelagic mud with stains of organic matter.

Core gravity MVP11_GC28 (Fig.3.60)

LONG-WGS84	LAT-WGS84	DEPTH (m)	RECOVERY (m)	SITE
15.534888	39.372324	552	3.12	R1MV mud volcano

Description of the core: The upper part of the GC28 core consisted of a completely disrupted section of dark grey mud, intercalated with deformed tephra layers. Gas bubbles and mud expulsion were observed. H_2S smelling occurred. Sulfides and Fe-oxy-hydroxides were occurring in the cores shown. Several mud samples (Cal-04, Cal-12, Cal-14, Cal-18, Cal-20 and Cal-21) were collected at different levels in the core (Fig. 3.60).

Box corer associated: MVP11_BC25 (Fig.3.61).

Description of the box core: The BC25 box core was rich in burrows filled with Pyrite-Marcasite or Sphalerite (Fig.3.61). Several samples of sulfide were collected (samples Cal-L, Cal-Q, Cal-Q_1).

Figure 3.60–The gravity core GC28.

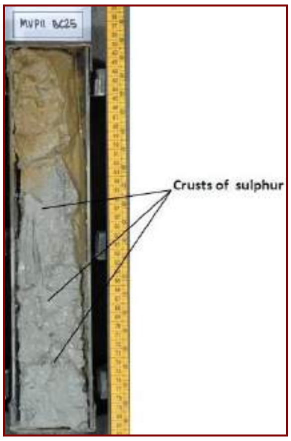

Figure 3.61-The Box core BC25.

Core gravity MVP11_GC29 (Fig.3.62)

LONG-WGS84	LAT-WGS84	DEPTH (m)	RECOVERY (m)	SITE
15.517343	39.353377	707	5.52 m	R1MV mudflow

Description of the core: No degassing and H_2S smelling were recorded. The upper part of the core was rich in water and grey and brown mud were mixed in the first 50 cm below the seafloor. At 50 cm b.s.f., a biogenic sand was found. Bioturbation

was present in the IV section. Downwards the mud was poorer in water with a grey-brown color. No expansion cracks in the lower section of the core were present. Sample of siderite (Cal-U) and several samples of pyrite crusts were collected from the lower section of the core (sample Cal-S, Cal-Z, Cal-W, Cal-X). In the core catcher pumice fragments, sulfides and native sulfur were present. In the core catcher pumices of several grain sizes occurred along with sulfur crystals.
Box corer associated: MVP11_BC26 (Fig.3.63).

Description of the box core: The BC26 box core showed a soft brown hemipelagic mud cap followed by grey mud.

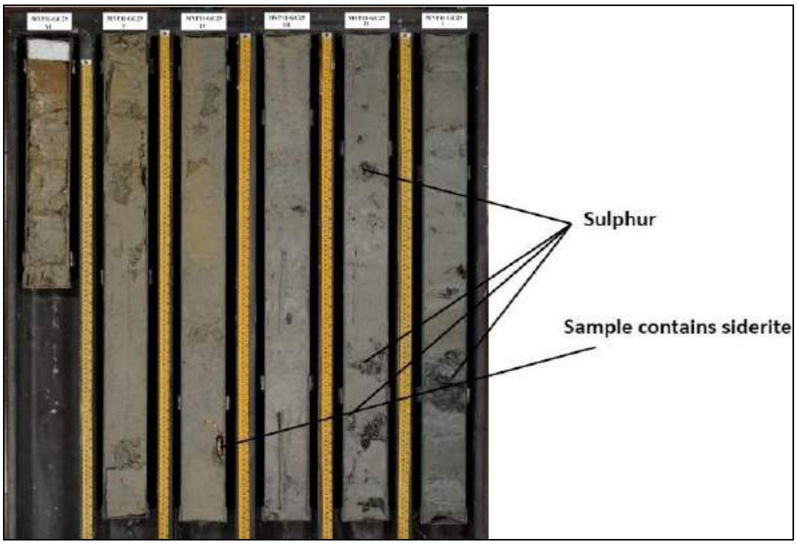

Figure 3.62-The gravity core GC29.

Figure 3.63-The Box Core BC26.

Core gravity MVP11_GC30 (Fig.3.64)

LONG-WGS84	LAT-WGS84	DEPTH (m)	RECOVERY (m)	SITE
15.492615	39.331974	957	5.40	R1MV mudflow

Description of the core: Degassing after the core was retrieved on the deck. The core displayed some small burrows made of siderite and evidence of chemical alteration and oxidation characterized the tephra layers.

Box corer associated: MVP11_BC27 (Fig.3.65).

Description of the box core: The BC27 box core showed reddish brown hemipelagic mud rich in water and biotubation and organic matter in the bottom section.

Figure 3.64-The gravity core GC30.

Figure 3.65–The Box core BC27.

Core gravity MVP11_GC31 **(Fig.3.66)**

LONG-WGS84	**LAT-WGS84**	**DEPTH (m)**	**RECOVERY (m)**	**SITE**
15.506966	39.3 95636	617	5.79 m	R1MV mud volcano

Description of the core: A gentle degassing was observed after the core was retrieved on board and a very subtle H_2S smell was recognized. The GC31 core was very similar to the GC27 core and did not show any particular evidence of the presence of fluids within the sediment. Its upper part was found in the head of the coring device.

Box corer associated: MVP11_BC28 (Fig.3.67).

Description of the core: The BC28 box core showed hemipelagic mud with the presence of a tiny tephra layer inside.

Figure 3.66-The gravity core GC31.

Figure 3.67–The Box core BC28.

MarBeep14

Four samples of concretions were obtained from sampling stations collected during the second campaign in June 2014 (Table 2.3) and were analyzed for mineralogical, petrographical and geochemical composition.

Five water samples were collected from 549 and 755 m depths by rosette sampler (Fig. 2.11) in correspondence of the R1MV (MB14_ROS5, MB14_ROS6 and MB14_ROS7) and RMV (MB14_ROS8 and MB14_ROS9) structures whilst two additional water samples (MB14_BC10 and MB14_BC11) were directly collected from the box-corer in correspondence of the two gas discharges (see below). Each water sample was divided into three aliquots, the first one was transferred to a 125 mL plastic bottle for the determination of the main anions while the second one was acidified with 1% Suprapur HCl in a 50 mL plastic bottle for the cation analysis. Both aliquots were filtered at 0.45 µm.

The third (not filtered) aliquot was transferred to pre-weighed 100mL glass bottle, where 5 mL of a 1M Na_2CO_3 solution were previously added, for the determination of free-CO_2. In addition, two gas samples were collected at the sea surface above the R1MV (MB14_BC05) and RMV (MB14_BC09) structures from two box-corers by connecting a silicon tube to a 250 mL pre-evacuated gas flask to the water vent for the analysis of the main component and the carbon isotopic ratio in CO_2.

3.3- Analytical Results

3.3.1- Mineralogical analysis

Organogenic carbonate crusts

The carbonate crust samples were found at the sea-bottom surface, a few meters in the sub-seafloor, sometimes accompanied by the presence of traces of benthic organisms that indicates an exposition to the seabed. Occasionally, carbonates were associated with shells of lucinids and solemids, i.e. bivalve organisms that live in symbiosis with bacteria that oxidized sulfides and are indicators of cold seep environments.

The XRD analyses of the carbonate crusts showed that their mineralogical composition was consisting of carbonate minerals (calcite-aragonite-dolomite) and abundant concentrations of quartz, feldspars, phyllosilicates. It is to point out that in several samples (Cal-H, Cal- BB, Cal-CC, Cal-HH, Cal-AA) dolomite was absent. Some samples contained pyroxene (Table 3.2). The quantitative analysis of the mineralogical composition was determined by X-Ray diffraction analyses coupled with Rietfield refinement. The latter was performed using Maud v2.2. Calcite ranged from 10.7 to 35.2 %wt, aragonite from 29.5 to 70.0 % wt and dolomite from 0.3 to 2.9 % wt (Table 3.3).

Rock samples	Quartz	Feldspars	Phyllosilicates	Calcite	Dolomite	Aragonite	Other
Cal-B	x	x (anorthite)	x (probably mica- illite- chlorite- kaolinite)	x	x	x x	Pyroxene
Cal-C	x	x (albite)	x (probably mica- illite- chlorite- kaolinite)	x x	x	x x	Pyroxene
Cal-H	x	x x (albite)	x (probably mica- illite- chlorite- kaolinite)	x	-	x x	Pyroxene
Cal-N	x	x (albite- orthoclase)	x (probably mica -kaolinite)	x x	x	x x	-
Cal-BB	xx	xx (albite)	x (probably mica- illite- chlorite- kaolinite	x	-	x	-
Cal-CC	xx	xx (anorthite)	x (probably mica –illite – chlorite –kaolinite)	xx	-	x	-
Cal-HH	xx	xx (albite)	x (probably mica –illite – chlorite –kaolinite)	xx	-	x	halite
Cal-NN	xx	xx (anorthite)	x (probably mica –illite – chlorite –kaolinite)	xx	x	x	-
Cal-AA	xx	x(albite)	x (probably mica- illite- chlorite- kaolinite)	x	-	x	Pyroxene (omphacite)

Table 3.2: Mineralogy composition of the carbonate crusts (x: medium content xx: maximum content).

samples		Quartz	Calcite	Aragonite	Dolomite	Albite(Ca)	Illite	Anortite	Augite	Kaolinite
Cal-B	wt%	8.27	17.18	48.83	1.81	8.85	2.15	1.61	11.27	-
Cal-C	wt%	9.66	35.24	29.51	2.87	7.38	1.68	2.59	11.04	-
Cal-H	wt%	9.16	23.01	46.18	0.31	7.36	3.45	3.26	7.23	-
Cal-N	wt%	11.5	27.06	38.39	1.77	6.85	3.75	2.06	8.58	-
Cal-BB	wt%	12.82	12.87	49.9	-	8.65	7.19	6.88	-	1.69
Cal-CC	wt%	11.98	12.22	45.46	-	12.83	7.1	5.56	-	4.85
Cal-HH	wt%	9.16	10.72	53.95	-	5.35	11.89	5.26	-	3.68
Cal-NN	wt%	9.67	14.87	53.78	-	6.66	6.45	5.98	-	2.59
Cal-AA	wt%	6.04	10.48	69.98	-	4.09	3.92	3.47	-	2.02

Table 3.3: Relative abundance (in %) of the carbonate phases from the organogenic carbonate crusts.

Siderite concretions

This is a particular form of carbonate that was only found in the mud volcanoes a few meters below the sea-bottom. They have a typical tubular shape. The XRD analysis of the tubular carbonates showed that they are largely dominated by siderite although quartz, phyllosilicates and rare feldspar also occurred (Table 3.4). In one sample (Cal-R), calcite was found.

Rock samples	Quartz	Feldspars	Phyllosilicates	Siderite	Other
Cal-I	x	tace(albite)	x	xx	-
Cal-G	x	traces	x	xx	-
Cal-M	x	traces	x	xx	-
Cal-E	x	trace (albite)	x (probably mica-illite-chlorite)	xx	-
Cal-R	x	trace	x	xx	trace of calcite
Cal-A	x	-	x	xx	-
Cal-V	x	x (albite)	x	xx	-
Cal-U	x	x (albite-microcline)	x (probably mica-kaolinite)	xx	-
Cal-RR	x	x (albite)	x (mica-illite)	xx	-
Cal-EE	x	traces (albite-microcline)	x (mica-illite-kaolinite)	xx	-
Cal-MB4	X	-	x (mica-illite-kaolinite)	XX	-

Table 3.4: Mineralogy composition of the tubular-shaped carbonates. Symbols as in Table 3.2.

Iron oxy-hydroxide crusts

Iron oxy-hydroxide crusts were found at the seafloor and in the upper part of the sedimentary column (a few centimeters below the seafloor). The XRD analysis of the iron oxy-hydroxide crusts (Table 3.5) showed the presence of oxides (FeOOH and hematite), quartz, feldspar, phyllosilicates. It is to remark that sample Cal-T by XRD was characterized by amorphous oxides. Halite was observed in the two samples (Cal-T and Cal-Y).

Rock samples	Quartz	Halite	Feldspars	Phyllosilicates	Oxy-hydroxides
Cal-F	x	-	-	x (probably mica-illite)	x (goethite)
Cal-P	x	-	x (albite-anorthoclase)	x (probably mica-illite)	Trace (goethite)
Cal-T	x	x	x (albite)	x (probably mica-illite-chlorite-kaolinite)	-
Cal-Y	x	x	x (albite)	trace	hematite

Table 3.5: Mineralogy composition of the iron oxy-hydroxide crusts. Symbols as in Table 3.2.

Pyrite and sulfide crusts

Pyrite crusts and pavements, pyritized bioturbational structures and sulfur-lined burrows were found in the sedimentary succession at 20–50 cm below the seafloor. XRD analysis of pyrite and sulfide crusts showed moderate to abundant concentration of sulfide minerals (such as pyrite and subordinate sphalerite, marcasite), quartz, feldspar, with traces of phyllosilicates and rare and melanterite (Table 3.6). The presence of halite was detected in the samples Cal-W and Cal-X.

Rock samples	Quartz	Halite	Feldspars	Phyllosilicates	Sulfides
Cal-D	x	-	trace	-	xx (pyrite-marcasite-sphalerite)
Cal-Q	x	-	-	trces	xx (pyrite-marcasite-sphalerite)
Cal-O	x	-	x (anorthite)	traces	xx (pyrite-marcasite-sphalerite)
Cal-L	x	-	-	traces	xx (pyrite-marcasite-sphalerite)
Cal-S	x	-	x (albite)	traces	xx (pyrite-marcasite)
Cal-Z	x	-	x (albite)	traces	xx (pyrite-marcasite)
Cal-W	x	x	x (albite)	x (probably mica-kaolinite)	x (pyrite)
Cal-X	x	x	x (anorthite)	traces	x (pyrite)
Cal-MB1	x	-	-	-	xx (Pyrite- sphalerite- marcasite)
Cal-MB2	x	-	-	-	xx (Pyrite- marcasite-melanterite)
Cal-MB3	x	-	-	-	xx (Pyrite- marcasite-melanterite-saphalerite)

Table 3.6: Mineralogical composition of pyrite and sulfur crusts. Symbols as in Table 3.2.

Cohesive mud samples

Mineralogical composition of the mud samples is reported in Table 3.7 and showed that their mineral composition was mainly consisting of quartz, halite, feldspars (plagioclase and k-feldspar), phyllosilicates, except of the sample Cal-14 (see in CHAPTER 2) contains pyrite; furthermore in many samples the presence of calcite, dolomite, siderite, hematite and pyrite (Table 3.7) was also recognized, although in very low amount.

Unconsolidated samples	Quartz	Halite	Feldspars	Phyllosilicates	other
Cal-1	x x	x	x (albite)	x x (probably mica- illite-kaolinite-chlorite)	Hematite
Cal-2	x x	x	x (albite-microcline)	x x (probably mica- illite-kaolinite-chlorite)	-
Cal-3	x x	x	x (albite-microcline)	x x (probably mica- illite-kaolinite-chlorite)	-
Cal-4	x x	x	x (anorthoclase)	x x (probably mica-illite-kaolinite-chlorite)	Calcite
Cal-5	x x	x	x (albite-microcline)	x x (probably mica- illite-kaolinite-chlorite)	-
Cal-6	x x	x	x (albite-microcline)	x x (probably mica- illite-kaolinite-chlorite)	Dolomite
Cal-7	x x		x (albite-microcline)	x x (probably mica- illite-kaolinite-chlorite)	Siderite
Cal-8	x x	x	x (anorthite)	x x (probably mica- illite-kaolinite-chlorite)	-
Cal-9	x x	x	x (albite - anorthoclase)	x x (probably mica- illite-kaolinite-chlorite)	Calcite
Cal-10	x x	x	x (albite-microcline)	x x (probably mica- illite-kaolinite-chlorite)	Calcite
Cal-11	x x	x	x (albite-microcline)	x x (probably mica- illite-kaolinite-chlorite)	Hematite
Cal-12	x x	x	x (albite)	x x (probably mica- illite-kaolinite-chlorite)	Hematite
Cal-13	x x	x	x (albite)	x x (probably mica- illite-kaolinite-chlorite)	-
Cal-14		x	-	-	Pyrite-marcasite-sulfur
Cal-15	x x	x	x (albite - microcline)	x x (probably mica- illite-kaolinite-chlorite)	Calcite
Cal-16	x x	x	x (albite)	x x (probably mica- illite-kaolinite-chlorite)	Calcite
Cal-17	x x	x	x (albite-microcline)	x x (probably mica- illite-kaolinite-chlorite)	Calcite
Cal-18	x x	x	x (albite)	x x (probably mica- illite-kaolinite-chlorite)	-
Cal-19	x x	x	x (albite - microcline)	x x (probably mica- illite-kaolinite-chlorite)	-
Cal-20	x x	x	x (albite - microcline)	x x (probably mica- illite-kaolinite-chlorite)	-
Cal-21	x x	x	x (albite - microcline)	x x (probably mica- illite-kaolinite-chlorite)	-
Cal-22	x x	x	x (albite - microcline)	x x (probably mica- illite-kaolinite-chlorite)	Hematite
i	x x	x	x (albite - anorthoclase)	x x (probably mica- illite-kaolinite-chlorite))	-
Cal-24	x x	x	x (albite - microcline)	x x (probably mica- illite-kaolinite-chlorite)	-
Cal-25	x x	x	x (albite)	x x (probabile miche-illite-kaolinite-clorite)	-
Cal-26	XX	X	X (albite)	XX (probably mica-illite-kaolinite-chlorite)	-
Cal-27	XX	X	X (albite)	XX (probably mica-illite-kaolinite-chlorite)	Calcite- dolomite - manganesifera Fe ((Mn,Zn) Co3)$_2$
Cal-28	XX	X	X (anorthite)	XX (probably mica-illite-kaolinite-chlorite)	-
Cal-29	XX	X	XX (albite)	XX (probably mica-illite-kaolinite-chlorite)	Calcite-hematite
Cal-30	XX	X	X (anorthite)	XX (probably mica-illite-kaolinite-chlorite)	Calcite-hematite
Cal-31	XX	X	X (albite- microcline)	XX (probably mica-illite-kaolinite-chlorite)	-
Cal-32	XX	X	X (anorthite)	XX (probably mica-illite-kaolinite-chlorite)	Calcite- hematite

Table 3.7: Mineralogical composition of the mud samples. Symbols as in Table 3.2.

The clay fraction, analyzed in 4 samples, showed the presence of illite, vermiculite, chlorite, kaolinite with the exception of Cal-21 where chlorite was absent (Table 3.8).

Unconsolidated samples	**Illite**	**Kaolinite**	**Clorite**	**Vermiculite**
Cal-6	x	x	x	x
Cal-11	x	x	x	x
Cal-15	x	x	x	x
Cal-21	x	x	-	x

Table 3.8: Mineralogical composition of the clay fraction (< 4µm) carried out in 4 samples. Symbols as in Table 3.2.

3.3.2 -Petrographic analyses

Petrographic were only carried out on the carbonate samples and classified according to Dunham (1962) and the modified version of Embry and Klovan (1971), on the basis of the grain/micrite ratio.

Organogenic carbonate crusts

The optical microscopy observations in transmitted light showed the typical composition of a micritic carbonate where size of quartz grains was about 100 µm with sub-angular in shape. Plagioclase, pyroxene, iron oxy-hydroxides biotite and remnants of organogenic carbonate (Figs. 3.10 and 3.11) were also found.

Small fragments of volcanic rocks (pumice and scoria) were relatively common. The porosity was relatively low. The amount of grains in the matrix is > 10%, therefore, according to Dunham (1962) this sample can be classified as Wackestone.

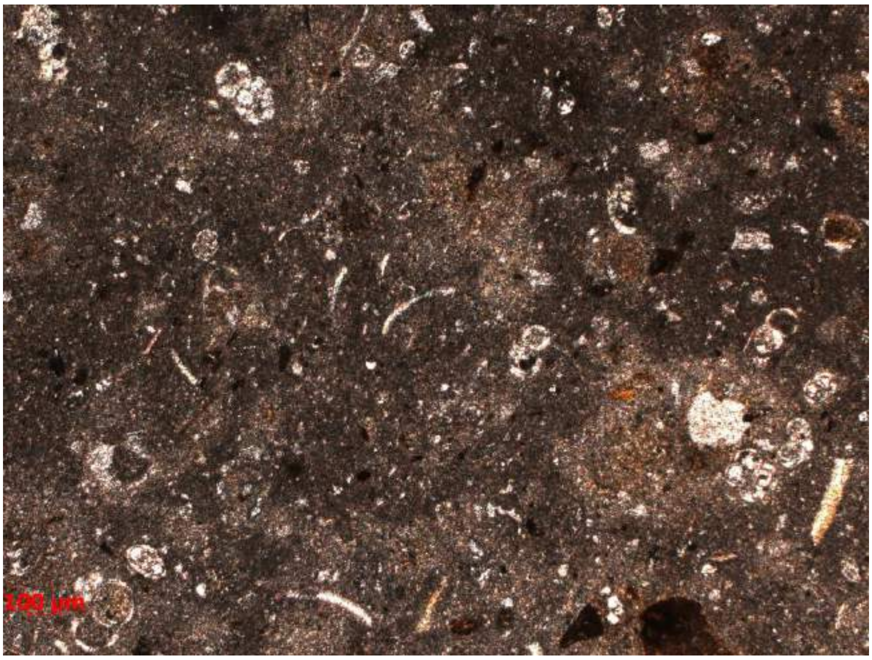

Figure 3.10- Photomicrograph of the sample Cal_C in plan polarized light (PPL), showing a typical composition of micrite carbonate, where quartz a sub-angular shape. Note the presence of organogenic fragments.

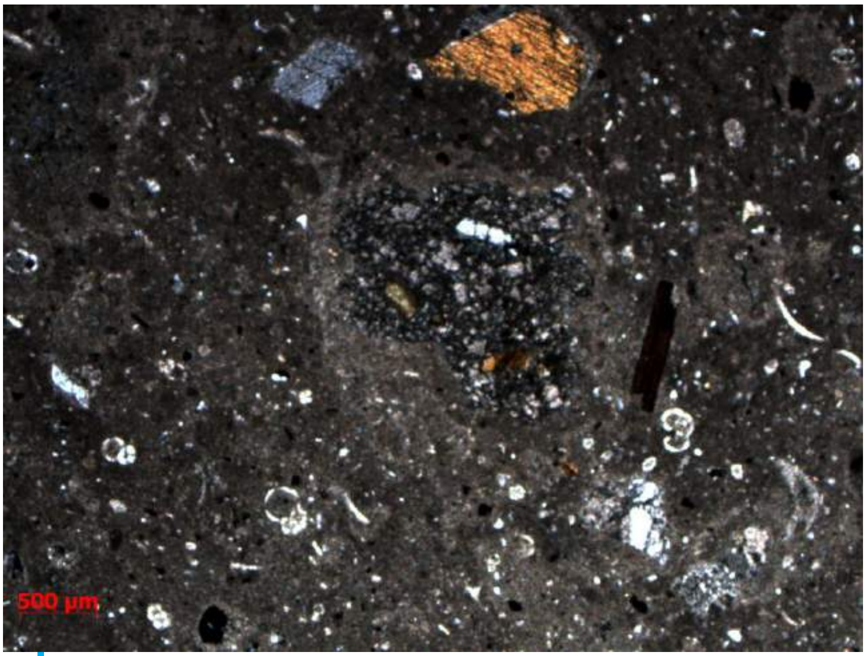

Figure 3.11- Photomicrograph of the sample Cal_B in cross-polarized light (CPL) showing a typical composition of micrite carbonate with organogenic fragments.

<u>Siderite concretions</u>

The observations by optical microscopy in transmitted light showed fine to very fine granules of siderite (sideritic micrite), whose dimensions ranged between 5 and 50 µm, quartz (size between 30-100 µm) and muscovite (Fig.3.12a). Iron oxy-hydroxides were observed to fill small veins and/or fractures, as observed in the samples Cal_M (Fig. 3.12b) and Cal_MB4 (Fig. 3.14). The porosity was low. The amount of grains in most samples is < 10% and this suggested its classification as mudstone (Dunham 1962). Except for the sample Cal-E’, which appeared as rock-grained Packstones (Fig. 3.13).

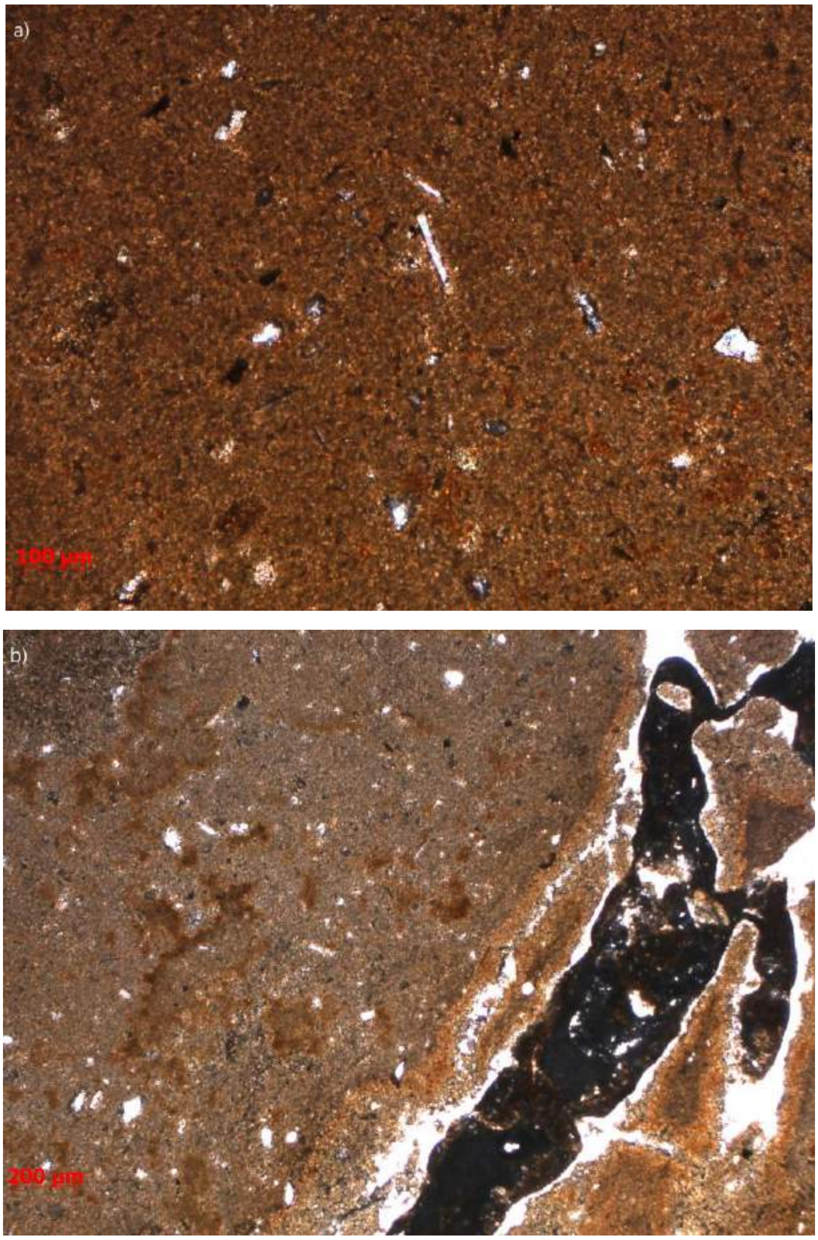

Figure 3.12- Photomicrograph of the sample Cal_ M. a) in cross-polarized light (CPL), showing the presence of muscovite and quartz and b) in plane polarized light (PPL), showing the presence of iron oxy-hydroxides in small fractures and veins.

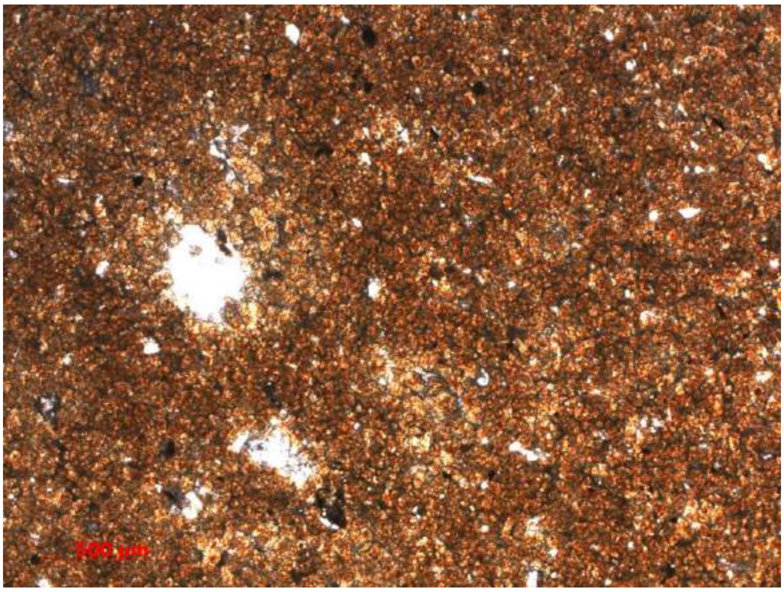

Figure 3.13- Photomicrograph of the sample Cal_E in plane polarized light (PPL), showing a Packstone-like structure. Most sample is made of siderite grains.

Figure 3.14- Photomicrograph of the sample Cal_MB4 in cross-polarized light (CPL) of a micrite rock composed by a siderite-rich matrix with the presence of iron oxy-hydroxides.

3.3.3- SEM-EDS semi-quantitative chemistry

Organogenic carbonate crusts

Semi-quantitative chemical analyses by SEM-EDS were conducted on the thin sections of carbonates (sample Cal-A, sample Cal-B and sample Cal-H). SEM analyses on the sample Cal-C, reveled the tow carbonate textures: i) darker micrite precipitated in the porosity of the host sediment where quartz, plagioclase and pyroxene crystals, iron oxy-hydroxides, shell fragments and foraminifera were abundant and ii) acicular calcite that fills the fractures and open cracks as shown in

(Fig. 3.15). On the sample Cal-C, two pyroxene crystals were also analyzed (Fig. 3.16), likely referred to augite or diopside.

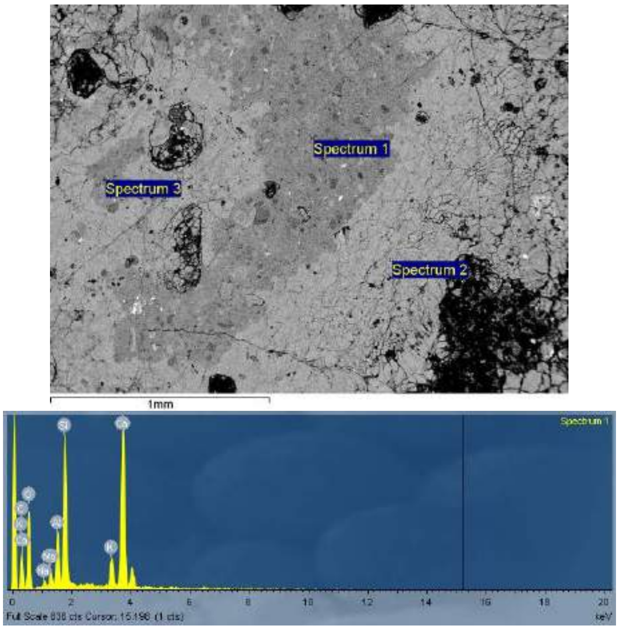

Spectra	Wt% Na	Wt% Mg	Wt% Al	Wt% Si	Wt% K	Wt% Ca	Wt% O	Wt% Total
Spectrum 1	1.21	1.87	5.75	16.96	4.71	30.35	39.16	100
Spectrum 2	-	-	-	-	-	71.47	28.53	100
Spectrum 3	-	5.88	2.26	4.69	-	54.29	32.89	100

Figure 3.15-SEM Photomicrograph of the sample Cal-C and EDS spectrum. it is to remark darker ones where it seems to dominate the silicate (spectrum 1) likely feldspar and organogenic remnants. Whereas Spectrum 2 and 3 are indicative of the presence of calcite and dolomite, respectively.

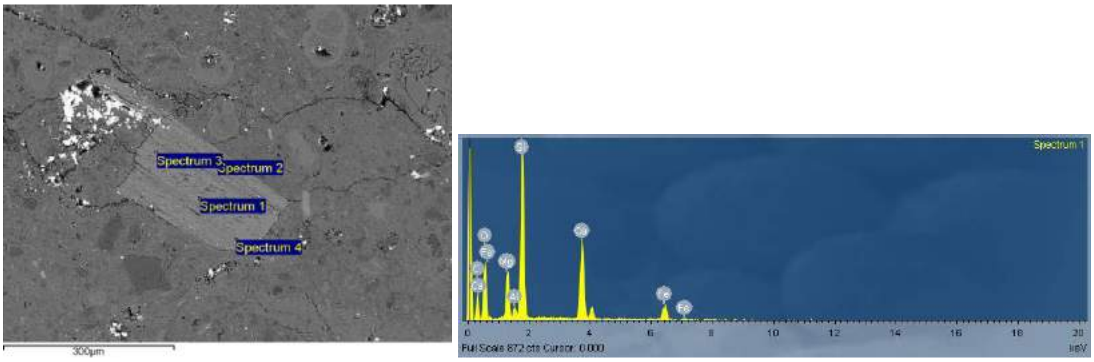

Spectra	Wt% Mg	Wt% Al	Wt% Si	Wt% Ca	Wt% Fe	Wt% O	Wt% Total
Spectrum 1	7.57	1.48	24.42	16.10	7.68	42.75	100
Spectrum2	7.32	1.05	24.91	15.59	8.37	42.76	100
Spectrum3	8.69	1.38	24.9	15	6.78	43.25	100
Spectrum 4	7.62	1.43	24.57	16.92	6.54	42.91	100

Figure 3.16-SEM Photomicrograph of the sample Cal-C and the semi-quantitative analysis of two pyroxene crystals.

The sample Cal-B showed that dolomite was abundantly present, has a micro-granular or acicular habit (Fig.3.17). There were also unidentified mineral containing Cu, Zn (Fig. 3.17). And the presence of complex textures (Fig. 3.18), whose grains were consisting of Fe, Ti oxy-hydroxides (spectrum 1), silicatic matrix (spectrum 2), anhedral calcite (spectrum3), acicular aragonite (spectrum 4).

It is noted in the sample Cal_H, calcite dominated, has acicular habit and some of Mg (Fig.3.19). There were also organogenic (foraminifera) remnants similar to those found in both of the two samples, with quartz and plagioclase grains (Fig.3.20).

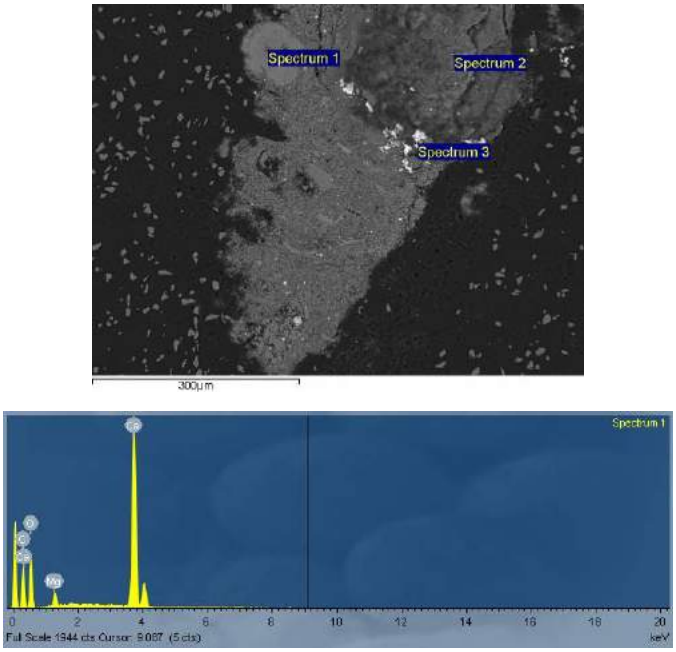

Spectra	Wt% Mg	Wt% Al	Wt% Si	Wt% K	Wt% Ca	Wt% Fe	Wt% Cu	Wt% Zn	Wt% O	Wt% Total
Spectrum 1	4.48	-	-	-	66.17	-	-	-	29.36	100
Spectrum 2	5.94	6.73	9.88	0.99	37.96	1.55	-	-	36.95	100
Spectrum 3	-	4.77	-	-	1.11	0.91	61.99	8.56	22.65	100

Figure 3.17-SEM Photomicrograph of the sample Cal-B. Spectrum 1 was likely related to dolomite, whereas spectra 2 and 3 was an unidentified mineral containing abundant Cu and Zn.

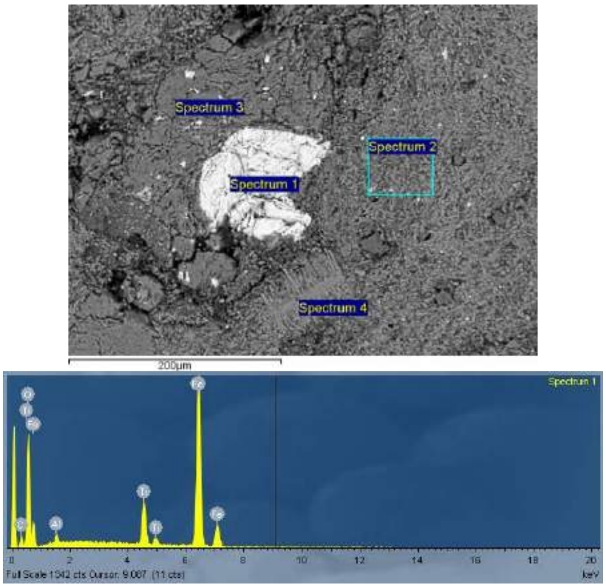

Spectra	Wt% Na	Wt% Mg	Wt% Al	Wt% Si	Wt% K	Wt% Ca	Wt% Ti	Wt% Fe	Wt% O	Wt%Total
Spectrum 1			1.22				8.36	65.08	25.32	100
Spectrum 2		2.33	3.79	10.64	1.12	42.07	0.81	2.1	36.34	100
Spectrum 3	2.66	0.56	7.68	34.35	2.43	2.36		0.93	48.9	100
Spectrum 4						66.59			27.7	100

Figure 3.18-SEM Photomicrograph of the sample Cal-B and EDS analysis.

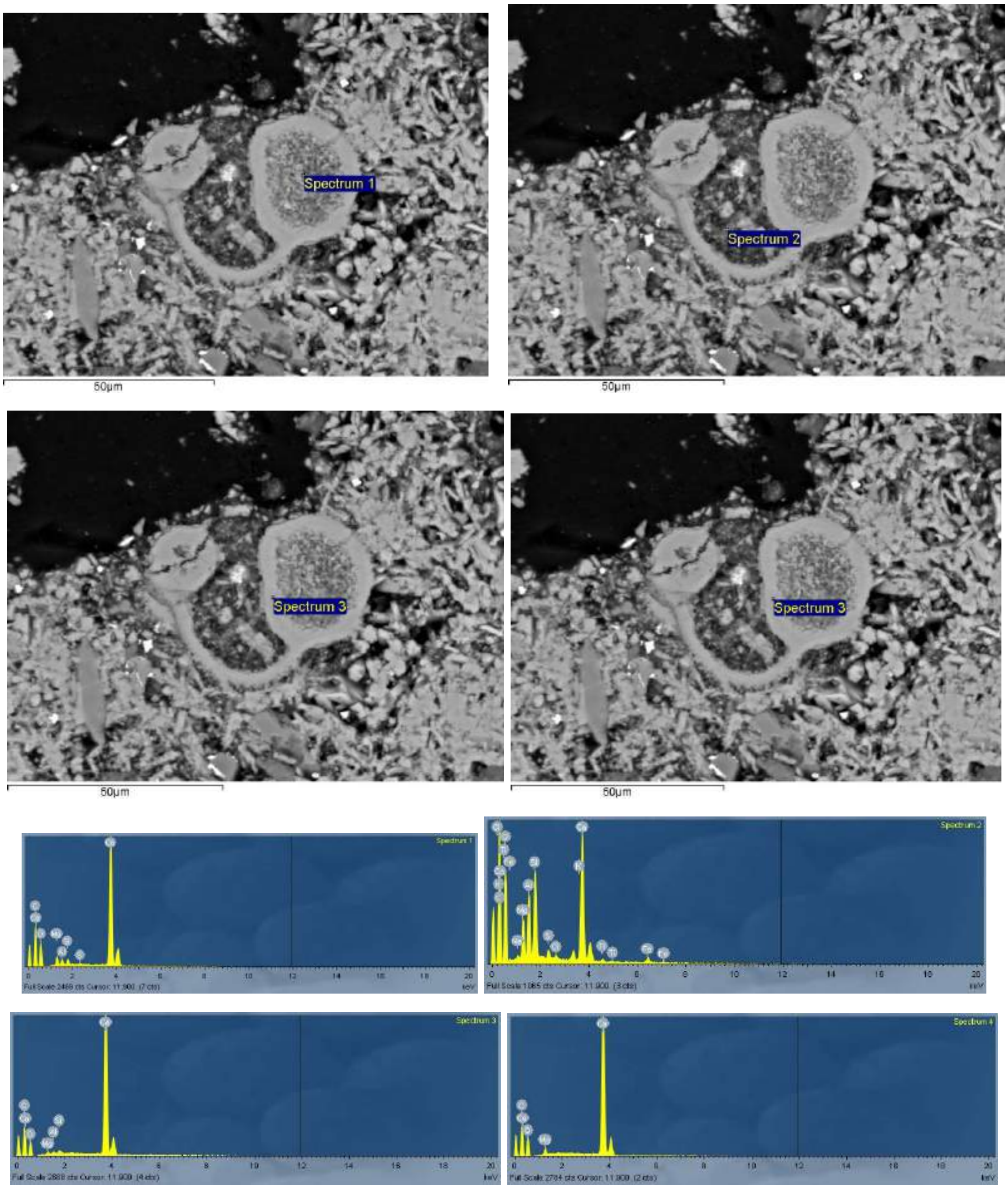

Spectra	Wt% Mg	Wt% Al	Wt% Si	Wt% S	Wt% Ca	Wt% O	Wt% Total
Spectrum 1	3.39	1.74	1.64	0.49	61.73	31.01	100
Spectrum 2	5.84	8.71	11.97	1.38	26.02	39.61	100
Spectrum 3	1.24	0.84	0.92	-	67.45	29.54	100
Spectrum 4	2.98	-	-	-	67.93	29.05	100

Figure 3.19–SEM Photomicrograph of the sample Cal_H and EDS analysis: calcite with some Mg (spectra 1, 3 and 4); calcite affected by some silicate minerals (spectrum 2).

a)

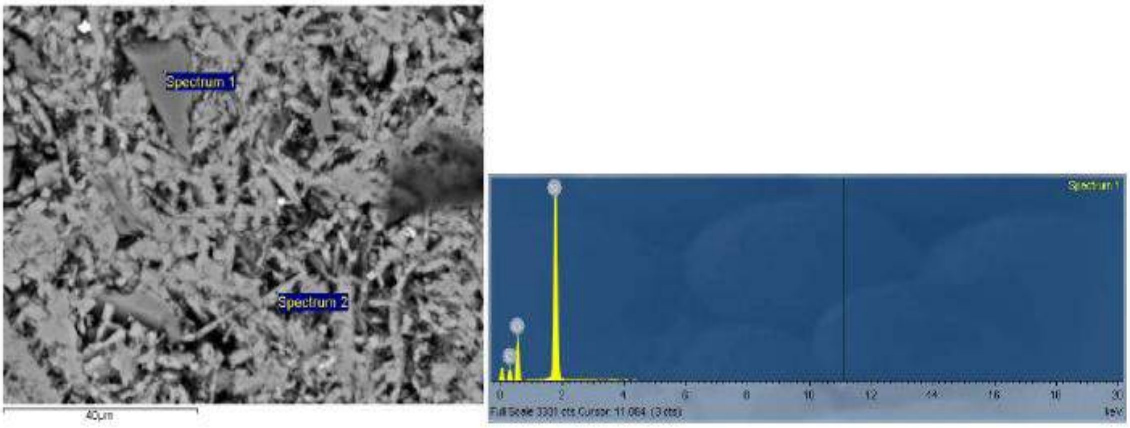

Spectra	Wt% Mg	Wt% Al	Wt% Si	Wt% Cl	Wt% K	Wt% Ca	Wt% O	Wt% Total
Spectrum 1	-	-	46.74	-	-	-	53.25	100
Spectrum 2	0.58	4.05	6.28	0.41	1.72	53.9	33.02	100

b)

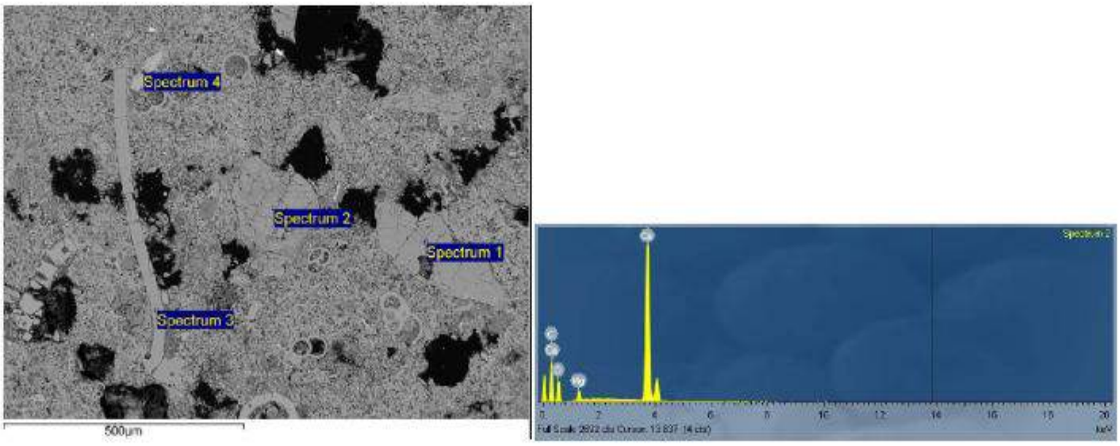

Spectra	Wt% Na	Wt% Mg	Wt% Al	Wt% Si	Wt% S	Wt% Cl	Wt% K	Wt% Ca	Wt% Ti	Wt% Fe	Wt% O	Wt% Total
Spectrum 1	2	-	13	23	1	1	3	9	-	1	46	100
Spectrum 2	-	4	-	-	-	-	-	67	-	-	29	100
Spectrum 3	-	5	-	-	1	-	-	65	-	-	30	100
Spectrum 4	-	6	10	19	-	0	8	-	2	14	41	100

Figure 3.20-SEM Photomicrograph of the sample Cal_H and EDS analysis: a) quartz (spectrum1) and silicate mineral (spectrum 2), b) organogenic (foraminifera) remnants affected by silicate minerals.

Siderite concretions

The chemical analyses by SEM were conducted on the thin sections of samples: Cal-A, Cal-M, Cal-G, Cal-I, Cal-E and Cal-MB4. The SEM-EDS analysis showed the presence of siderite and quartz as shown in the sample cal-G (Fig.3.21) and sample Cal-I (Fig.3.22).

In the sample Cal_A, siderite appeared to be precipitated as small rounded crystals whose size was of about (4-5µm) and aligned along levers features that may likely resemble burrowing structures (Fig.3.23a). In other areas of the sample Cal_A siderite was always precipitating as small crystals, which appeared to have an almost hexagonal shape and were grouped together inside to what could be either a fracture or an empty space left by a burrowing structure (Fig.3.23b).

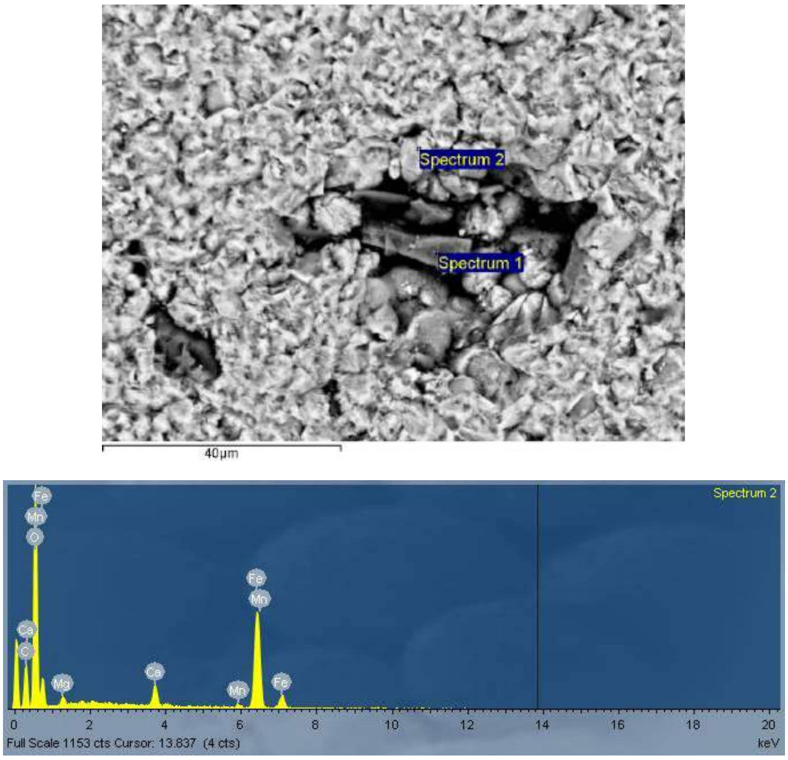

Spectra	Wt% Si	Wt% Fe	Wt% O	Wt% Total
Spectrum 1	46.21	0.89	52.90	100
Spectrum 2	-	66.34	23.65	100

Figure 3.21-SEM Photomicrograph of the sample Cal_G and EDS analysis: spectrum 1: quartz and spectrum 2: siderite.

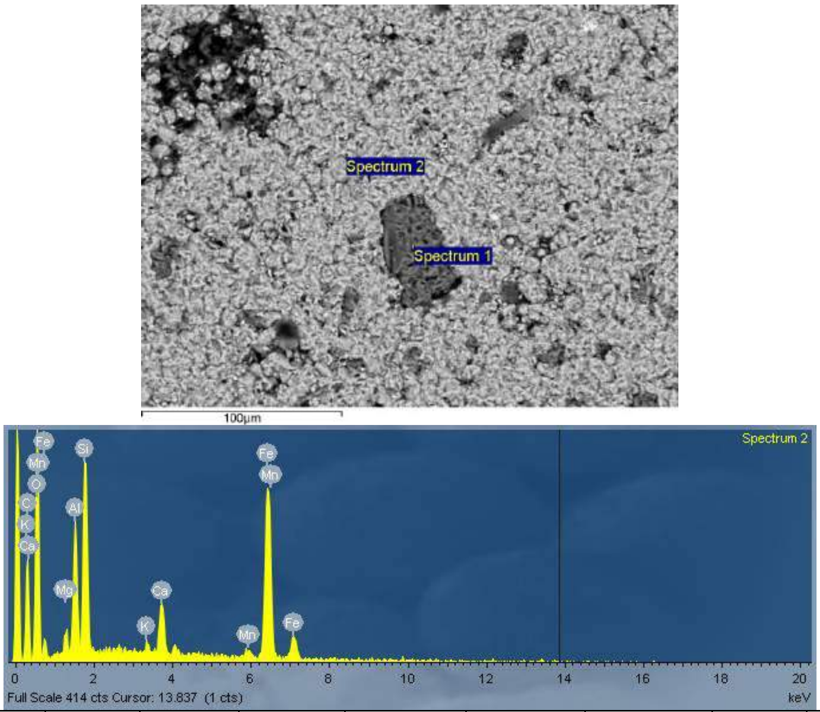

Spectra	Wt% Mg	Wt% Al	Wt% Si	Wt% Ca	Wt% Mn	Wt% Fe	Wt% O	Wt% Total
Spectrum 1	-	-	46			1	53	100
Spectrum 2	2	8	13	4	1	36	35	100

Figure 3.22-SEM Photomicrograph of the sample Cal_I and EDS analysis: spectrum 1: quartz and spectrum 2: siderite contaminated by silicate minerals.

a)

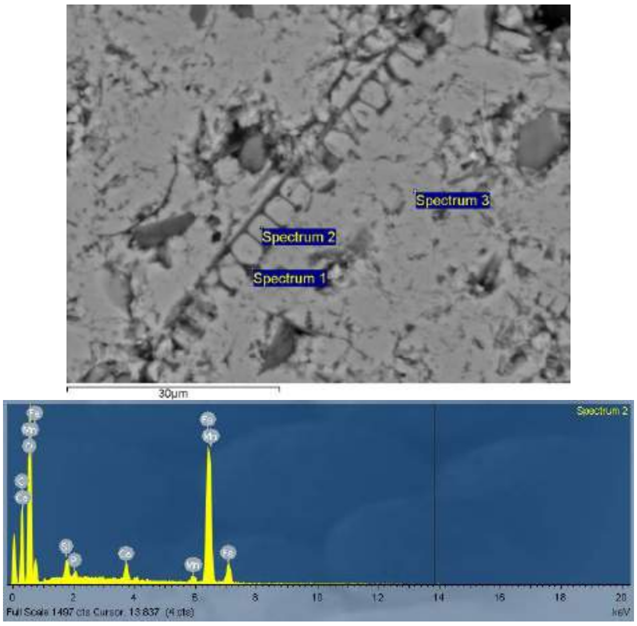

Spectra	Wt% Al	Wt% Si	Wt% P	Wt% Ca	Wt% Mn	Wt% Fe	Wt% O	Wt%Total
Spectrum 1	1.20	19.97		1.19	0.63	40.30	36.14	100
Spectrum 2	-	2.98	1.01	2.70	2.38	65.64	25.28	100
Spectrum 3	0.69	5.59	0.60	2.22	3.21	60.72	26.97	100

b)

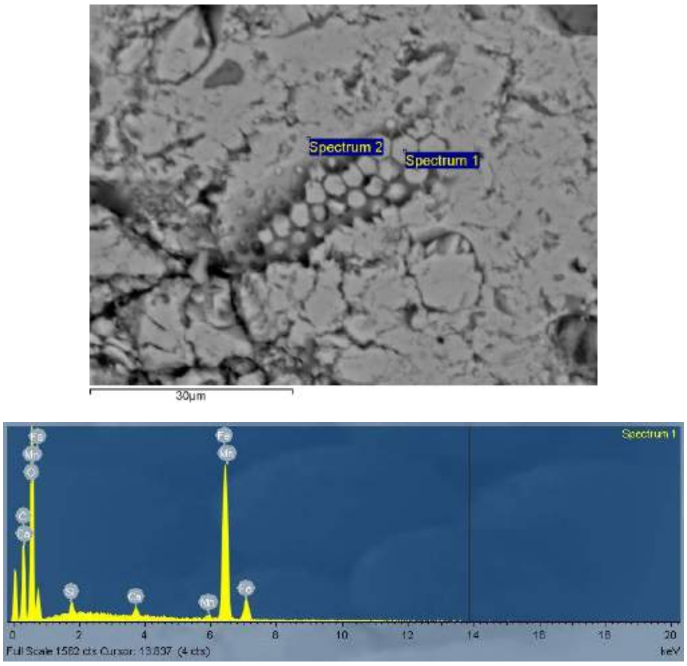

Spectra	Wt% Al	Wt% Si	Wt% Ca	Wt% Mn	Wt% Fe	Wt% O	Wt% Total
Spectrum 1		1.94	1.47	1.45	71.44	23.69	100
Spectrum 2	0.57	2.02	1.70	1.54	70.13	24.03	100

Figure 3.23 –SEM Photomicrograph of the sample Cal_A, a) siderite occurs as small rounded and aligned crystals b) siderite is present as small crystals with a hexagonal habitus. All spectra are of siderite although affected by the presence of silicate minerals.

Iron oxy-hydroxides

The chemical analyses by SEM were conducted on three samples (sample Cal-T, sample Cal-P and sample Cal-F). In the sample Cal-T, very small crystals of iron oxy-hydroxides with some titanium immersed in a paste silicate where the Fe is present (Fig. 3.24). In other portion of Cal-T there was possibly the presence of amorphous Fe-oxy-hydroxides. Whereas the samples Cal-P showed the presence of crystals of Fe oxides far more organized than in sample Cal-T, can be clearly seen the graininess, there are traces of Mn and Ti and it’s all surrounded by terrignous detritus (Fig. 3.25). In the sample Cal-F showed oxides of Fe in small crystals embedded in a matrix of clay minerals as shown in (Fig.3.26).

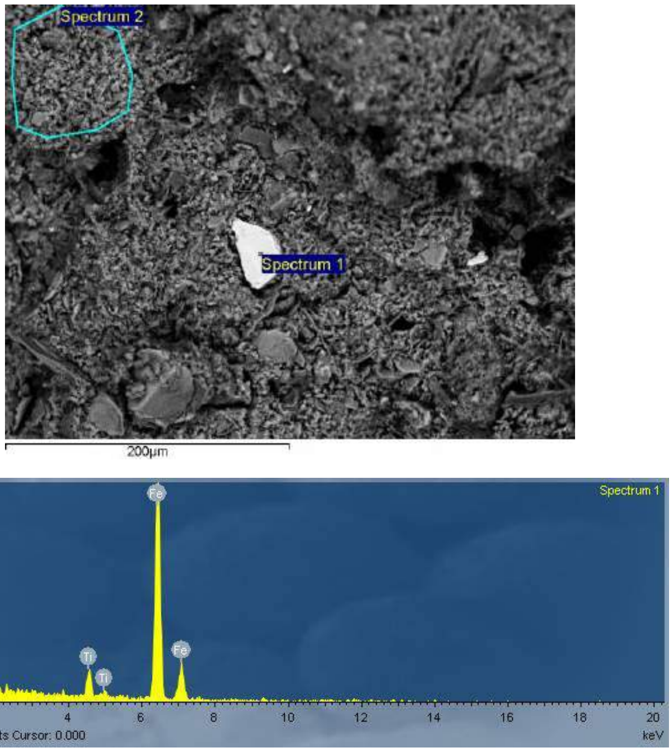

Spectra	Wt% Mg	Wt% Al	Wt% Si	Wt% K	Wt% Ti	Wt% Fe	Wt% O	Wt% Total
Spectrum 1	3.79	4.04	-	-	3.64	62.19	26.34	100
Spectrum 2		10.17	27.69	3.30	-	13.66	45.18	100

Figure 3.24-SEM Photomicrograph of the sample Cal-T and EDS analysis of Fe-oxides.

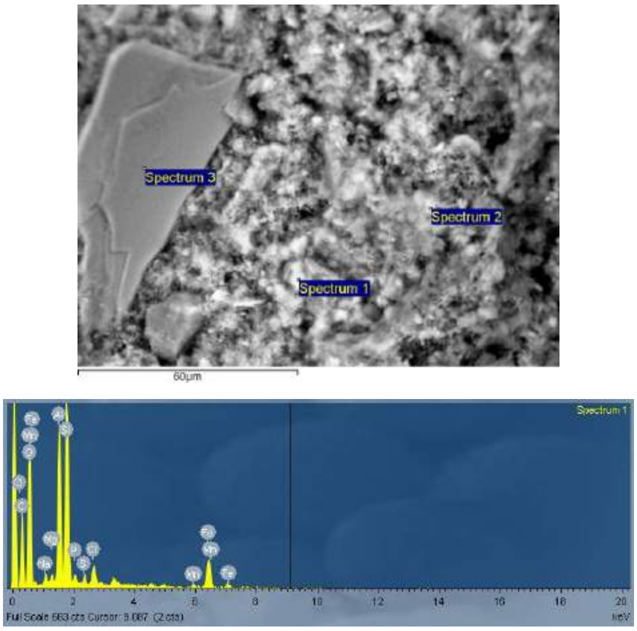

Spectra	Wt% Na	Wt% Mg	Wt% Al	Wt% Si	Wt% P	Wt% S	Wt% Cl	Wt% K	Wt% Ca	Wt% Ti	Wt% Mn	Wt% Fe	Wt% O	Wt% Total
Spectrum 1	1.52	0.87	15.15	20.29	1.49	1.09	2.44	-	-	-	0.96	11.38	44.8	100
Spectrum 2	1.84	0.83	15.06	21.15	-	3.77	1.87	1.97	2.26	-	-	4.39	46.88	100
Spectrum 3	-	-	6.36	8.17	-	-	-	9.01	-	6.78	-	37.58	32.10	100

Figure 3.25 -SEM Photomicrograph of the sample Cal-P and EDS analysis shows the presence of Fe-oxides and traces of Mn and Ti.

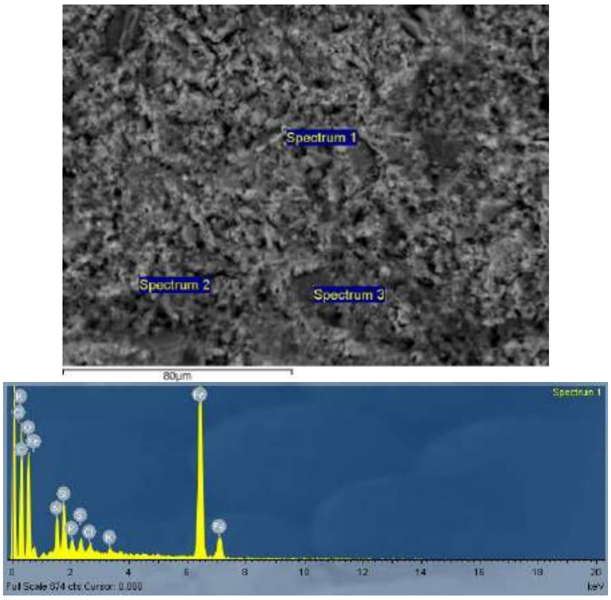

Spectra	Wt% Na	Wt% Mg	Wt% Al	Wt% Si	Wt% P	Wt% S	Wt% Cl	Wt% K	Wt% Ti	Wt% Fe	Wt% O	Wt% Total
Spectrum 1	-	-	4.11	5.30	1.49	1.48	0.93	0.62	-	56.06	30.01	100
Spectrum 2	1.74	1.15	7.15	10.45	2.17	1.26	1.19	0.85	-	38.52	35.52	100
Spectrum 3		1.60	17.61	23.33	-	-	-	1.94	0.71	8.27	46.54	100

Figure 3.26 -SEM Photomicrograph of the sample Cal-F and EDS analysis of Fe-oxides

Pyrite and sulfide crusts

The EDS analysis was carried out on the thin sections of samples Cal-D, Cal-MB1 and Cal-MB2 and samples Cal- K and Cal-Q_1. The two latter were not analyzed by XRD since their dimensions were of about 2-3 cm. On the sample Cal-Q_1 crystals of pure sulfur were recognized (Fig.3.27), whereas sample Cal-K contained framboids of pyrite, probably corresponding to framboidal pyrite in matrix of clay minerals (Fig. 3.28). The SEM analysis on the thin section of the sample Cal-D showed that the sample was homogeneous even though granular. The spectrum done in a homogeneous area and composed of Fe (23%), S (30%), therefore is pyrite (Fig. 3.29). The sample is very homogeneous, it only changes the porosity, within the vacuoles are feldspars associated with pyrite, feldspar and quartz (Fig.3.30). A chalcopyrite crystal was also observed (Fig. 3.31).

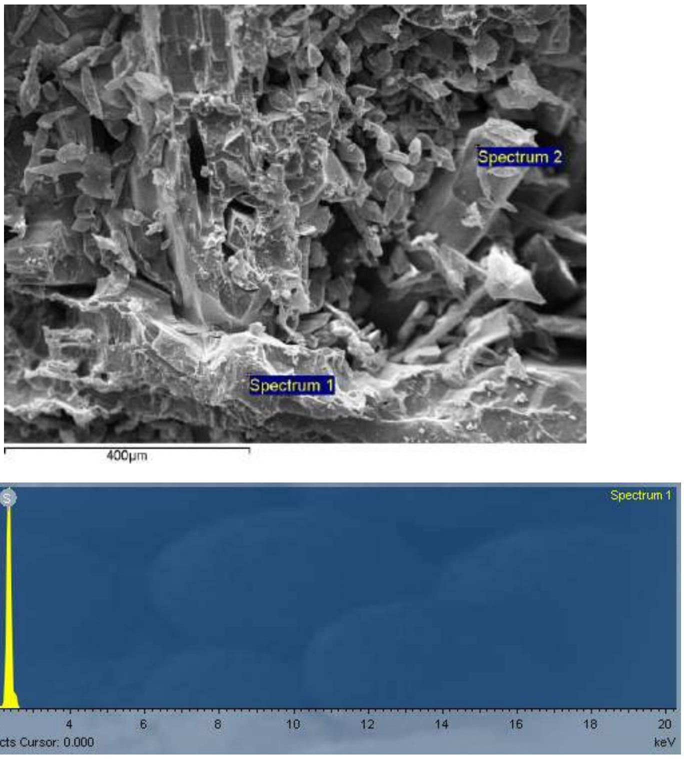

spectra	Wt % S
spectrum 1	40.05
spectrum 2	40.05

Figure 3.27-SEM Photomicrograph of the sample Cal-Q_1 and EDS analysis of crystals of sulfur.

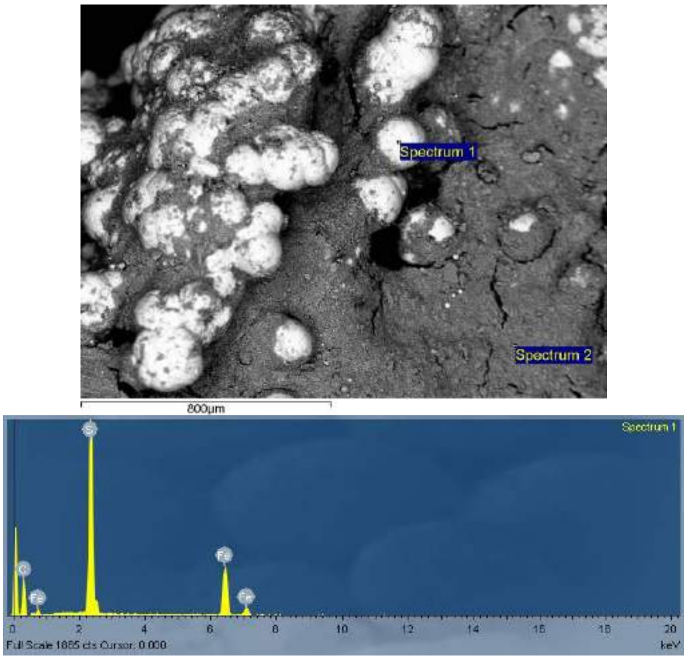

Spectra	Wt% Mg	Wt% Al	Wt% Si	Wt% S	Wt% Cl	Wt% K	Wt% Fe	Wt% Mo	Wt% Total
Spectrum 1	-	-	-	68.1	-	-	31.9	-	100
spectrum 2	1.56	10.75	28.15	-	1.03	3.65	4.84	3.48	100

Figure 3.28-SEM Photomicrograph of the sample Cal-K and EDS analysis of framboidal pyrite.

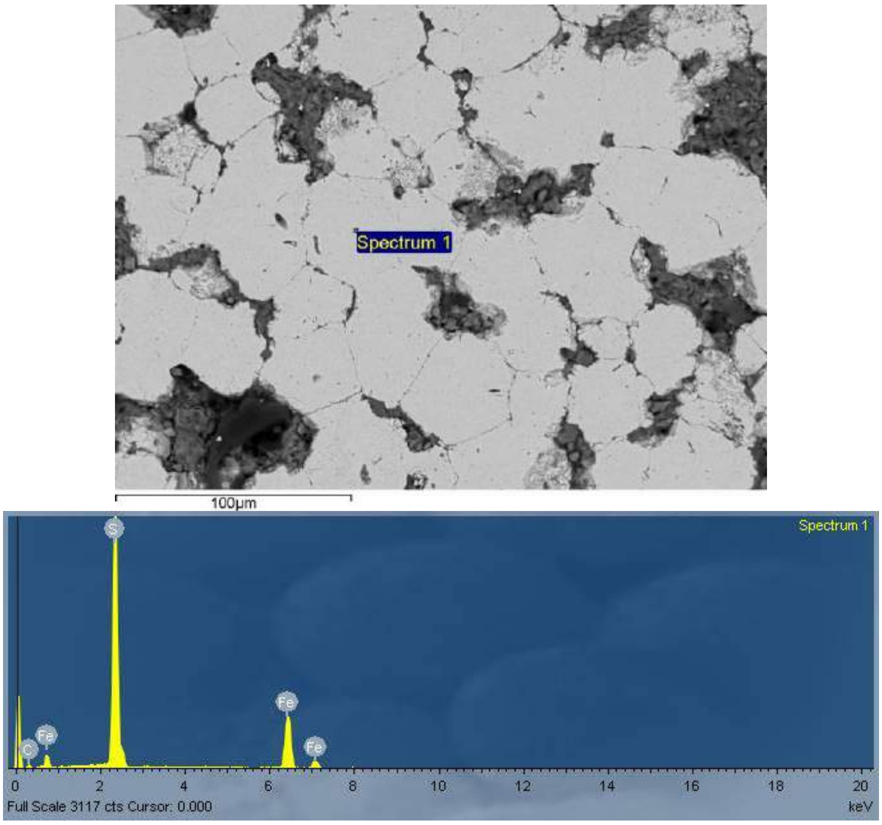

Spectrum	Wt% S	Wt% Fe
Spectrum 1	33.0	69.0

Figure 3.29-SEM Photomicrograph of the sample Cal-D and EDS analysis of pyrite.

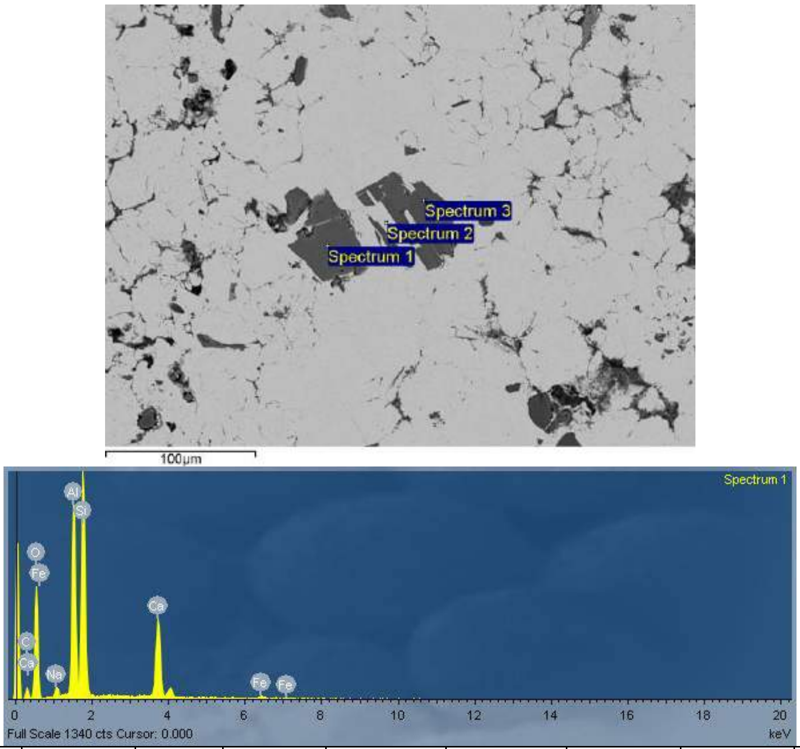

Spectra	Wt% Na	Wt% Al	Wt% Si	Wt% S	Wt% Ca	Wt% Fe	Wt% O	Wt%Total
Spectrum 1	1.62	16.20	23.15	-	11.64	1.09	46.30	100
Spectrum 2	-	-	-	28.46	-	22.49	49.05	100
Spectrum 3	1.54	16.25	24.27	-	10.94	-	47.00	100

Figure 3.30-SEM Photomicrograph of the sample Cal-D and EDS analysis: spectra 1 and 3: feldspar and spectrum2: pyrite.

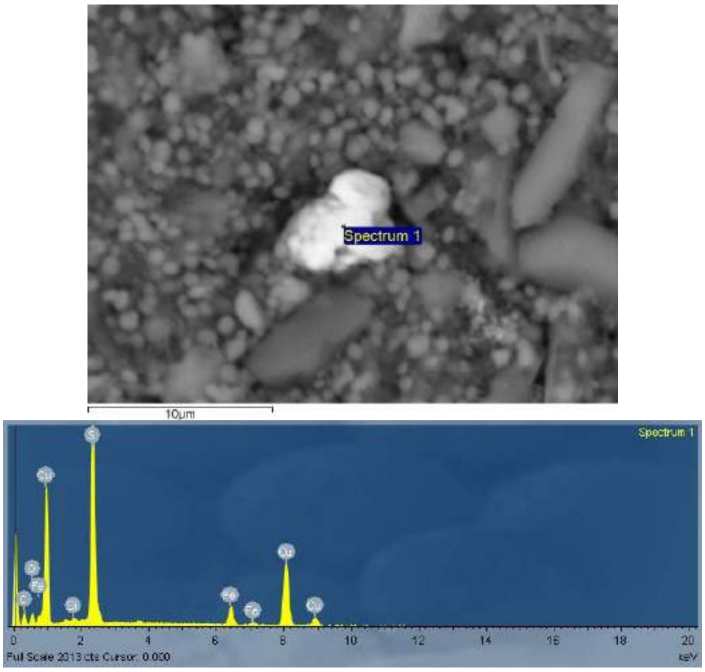

Spectrum	Wt % S	Wt% Fe	Wt % Cu	Wt% Total
Spectrum 1	18.53	5.29	36.97	100

Figure 3.31-SEM Photomicrograph of the sample Cal-D and EDS analysis of chalcopyrite.

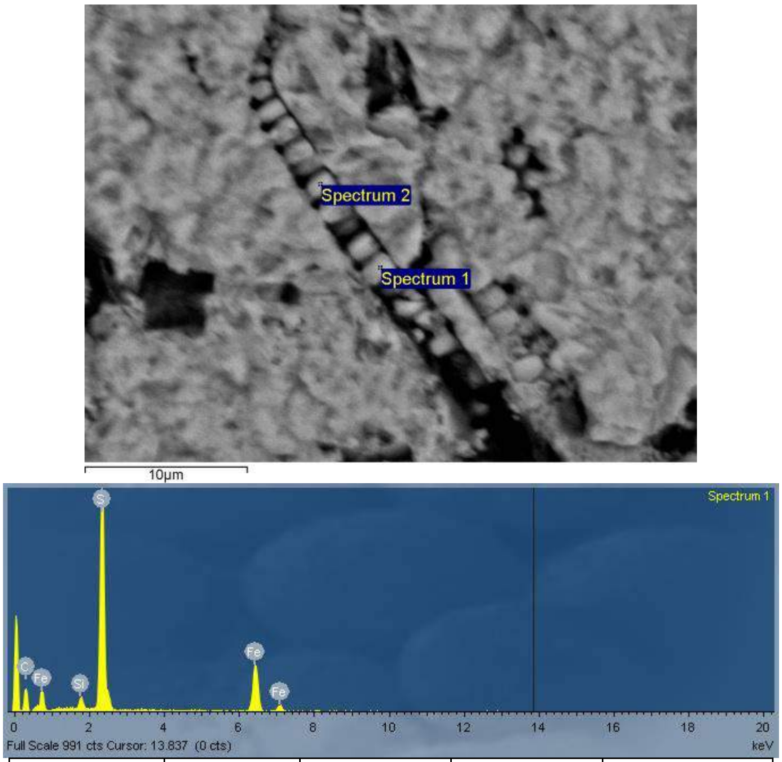

Spectra	Wt% Si	Wt% S	Wt% Fe	Wt% Total
Spectrum 1	1.36	27.67	21.76	100
Spectrum 2	0.92	28.25	21.37	100

Figure 3.32-SEM Photomicrograph of the sample Cal-MB1and SED analysis shows the presence of pyrite.

3.3.4 - EMP mineral chemistry

EMP analyses were performed on thin sections of organogenic carbonate crusts (sample Cal-B and Cal-C) for determination the quantitative chemical analyses of Ca, Mg, Fe, Mn, Sr, Si and O, the first five elements recalculated as carbonate. These analyses showed that the most common mineral was calcite ($CaCO_3$) with a few contents Manganese carbonate ($MnCO_3$), Strontium carbonate ($SrCO_3$) and Silica (SiO_2) (Fig.3.33).

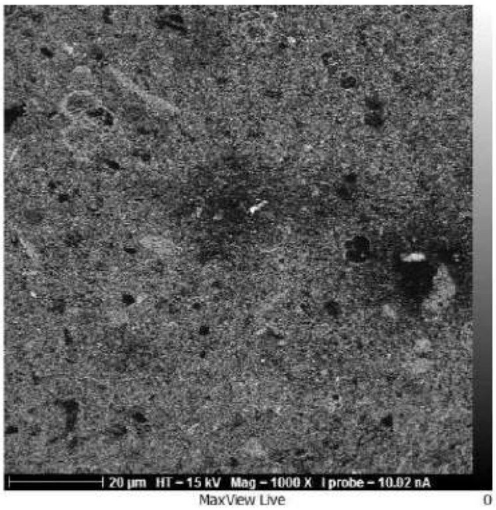

Point	SiO_2	$MnCO_3$	$MgCO_3$	$CaCO_3$	$SrCO_3$
C1	<0.01	0.17	0.4	84.65	1.37
C2	<0.01	<0.01	1.59	75.24	1.41

Figure 3.33-EMP-BSE Photomicrograph of the sample Cal-C and chemical composition of calcite.

It was also observed a relative quantity of magnesite ($MgCO_3$) in several spots from the samples Cal-C (Fig.3.34 and Fig.3.35) and Cal-B (in Fig.3.36 and Fig.3.37).

Point	SiO_2	$MnCO_3$	$MgCO_3$	$CaCO_3$	$SrCO_3$
C5	0.21	0.06	8.91	85.68	0.08
C6	19.93	0.01	3.59	52.29	0.91

Figure 3.34–EMP-BSE Photomicrograph of the sample Cal-C where calcite showed a strong Mg-CO_3 component.

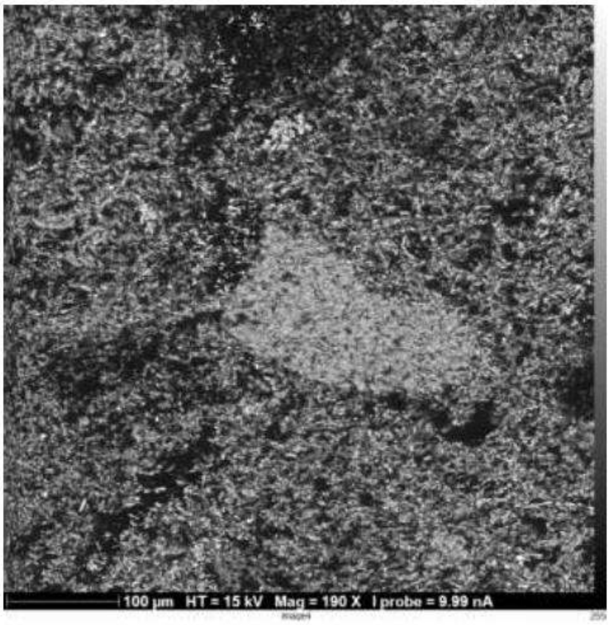

Point	SiO_2	$MnCO_3$	$MgCO_3$	$CaCO_3$	$SrCO_3$
C10	**0.3**	**0.1**	**12.45**	**75.16**	**<0.01**

Figure 3.35–EMP-BSE Photomicrograph of the sample Cal-C where calcite showed a strong Mg-CO_3 component.

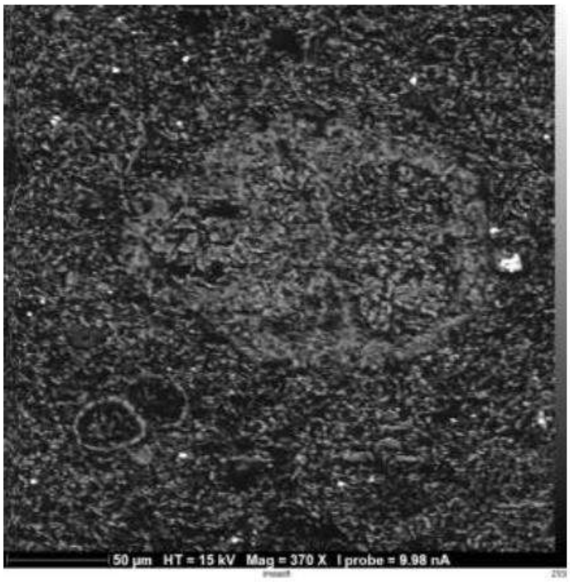

Point	SiO_2	$MnCO_3$	$MgCO_3$	$CaCO_3$	$SrCO_3$
B1	0.06	1.34	5.36	82.61	1.36

Figure 3.36 –EMP-BSE Photomicrograph of the sample Cal-B where calcite showed a strong Mg-CO_3 component.

Point	SiO_2	$MnCO_3$	$MgCO_3$	$CaCO_3$	$SrCO_3$
B2	1.22	0.01	7.49	77.99	<0.01

Figure 3.37–EMP-BSE Photomicrograph of the sample Cal-B where calcite showed a strong Mg-CO_3 component.

3.3.5 The Calcimetric analysis

This analysis was carried out on selected mud samples contain calcium for determine the amount of $CaCO_3$ .The results of this analysis are summarized in Table 3.9 and showed that the high content of $CaCO_3$ were detected in the samples Cal-17, Cal-27 and Cal-30.

Samples	CO_2	Y	$CaCO_3$ (%)
Cal-16	13	4.82	8.911
Cal-9	18	4.89	11.446
Cal-15	16	4.86	10.432
Cal-10	20	4.92	12.46
Cal-17	84	5.81	44.908
Cal-27	50	5.34	27.67
Cal-29	33	5.102	19
Cal-30	35.3	5.1342	20.31
Cal-32	25	4.99	15

Table 3.9: Results of the calcimetric analysis for the mud samples

3.3.6- Analytical Chemical

All samples were analyzed for their geochemical composition: major, minor, trace elements (including the rare earth elements – REE). With respect to Na_2O in order to rule out any Na-Cl component attributable to seawater, the following correction was applied:

$$Na^{*}= Na_{(total)}- Na_{cl}),$$

Where $Na_{(total)}$ is the measured value of Na by XRF and Na(Cl) is Na stoichiometrically related to Cl, thus reflecting the presence of halite. Each Na* value was then recalculated as Na_2O.

For trace elements and REE were normalized to Post Archean Average Australian Shale (PAAS, Taylor and McLennan, 1985). We calculated Y/Ho, Ce, Eu and Gd anomalies for the studied samples. Light REE (LREE) fractionation was calculated as Pr_{SN}/Yb_{SN} and Medium REE (MREE) enrichment was calculated as Gd_{SN}/Yb_{SN}. Normalized Ce, Eu and Gd anomalies were calculated using the geometric equation given by Lawrence et al.(2006):

$$(Ce/Ce^{*}):\ Ce_{SN} / [Pr_{SN} * (Pr_{SN} / Nd_{Sn}]$$

$$(Eu/Eu^{*}):\ Eu_{SN} / [(Sm_{SN})^{2} * Tb_{SN}]^{1/3}$$

$$(Gd/Gd^{*}):\ Gd_{SN} / [(Tb_{SN})^{2} * Sm_{SN}]^{1/3}$$

Organogenic carbonate crusts

The major and trace elements composition is reported in the Appendix (A) whereas the statistical distribution for major and selected of trace elements reported in (Table 3.10). The results of major elements showed that the concentration of CaO and L.O.I. were ranging from 29.65 and 43.41% and from 27.19 to 34.6 Wt%, while that of SiO_2 was from 10.8 to 21.49%, the Al_2O_3 was from 4.4 to 8.51 Wt %, the K_2O was from 0.8 to 1.6 %, the MgO and Fe_2O_3 were from 1.5 to 3.3 Wt % and from 2.2 to 4.8 Wt % respectively. For the concentration of each of Na_2O, MnO, P_2O_5 and TiO_2 were low a 0.38, 0.03, 0.07and 0.28 Wt% respectively. The concentrations of selected trace elements are also listed in Table 3.10. Among trace elements the

Strontium had the highest values being comprised between 3265 to 5968 mg/kg. A large variability was shown by the of Ba contents since they were between 24 and 355 mg/kg. Some elements showed variable concentrations, such as V, Zr, Zn, Mo and Cu (from 61 to 102 mg/kg, from 53 to 112 mg/kg, from 26 to 42 mg/kg, from 0,9 to 56 mg/kg and from 10 to 20 mg/kg respectively). The total REE (∑REE) in the carbonate crusts were ranging from 60.72 to 107.59 mg/kg (Table 3.11). The highest contents were recorded in the sample Cal-CC whereas the lowest were referred to sample Cal-AA. The samples which have high and low concentration of REE are associated with higher concentrations of CaO and SiO_2

Elements	**Max**	**Min**	**Average**	**Median**
SiO_2	21.59	10.8	16.63	15.81
Al_2O_3	8.63	4.43	6.44	5.9
MgO	3.28	1.48	2.28	2.07
CaO	43.41	29.65	37.49	39.8
K_2O	1.6	0.8	1.22	1.14
Na_2O	0.81	0.38	0.52	0.49
MnO	0.1	0.03	0.056	0.06
Fe_2O_3	4.89	2.18	3.17	3.1
TiO_2	0.5	0.28	0.37	0.35
P_2O_5	0.2	0.07	0.108	0.1
L.O.I.	34.6	27.19	31.19	31.16
Ba	384	24	262.22	283
Co	15.2	1	6.36	4.7
Rb	57	23	40.58	39.4
Sr	5968	3265	4640.77	4860
Th	7.3	4.1	5.62	5.5
U	28.5	5.3	10.655	8
V	102	61	79	77
Zr	112	53	81.43	81.5
Y	16	9	11.78	11
Mo	56	0.9	18.26	10
Cu	20	10	15.1	15.5
Zn	42	26	34.57	40
Ni	80	9.7	33.67	30

Table 3.10: Mean values of chemical data for carbonate crusts. Major elements in Wt%, trace elements in mg/kg.

Samples	Cal-B	Cal-C	Cal-N	Cal-H	Cal-BB	Cal-CC	Cal-AA	Cal-NN	Cal-HH
La	19	18.8	21.6	22.2	16.2	23	13.6	14.5	21.2
Ce	36.5	37.7	43.1	42.6	31.7	45.3	26.3	28.2	40.3
Pr	3.86	3.93	4.5	4.54	3.57	4.98	2.87	3.13	4.42
Nd	14.7	14.9	17.6	15.5	13.7	19.2	10.6	11.6	16.6
Sm	2.73	2.77	3.08	3.14	2.6	3.7	2	2.2	3.3
Eu	0.61	0.56	0.67	0.64	0.54	0.86	0.42	0.51	0.68
Gd	2.17	2.27	2.97	2.74	2.3	3.3	1.5	2.1	2.8
Tb	0.35	0.38	0.44	0.42	0.3	0.5	0.2	0.3	0.4
Dy	2.04	1.85	2.13	2.05	2	2.7	1.3	1.7	2.4
Ho	0.37	0.42	0.51	0.45	0.4	0.5	0.2	0.4	0.5
Er	1.23	1.17	1.04	1.33	1.1	1.6	0.7	1	1.3
Tm	0.17	0.17	0.18	0.16	0.18	0.24	0.12	0.15	0.21
Yb	1.09	0.93	1.44	1.22	1.2	1.5	0.8	1	1.3
Lu	0.15	0.17	0.18	0.17	0.16	0.21	0.11	0.16	0.19
∑REE	84.97	86.02	99.44	97.16	75.95	107.59	60.72	66.95	95.6
Y/Ho	25.9	25.7	26.1	25.3	27.5	32.0	45.0	27.5	28.0
Ce/Ce*	1.04	1.05	1.08	0.93	0.98	1.01	0.98	0.96	0.99
Eu/Eu*	1.18	1.04	1.11	1.06	1.13	1.20	1.20	1.20	1.11
Gd/Gd*	1.00	0.98	1.13	1.06	1.19	1.08	1.11	1.15	1.11
Pr_{SN}/Yb_{SN}	1.13	1.35	1.00	1.19	0.95	1.06	1.15	1.00	1.09

Table 3.11.: Rare earth elements (REE in mg/kg) of carbonate crusts.

Siderite concretions

The major and trace elements composition is reported in the Appendix (B). Table 3.12 showed the statistical distribution of major and selected of trace elements for the siderite. The highest concentration of major elements were referred to those of $Fe_2O_{3(total)}$ (from 36.2 to 53.3 wt %) and L.O.I. from 23.47 to 33.83 Wt%, whereas those of SiO_2 were ranging from 5.54 to 23.37%, the Al_2O_3 were from 2.2 to 9.7 %, the MgO and CaO were ranging from 0.7 to 2.1 % and from 1.1 to 5.6 % respectively. While those of MnO, P_2O_5 and TiO_2 are lower ranging from 0.3 to 1.6%, 0.1 to 0.5 % and 0.1 to 0.3% respectively. Among the trace elements (Table 3.12), the contents of Ba were from 45 and 179 mg/kg and those of Sr were between 56.7 and 142 mg/kg. The redox sensitive elements, such as Co, V, Zr, Mo, Zn and Ni showed variable concentrations (from 21.3 to 168 mg/kg, from 96 to 243 mg/kg, from 29.8 to 165.6 mg/kg, from 1.1 to 82.2 mg/kg, from 49 to 350 mg/kg and from 11.1 to 138.3 mg/kg respectively). Highly variable (∑REE) content were detected in siderite samples where they were ranging from 46.03 to 130.98 mg/kg (Table 3.13).

Elements	**Max**	**Min**	**Average**	**Median**
SiO_2	23.37	5.54	14.26	14.2
Al_2O_3	9.97	2.22	5.74	5.01
MgO	2.11	0.73	1.32	1.23
CaO	5.58	1.14	3.33	3.19
K_2O	1.26	0.09	0.64	0.61
Na_2O	2.38	0.29	0.72	0.55
MnO	1.64	0.32	0.82	0.76
Fe_2O_3	53.44	36.48	45.64	47.25
TiO_2	0.32	0.12	0.21	0.185
P_2O_5	0.46	0.14	0.26	0.26
L.O.I	33.83	23.47	27.45	27.04
Ba	179	45	106	98
Co	168	21.3	64.79	57.5
Rb	38	12.4	23.94	22.05
Sr	142	56.7	91.32	83.5
Th	4.7	1.4	2.85	2.55
U	13.5	0.5	4.06	2.4
V	243	96	165.1	162.5
Zr	165.6	29.8	100.5	87
Y	57.4	13.7	27.81	26
Mo	82.2	1.1	32.16	38
Cu	38.3	5.5	18.71	20
Pb	37.5	4.8	17.56	17
Zn	350	49	191.5	175
Ni	138.3	11.1	49.4	35

Table 3.12.: Mean values of chemical data for the Carbonates of tubular form. Major elements in Wt%, trace elements in mg/kg.

Samples	**Cal-I**	**Cal-G**	**Cal-M**	**Cal-E**	**Cal-R**	**Cal-A**	**Cal-V**	**Cal-U**	**Cal-EE**	**Cal-RR**
La	16.9	10.7	8.2	16.7	21.5	9.7	13.7	18.1	12.4	22
Ce	31.8	18	18	33	43	18	24	36	24.8	52.7
Pr	3.16	1.87	1.95	4.02	5.09	1.89	2.49	3.96	2.85	4.69
Nd	14.6	7.5	9.1	17.3	22.9	6.9	10.2	15.4	12.2	19.2
Sm	2.55	1.58	1.94	4.56	5.66	1.82	2.2	3.6	3.2	4.1
Eu	0.58	0.36	0.4	1.11	1.55	0.44	0.54	0.82	0.78	0.97
Gd	3.24	1.79	2.23	5.63	8.46	2.53	2.8	3.6	3.9	4.7
Tb	0.55	0.27	0.39	0.95	1.41	0.44	0.5	0.6	0.7	0.8
Dy	3.17	1.43	2.47	5.67	7.9	2.61	3	3.6	4.2	4.4
Ho	0.76	0.39	0.61	1.26	1.9	0.61	0.7	0.7	0.8	0.9
Er	2.48	0.95	2	3.62	5.56	1.88	2.1	2.1	2.4	2.6
Tm	0.36	0.14	0.27	0.51	0.73	0.27	0.31	0.3	0.39	0.4
Yb	2.21	0.9	1.72	3.37	4.61	1.86	2	2	2.5	2.5
Lu	0.38	0.15	0.31	0.49	0.71	0.28	0.31	0.29	0.34	0.36
∑REE	82.74	46.03	49.59	98.19	130.98	49.23	64.85	91.07	71.46	120.32
Y/Ho	35.4	35.1	38.4	30.2	30.2	25.6	37.1	31.4	32.5	32.2
Ce/Ce*	1.3	1.1	1.2	1.0	1.1	1.0	1.1	1.0	1.1	1.3
Eu/Eu*	1.0	1.1	0.9	1.1	1.2	1.0	1.1	1.1	1.1	1.1
Gd/Gd*	1.1	1.2	1.1	1.1	1.2	1.1	1.1	1.1	1.1	1.1
Pr_{SN}/Yb_{SN}	0.5	0.7	0.4	0.4	0.4	0.3	0.4	0.6	0.4	0.6

Table 3.13: Rare earth element (in mg/kg)of carbonates of tubular form.

Iron oxy-hydroxides

The chemical analyses (major and trace element compositions) are reported in the Appendix(C), whereas the table statistics (Table 3.14) showed the background concentrations of the major and selected trace element. With regard to major elements found that the highest concentrations were referred to those of $Fe_2O_{3(total)}$ (from 19.95 to 52.82 wt %) and SiO_2 was from 20.54 to 38.29 %, while those of Al_2O_3 was from (10.07 to 17.5 %), Na_2O (from 0.07 to 11.48 %), K_2O (from 1.37 to 3.23 %). The other major elements (CaO, MgO, MnO, P_2O_5 and TiO_2 are present in small concentrations (0.49, 1.12, 0.43, 0.35 and 0.38 % respectively). The trace element data are also listed in Table 3.14 and showed Ba in samples had the highest concentration, being composed between 181-532 mg/kg among the analyzed trace elements. While some elements showed variable concentrations such as Sr, Rb, V and Zr (from 116.7 to 266 mg/kg, from 46 to 102 mg/kg, from 140 to 198 mg/kg and from 72.3 to 187.6 mg/kg respectively). Total REE contents in the iron oxy-hydroxides samples ranged between 170.90 and 318.01 mg/kg (Table 3.15). The oxy-hydroxide concretions have a rather flat REE pattern (average $Pr_{SN}/Yb_{SN} = 1.1$). These samples lacked substantial Gd anomaly and show slightly positive Ce and Eu anomalies. The average Y/Ho of the oxy-hydroxide concretion is 23.44.

Elements	**Max**	**Min**	**Average**	**Median**
SiO_2	38.29	20.54	31.99	37.14
Al_2O_3	17.5	10.07	13.74	13.65
MgO	1.96	1.12	1.6	1.74
CaO	1.35	0.49	1.04	1.3
K_2O	3.23	1.37	2.41	2.65
Na_2O	11.48	0.07	3.94	0.27
MnO	0.43	0.04	0.19	0.11
Fe_2O_3	52.82	19.95	32.83	25.72
TiO_2	0.95	0.38	0.72	0.84
P_2O_5	2.97	0.56	1.84	1.99
L.O.I	10.62	7.76	9.3	9.54
Ba	532	181	370.33	398
Co	21.7	5.1	13.5	13.7
Rb	102	46	76.36	81.1
Sr	266	116.7	204.66	231.3
Th	15.5	6.4	10.83	10.6
U	13.2	2.2	9.2	12.2
V	198	140	171	175
Zr	187.6	72.3	136.56	149.8
Y	37.3	22.7	29.4	28.2
Mo	97.1	37.6	62.73	53.5
Cu	41	25.2	32.83	32.3
Pb	74	54.7	62.2	57.9
Zn	83	53	65.66	61
Ni	33.9	11.5	20.93	17.4

Table 3.14: Mean values of chemical data for the Iron oxy-hydroxides. Major elements in Wt%, trace elements in mg/kg.

Samples	Cal-F	Cal-P	Cal-T
La	27.6	48.1	43.8
Ce	77.4	159.6	87.8
Pr	7.87	13.48	9.77
Nd	32.4	53.5	35.5
Sm	6.36	10.53	7.3
Eu	1.33	2.34	1.62
Gd	5.94	9.03	6.4
Tb	0.92	1.54	1.01
Dy	4.58	7.93	5.57
Ho	1.01	1.68	1.1
Er	2.73	4.75	3.29
Tm	0.34	0.68	0.44
Yb	2.13	4.16	2.88
Lu	0.35	0.69	0.49
∑REE	170.96	318.01	206.97
Y/Ho	22.5	22.2	25.6
Ce/Ce*	1.2	1.4	0.9
Eu/Eu*	1.1	1.1	1.1
Gd/Gd*	1.1	1.0	1.0
Pr_{SN}/Yb_{SN}	1.2	1.0	1.1

Table 3.15.: Rare Earth Elements (in mg/kg)of Iron oxy-hydroxides.

Crusts of pyrite and sulfur

A total of major and trace elements of sulfides are summarized in the Appendix (D). The statistical distribution for major elements (Table 3.16) showed that the concentration of S was raging from 8.67 to 20.39 wt% while that of SiO_2, Al_2O_3 and Fe_2O_3 were from 7.48 to 34.89 %, 3.14 to 21.05% and 10.9 to 31.25% respectively. Whereas for the concentration of other major elements CaO, MgO, K_2O, Na_2O, MnO, TiO_2 and P_2O_5 were low (3.31, 0.96, 2.44, 1.72, 0.06, 1.01 and 0.23% respectively). Some of trace elements are reported in Table 3.16 and showed variable concentrations. The contents of Ba were from 41 to 276 mg/kg and Sr were from 24.9 to 286 mg/kg. And the concentrations of redox sensitive element such as Co, V, Zr, Mo, Zn, and Ni were ranging from 8 to 250.4 mg/kg, from 26 to 136 mg/kg, from 18 to 187 mg/kg, from 11 to 254.2 mg/kg, from 58 to 329 mg/kg and from 20 to 160.3 mg/kg respectively). The REE content of the samples were variable, ranging from 18.11 to 132.51 mg/kg (Table 3.17). Sulfides samples show slight enrichment of LREE compared to HREE (average Pr_{SN}/Yb_{SN} = 1.37) and general lack of Ce, Gd as well as Eu anomalies. The average Y/Ho ratio in the sulfide concretions is about 23.63.

Elements	Max	Min	Average	Median
SiO_2	34.89	7.48	16.82	13.39
Al_2O_3	21.05	3.14	7.77	5.31
MgO	0.96	0.28	0.611	0.59
CaO	3.31	0.18	0.85	0.42
K_2O	2.44	0.55	1.25	1.06
Na_2O	1.72	0.08	0.79	0.59
MnO	0.06	0.02	0.033	0.03
Fe_2O_3	31.25	10.9	22.66	27.2
TiO_2	1.01	0.12	0.33	0.21
P_2O_5	0.23	0	0.106	0.1
S	20.39	8.67	16.18	18.16
L.O.I	45.63	15.44	32.57	33.04
Ba	276	41	138.37	92
Co	250.4	8	59.97	37.6
Rb	65	12	30.86	19
Sr	286	24.9	105.78	66.8
Th	11.1	1.4	4.55	2.5
U	12.6	0.8	5.28	2.5
V	136	26	54	39
Zr	187	18	61.75	31.2
Y	16	1.7	6.08	2.85
Mo	254.2	11	111.175	73.4
Cu	30	6.6	15.28	13.8
Pb	62	7	21.11	16
Zn	329	58	155.37	155.5
Ni	160.3	20	77.73	70.85

Table 3.16: Mean values of chemical data for crusts of pyrite and sulfur. Major elements in Wt%, trace elements in mg/kg.

Samples	Cal-D	Cal-O	Cal-L	Cal-Q	Cal-S	Cal-Z	Cal-W	Cal-X
La	5.1	9.5	7.3	4.8	6.2	6.3	27.5	26.9
Ce	8.4	17.2	12.9	8	11	12.2	54.4	55.9
Pr	0.92	1.8	1.41	0.82	1.17	1.29	5.57	6.34
Nd	3.2	6.6	4.8	2.6	4.2	4.4	19.6	23.9
Sm	0.62	1.09	0.75	0.46	0.8	0.8	3.3	4.8
Eu	0.12	0.25	0.16	0.09	0.15	0.15	0.85	1.01
Gd	0.47	0.83	0.74	0.45	0.5	0.6	2.6	4.3
Tb	0.07	0.12	0.1	0.06	<0.1	<0.1	0.4	0.7
Dy	0.42	0.69	0.48	0.29	0.4	0.5	2.2	3.6
Ho	0.08	0.12	0.14	0.08	<0.1	0.1	0.4	0.7
Er	0.25	0.32	0.37	0.2	0.3	0.4	1.1	1.9
Tm	0.03	0.04	0.04	0.03	<0.05	0.06	0.19	0.28
Yb	0.26	0.28	0.35	0.2	0.3	0.3	1.2	1.9
Lu	0.03	0.03	0.05	0.03	<0.04	0.05	0.16	0.28
∑REE	19.97	38.87	29.59	18.11	25.02	27.15	119.47	132.51
Y/Ho	26.3	22.5	21.4	21.3	0.0	0.0	27.5	22.9
Ce/Ce*	0.9	1.0	0.9	0.9	1.0	0.9	1.0	1.0
Eu/Eu*	1.1	1.3	1.1	1.0	1.1	1.1	1.4	1.1
Gd/Gd*	1.0	1.1	1.2	1.2	0.9	1.1	1.0	1.0
Pr_{SN}/Yb_{SN}	1.1	2.1	1.3	1.3	1.2	1.4	1.5	1.1

Table 3.17: Rare Earth Element of crusts of pyrite and sulfur (mg/kg).

Cohesive mud

The chemical data of mud samples are tabulated in the Appendix(E). In the table statistics (Table 3.18) showed that the concentrations of SiO_2 was higher compared to the previous groups (from 11.95 to 56.31 wt%) and with moderately high Al_2O_3 (from 4.65 to 23.86 wt %) and strong variation in Fe_2O_3 values (from 3.6 to 26.92%). Whereas those of CaO were ranging from 0.86 to 31.73%, Na_2O were from 0 to 18.58 %, MgO were from 0.26 to 2.89 % and K_2O were from 1.38 to 6.07 %. The other major elements (MnO, Ti_2O and P_2O_5) were low (0.53, 1.63 and 0.42 % respectively). The trace element data (Table 3.18) showed that Ba had the highest values (107-937 mg/kg), followed by Sr (81.5-800.3 mg/kg), Rb (58.5-210 mg/kg) and Zr (107-494.1 mg/kg). And some of trace element showed variable concentrations such as V, Cu, Zn and Ni (from 22 to 216 mg/kg, from 3.8 to 110 mg/kg, from 35 to 137 mg/kg and from 8.4 to 80 mg/kg respectively).

A general enrichment of REE was recognized in the mud samples (Table 3.19) were ranging from 133.42 to 459.83 mg/kg. The mud samples have high HREE depletion compared to LREE (Pr_{SN}/Yb_{SN} up to 1.7)and no Ce and Eu anomalies were recorded in the samples. The average Y/Ho ratio is of 25.01.

Elements	Max	Min	Average	Median
SiO_2	56.31	11.95	43.8	45.96
Al_2O_3	23.86	4.65	17.02	17.94
MgO	2.89	0.26	1.68	1.61
CaO	31.73	0.86	5.92	1.69
K_2O	6.07	1.38	3.53	3.67
Na_2O	18.58	0	4.69	0.42
MnO	0.53	0.02	0.104	0.08
Fe_2O_3	26.92	3.69	8.35	7.63
TiO_2	1.63	0.28	1.08	1.12
P_2O_5	0.42	0.05	0.18	0.17
L.O.I	37.35	6.24	12.51	11.09
Ba	937	107	512.62	497.5
Co	51.5	6	15.73	12.3
Ga	24.7	11.3	19.73	20.2
Nb	75.8	11.1	26.37	22.05
Rb	210	58.5	114.82	117.05
Sr	800.3	81.5	344.71	304.6
Th	44.9	7.2	16.19	15.4
U	13.3	2.6	6.28	4.95
V	216	22	162.18	166
Zr	494.1	107.6	212.67	191.4
Y	38.9	17.7	25.79	25.05
Mo	77.8	0.7	15.04	8.95
Cu	110	3.8	39.83	40.05
Pb	41.7	8.1	19.39	18.15
Zn	137	35	72.43	70.5
Ni	80	8.4	33.64	30.45

Table 3.18: Mean values of chemical data for cohesive mud. Major elements are in Wt%, trace elements are in mg/kg

samples	La	Ce	Pr	Nd	Sm	Eu	Gd	Tb	Dy	Ho	Er	Tm	Yb	Lu	∑REE	Y/Ho	Ce/Ce*	Eu/Eu*	Gd/Gd*	Pr_{SN}/Yb_{SN}
Cal-1	50.8	101.6	10.9	41.5	7.31	1.51	6.19	0.99	4.89	1.11	3.28	0.43	2.84	0.44	233.79	23.8	1.0	1.1	1.0	1.2
Cal-2	54.4	105.8	11.48	38.7	7.61	1.67	6.52	1.01	5.71	1.22	3.43	0.47	3.06	0.43	241.51	23.8	0.9	1.1	1.1	1.2
Cal-3	54.1	105.7	11.05	42.5	7.36	1.52	6.54	1.04	5.68	1.21	3.45	0.47	3.41	0.48	244.51	24.9	1.1	1.1	1.0	1.0
Cal-4	53.2	96.9	9.66	35.2	6.17	1.37	4.76	0.78	3.97	0.91	2.57	0.34	2.5	0.35	218.68	21.8	1.1	1.2	1.0	1.2
Cal-5	52.1	101.4	10.72	39.6	7.52	1.52	6.42	0.98	5.4	1.13	3.4	0.42	2.91	0.44	233.96	22.8	1.0	1.1	1.1	1.2
Cal-6	60.4	118.7	12.79	45.7	8.72	1.8	7.75	1.26	6.62	1.4	4.1	0.55	3.46	0.57	273.82	25.7	1.0	1.0	1.0	1.2
SCal-7	29.6	58.8	6.47	24.6	4.91	1.07	5.1	0.83	4.97	1.02	2.95	0.41	2.56	0.39	143.68	28.2	1.0	1.0	1.1	0.8
Cal-8	51	100.7	10.88	41.2	7.24	1.49	5.99	0.91	4.37	1.04	2.84	0.39	2.54	0.39	230.98	23.2	1.0	1.1	1.1	1.4
Cal-9	41.7	83.1	8.85	34.1	5.87	1.2	5.27	0.8	4.48	0.98	2.56	0.38	2.41	0.38	192.08	23.6	1.0	1.1	1.1	1.2
Cal-10	47.8	87.9	9.59	36.4	6.45	1.29	5.65	0.85	4.53	0.92	2.82	0.37	2.46	0.35	207.38	27.1	1.0	1.0	1.1	1.2
Cal-11	54.2	104.9	11.15	43.2	7.39	1.47	6.6	1.01	5.1	1.08	3.08	0.41	3.16	0.42	243.17	25.6	1.1	1.0	1.1	1.1
Cal-12	53.9	112.3	11.66	38.2	7.54	1.29	5.59	0.85	4.37	0.83	2.31	0.37	2.57	0.35	242.13	22.3	0.9	0.9	1.0	1.4
Cal-13	51.1	98	10.9	41.6	7.5	1.52	6.21	0.99	5.11	1.04	3.1	0.42	2.88	0.46	230.83	26.3	1.0	1.1	1.0	1.2
Cal-14	117	204.9	21.48	74.9	11.84	0.97	9.18	1.4	7.52	1.48	4.25	0.6	4.01	0.6	459.83	26.3	1.0	0.4	1.0	1.7
Cal-15	44.5	83.3	9.61	33.7	6.63	1.31	5.72	0.84	4.3	0.99	2.57	0.38	2.63	0.37	196.85	23.8	0.9	1.0	1.1	1.2
Cal-16	48.7	91.9	9.91	34.4	6.2	1.32	5.6	0.84	4.93	0.99	2.68	0.36	2.2	0.37	210.4	23.7	0.9	1.1	1.1	1.4
Cal-17	29.7	56	6.13	23.8	4.18	0.88	3.99	0.59	3.33	0.71	1.95	0.25	1.65	0.26	133.42	24.9	1.0	1.1	1.1	1.2
Cal-18	60.4	117.9	12.51	41.9	7.61	1.31	5.9	0.89	5	0.95	2.68	0.36	2.41	0.37	260.19	21.8	0.9	0.9	1.0	1.7
Cal-19	44.7	100.7	10.2	34.6	6.88	1.43	5.58	0.91	4.64	0.96	2.79	0.39	2.58	0.37	216.73	25.5	1.0	1.1	1.0	1.3
Cal-20	51.9	111.5	10.84	39.9	6.95	1.37	5.64	0.84	5.12	0.88	2.66	0.42	2.45	0.43	240.9	24.2	1.1	1.1	1.1	1.4
Cal-21	49.6	98.3	9.5	33.3	6.52	1.23	4.85	0.76	4.61	0.88	2.26	0.38	2.65	0.37	215.21	23.1	1.0	1.0	1.0	1.1
Cal-22	52.3	115.5	11.17	38.7	7.94	1.56	6.58	1.07	5.54	1.33	3.26	0.51	3.33	0.52	249.31	22.3	1.0	1.0	1.0	1.1
Cal-23	51.3	111.6	10.87	38.9	7.27	1.51	6.35	1.03	5.61	1.09	3.13	0.49	2.73	0.45	242.33	24.1	1.1	1.1	1.0	1.3
Cal-24	45.4	93.2	9.98	33.6	7.11	1.43	6.31	0.91	5.06	1.07	2.65	0.4	2.46	0.42	210	23.5	0.9	1.1	1.1	1.3
Cal-25	47.4	98.8	10.57	36.8	7.23	1.47	6.35	1.03	5.6	1.19	2.92	0.45	3.18	0.5	223.49	24.4	0.9	1.0	1.0	1.1
Cal-26	51.7	112.4	10.95	39.3	7.58	1.5	6.49	1.06	6.33	1.28	3.26	0.47	2.9	0.56	245.78	23.7	1.1	1.0	1.0	1.2
Cal-27	39.7	77.1	8.46	31.7	5.9	1.22	5.2	0.8	4.5	0.9	2.6	0.42	2.5	0.38	181.38	27.8	1.0	1.1	1.1	1.1
Cal-28	65.8	130	13.7	47.2	9.1	1.78	7.6	1.1	6	1.1	3.2	0.53	3.3	0.44	290.85	30.0	0.9	1.1	1.1	1.3
Cal-29	35.2	68.6	7.52	28.7	5.2	1.27	4.6	0.8	4	0.8	2.2	0.33	2.4	0.3	161.92	27.5	1.0	1.2	1.0	1.0
Cal-30	35.4	68.3	7.69	28.2	5.5	1.11	4.7	0.8	4.1	0.8	2.3	0.34	2.3	0.34	161.88	30.0	0.9	1.0	1.0	1.1
Cal-31	42.4	86.6	9.44	35.1	6.9	1.46	5.6	0.9	5.2	1	2.8	0.44	2.8	0.41	201.05	26.0	1.0	1.1	1.0	1.1
Cal-32	36.9	75.3	8.32	31.1	6	1.29	5.1	0.8	4.4	0.8	2.4	0.37	2.4	0.34	175.52	28.8	1.0	1.1	1.0	1.1

Table 3.19: Rare Earth Elements of cohesive mud samples (mg/kg).

3.3.6- Stable isotope analyses

Stable isotopes of Carbon and Oxygen were measured on different mineral phases (calcite, dolomite and siderite) including organogenic carbonate crusts (Cal-B, Cal-C, Cal-N, Cal-H, Cal-BB, Cal-CC, Cal-NN, Cal-HH and Cal-AA), siderite concretions (Cal-I, Cal-G, Cal-M, Cal-E, Cal-R, Cal-A, Cal-u, Cal-EE, Cal-RR and Cal-V) and selected samples from cohesive mud sediments (Cal-9, Cal-15, Cal-17, Cal-10 and Cal-16). The sulfur isotopic composition was determined in crusts of pyrite (Cal-D) and native sulfur (Cal-Q_1), the only providing enough quantity and a sufficiently pure mineral phase.

Organogenic carbonate crusts

The carbon and oxygen isotope of carbonate crusts can be divided into two groups. Group I showed relatively depleted $\delta^{13}C$ values as they were ranging between -9.94‰ and -39.26‰ (V-PDB) and enriched in $\delta^{18}O$, being characterized by values comprised between 1.41‰ and 5.50‰ (V-PDB), as shown by carbonates characterized by the presence of calcite and dolomite composition (Table 3.20). The group II is also depleted in $\delta^{13}C$ (-26.30‰ to -45.41‰) and enriched in $\delta^{18}O$ between 2.83‰ to 5.14‰ and are represented by samples of calcite-aragonite carbonate content (Table 3.20).

Rock samples	δ ^{13}C (V-PDB)	δ^{18} O (V-PDB)	Mineralogy (%)		
			Calcite	Dolomite	Aragonite
Cal-B	-39.26	4.27	17.1	1.8	48.8
	-33.40	4.57	0.0	100.0	0.0
Cal-C	-35.43	5.50	35.2	2.8	29.5
	-23.82	5.04	0.0	100.0	0.0
Cal-N	-35.80	4.69	27	1.7	38.3
	-9.94	1.41	0.0	100	0.0
Cal-AA	-40.71	3.34	10.5	0.0	45.5
Cal-NN	-43.66	5.14	14.9	0.0	69.9
Cal-CC	-44.22	5	12.2	0.0	45.5
Cal-H	-26.30	2.83	23.0	0.3	46.2
Cal-HH	-48.79	4.48	10.7	0.0	53.9
Cal-BB	-45.41	4.85	12.9	0.0	49.9

Table 3.20: Oxygen and Carbon stable isotopes of carbonate crusts.

Siderite concretions

A total of 10 siderite carbonate samples were analyzed for stable carbon and oxygen isotopes (Table 3.21). The $\delta^{13}C$ values of these samples were between 3.15-10.64‰, with $\delta^{18}O$ values ranging from 8.72 to 9.94‰.

Rock samples	**$\delta^{13}C$ (‰V-PDB)**	**$\delta^{18}O$ (‰V-PDB)**
Cal-I	10.64	9.18
Cal-G	8.37	9.47
Cal-M	3.15	8.79
Cal-E	8.33	9.6
Cal-R	7.71	9.94
Cal-A	8.73	8.72
Cal-U	10.3	9.31
Cal-EE	9.12	9.14
Cal-RR	8.69	9.33
Cal-V	10.42	9.5

Table 3.21: Oxygen and Carbon stable isotopes of siderite.

Cohesive mud samples

Stable isotopes of carbon and oxygen were analyzed in selected mud samples which contain calcite. The $\delta\ ^{13}C$ values from -21.86 to 0.04 and $\delta\ ^{18}O$ from -10.46 to 2.36. (Table 3.22).

Unconsolidated samples	**$\delta^{13}C$ (‰V-PDB)**	**$\delta^{18}O$ (‰V-PDB)**
Cal-9	-0.81	-0.8
Cal-15	0.04	0.11
Cal-17	-2.57	2.36
Cal-10	-10.86	-6.09
Cal-16	-21.86	-10.46

Table 3.22: Oxygen and Carbon stable isotopes of calcite in selected mud samples.

Crusts of pyrite and sulfur

The isotope $\delta^{34}S$ value pyrite (Cal-D) was of -32.7‰, while that measured in the native sulfur (Cal-Q_1) was of -15.34‰ (Table 3.23).

Rock Samples	Minerals	$\delta^{34}S$ (‰V-CDT)
Cal-D	Pyrite	-32.7
Cal-Q1	Sulfur	-15.34

Table 3.23: Sulfur isotopic (‰ V-CDT) composition in pyrite and native sulfur.

3.3.7-Gas and water analyses

The chemical composition of the gas samples from fast venting sites is shown in Table 3.24, where dominated by the CO_2 (up to 98% by vol.) and followed by N_2 (up to 1.26 % by vol.) and methane (< 0.06% by vol.). The carbon and oxygen isotopic ratios of CO_2 were also reported in Table 3.24, where the $\delta\ ^{13}C$-CO_2 and the $\delta^{18}O$-CO_2 values were -1.8 and -1.1 V-PDB ‰ and -2.4 and -4.4 V-PDB ‰, respectively.

The chemical composition (in mg/L) of the water samples collected from the rosettes are listed in Table 3.25 and showed the water samples are characterized by a high Cl^- and Na^+ (from 23132 to 23639 mg/L and from 12575 to 12874 mg/L respectively). Whereas the concentration of other main dissolved species (SO_4^{-2} from 3824 to 3920 mg/L, Ca^{+2} from 482 to 521 mg/L, Mg^+ from 1482 to 1527 and K^+ from 473 to 598 mg/L). Alkalinity, Br^- and F^- concentrations (up to 243, 79 and 2.52 mg/L, respectively) were slightly higher than those in the mean ocean water. Free-CO_2 contents were comprised between 11.2 and 14 mmol L^{-1}.

Sampling station	CO_2 (%)	N_2 (%)	O_2 (%)	Ar (%)	CH_4 (%)	$\delta^{13}C_{CO2}$ (‰)	$\delta^{18}O_{CO2}$ (‰)
MB14 BC05	98.73	1.08	0.11	0.026	0.056	-1.1	-4.4
MB14 BC09	98.61	1.26	0.053	0.031	0.051	-1.8	-2.4

Table 3.24: Chemical composition (in % by vol.) and $d^{13}C$-CO_2 and $d^{18}O$-CO_2 (V-PDB), values of the venting gases.

Sample	**Alk.**	**F^-**	**Cl^-**	**Br^-**	**NO_3^-**	**SO_4^{2-}**	**Ca^{2+}**	**Mg^{2+}**	**Na^+**	**K^+**	**NH_4^+**	**CO_2**
MB14_ROS05	232	1.95	23606	61	11.5	3876	482	1512	12837	598	24.28	11.8
MB14_ROS06	232	1.20	23413	79	n.d.	3901	507	1527	12874	512	n.d.	11.2
MB14_ROS07	231	2.32	23639	72	n.d.	3920	506	1494	12692	483	n.d.	14.0
MB14_ROS08	159	2.52	23323	74	9.0	3918	521	1482	12575	473	n.d.	12.9
MB14_ROS09	243	n.d.	23132	70	20.1	3824	486	1499	12896	544	n.d.	11.9

Table 3.25: Chemical composition of the major compounds (in mg/L) and free-CO_2 is in mmol L^{-1} of studied waters recovered by rosette samplers.

Chapter 4: Discussion

4.1. Major and trace element chemistry

In this chapter the chemical (major, trace and REE elements) features of the studied samples will be discussed in order to highlight the possible sources have generated the elemental compositions of the deep-sea sediments and their relationships with the mineralogical observations presented in Chapter 3. These geological materials consist of different lithological detritical and authigenic products such as continental mineralogical phases, hydrothermal and/or hydrogeneous Mn-Fe deposits and biogenic carbonates (e.g. Dymond, 1981; Plank & Langmuir, 1998; Plank, 2013; Klaver et al., 2015). Geochemical characterization of deep-sea sediments reflects a diversified set of natural sources and processes (e.g. erosion of rocks, early diagenesis, weathering, wind-blown dust, volcanic activity, forest fires and inorganic precipitation from seawater), as well as anthropogenic impacts (Tranchina et al., 2008). As mentioned in the previous chapters, in this work 5 groups of samples were considered and in particular: organogenic carbonate crusts, siderite-rich samples, sulfide-rich samples, Fe-Mn-oxides and mud samples.

The first step was that to characterize the samples of each groups by ternary diagrams built on the basis of selected major elements. Then, the major elements were plotted versus selected trace elements according to their geochemical behavior. Finally, spider diagrams and REE patterns were also drawn. The former were divided according to low field strength elements (LFSE) or large ion lithophile elements (LILE — K, Rb, Cs, Sr and Ba), higher field strength elements (HFSE — Th, U,Ce, Pb, Zr, Hf, Ti, Ta and Nb), transition trace elements (TTE — Cr, Ni, Cu, Sc, V and Zn), Pb and As. In the study of deep-sea sediments and related products, REEs are considered useful parameters for assessing both depositional processes and sediment provenance. Furthermore, important hints can be obtained for highlighting paleo-environmental changes due to their conservative behavior during sediment formation (e.g.Taylor & McLennan, 1985).

As previously mentioned, major elements are a complementary tool of the mineralogical composition. In order to understand the major elements distribution in the study area, binary and ternary variation diagrams were constructed accordingly. The representation of major elemental concentrations, determined by XRF, for organogenic carbonate crusts on the SiO_2-(Al_2O_3+Fe_2O_3)-(CaO+MgO) ternary plot (Fig. 4.1), as expected, shows that these samples are (CaO+MgO) dominated with a relatively constant SiO_2/(Al_2O_3+Fe_2O_3) ratio. The total amount of $CaCO_3$ (%) was not that retrieved by calcimetric analyses but it was indirectly calculated from the total Ca concentration (Ca_{tot}) with a correction for the Ca inventory supported by the detrital component (e.g. Cangemi et al., 2010 and references there in), as follows:

$$CaCO_3 = 2.5\ [Ca_{tot} – (Al_{tot} * Ca\ /Al_{average\ shale})]$$

Where the Ca /$Al_{average\ shale}$ ratio is 0.276. The organogenic carbonate crusts display a $CaCO_3$ content between 49.4 to 75.0 %.

The compositional variations in term of major elements for the tubular authigenic siderite and the sulfide samples are presented in the (Na_2O+K_2O)-SiO_2-Fe_2O_3 ternary diagram of Fig. 4.2 and Fig. 4.3, respectively. Both diagrams show that most samples have a substantially constant SiO_2/(Na_2O+K_2O) ratio with the exception of Cal-E and Cal-U (Fig. 4.2) and Cal-O (Fig. 4.3), whose ratios are clearly different. Moreover, a relatively wide range in terms of Fe_2O_3 is observed for both sulfide and siderite, although the latter systematically showed higher iron contents. The latter are also characterized by the presence of different content silicate minerals as highlighted by the mineralogical observations (see Chapter 3).

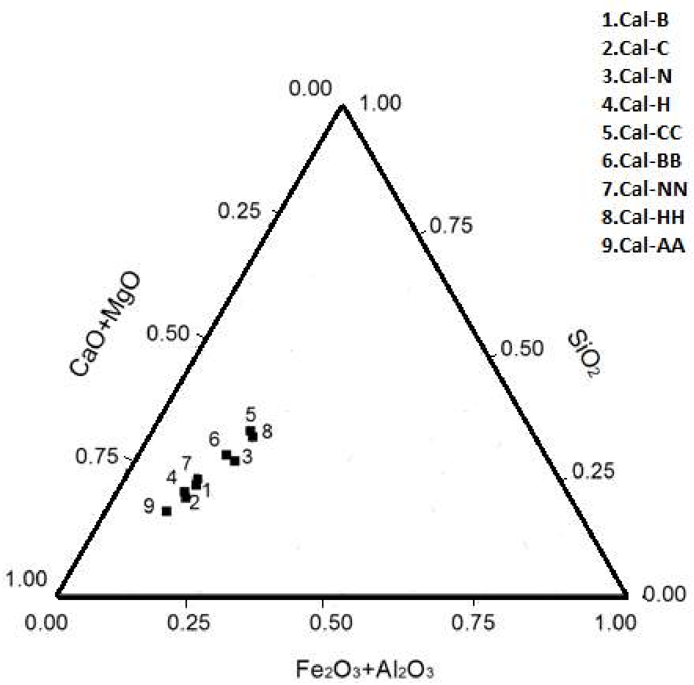

Figure 4.1 – SiO_2-(CaO+MgO)-(Fe_2O_3+Al_2O_3) ternary plot for the organogenic carbonate samples

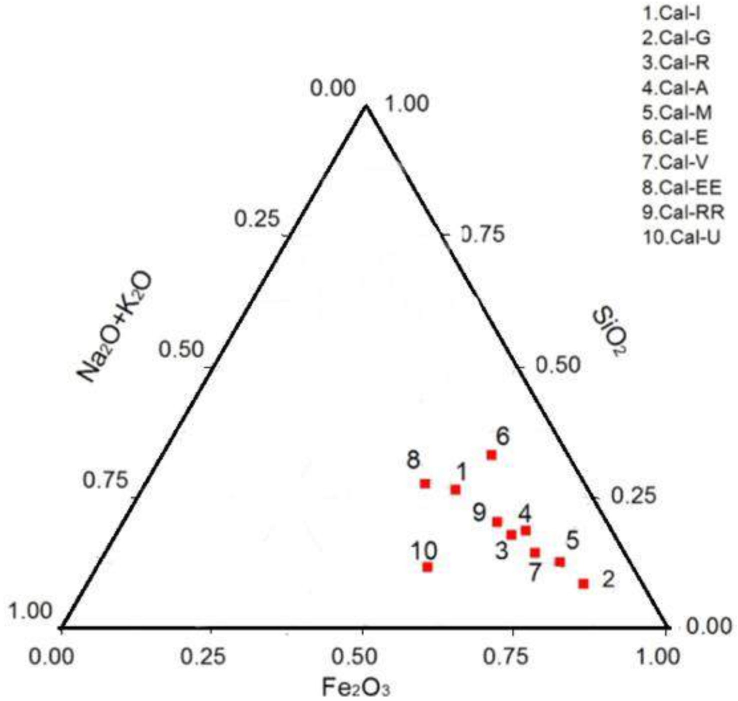

Figure 4.2 – SiO_2- (Na_2O+K2O)-Fe_2O_3 triangular plot for tubular carbonate (siderite) samples. 1=Cal-I, 2= Cal-G, 3=Cal-R, 4=Cal-A, 5=Cal-M, 6=Cal-E, 7=Cal-V, 8=Cal-EE, 9=Cal-RR and 10=Cal-U.

In Fig. 4.4. the SiO_2-Fe_2O_3-(MnO+TiO_2) ternary diagram for the three Fe(Mn)-rich samples is reported. Two samples (namely, Cal-T and Cal-P) are enriched both in SiO_2 and Fe_2O_3, whereas the other one (Cal-F) is enriched in Fe_2O_3. All the three samples contain small proportions of (MnO+ TiO_2).

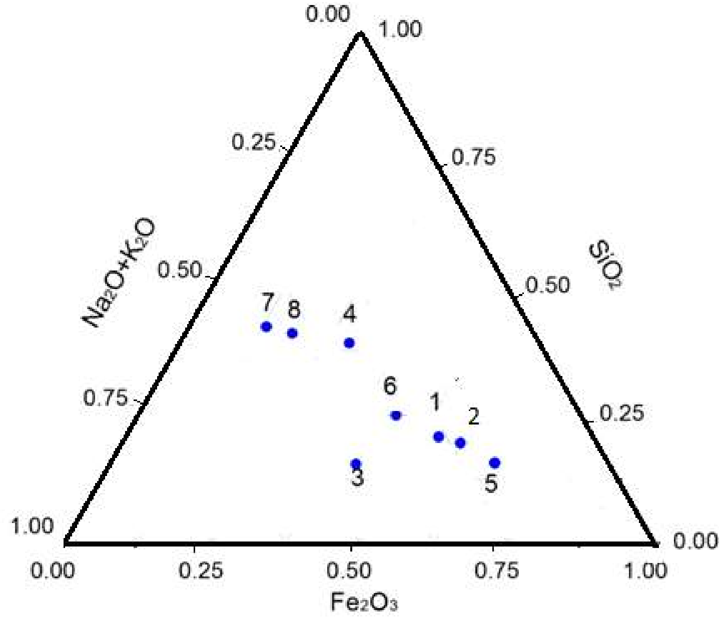

Figure 4.3 – SiO_2- (Na_2O+K_2O)- Fe_2O_3 diagram of sulfide rich samples showing a clear negative correlation between SiO_2 and Fe_2O_3. 1=Cal-D; 2=Cal-Q; 3=Cal-O; 4=Cal-L; 5=Cal-S; 6=Cal-Z; 7=Cal-X and 8=Cal-W.

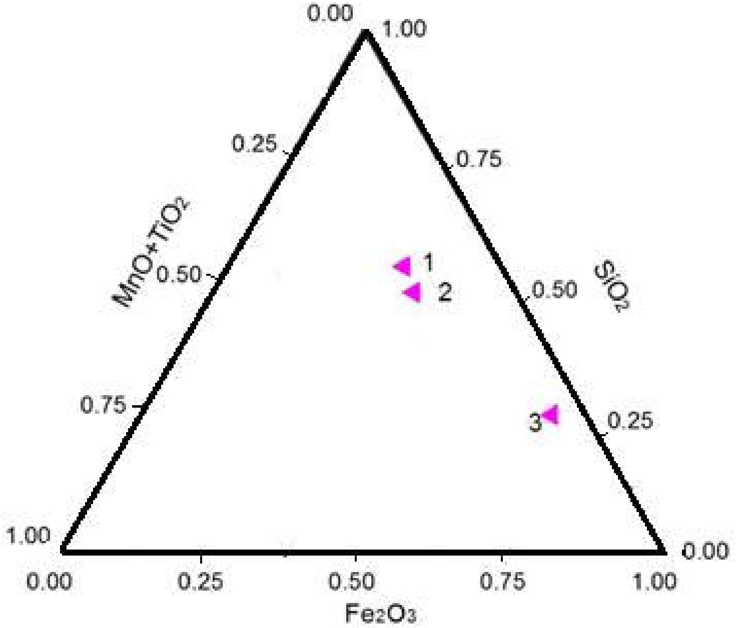

Figure 4.4 - SiO_2- (MnO+TiO_2)-Fe_2O_3 plot for Fe(Mn)-rich oxides. 1=Cal-T; 2=Cal-P and 3=Cal-F.

The relatively large compositional variation observed in the mud samples is likely affected by several factors such as weathering, provenance, transport and diagenesis. Several major elements are commonly used to quantify the weathering effects. Nesbitt & Young (1984,1996), Nesbitt et al. (1996) and Nyakairu & (2001 and references there in) have applied the Al_2O_3-(CaO+Na_2O)-K_2O (A-CN-K) and

Al_2O_3-(CaO+Na_2O+K_2O)-(Fe_2O_3+MgO) (A-CNK-FM) ternary plots as the most useful representation to be used for mud samples in order to highlight weathering.

As can be observed when comparing Fig. 4.5 and Fig. 4, the first diagram better displays the weathering process that affected mud samples. In fact in Fig.4.5, all the investigated mud samples display an inverse correlation between Al_2O_3 and (CaO+Na_2O), and a Al_2O_3/K_2O ratio relatively constant. This can be due to a gradual, though rapid, depletion of Ca and Na, which are relatively promptly lost during chemical weathering.

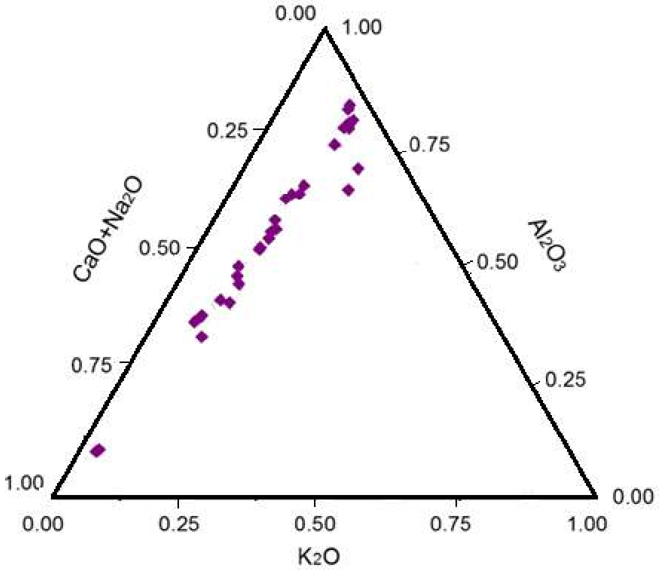

Figure 4.5- Al_2O_3- (CaO+Na_2O)-K_2O ternary plot for the mud samples.

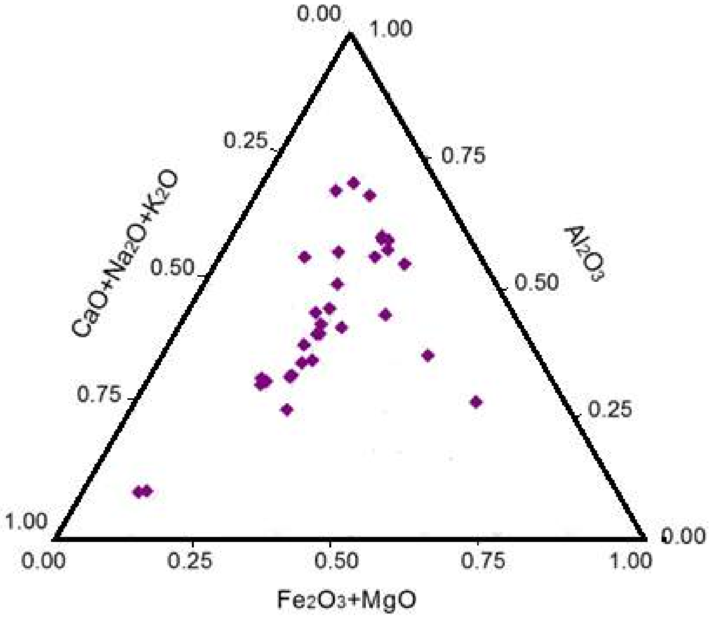

Figure 4.6- Al_2O_3-(CaO+Na_2O+K_2O)-Fe_2O_3+MgO ternary plot for the mud samples.

For discriminating the source(s) of the mud samples, some distinct elemental compositions of mud samples are commonly applied to define the presence of terrigenous detritus, authigenic and hydrothermally-altered components.

At this regard, Shao et al. (2015) proposed the Al-Mg-Fe ternary plot (Fig. 4.7) for mud samples from the Okinawa Trough, located between the East China Sea (ECS) and the Eurasian continental margin. Al was assumed to be associated with terrigeneous clays, while Mg and Fe were considered as representative of hydrothermal clays (e.g. chlorite) and sulfides, respectively.

The mud samples from the Paola Basin were characterized by concentrations of Al, Mg and Fe similar to those from the East China Sea and Changjiang and Taiwan rivers (Shao et al., 2015 and references therein). Consequently, in the Al-Mg-Fe ternary diagram (Fig. 4.7) most samples distribute close to the Al corner, suggesting a relevant contribution of clays fed by a detrital source. On the other hand, two samples (Cal-14 and Cal-7) are enriched in Fe, which indicates the presence of sulfides and siderite, as also evidenced by petrographical and mineralogical observations (Chapter 3). To support the fact that mud samples are mainly characterized by a continental supply, the Ti versus Zr (in ppm) binary plot (Shao et al., 2015 and references therein) is used since terrigenous clays are normally enriched in Ti (and V and Sc) but depleted in Zr (Fig.4.8). Aluminum and Ti show a relatively conservative behavior during earth surface processes and are relatively unaffected by chemical weathering and diagenetic alteration. This implies that they are primarily hosted in the detrital fraction of marine sediments (e.g. Taylor and McLennan, 1985; Martinez et al., 2007). Hydrothermal clays are supposedly to be precipitated from hydrothermal systems or formed by alteration processes of geological material influenced by hot fluids, which are responsible of the low Ti concentrations (e.g. Shao et al., 2015). All the studied samples are enriched in Ti and depleted in Zr, with the exception of (Cal-14), allowing to conclude that the mud samples from the Paola Basin are dominated by a strong component of detrital fraction.

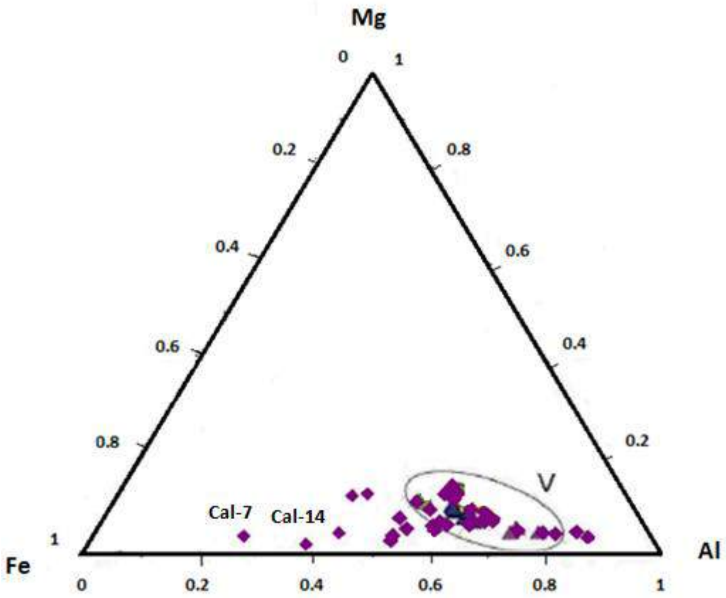

Figure 4.7- The ternary plot of Al, Mg and Fe in the bulk clay samples. Symbol: purple diamonds = mud samples from the Paola Basin.(V): The terrigenous clays (ECS shelf, Changjiang and Taiwan rivers) from Shao et al. (2015).

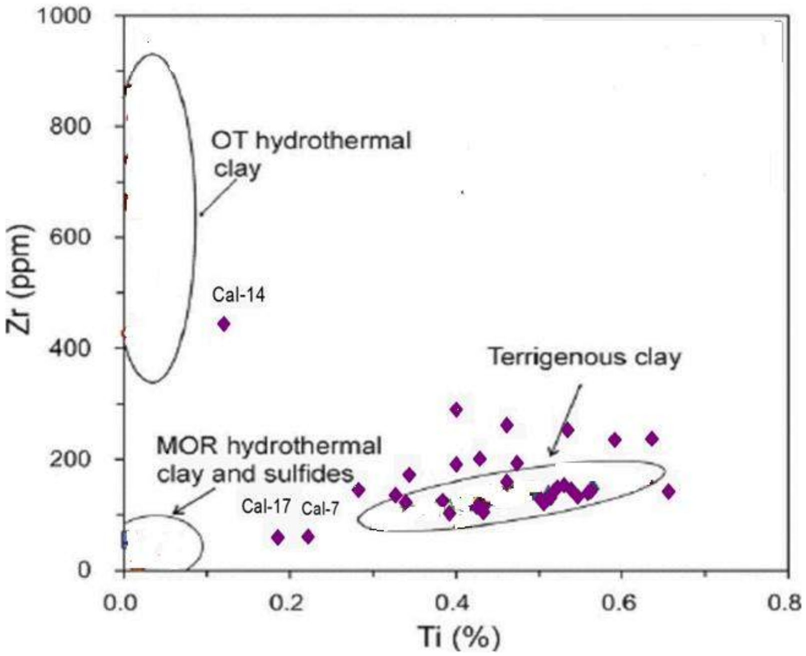

Figure 4.8- plots of Ti vs. Zr in the bulk clay samples. Symbol purple diamonds = mud samples from the Paola Basin from Shao et al. (2015)..

The large variation in terms of SiO_2 concentrations, whose contents were comprised between 5.54 (Cal-G) and 56.29 (Cal-28) wt. % (Table 3.11 and Table 3.17), was used as a main parameter to be plotted versus the other main chemical variables. SiO_2 is chosen as the plotting parameter for many rock series because it is commonly the major rock constituent and shows greater variability than any other oxides (Rollinson, 1993). For these reasons, SiO_2 can also highlight possible geochemical peculiarities that characterize our sample dataset. In Fig. 4.9 and 4.10, SiO_2 contents are plotted versus those of Al_2O_3, K_2O, TiO_2 and CaO and Na_2O, Fe_2O_3, MnO, P_2O_5, L.O.I. and MgO (in wt. %) for all samples. Positive correlations between SiO_2 and Al_2O_3, K_2O and TiO_2 (Fig. 4.9a, b and c, respectively) are observed where the mud samples are characterized by the highest SiO_2 contents. Moreover, in the Al_2O_3 vs. SiO_2 diagram (Fig. 4.9a) two distinct distributions are evidenced since the mud samples are displaced to the right with respect to the trend depicted by the other samples, suggesting that at a given content of Al_2O_3, SiO_2 is enriched in the clay-rich samples, likely due to a higher content of quartz (presented in Chapter 3). A peculiar behavior is observed when the CaO vs. SiO_2 diagram (Fig. 4.9d) is considered, since an inverse correlation between these two parameters is shown for the carbonate organic crusts and part of the mud samples. A second trend can be observed for some mud rocks and the Fe(Mn)-oxide and sulfide samples since they tend to be distributed parallel to the x-axis for CaO content lower than 5%, which is related to a progressively increase in the silicate mineral contents. This is also supported by the Na_2O, Fe_2O_3 and MnO vs. SiO_2 diagrams (Fig. 4.10a,b, c, respectively), which show a behavior similar to that observed in the CaO vs. SiO_2 diagram (Fig. 4.9d). However, it is to remark that the sulfide and Fe(Mn)-oxide samples are, as expected, enriched in Fe_2O_3 (Fig. 4.10b). In the (Fig.4.10d) the P_2O_5 vs SiO_2 diagram is shown, where a positive correlation between these two parameters is observed with the exception of two samples (Cal-P and Cal-F). The inverse correlation between L.O.I. and SiO_2 (Fig. 4.10e) is indicative of the higher concentrations of volatile components (CO_2) released by the carbonate-rich rocks (organic crusts and siderite-rich samples) during the ignition at 950 °C, whereas the mud samples have lower L.O.I. contents (5 to 20 %). No significant correlation is evidenced in the MgO vs. and SiO_2 (Fig. 4.10f) diagram since the two most representative groups of our rock dataset (carbonate organic crusts and mud samples) are characterized by similar MgO concentrations and only the different contents of SiO_2 allows to discriminate between them. The lower concentrations of MgO are shown by the sulfide samples.

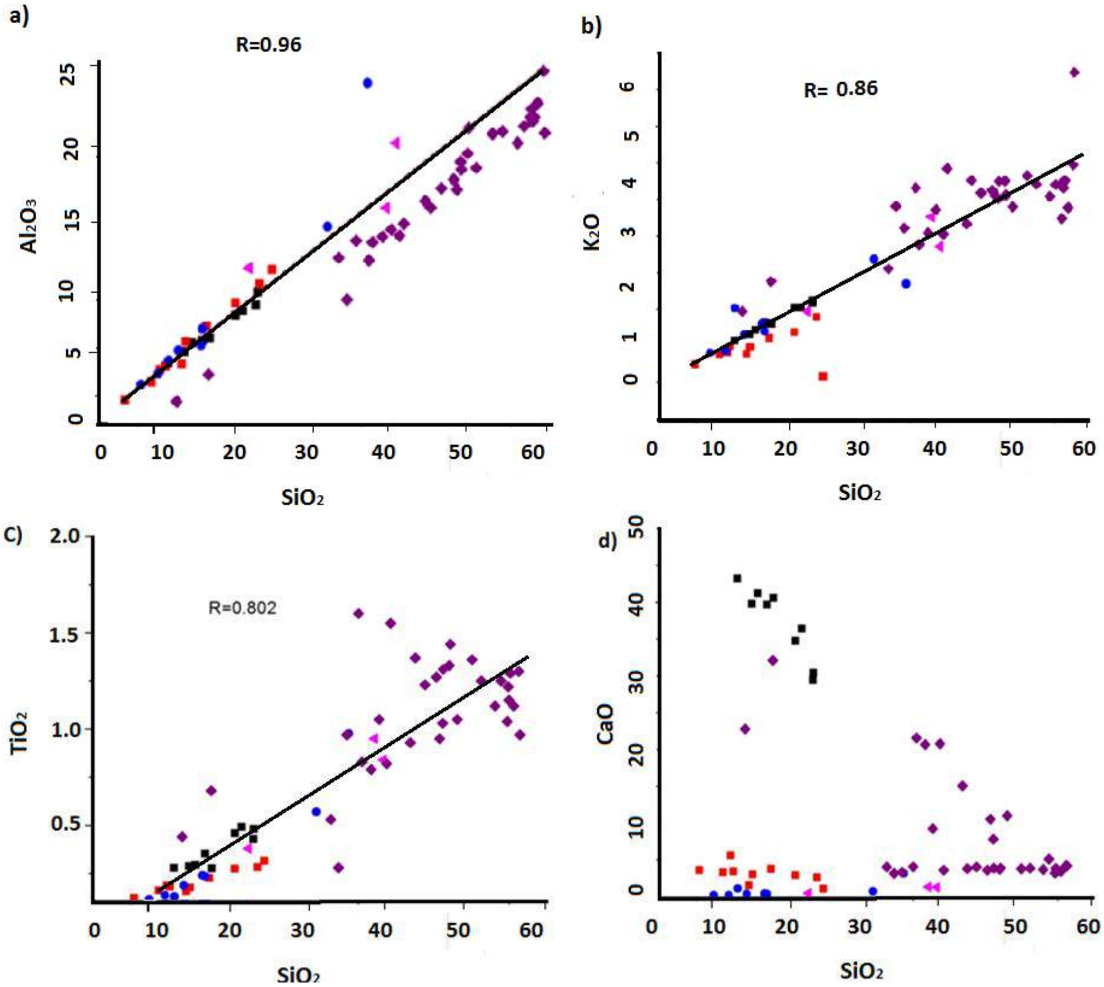

Figure 4.9-Binary diagrams of Al_2O_3,K_2O, TiO_2 and CaO (%) vs. SiO(%). Legend: black square = organogenic carbonate crusts; red squares = tubular authigenic siderites; blue circles = sulfides; magenta triangles = iron oxides; purple diamonds = mud samples.

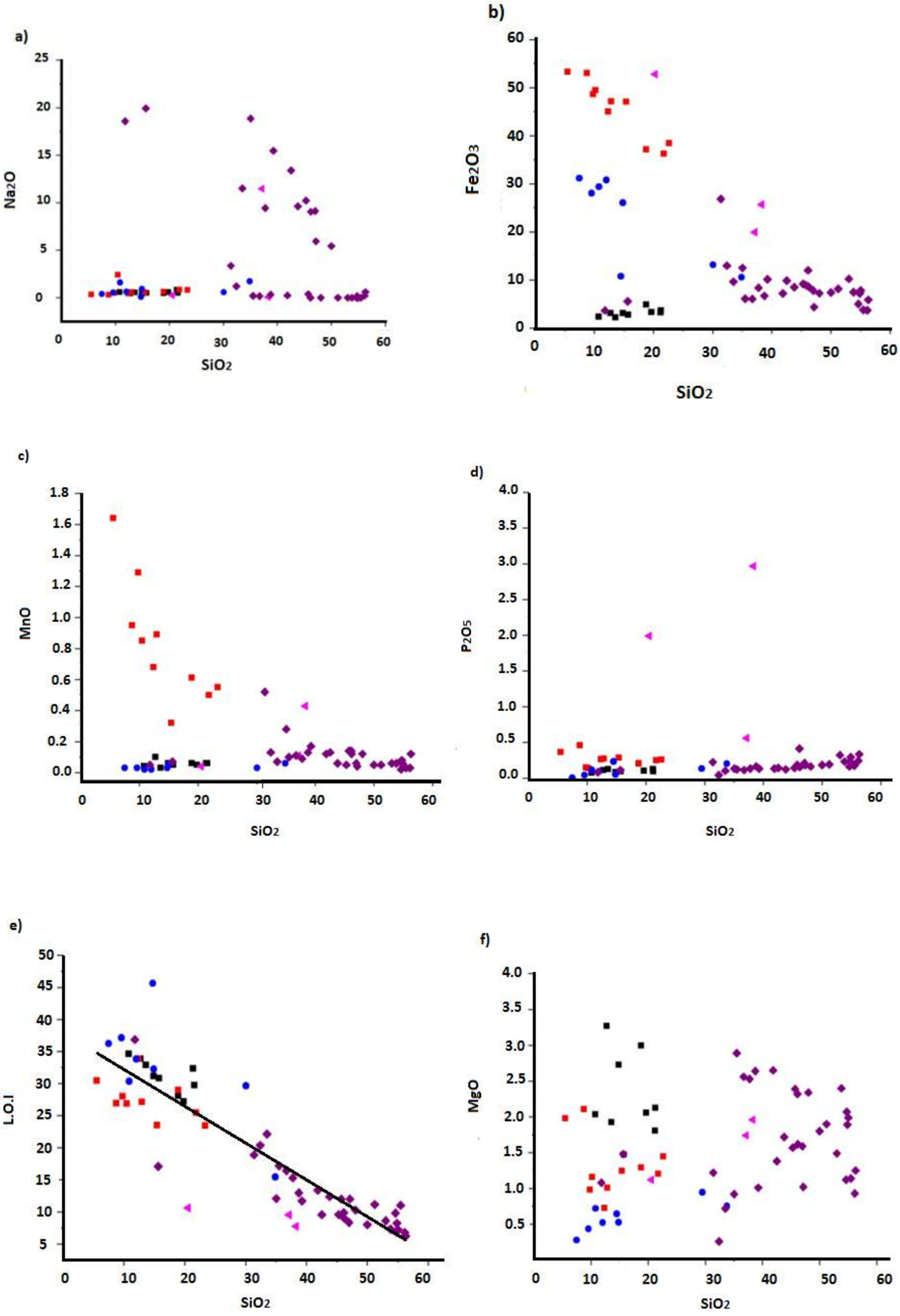

Figure 4.10- Binary diagrams of Na2O,Fe2O3,MnO,P2O5,L.O.I and MgO (%) vs. SiO2 (%). Symbols as in Fig.4.9.

As shown for the Ti vs. Zr (Fig. 4.8) diagram, sedimentary processes (weathering, transport, diagenesis and metamorphism, e.g. Nyakariru and Koeberl, 2001 and references therein) can better be highlighted when the trace elements are taken into account. Moreover, the geochemical variability of these elements is also linked to the main lithological features. As previously mentioned, Al is likely related to a detrital component (Shao et al., 2015) when marine sediments are considered since this element is commonly recalcitrant to alteration processes. This means that we may attempt to use this geochemical parameter as representative of the terrigenous detritus and verify how selected elements behave when plotted versus Al.

In Fig.4.11 the correlation between some elements vs. Al_2O_3 is reported for the mud samples, such as the alkali elements (K, Rb, Cs), the alkaline earth elements (Sr, Ba) the high field strength elements (Ti, Nb, Ta, Hf, Zr) and Th and U (Plank and Langmuir, 1998). Representative examples for each group, e.g. Rb, Sr, Zr, Nb, and U, are plotted vs. Al_2O_3 (Fig.4.11). Based on their correlation with Al_2O_3 several of these elements are typically detrital such as Rb, Zr and Nb, since the ratios of these elements to Al_2O_3 are constant in some of mud sample (Fig.4.11a,b,c), with the exception of a few samples (Cal-17, Cal-23,Cal-14, Cal-28). On the other hand, there are trace elements that are weakly correlated with Al_2O_3, e.g. Sr (Fig.4.11d). Strontium concentrations are dependent on the proportion of carbonate, and the highest contents are related to the carbonate-rich samples (Plankand Langmuir, 1998), e.g. samples Cal-17, Cal-29, Cal-27, which contain $CaCO_3$ (see Chapter 3). No correlation is shown by the U vs. Al_2O_3 (Fig.4.11e) likely due to the fact that uranium is controlled by the redox state (Klaver et al., 2015 and references there in).

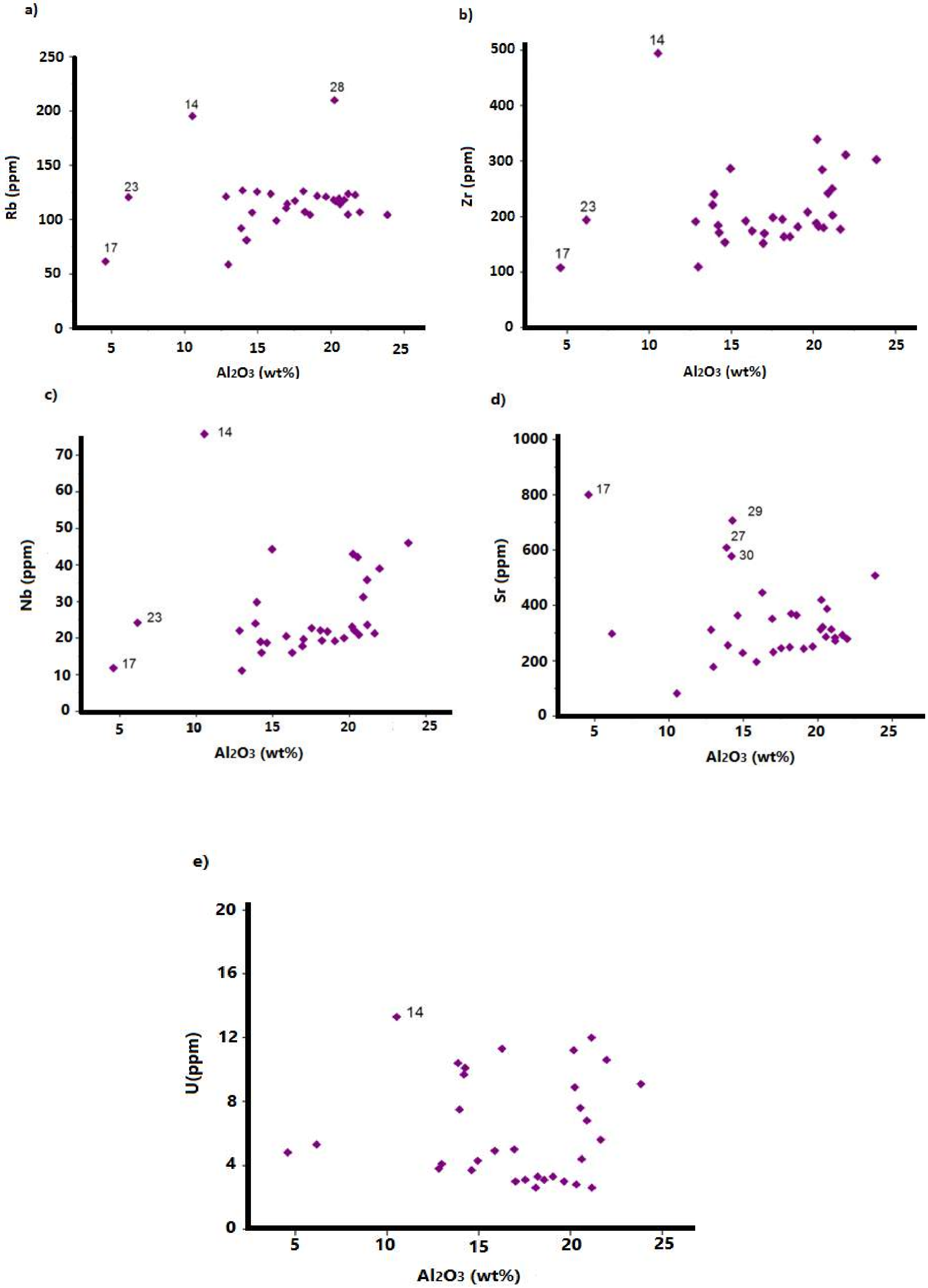

Figure 4.11- Binary diagrams of Rb, Zr, Nb, Sr, and U vs. Al_2O_3 for the mud samples.

4.2 Spider diagram and REE patterns

Trace elements are classified according to their behavior in magmatic systems in to the compatible when they preferentially partitioned in the solid (mineral) phase and they are incompatible when they enirch in the melt phase. To highlight their behavior, spider diagram are normaly used where trace elements are normalized (to a reference rock, e.g. primitive mantle composition) and plotted this incresing compatibility from the left to the right of these multi-element diagrams. A similar approach can be used for sedimentary rocks. For example, trace elements in clastic deposits are archiving useful information about sedimentary provenance and composition of crustal source regions (e.g., Bhatia and Crook 1986; McLennan et al. 1990; Floyd et al. 1991; Garver and Scott 1995; Unterschutz et al. 2002; Petersen et al. 2004). Trace elements including large-ion lithophile elements (LILEs), high-field-strength elements, and rare earth elements (REEs) are efficiently transferred into sedimentary rocks, are strongly excluded from seawater, and have low potential for post-depositional mobility (Taylor and McLennan 1985; McLennan, 1993). Normalized multi-element and REE diagrams as well as multiple trace-element plots are also used to assess temporal and spatial variations in the composition sedimentary deposits (e.g. LaMaskin et al, 2008 and references therein). Furthermore, trace element pattern are also useful for reconstructing environmental and physical-chemical variations (e.g., Franchi et al., 2016 and references therein). All the analyzed elements concentrations were normalized to the Post-Archean average Australian Shale (Taylor and Mclennan, 1981). In the spider diagram (Fig.4.12), the elements are ordered according to the most mobile elements (LILE, including Cs, Ba, Rb, and Sr), Th and U and the immobile elements (HFSE, Zr, Hf,Y, Nb and Ta) in order of increasing compatibility. The concentrations of trace elements vary widely and most of the elements have a lower abundance than that of PAAS. LILE distribution in the analyzed samples is variable. Most of them are moderately to strongly depleted in LILE when compared to PAAS (Fig.4.12). The alkali elements such as Rb and Cs are also variable and higher values were found in mud samples (Fig.4.12e). As shown in (Fig.4.12a,c,e), the samples are enriched in Sr with respect to PAAS. With the exception of mud samples, all studied samples are depleted in Th when compared to PAAS. Additionally, elevated uranium concentrations are recorded in some of studied samples.

The distribution of HFSE significantly differs with respect to those of PAAS and is normally characterized by depleted characteristics except for some elements in a few samples. Zr and Hf are variably concentrated in the studied samples and are highly enriched in the mud samples (Fig.4.12e), while tubular carbonate siderite and Fe-Mn oxides samples show a negative Zr and Hf (Fig.4.12b,d). The average concentration of Y in some of studied samples is higher when compared with PAAS as shown in (Fig.4.12b,d,e). HFSE are preferentially partitioned into melts during crystallization and anatexis (Feng and Kerrich, 1990) and due to their relatively low mobility during weathering, transport, diagenesis, and metamorphism, these elements are used for provenance determination together with REEs. By looking at the spider diagrams for the five lithologies collected from the Paola Ridge, it is possible to recognize different incompatible to compatible element patterns. The carbonate crusts show a relatively flat pattern with the exception of Sr and U, which tend to be enriched in the carbonate phase with respect to PAAS (Fig. 4.12a). The spider diagram of the tubular carbonate siderites (Fig. 4.12b) displays and increasing trend from the incompatible to the compatible elements with positive and negative spikes related to U and Hf, respectively. U and Sr positive spikes and a slightly flat pattern characterize the sulfide samples (Fig. 4.12c) from the Paola Ridge. Similarly to what observed for the tubular sideritic samples, the Fe-Mn oxides also have an increasing trend from incompatible to compatible elements (Fig. 4.12d). Finally, the mud samples depict a different trend with respect to those shown by the previous lithoologies. They indeed are slightly depleted in Cs, Ba and Rb, then the normalized values for U and Sr show positive spikes and a substantial flat pattern, oscillating around 1, is shown by the other elements, although a slight negative spikes is observed for Hf.

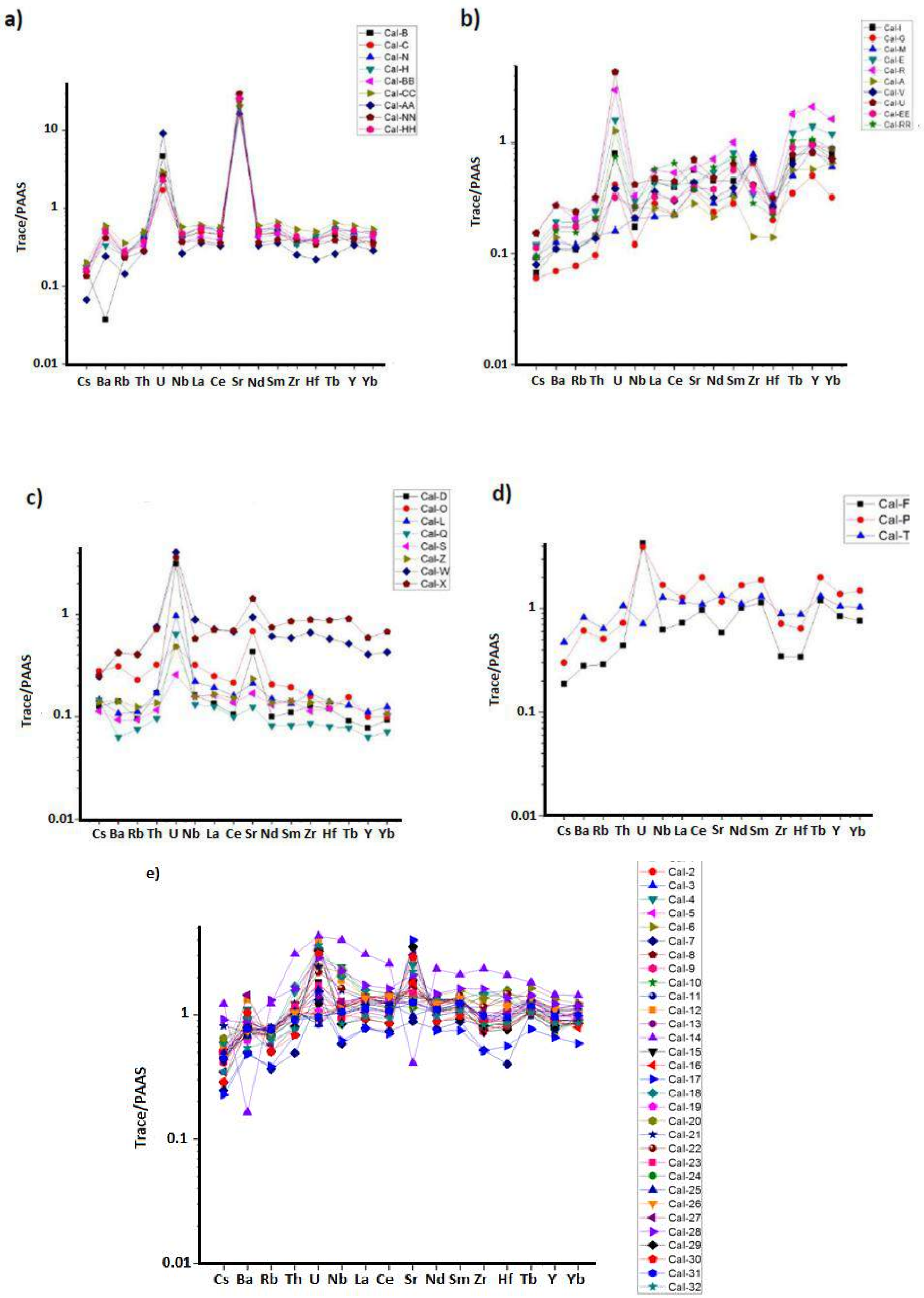

Figure 4.12- spider diagram for selected elements normalized to PAAS (Post-Archean Australian Shale; Taylor and McLennan (1985); a) carbonate crusts; b) tubular carbonate siderite; c) sulfide samples; d) Fe-Mn oxides and e) mud samples.

4.2.1 Rare earth elements (REE)

The REE are regarded as the least soluble trace elements and are relatively immobile during low-grade metamorphism, weathering (Rollinson,1993). The REE Patters can be used as proxy for reconstruction of the environmental conditions of early diagenesis. The REE distribution tends to be significantly vary in sediments due to redox variations within the pore water (e.g., Haley et al., 2004). The REE pattern variation can therefore be used to investigate the modification of redox conditions in sediments.

The shale-normalized REE patterns of investigated samples are plotted in Fig.3.13 and display a wide variation according to the different lithologies. As previously mentioned, the mud samples are dominated by a strong component of detrital fraction. This likely explains the reason why mud samples shows REE patterns pretty similar each other with the exception of Cal-28 (Fig.4.13e).

With regard to carbonates, the use of carbonates as a proxy for the REE content of ancient seawater is complicated by possible modification due to the presence of i) REE-bearing terrigenous components with non-seawater-like patterns (Goldstein and Jacobsen, 1988; Elderfield et al., 1990); ii) Fe- and Mn-oxy-hydroxides (Bau et al., 1996; Bayon et al., 2004) and iii) phosphates, which might have a non-uniform REE incorporation (German and Elderfield, 1990; Byrne et al., 1996). To avoid the terrigenous contamination, Rongemaille et al. (2011) proposed the usage of weak acetic acid solution (5% v/v) for quantitative leaching of carbonate samples with exception for siderite.

4.2.2 Carbonate crust REE pattern

The shale-normalized REE of the carbonate crust samples (Fig. 4.13a) show a non marine seawater trend (Zhang and Nozaki, 1996). They are characterized by a slight enrichment of light LREE compared to HREE (Pr_{SN}/Yb_{SN} between 0.95 and 1.35). No Ce and Gd anomalies were recorded whilst Eu anomaly is slightly positive (Table 3.10). Terrigenous compounds present in limestone deposits are able to mask the seawater signature, even when present at concentrations well below 1% (e.g. Murray et al., 1991), because clay minerals have very high partition coefficients for REE (Oliver and Boyet, 2006). Al_2O_3, SiO_2, Zr and Rb distributions are considered proxies for concentrations of terrigenous minerals since they closely correlate with the clay content. Although the high contents of both Al_2O_3 and SiO_2, there is no correlation (R^2=0.52 and 0.54, respectively) with ∑REE and LREE (Fig.3.14 A-D), while Zr and Rb are weakly correlated with ΣREE (Fig.3.14F-G), suggesting a minor contribution from acid-leached terrigenous minerals to the overall REE budget. The other potential contaminants of limestone, such as Fe and P compounds have a high affinity for REE and also incorporate REE disproportionally (German and Elderfield, 1990; Bau et al., 1996; Reynard et al., 1999; Bayon et al., 2004; Bau and Koschinsky, 2009), do not show significant correlations with ΣREE and LREE (Fig.3.14H-I).

The REE pattern of both limestones and Fe-oxy-hydroxides are relatively flat (average Pr_{SN}/Yb_{SN}=1.10 and 1.01, respectively) with a slight MREE enrichment (Gd_{SN}/Yb_{SN}=1.28 and 1.45, respectively), which is typical of precipitates formed in oxic to sub-oxic pore water (Haley et al., 2004). Flat REE pattern and absenc of Ce anomalies in the limestone concretions and oxy-hydroxides likely suggest that they incorporated high amounts of organic matter and precipitated within highly alkaline pore water under sub-oxic conditions.

4.2.3 Siderite REE pattern

The REE patterns of siderite (Fig.4.13c) are showing a general depletion of LREE and a quasi-marine trend (Zhang and Nozaki, 1996) with strong HREE enrichment. The siderite samples showed that the average LREE/HREE ratio (Pr_{SN}/Yb_{SN} is 0.45) and Ce and Gd anomalies are lacking or slightly positive (between 1.00-1.34 and 1.05-1.21, respectively in Table 3.12).

Within siderite samples Rb shows weak correlation with ΣREE(Fig.3.14G) while Al, Si and Zr do not correlate with LREE and ΣREE (Fig.3.14A-F). Therefore, a substantial terrigenous contamination can be ruled out. Since no correlation between Fe, Mn and P and LREE and ΣREE is present (Fig.3.14H-I), contamination by Fe-Mn-oxy-hydroxides and phosphates is not occurring.

The precipitation of siderite probably occurred under prolonged anoxic conditions with high pore-water alkalinity and high Fe concentration as suggested by the enrichment of MREE (Haley et al., 2004) and the lack of Ce anomaly (Franchi et al., 2015). The siderite precipitation rate is three orders of magnitude slower than that of calcite (e.g. Wittkop et al., 2014), and therefore, the formation of siderite concretions is likely to be stable under supersaturated conditions fostering LREE fractionation.

4.2.4 The Y/Ho ratio

Another important parameter is the Y/Ho ratio since the Y and Ho are considered to have a similar geochemical behavior in seawater and also provides important information for seawater characterization. Both igneous rocks and epiclastic sediments show the chondritic Y/Ho ratio of about 26-28 (Bau, 1996 and references therein), on the contrary, modern seawater and related marine precipitates are often characterized by super-chondritic (up to 90) Y/Ho ratio (Bau, 1996; Zhang et al., 1994; Bau et al., 1997; Nozaki et al., 1997). Two geochemical feature: super-chondritic Y/Ho ratio (up to 90) and positive La anomaly are typical of modern seawater signatures (e.g.,Bau, 1996; Webb and Kamber, 2000; Allwood et al., 2010; Franchi et al., 2015). In this study, the average Y/Ho ratio of the limestone samples is 29.2. (Table 3.10). And the siderite samples show the Y/Ho ratios range from 25.6 to 38.4 (Table 3.12). Therefore, carbonates from Paola Ridge show average Y/Ho ratio of ca. 31, close to chondritic values and lacking the linear correlation between Y/Ho and La anomalies (Fig3.15). In addition, deep fluids, including hydrothermal fluids, have higher concentrations of REE, compared to that of seawater, and chondritic Y/Ho ratios (e.g.,Klinkhammer et al., 1994; Bau and Dulski, 1999). The variation in redox condition during the formation of authigenic carbonates can be outlined by using specific trace elements (such as U and Mo) and tracking the variation of redox sensitive REE (i.e. Eu and Ce). Molybdenum can be used as tracer for anoxic conditions (Neubert et al. 2008) and the strong enrichment of Mo was observed in mud volcano sediments in an area of intense seepage (e.g.,Hein et al., 2006). Under oxic conditions Mo has a conservative behavior, while under anoxic conditions it tends to be accumulated in organic matter and iron sulfides (Helz et al., 1996; Neubert et al., 2008; Algeo and Tribovillard, 2009). The high Mo contents in limestone(average 18.3 ppm) and siderite (average 36.4 ppm) concretions point toward suboxic to anoxic conditions during carbonates precipitation. Other evidences can be inferred of redox conditions, the variation of the Ce anomaly is thought to be indicative of redox state (Haley et al., 2004 and citations therein) being negative (*ca*. 0.2-0.4) under oxic conditions and positive under anoxic conditions (e.g., Oliver and Boyet, 2006; Hu et al., 2014). On the other hand Ce tends to be accumulated in Fe-oxy-hydroxides and organic matter, but "false" negative Ce anomalies may be induced within the authigenic carbonates (see discussion in Bayon et al., 2004). The lack of Ce anomaly in both limestone and siderite at Paola Ridge show anoxic to suboxic conditions and high organic matte contents.

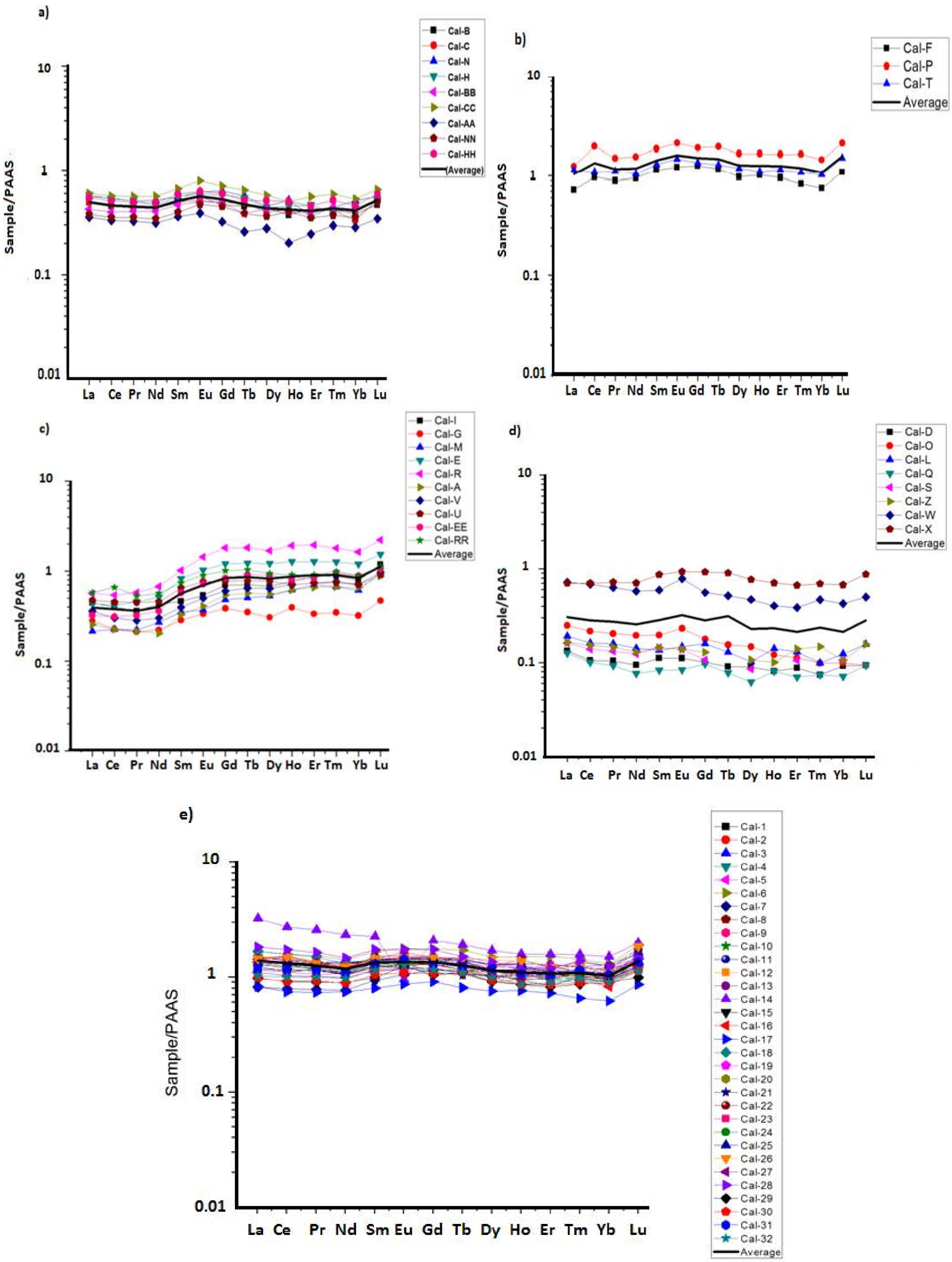

Figure 3.13- PAAS-normalized REE patterns of samples a) limestones, b) oxy-hydroxides, c) siderites, d) sulfides and e) muddy sediments.

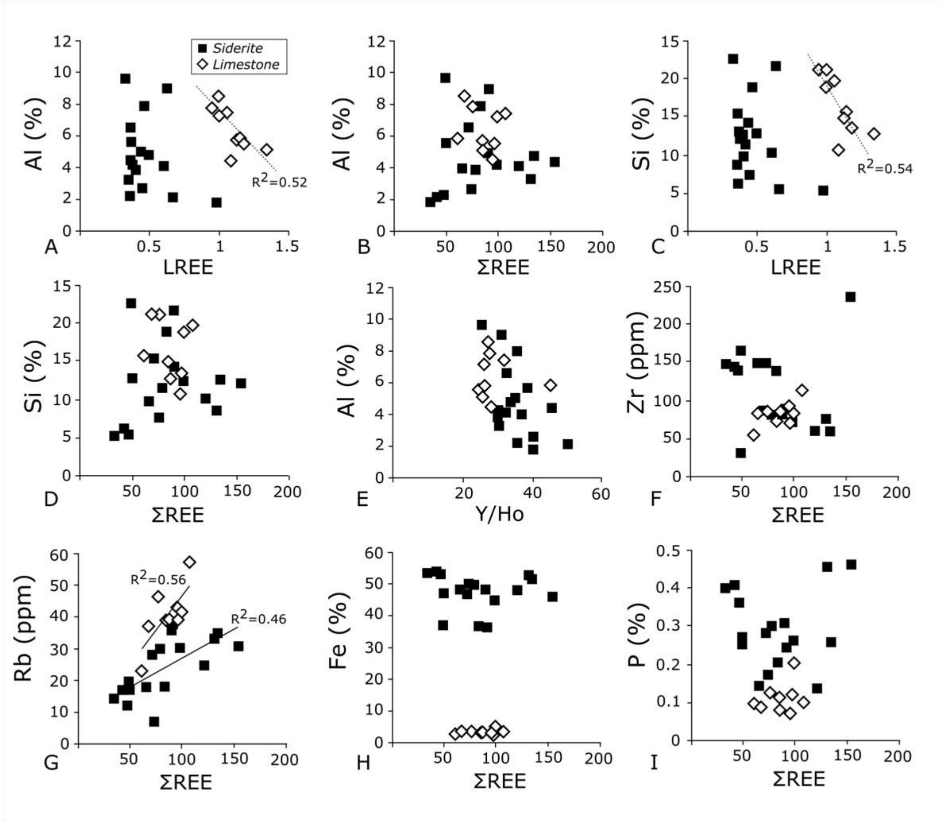

Figure 3.14- Binary diagrams of terrigenous contaminant proxies versus ΣREE, LREE for the limestone and siderite concretions (Franchi et al.,2016).

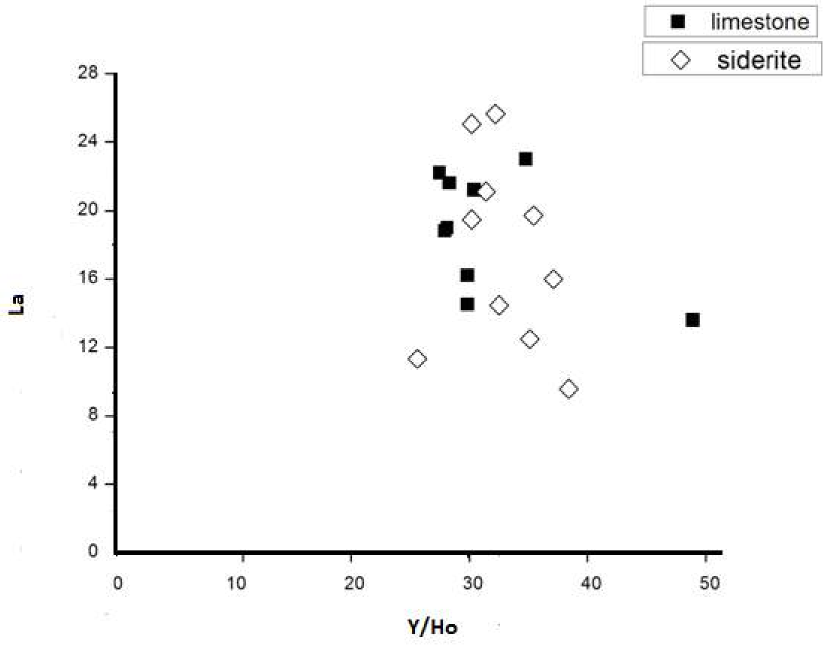

Figure.3.15-- Binary diagram of Y/Ho and La for limestone and siderite.

4.3 Stable isotopes

The oxygen and carbon isotope composition was studied in (Calcite, dolomite and siderite). The carbon isotope composition of authigenic carbonates provide information about the source of carbon incorporated during carbonate precipitation (Paull et al., 2007; Peckmann and Thiel, 2004; Naehr et al.,2000 and references therein). The possible sources of carbon to the pore fluids include: - biogenic methane ($\delta^{13}C$ <-65‰), or thermogenic methane ($\delta^{13}C$ -30‰ to -50‰), - sedimentary organic matter ($\delta^{13}C$ =-25‰), marine biogenic carbonate ($\delta^{13}C$ =0‰) or seawater CO_3^{2-}($\delta^{13}C$ = 0±3‰)(Naehr et al., 2000; Chen et al., 2007; Campbell, 2006 and references therein). The oxygen isotopic composition in carbonate is normally used to infer the seawater/porewater temperature and oxygen isotopic composition of the precipitating fluids (e.g. Mansour and Sassen, 2011 and references therein).

Stable isotopes of organogenic crusts in the mud diapirs were strong depleted in ^{13}C (Fig. 4.16). The negative $\delta\ ^{13}C$ values (-26.3‰ to -41.50‰ V-PDB) indicating ^{13}C-poor dissolved inorganic carbon (DIC) issued from methane oxidation as the source of carbon (Peckmann et al., 2001). Nevertheless, the variable carbon isotopic composition of the samples indicating to a mixing processes between thermogenic and biogenic or fractionation of CH_4 while uprising. Whereas the siderite carbonates at Paola Ridge showed positive $\delta^{13}C$ values (from 3.2‰ to 10.6‰ V-PDB in Fig. 4.16), which suggest precipitation from ^{13}C-rich DIC. These positive $\delta^{13}C$ values can be considered as rather typical of precipitation in the methanogenic zone (e.g., Curtis and Coleman, 1986; Mozley and Wersin, 1992; Whiticar, 1999).

The $\delta^{18}O$ values of carbonate crusts and siderite carbonate range from 2.5‰ to 5.5‰ and 3.15‰ to 10.64‰ V-PDB respectively. At the average value of the present-day bottom water temperature (13.8 °C) and $\delta^{18}O$ value of water (1.5‰) in the Mediterranean Sea, the theoretical $\delta^{18}O$ values of calcite (Kim and O'Neil, 1997), aragonite (Kim et al., 2007), dolomite (Fritz and Smith, 1970) and siderite (Carothers et al., 1988) precipitated in isotopic equilibrium with seawater are expected to be of 1.5‰, 2.3‰, 5.1‰ and 5.6‰ (V-PDB), respectively. The $\delta^{18}O$

values obtained from the Paola Ridge carbonates are approach the theoretical values except for those of siderite, which are mostly enriched in ^{18}O by 3 to 4‰.

As the^{13}C enrichment of siderite can be explained with incorporation of heavy C derived from methanogenesis the enrichment of ^{18}O is more cumbersome. The ^{18}O enrichment in carbonates may be explained by different processes occurring in the sedimentary environment, as follows: 1) dissociation of gas hydrates that releases ^{18}O-rich water in the sediments (e.g. Bohrmann et al., 1998; Aloisi et al., 2000; Maekawa, 2004; Hein et al., 2006); 2) crustal/igneous CO_2 circulation (Muehlenbachs and Hodges, 1978; Clayton and Epstein, 1961; Cocker et al., 1982); 3) interaction with hydrothermal fluids that may yield values as high as 6.5‰ (Clayton and Epstein, 1961); 4) dehydration of clays minerals at great burial depths (Dählmann and de Lange, 2003); 5) precipitation of carbonates during glacial times when lower temperatures and isotopically heavier seawater caused a 3 to 4 ‰ $\delta^{18}O$-shift of carbonates in the Mediterranean Sea (e.g., Vergnaud-Grazzini, 1971). Other sources of heavy oxygen can be due to the circulation of deep crustal water (e.g. Lécuyer and Allemand, 1999).

At Paola Ridge, the presently venting of CO_2 (Tables 3.24, 3.25) suggests that the likely source of heavy oxygen isotopes can be related to deep fluids circulation (e.g. Clayton and Epstein, 1961; Lécuyer and Allemand, 1999; Lietard and Pierre, 2009). Particularly, the presence of CO_2-rich gas discharges, characterized by δ ^{13}C-CO_2 values slightly lower than -1‰ V-PDB, is apparently suggesting the presence of a deep (hydrothermal)-seated source feeding these gas vents. Such values are indeed similar to those found in the fumarolic gas discharges of the Island of Volcano (e.g., Paonita et al., 2002) and Solfatara, Somma-Vesuvius and related submarine emissions (e.g., Chiodini et al., 2001; Caliro et al., 2007; Vaselli et al., 2011; Passaro et al., 2016) and many gas vents distributed along the peri-Tyrrhenian strip (e.g., Minissale et al., 1997) of the Italian peninsula, whose origin is mainly related to thermometamorphic processes of marine limestone, although small contributions from magmatic cannot be excluded. Unfortunately, no He isotopes were analyzed to define the presence of a mantle input.

At Paola Ridge CO_2-rich-gas venting was only recorded along the mud volcanoe structures (RMV and R1MV) where siderite concretions occur. This co-occurrence suggests a genetic relation between CO_2 venting and siderite precipitation and therefore a likely ^{18}O enrichment of the iron carbonates related to crustal/igneous CO_2 circulation.

As far as the sampled waters are concerned, their chemical composition is approaching that of the oceanic water by Taylor and McLennan (1985), though a little bit more saline, as it is typical of relatively close basin such as the Mediterranean Sea. However, it is worth to mention that the concentrations of SO_4^{2-} are >20 % higher than that of the Mediterranean Sea. Similarly, the free-CO2 showed relatively high values with particular reference to the water sample MB14_BC10 (36.4 mmol L^{-1}), which also had the highest SO_4 content (~4,500 mg L^{-1}). This may indicate the presence of oxidation processes of H_2S, whose formation could be due to either a reduced environment or gas seeps. The latter hypothesis is apparently supported by the absence of H_2S in the analyzed gases.

Through the investigations conducted on venting gas and bottom seawater at Paola Ridge showed the absence of substantial concentrations of methane, this lack of methane suggests that the methane seepage, active for the last 10k year (40k years according to Rovere et al, 2015), is currently ceased.

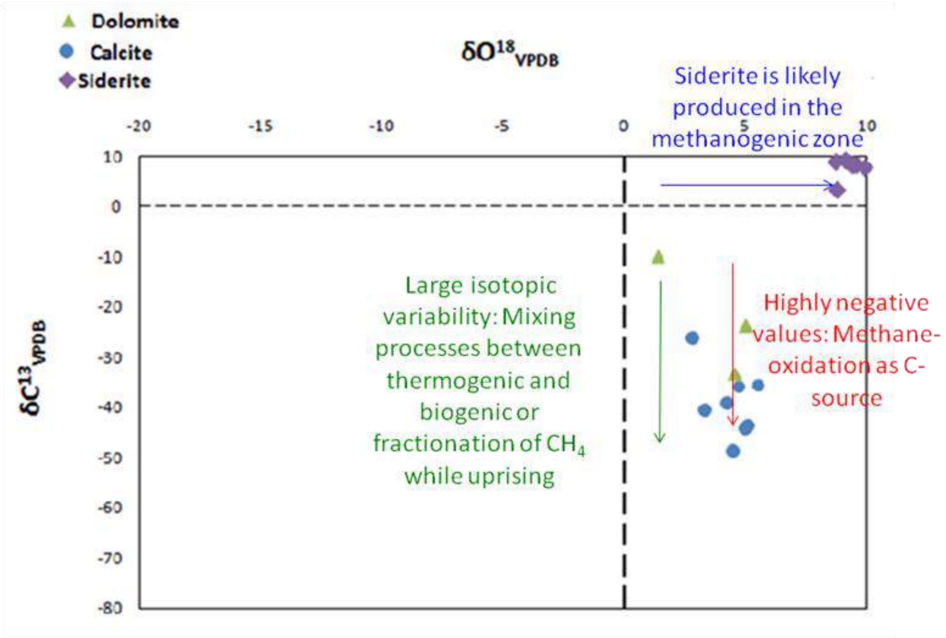

Figure 4.16- Carbon and oxygen compositions of carbonate crusts and siderite carbonates from the Paola Ridge.

The S stable isotope composition of the Paola Ridge pyrite showed δ^{32}S value (-32.7‰ CDT) comparable with those reported from the Black Sea authigenic pyrite (-37.4<δ^{32}S<-25.1‰, Calvert et al., 1996). This ^{32}S depletion coupled with shallow sub-bottom findings of pyrite burrows may suggest that S can be sourced from ^{32}S-depleted H_2S from the water column (Peckmann et al., 2001). Sulfur isotopic composition of pyrite and sulfur indicate that they were likley produced by bacterial reduction of marine sulfate within anoxic sediments.

Chapter 5: Conclusions

During two oceanographic cruises (2011 and 2014), high resolution swath bathymetry and backscatter data, seismic CHIRP profiles, multibeam water column acoustic measurements, coring and box coring samples were collected from deep-water cold seeps (500-1000 m) of the Paola Ridge, in the Southern Tyrrhenian Sea in order to carry out mineralogical, petrographic and geochemical analyses on both authigenic minerals (oxy-hydroxide, sulfide and carbonate samples) and mud samples. Water and gases were collected during the second cruise. Authigenic carbonates (calcite/aragonite and siderite) were sampled from shallow sub-bottom sediments. The calcite/aragonite concretions showed negative $\delta^{13}C$ (as low as -48.8‰ V-PDB) and positive $\delta^{18}O$ (up to 5.5‰ V-PDB) values, whereas siderite concretions were characterized by strong enrichment in both heavy carbon and oxygen isotope. The depleted $\delta^{13}C$ values with the presence of chemosymbiotic bivalves (*Lucinoma kazani*) suggested a precipitation of calcite and aragonite concretions within the AOM zone. The isotopic composition of siderite pointed to the precipitation within the methanogenic zone and was probably affected by intense crustal CO_2 venting (still ongoing) that induced sensible ^{18}O enrichment. At the Paola Ridge, along the RMV and R1MV structures, CO_2-rich gas discharges were indeed recognized and sampled. They were dominated by CO_2, whose carbon isotopic values were slightly <-1 ‰ V-PDB, suggesting the presence of a deep-seated source feeding these gas vents. Nevertheless, the Y/Ho chondritic ratio of both limestones and siderite may likely be indicating a clear influence of deep sited fluids.

Therefore, the results allowed to depict the depths of the biogeochemical zones of the sediments: i) an oxic zone at the bottom of the sea is a pavement made of amorphous oxides of Fe and goethite; ii) an AOM and sulfate reduction zone, located a few cm below the bottom of the sea as suggested by the significantly negative $\delta^{13}C$ values measured in the calcite/aragonite concretions; ii) a methanogenic zone, a few meters below the bottom of the sea where precipitation of iron carbonate (siderite) in the burrow occurs. The REE patterns showed that the precipitation of limestone and siderite occurred under different chemo-physical conditions.

The flat REE pattern and the absence of any Ce anomaly in the aragonite/calcite concretions suggested that the precipitation occurred under sub-oxic conditions, while the siderite REE patterns, characterized by LREE fractionation and lack of Ce anomaly, were likely indicating that siderite was precipitated under anoxic conditions. Finally, the presence of intense CO_2 venting along the two mounded morphologies (RMV and R1MV), previously described as mud volcanoes, and the presence the precipitation of siderite and iron sulfides indicated that RMV and R1MV structures were not related to seepage of biogenic or thermogenic methane.

As far as the mud samples are concerned, specifical geochemical parameters such as Al-Mg-Fe and Ti and Zr and their mineralogy indicated that their source was mostly related to a significant terrigeneous component.

In conclusion, this thesis provided new findings related to both the geological setting and morphology of the Paola Ridge, discriminating between authigenic minerals along the mud volcanoes and diapirs. However, it has to be pinpointed that one of the most striking results was the unexpected presence of a significant CO_2-venting from those morphologies that were considered as mud volcanoes and, consequently, dominated by a CH_4-rich gas phase. This is suggesting that, at least presently, the so-called mud volcanoes are fed by a deep (hydrothermal) source, possibly affected by a mantle signature, likely replacing (not timely constrained) a methane (thermogenically originated) source. Alternatively, it has to be modified the term of mud volcanoes for the RMV and R1MV structures and consider these morphologies as dome-like(?) structures related to preferred pathways for the gas migration to the surface, a feature common to other, structurally controlled hydrothermal systems, and possibly formed by gas pressurization at depth.

The multi-disciplinary approach carried out in the present PhD thesis has pointed out the importance of incrementing the geochemical investigations on sea sediments and authigenic minerals coupled with water and gas sampling in order to better characterized the depositional environments, particularly in areas such as the Tyrrhenian Sea. Its morphology is indeed relatively complex and resembles that of oceanic basins where an abyssal plain, numerous seamounts and active, quiescent and extinct volcanoes along with and continental shelves occur.

ACKNOWLEDGEMENTS

The realization of this thesis was only possible by the intervention of many people with their advice and their indications. Heartfelt thanks to my family, who has always been by my side and all my friends in Syria and Italy.

I would like to thank the University of Tishreen and Department of Earth Sciences-University of Florence for the support during the study period.

I want to thank the supervisor on my studies Dr. Mohammed Issa for his precious advices offered thoughout the coutse of study.

Special thanks to my Tutor and Co TuTors: Prof. Orlando Vaselli, Dr. Marzia Rovere, Dr. Fabiano Gamberi and Dr. Elena Pecchioni, because they are the people who have made this possible and they allowed me and spurred to new experiences.

I want also to thank Prof. Franco Tassi, Dr. Enrico Selmo (University of Parma), who helped me in the management of analytical part.

In addition, I thank researchers for their help: Dr. Samuele Ciattini, Dr. Luciano Giannini and Dr. Fulvio Franchi (Department of Earth and Environmental Sciences Botswana International University of Science and Technology (BIUST).

REFERENCES

Aharon P. (1994). Geology and biology of modern and ancient submarine hydrocarbon seeps and vents : An introduction. Geo-Marine Letters 14, 69-73.

Algeo T., Tribovillard N. (2009). Environmental analysis of paleoceanographic systems based on molybdenum–uranium covariation. Chem. Geol., 268, 211-225.

Al-Aasm I.S., Taylor B.E., South, B. (1990). Stable isotope analysis of multiple carbonate samples using selective acid extraction. Chem. Geol., 80:119−125.

Aloisi G., Pierre C., Rouchy J.-M., Foucher J.P., Woodside J. (2000). Methane-related authigenic carbonates of eastern Mediterranean Sea mud volcanoes and their possible relation to gas hydrate destabilisation. Earth Planet. Sci. Lett. 184, 321-338. Allwood A.C., Kamber B.S., Walter M.R., Burch I.W., Kanik I. (2010). Trace elements record depositional history of an Early Archean stromatolitic carbonate platform. Chem. Geol. 270, 148-163.

Argnani A., Trincard F. (1988). Paola Slope basin: evidence of regional contraction on the eastern Tyrrhenian margin. Mem. Soc. Geol. It., 44, 93-105.

Argnani A., Trincard F. (1993). Growth of a slope ridge and its control on sedimention: Paola slope basin (eastern Tyrrhenian margin). Spec. PublsInt. ASS. Sediment. 20, 467-480.

Arhangelski A. (1932). Some words about genesis of mud volcanoes on the Apsheron peninsula and Kerch–Taman area: Bull. MOIP, Ser. Geol, v. 3, p. 269-285.

Baker P.A., Kastner M. (1981). Constrains on the formation of sedimentary dolomite. Science 213 (4504), 214–216.

Banchelli A., Fratini F., Germani M., Malesani P., Manganelli Del Fa C. (1997). The sandstone of florentine historic buildings: individuation of the marker and determination of the rock used in some fiorentine monuments. Science and Technology for Cultural Heritage 6 (1), 13–22.

Barberi F., Gasparini P., Innocenti F., Villari L. (1973). Volcanism of the southern Tyrrenian sea and its geodynamic implications, J. Geophys. Res., 78, 5221-5232.

Barber A. J., Tjokrosapoetro S., Charlton T. R. (1986). Mud volcanoes, shale diapirs, wrench faults and me´langes in accretionary complexes, eastern Indonesia, *AAPG* Bull., 70, 1729–1741.

Barry J.P., Greene H.G., Orange D.L., Baxter C.H., Robison B.H., Kochevar R.E., Hybakken J.W., Reed D.L., McHugh C.M. (1996). Biologic and geologic characteristics of cold seeps in Monterey Bay, California. Deep-Sea Research, 43, 1739–1762.

Bau M. (1996). Controls on the fractionation of isovalent trace elements in magmatic and aqueous systems: evidence from Y/Ho, Zr/Hf, and lanthanide tetrad effect. Contrib. Mineral. Petrol. 123, 323-333.

Bau M., Dulski P. (1999). Comparing yttrium and rare earths in hydrothermal fluids from the Mid-Atlantic Ridge: implications for Y and REE behaviour during near-ventmixing and for the Y/Ho ratio of Proterozoic seawater. Chem. Geol. 155, 77-90.

Bau M., Koschinsky A. (2009). Oxidative scavenging of cerium on hydrous Fe oxide: evidence from the distribution of rare earth elements and yttrium between Fe oxides and Mn oxides in hydrogenetic ferromanganese crusts. Geochem. J. 43, 37-47.

Bau M., Koschinsky A., Dulski P., Hein J.R. (1996). Comparison of the partitioning behaviours of yttrium, rare earth elements, and titanium between hydrogenetic marine ferromanganese crusts and seawater. Geochim.Cosmochim.Acta 60, 1709-1725.

Bau M., Möller P., Dulski P. (1997). Yttrium and lanthanides in eastern Mediterranean seawater and their fractionation during redox-cycling. Mar. Chem. 56, 123-131.

Bayon G., German C.R., Burton K.W., Nesbitt R.W., Rogers N. (2004). Sedimentary Fe–Mnoxy-hydroxides as paleoceanographic archives and the role of aeolian flux in regulating oceanic dissolved REE. Earth Planet. Sci. Lett. 224, 477-492.

Bayon G., Dupré S., Ponzevera E., Etoubleau J., Chéron S., Pierre C., Mascle J.,

Beccaluva L., Rossi P. L., Serri G. (1982). Neogene to Recent volcanism of the southern Tyrrhenian-Sicilian area: Implications for the geodynamic evolution of the Calabrian arc, Earth Evol. Sci., 3, 222–238.

Beccaluva L., Gabbianelli G., Lucchini F., Rossi P. L., Savelli C. (1985). Petrology and K/Ar ages of volcanics dredged from the Eolian seamounts: Implications for geodynamic evolution of the southern Tyrrhenian basin, Earth Planet. Sci. Lett., 74(2), 187–208.

Beccaluva L., Bonatti E., Dupuy C., Ferrara G., Innocenti F., Lucchini F. (1990). Geochemistry and mineralogy of volcanic rocks from ODP sites 650, 651, 655, and 654 in the Tyrrhenian Sea. In: Stewart N.J. (Ed.), Proceedings of the Ocean Drilling Program, Scientific Results, vol. 107. U.S. Gov. Print. Off., Washington, D.C., pp. 49–74.

Behrens E.W. (1988). Geology of a continental slope oil seep, northern Gulf of Mexico. Bull. Am. Ass. Petrol. Geol. 72, 105-114.

Berner R.A. (1981). A new geochemical classification of sedimentary environments: Journal of Sedimentary Petrology, v. 51, p. 359-365.

Bhatia M.R., and Crook K.A.W. (1986). Trace element characteristics of graywackes and tectonic discrimination of sedimentary basins: Contributions to Mineralogy and Petrology, v. 92, p. 181–193.

Boetius A., DE lange G.J. (2013). Formation of carbonate chimneys in the Mediterranean Sea linked to deep-water oxygen depletion. Nat. Geosci. 6, 755-760.

Boetius A., Ravenschlag K., Schubert C.J., Rickert D., Widdel F., Giesecke A., Amann R., Jorgensen B.B., Witte U., Pfannkuche O. (2000). A marine microbial consortium apparently mediating anaerobic oxidation of methane. Nature 407, 623– 626.

Bohrmann G., Greinert J., Suess E., Torres M.E. (1998). Authigenic carbonates from the Cascadia subduction zone and their relation to gas hydrate stability. Geology 26, 647-650.

Bonardi G., Cavazza W., Perrone V., Rossi R. (2001). Calabria-Peloritani Terrane and Northern Ionian Sea. In: Vai, G.B., Martini, I.P. (Eds.), Anatomy of an Orogen: The Apennines and Adjacent Mediterranean Basins. Kluwer Academic Publishers,Dordrecht/Boston/London, pp. 287–306.

Bonini M., Tassi F., Feyzullayev A.A., Aliyev C.S., Capecchiacci F., Minissale A. (2013). Deep gases discharged from mud volcanoes of Azerbaijan: New geochemical evidence. Marine and Petroleum Geology 43, 450–463.

Bonini M. (2012). Mud volcanoes: Indicators of stress orientation and tectonic controls. Earth Sci. Rev. 115, 121-152.

Borowski W.S., Paull C.K., Ussler W. III. (1999). Global and local variations of interstitial sulfate gradients in deep-water, continental margin sediments: Sensitivity to underlying methane and gas hydrates. Mar. Geol. 159, 131-154.

Bouillin J.P., Durand-Delga M., Olivier P.H. (1986). Betic-Rifian and Tyrrhenian Arcs: distinctive features, genesis and development stages. In: Wezel, F.C. (Ed.), The Origin of Arcs. Elsevier Science, Amsterdam, pp. 281–304.

Brown K.M. (1990). The nature and hydrogeologic significance of mud diapirs and diatremes for accretionary systems: Journal of Geophysical Research: Solid Earth (1978–2012), v. 95, p. 8969-8982.

Brown K. M. (1990). The nature and hydrogeologic significance of mud diapir and diatremes for accretionary systems. Journal of Geophysical Research. 95, (B6), 8969-8982.

Brown K. M., Westbrook G. K. (1988). Mud diapirism and subcretion in the Barbados Ridge Complex, *Tectonics*, *7*, 613–640.

Burns S.J., Baker P.A. (1987). A geochemical study of dolomite in the Monterey Formation, California: Journal of Sedimentary Petrology, v. 57, p. 128–139.

Burton E.A. (1993). Controls on marine carbonate cement mineralogy: review and reassessment. Chemical Geology 105, 163–179.

Burton E.A., Walter L.M. (1987). Relative precipitation rates of aragonite and Mg calcite from seawater: temperature or carbonate ion control? Geology 15,111–114.

Burton E.A., Walter L.M.(1990). The role of pH in phosphate inhibition of calcite and aragonite precipitation rates in seawater. Geochimica et Cosmochimica Acta 54 (3), 797–808.

Byrne R.H., Liu X., Schijf J. (1996). The influence of phosphate coprecipitation on rare earth element distributions in natural waters.Geochim. Cosmochim. Acta 60, 3341-3346.

Caliro S., Chiodini G., Moretti R., Avino R., Granieri D., Russo M., Fiebig J. (2007). The origin of the fumaroles of La Solfatara (CampiFlegrei, South Italy). Geochim.Cosmochim.Acta, 71, 3040-3055.

Camerlenghi A., Cita M. B., Della Vedova B., Fusi N., Mirabile L., Pellis G. (1995). Geophysical evidence of mud diapirism on the Mediterranean Ridge accretionary complex, Mar. Geophys. Res., 17, 115–141.

Camerlenghi A., Pini GA. (2009). Mud volcanoes, olistostromes and Argille scagliose in the Mediterranean region. Sedimentology, 56, 319-365.

Campbell K.A., Nelson C.S., Alfaro A.C., Boyd S., Greinert J., Nyman S., Grosjean E., Logan G.A., Gregory M.R., Cooke S., Linke P., Milloy S., Wallis I. (2010). Geological imprint of methane seepage on the seabed and biota of the convergent Hikurangi Margin, New Zealand: Box core and grab carbonate results. Mar. Geol., 272, 285-306.

Cangemi M., Di Leonardo R., Bellanca A., Cundy A., Neri R., Angelone M. (2010). Chemical Geology 276, 294-308.

Carothers W.W., Adami L.H., Rosenbauer R.J. (1988). Experimental oxygen isotope fractionation between siderite-water and phosphoric acid liberated CO_2-siderite.Geochim. Cosmochim. Acta 52, 2445-2450.

Cella F., Fedi M., Florio G., Rapolla A. (1998). Optimal gravity modelling of the lithoasthenosphere system in Central Mediterranean. Tectonophysics 287 (1–4), 117–138.

Chen S.C., Hsu S.K., Wang Y., Chung S.H., Chen P.C., Tsai C.H., Lin H.S., Lee Y.W. (2014).Distribution and characters of the mud diapirs and mud volcan off southwest Taiwan, Journal of Asian Earth Sciences, v.92, p.201-214.

Chen Y., Matsumoto R., Paull C. K., Ussler III W., Lorenson T., Hart P., Winters W. (2007). Methane-derived authigenic carbonates from the northern Gulf of Mexico — MD02 Cruise. Journal of Geochemical Exploration 95, 1–15.

Childress J. J., Fisher C. R., Brooks J. M., Kennicutt M. C., II.Bidigare R., Anderson A. E. (1986). A methanotrophic marine molluscan (Bivalvia, Mytilidae) symbiosis: mussels fueled by gas. Science 233: 1306-1308.

Chiodini G., Marini L., Russo M. (2001). Geochemical evidence for the existence of high-temperature hydrothermal brines at Vesuvio volcano, Italy. Geochim.Cosmochim.Acta 65, 2129-2147.

Cipriani C. (1958) . Ricerche sui minerali costituenti le arenarie: I sulla composizione mineralogica della frazione argillosa di alcune arenarie Macigno, Atti della Società Toscana di Scienze Naturali 65 86–106.

Clayton R.N., Epstein S. (1961). The use of oxygen isotopes in high-temperature geological thermometry.J. Geol. 69, 447-452.

Cocker J.D., Griffin B.J., Muehlenbachs K. (1982). Oxygen and carbon isotope evidence for seawater-hydrothermal alteration of Macquarie Island ophiolite.Earth Plan. Sci. Lett. 61, 112-122.

Coleman D.F., Ballard R.D. (2001). A highly concentrated region of cold hydrocarbon seeps in the southeastern Mediterranean Sea. Geo-Marine Letters 21, 162–167.

Coleman M.L. (1993). Microbial processes: Controls on the shape and composition of carbonate concretions. Mar. Geol. 113, 127-140.

Coleman M.L., (1985). Geochemistry of diagenetic non-silicate minerals: Kinetic considerations, in Eglinton, G., et al., eds., Geochemistry of buried sediments: London, Royal Society, p. 39-54.

Curtis C.D., Coleman M.L. (1986). Controls on the precipitation of early diagenetic calcite, dolomite, and siderite concretions in complex depositional sequences. In: Gautier, D.L. [Ed.], Roles of organic matter in sediment diagenesis: Society of Economic Paleontologists and Mineralogists Special Publication 38, 23-33.

Curtis C.D., Petrowski C., Ortel G. (1972). Stable carbon isotope ratios within carbonate concretions: a clue to place and time of formation. Nature 235, 98-100.

Dalla Valle G., Gamberi F. (2011). Pockmarks and seafloor instability in the Olbia continental slope (northeastern Sardinian margin, Tyrrhenian Sea). Marine Geophysical Research 32, 193–205.

Dählmann A., de Lange G.J. (2003). Fluid–sediment interactions at Eastern Mediterranean mud volcanoes: a stable isotope study from ODP Leg 160. Earth Planet. Sci. Lett. 212, 377-391.

De Astis G., Ventura G., Vilardo G. (2003). Geodynamic significance of the Aeolian volcanism (Southern Tyrrhenian Sea, Italy) in light of structural, seismological, and geochemical data, Tectonics, 22(4), 1040, doi:10.1029/2003TC001506.

D'Hondt S., Rutherford S., Spivack A.J. (2002). Metabolic activity of subsurface life in deep-sea sediments. Science, 295, 2067-70.

DeMets C., Gordon R.G., Argus D.F., Stein S. (1990). Current plate motions, Geophys. J. Int. 101, 425–478.

Dewey J.F., Helman M.L., Turco E., Hutton D.H.W., Knott S.D. (1989). Kinematics of the western Mediterranean. Alpine Tectonics. Geological Society of London Special Publication, 45, 265–283.

Dilek Y., 2006. Collision tectonics of the Mediterranean region: Causes and consequences. Geological Society of America, 409, 1-13.

Dimitrov LI. (2002). Mud volcanoes—the most important pathway for degassing deeply buried sediments. Earth Sci Rev 59:49–76.

Dimitrov L., Woodside J. (2003). Deep sea pockmark environments in the eastern Mediterranean. Mar. Geol. 195(1-4): 263-276.

Doglioni C., Gueguen E., Harabaglia P., Mongelli F. (1999). On the origin of W-directed subduction zones and applications to the western Mediterranean. Geological Society of London Special Publication 156, 541–561.

Dunham R. J. (1962). Classification of carbonate rocks according to depositional texture. In: Ham, W. E. (ed.), Classification of carbonate rocks: American Association of Petroleum Geologists Memoir, p. 108- 121.

Dymond J. (1981) Geochemistry of Nazca plate surface sediments: An evaluation of hydrothermal, biogenic, detrital, and hydrogenous sources. Mem. Geol. Soc. Am 154, 133–173.

Elderfield H., Upstill-Goddard R., Sholkovitz E.R. (1990). The rare earth elements in rivers, estuaries and coastal sea waters: processes affecting crustal input of elements to the ocean and their significance to the composition of sea water. Geochim. Cosmochim. Acta 54, 971-991.

Embry A.F., Klovan J.E. (1971). A Late Devonian reef tract on Northeastern Banks Island, NWT: Canadian Petroleum Geology Bulletin, v. 19, p. 730-781.

Fabbri A., Gallignani P., Zitellini N. (1981). Geological evolution of the peri-Tyrrhenian sedimentary basins, in Sedimentary Basins of Mediterranean Margins, edited by F. C. Wezel, pp. 101–126, Tecnoprint, Bologna, Italy.

Faccenna C., Piromallo C., Crespo-Blanc A., Jolivet L., Rossetti F. (2004). Lateral slab deformation and the origin of the western Mediterranean arcs. Tectonics 23, TC1012, 10.1029/2002TC001488.

Faccenna C., Becker T.W., Lucente F.P., Jolivet L., Rossetti F. (2001). History of subduction and back-arc extension in the Central Mediterranean, Geophys. J. Int. 145 (2001) 809– 820.

Faggion O., Pinna E., Savelli C., Schreider A.A. (1995). Geomagnetism and age study of Tyrrhenian seamounts. Geophysical Journal International 123 (3), 915–930.

Federico L., Capponi G., Crispini L., Scambelluri M. (2004). Exhumation of alpine high-pressure rocks: insights from petrology of eclogite clasts in the Tertiary Piedmontese basin (Ligurian Alps, Italy). Lithos 74, 21–40.

Feng D., Chen D., Peckmann J. (2009). Rare earth elements in seep carbonates as tracers of variable redox conditions at ancient hydrocarbon seeps. Terra Nova 21, 49-56.

Feng R., Kerrich R. (1990). Geochemistry of Fine-Grained Clastic Sediments in the Archean Abitibi Greenstone Belt, Canada: Implications for Provenance and Tectonic Setting. Geochimica et Cosmochimica Acta, 54, 1061-1081.

Fisher C.R. (1990). Chemoautotrophic and methanotrophic symbioses in marine invertebrates. Reviews in Aquatic Sciences 2 (3/4), 399–436.

Floyd D R.S., Leveridge B.E., Franke W. (1991). Geochemistry and provenance of Rhenohercynian synorogenic sandstones: implications for tectonic environment discrimination, in Morton, A.C., Todd, S.P., and Haughton, P.D.W., eds., Developments in Sedimentary Provenance Studies: Geological Society of London, Special Publication 57, p. 173–188.

Franchi F., Hofmann A., Cavalazzi B., Wilson A., Barbieri R. (2015). Differentiating marine vs hydrothermal processes in Devonian carbonate mounds using rare earth elements (Kess Kess mounds, Anti-Atlas, Morocco). Chem. Geol. 409, 69-86.

Franchi F., Turetta C., Cavalazzi B., Corami F., Barbieri R. (2016). Trace elements and REE geochemistry of Middle Devonian carbonate mounds (Maïder Basin, Eastern Anti-Atlas, Morocco): Implications for early diagenetic processes. Sed. Geol. 343, 56-71.

Franchi F., Rovere M., Gamberi F., Rashed H., Vaselli O., Tassi F., Zabel M. (2016). Tracing fluid composition and carbonate diagenesisalong Paola ridge (southern Tyrrhenian Sea): methane seepage*vs* CO_2 vent. Submitted to Marine Chemistry.

Francalanci L., Avanzinelli R., Nardini I., Tiepolo M., J. P. Davidson J. P., Vannucci R. (2012). Crystal recycling in the steady-state system of the active Stromboli volcano: A 2.5-ka story inferred from in situ Sr-isotope and trace element data, Contrib. Mineral. Petrol., 163(1), 109– 131, doi:10.1007/s00410-011-0661-0.

Francalanci L., Avanzinelli R., Tommasini S., Heuman A. (2007). A west-east geochemical and isotopic traverse along the volcanism of the Aeolian Island arc, southern Tyrrhenian Sea, Italy: Inferences on mantle source processes, Geol. Soc. Am. Spec. Pap., 418, 235–263, doi:10.1130/2007.2418(12).

Fritz P., Smith D.G.W. (1970). The isotopic composition of secondary dolomites.Geochim.Cosmochim.Acta 34, 1161-1173.

Fritz P., Binda P.L., Folinsbee F.E., Krouse H.R. (1971). Isotopic composition of diagenetic siderites from Cretaceous sediments in Western Canada. J. Sediment. Petrol. 41, 282-288.

Gamberi F., Rovere M. (2010). Mud diapirs,mud volcanoes and fluid flowing: the rear of the Calabrian Arc Orogenic Wedge (southeastern Tyrrhenian Sea). Basin Res. 22, 452-464.

Garver J.I., Scott T.J. (1995). Trace elements in shale as indicators of crustal provenance and terrane accretion in the southern Canadian Cordillera: Geological Society of America, Bulletin, v. 107, p. 440–453.

Geletti R., Del Ben A., Busetti M., Ramella R., Volpi V. (2008). Gas seeps linked to salt structures in the Central Adriatic Sea basin. Basin Research 20 (4), 473–487.

German C.R., Elderfield H. (1990). Application of the Ce anomaly as a paleoredox indicator: the ground rules. Paleoceanography 5, 823-83.

Ghisetti, F., Vezzani, L., 1982. Strutture tensionali e compressive indotti da meccanismi profondi lungo la linea del Pollino (Appennino meridionale). Bollettino della Società Geologica Italiana 101, 385–440.

Ghisetti F., Pezzino A., Atzori P., Vezzani, L. (1991). Un approccio strutturale per la definizione della linea di Taormina: Risultati preliminari: Memorie della Società Geologica Italiana, v. 47, p. 273–289.

Ghisetti F. (1979). Evoluzione neotettonica dei principali sistemi di faglie della Calabria centrale (Neotectonic evolution of main fault systems of Central Calabria). Boll. Soc. Geol. It. 98, 387–430.

Ginsburg G., Soloviev V. (1994). Mud volcano gas hydrates in the Caspian Sea: Bulletin of the Geological Society of Denmark, v. 41, p. 100.

Goes S., Giardini D., Jenny S., Hollenstein C., Kahle H.G., Geiger A. (2004). A recent tectonic reorganization in the south-central Mediterranean. Earth and Planetary Science Letters 226, 335– 345.

Goldstein S.J., Jacobsen S.B. (1988). Rare earth elements in river waters.Earth Planet. Sci. Lett. 89, 35-47.

Grandjacquet C., Mascle G. (1978). The structure of the Ionian Sea, Sicily and Calabria-Lucania. In Nairn A.E.M., Kanes W.H., Stehli F.G. Eds. – The Ocean Basins and Margins, 4b, 257-329.

Greinert J., Bohrmann G., Suess E. (2001). Gas hydrate-associated carbonates and methane-venting at Hydrate Ridge: classification, distribution, and origin of authigenic lithologies. In: Paull C.K., Dillon W.P. (Eds.), Natural Gas Hydrates—Occurrence, Distribution, and Dynamics, vol. 124. American Geophysical Union, Washington, D.C., pp. 99– 113.

Guarnieri P. (2006). Plio-Quaternary segmentation of the south Tyrrhenian forearc basin. Int J Earth Sci (Geol Rundsch), 95, 107–118.

Gubkin I., Feodorov S. (1940). Mud volcanoes of the USSR in connection with oil and gas prospects: Proc 27th Int Geology Congr, Moscow, part, v. 4, p. 33- 67.

Guliyev IS., Feizullayev AA. (1997). All about mud volcanoes. Nafta Press, Baku.

Gvirtzman Z., Nur A. (2001). Residual topography, lithospheric structure and sunken slabs in the central Mediterranean, Earth Planet. Sci. Lett., 187, 117 – 130.

Haley B.A., Klinkhammer G.P., McManus J. (2004). Rare earth elements in pore waters of marine sediments.Geochim.Cosmochim.Acta 68, 1265-1279.

Hein J.R., Normark W.R., McIntyre B.R., Lorenson T.D., Powell II C.L. (2006). Methanogenic calcite, ^{13}C-depleted bivalve shells, and gas hydrate from a mud volcano offshore southern California. Geology 34, 109-112.

Helz G.R., Miller C.V., Charnock J.M., Mosselmans J.F.W., Pattrick R.A.D., Garner C.D., Vaughan D.J. (1996). Mechanism of molybdenum removal from the sea and its concentration in black shales: EXAFS evidence. Geochim.Cosmochim.Acta 60, 3631-3642.

Higgins GE., Saunders JB. (1974) Mud volcanoes—their nature and origin. Verhandl Naturf Ges Basel 84:101–152.

Himmler T., Bach W., Bohrmann G., Peckmann J. (2010). Rare earth elements in authigenic methane-seep carbonates as tracers for fluid composition during early diagenesis. Chem. Geol. 277, 126-136.

Horvath F., Berckhemer H., Stegena L. (1981). Models of Mediterranean back-arc basin formation. Phil. Trans. R. Soc. Lond. 300, 383-402.

Hovland, M., Judd A. (1988). Seabed Pockmarks and Seepages, Trottman, New York.

Hovland M., Talbot MR., Qvale H., Olaussen S., Aasberg L. (1987). Methane-related carbonate cements in pockmarks of the North Sea. J Sediment Petrol 57:881–892.

Hovland M., Judd A. G., King L. H. (1984). Characteristic features of pockmarks on the north sea floor and scotian shelf, Sedimentology, 31, 471–480.

Hovland M., Gardner J.V., Judd A.G. (2002). The significance of pockmarks to understanding fluid flow processes and geohazards. Geofluids 2, 127-136.

Hu Y., Feng D., Peckmann J., Roberts H.H., Chen D. (2014). New insights into cerium anomalies and mechanisms of trace metal enrichment in authigenic carbonate from hydrocarbon seeps. Chem. Geol. 381, 55-66.

Ivanov M., Limonov A., Van Weering T.C. (1996). Comparative characteristics of the Black Sea and Mediterranean Ridge mud volcanoes: Marine geology, v. 132, p. 253-271.

Jakubov A. A., Ali-Zade A. A., Zeinalov M. M. (1971). Mud Volcanoes of the Azerbaijan SSR, 257 pp., Acad. of Sci. of the Azerbaijan SSR, Baku, Azerbaijan.

Jean M., Chaumillon E. (1997). From foreland to forearc domains: New multichannel seismic reflection survey of the Mediterranean ridge accretionary complex (Eastern Mediterranean). Marine Geology. 138. 237-259.

Jerosch K., Schlüter M., Foucher J.P., Allais A.G., Klages M., Edy C. (2007). Spatial distribution of mud flows, chemoautotrophic communities, and biogeochemical habitats at Håkon Mosby Mud Volcano. Marine Geology, 243, 1–17.

Jolivet L. (1990). Extension of thickened continental crust, from brittle to ductile deformation: Examples from Alpine Corsica and Aegean Sea: Annali di Geofisica, v36, p. 139- 153.

Jolivet L., Faccenna C. (2000). Mediterranean extension and the Africa-Eurasia collision. Tectonics. 19, 1095-1107.

Judd A., Hovland M. (2007). Seabed fluid flow, the impact on Geology, Biology, and the Marine Environment. University Press, Cambridge.

Kaluza M.J., Doyle E.H. (1996). Detecting fluid migration in shallow sediments: continental slope environment, Gulf of Mexico. In: Schumacher, D., Abrams, M.A. (Eds.), Hydrocarbon Migration and its Near-surface Expression. AAPG Memoir, vol. 66. Tulsa, OK, pp. 15–26.

Kamber B.S., Bolhar R., Webb G.E. (2004). Geochemistry of late Archaean stromatolites from Zimbabwe; evidence for microbial life in restricted epicontinental seas. Precambrian Res. 132, 379-399.

Kastens K.A., et al. (1988). ODP Leg 107 in the Tyrrhenian Sea: insights into passive margin and back-arc basin evolution. Geol. Soc. Am. Bull. 100, 1140–1156.

Kastens K.A. (1990). Proceedings of the Ocean Drilling Program. Scientific results, vol. 107. Ocean Drilling Program, College Station, Texas. 722 pp.

Kelts K., McKenzie J.A. (1984). A comparison of anoxic dolomite from deep-sea sediments: Quaternary Gulf of California and Messinian Tripoli Formation of Sicily, in Garrison, R.E., et al., eds., Dolomites of the Monterey Formation and other organic-rich units: Pacifi c Section, SEPM (Society for Sedimentary Geology) Special Publication 41, p. 19–28.

Kim S.-T., O'Neil J.R. (1997). Equilibrium and nonequilibrium oxygen isotope effects in synthetic carbonates.Geochim.Cosmochim.Acta 61, 3461-3475.

Kim S.-T., O'Neil J.R., Hillaire-Marcel, C., MucciA. (2007). Oxygen isotope fractionation between synthetic aragonite and water: Influence of temperature and Mg^{2+} concentration. Geochim.Cosmochim.Acta 71, 4704-4715.

Kim J.-H., Torres M.E., Haley B.A., Kastner M., Pohlman J.W., RiedelvM., Lee Y.J. (2012). The effect of diagenesis and fluidmigration on rare earth element distribution in pore fluids of the northern Cascadia accretionary margin. Chem. Geol. 291, 152-165.

Klaver M., Djuly T., Graaf S., Sakes A., Wijbrans J., Davies G., Vroon P. (2015). Temporal and spatial variations in provenance of Eastern Mediterranean Sea sediments: Implications for Aegean and Aeolian arc volcanism. Geochimica et Cosmochimica Acta. 153, 149–168.

Klinkhammer G.P., Elderfield H., Edmond J.M., Mitra A. (1994). Geochemical implications of rare earth element patterns in hydrothermal fluids from mid-ocean ridges.Geochim.Cosmochim.Acta 58, 5105-5113.

Klug H. P., Alexander L.E. (1969). Diffrazione dei raggi X : metodi per le sostanze policristalline e amorfe. Ed. Alba, Torino 1969.

Knott D., Turco E. (1991). Late Cenozoic kinematics of the Calabrian Arc. Tectonics, 10 (6), 1164–1172.

Kobayashi K. et al. (1992). Deep-tow survey in the Kaiko-Nankai cold seepage areas, Earth Planet. Sci. Lett., 109, 347–354.

Kopf A., Robertson A. H. F., Clennell M. B., Flecker R., (1998). Mechanism of mud extrusion on the Mediterranean Ridge, Geo Mar. Lett., *18*, 97–114.

Kopf A. (2002). Significance of mud volcanism. Rev. Geophys.,40, 1-51.

Krastel S., Spiess V., Ivanov M., Weinrebe W., Bohrmann G., Shashkin P., Heidersdorf F. (2003). Acoustic investigations of mud volcanoes in the Sorokin Trough, Black Sea: Geo-Marine Letters, v. 23, p. 230-238.

Krijgsman W., Blanc-Valleron M.M., Flecker R., Hilgen F.J., Kouwenhoven T.J., Merle D., Orszag-Sperber F., Rouchy J.M. (2002). The onset of the Messinian salinity crisis in the Eastern Mediterranean (Pissouri Basin, Cyprus). Earth and Planetary Science Letters, 194, 299-310.

LaMaskin T.A., Dorsey R.J., Vervoort J.D. (2008). Tectonic controls on mud rock geochemistry, Mesozoic rocks of Eastern Oregon and Western Idaho, U.S.A.: implications for cordilleran tectonics. J. Sed. Geol., 78, 765-783.

Lance S., Henry P., Le Pichon X., Lallemant S., Chamley H., Rostek F., Faugères J.-C., Gonthier E., Olu K. (1998). Submersible study of mud volcanoes seaward of the Barbados accretionary wedge: sedimentology, structure and rheology: Marine Geology, v. 145, p. 255-292.

Lawrence M.G., Greig A., Collerson K.D., Kamber B.S. (2006). Rare Earth Element and Yttrium Variability in South East Queensland Waterways.Aquat.Geochem. 12, 39-72.

Lécuyer C., Allemand P. (1999). Modelling of the oxygen isotope evolution of seawater: Implications for the climate interpretation of the δ^{18}O of marine sediments.Geochim.Cosmochim.Acta 63, 351-361.

Leloup J., Loy A., Knab N.J., Borowski C., Wagner M., Jørgensen B.B. (2007). Diversity and abundance of sulfate-reducing microorganisms in the sulfate and methane zones of a marine sediment, Black Sea. Environ. Microbiol. 9, 131-42.

León R., Somoza L., Medialdea T., González F.J., Díaz del Río V., Fernández-Puga M.C., Maestro A., Mata M.P. (2007). Sea-floor features related to hydrocarbon seeps in deepwater carbonate-mud mounds of the Gulf of Cádiz: from mud flows to carbonate precipitates. Geo-Mar. Lett. 27 (2–4), 237–247.

Lietard C., Pierre C. (2009). Isotopic signatures (δ^{18}O and δ^{13}C) of bivalve shells from cold seeps and hydrothermal vents.Geobios 42, 209-219.

Limonov A., Van Weering T.C., Kenyon N., Ivanov M., Meisner L. (1997). Seabed morphology and gas venting in the Black Sea mudvolcano area: observations with the MAK-1 deep-tow sidescan sonar and bottom profiler: Marine Geology, v. 137, p. 121-136.

Limonov A., Woodside J., Cita M., Ivanov M. (1996). The Mediterranean Ridge and related mud diapirism: a background: Marine Geology, v. 132, p. 7-19.

Maclean W.H. (1990). Mass change calculations in altered rock series: Mineralium Deposita, v. 25, p. 44–49.

MacDonald IR., Boland GS., Baker JS., Brooks JM., Kennicutt MC II., Bidigare RR. (1989). Gulf of Mexico hydrocarbon seep communities. 11. Spatial distribution of seep organisms and hydrocarbons at Bush Hill. Mar Biol 101, 235-247.

Maekawa T., (2004). Experimental study on isotopic fractionation in water during gas hydrate formation.Geochem. J. 38, 129-138.

Magalhães V.H., Pinheiro L.M., Ivanov M.K., Kozlova E., Blinova V., Kolganova J., Vasconcelos C., McKenzie J.A., Bernasconi S.M., Kopf A.J., Díaz-del-Río V., González F.J., Somoza L. (2012). Formation processes of methane-derived authigenic carbonates from the Gulf of Cadiz. Sediment. Geol. 243-244, 155-168.

Malinverno A., Ryan W.B.F. (1986). Extension in the Tyrrhenian Sea and shortening in the Apennines as result of arc migration driven by slab sinking in the lithosphere. Tectonics, 5, 227-245.

Mansour A.S., Sassen R. (2011). Mineralogical and stable isotopic characterization of authigenic carbonate from a hydrocarbon seep site, Gulf of Mexico slope: Possible relation to crude oil degradation. Marine Geology, 281 (1), 59-69.

Martinelli G. (1998). Mud volcanoes of Italy. Proceedings of V Int. Conference on ‘’Gas in Marine Sediments’’, Bologna 9 – 12 September, Italy, pp. 40–42.

Martinez N., Murray R., Thunell R., Peterson L., Mullerkarger F., Astor Y., Varela R. (2007). Modern climate forcing of terrigenous deposition in the tropics (Cariaco Basin, Venezuela). Earth Planet. Sci. Lett. 264 (3–4), 438–451.

Martinelli G., Judd A. (2004). Mud volcanoes of Italy: Geological Journal, v. 39, p. 49-61.

Matsumoto R. (1989). Isotopically heavy oxygen-containing siderite derived from the decomposition of methane hydrate. Geology. 17, 707-710.

Mazzoli S., Helman M. (1994). Neogene patterns of relative plate motion for Africa–Europe: some implications for recent central Mediterranean tectonics Geol. Rund., 83 (1994), pp. 464–468.

Mazurenko L.L., Soloviev V.A., Gardner J.M., Ivanov M.K. (2003). Gas hydrates in the Ginsburg and Yuma mud volcano sediments (Moroccan margin): results of chemical and isotopic studies of pore water. Mar. Geo!. 195, 201-210.

Mclennan S.M. (1993). Weathering and global denudation: Journal of Geology, v. 101, p. 295–303.

Milkov A.V. (2000). Worldwide distribution of submarine mud volcanoes and associated gas hydrates. Marine Geology, 167, 29–42.

Minissale A., Magro G., Vaselli O., Verrucchi C., Perticone I. (1997). Geochemistry of water and gas discharges from the Mt. Amiata silicic complex and surrounding areas (central Italy). J. Vulcanol. Geotherm. Res. 79, 223-251.

Moore S.E., Ferrell R.E. Aharon P. (1992). Diagenetic siderite and other ferroan carbonates in a modern subsiding marsh sequence. J. Sediment. Petrol, 62:357-366.

Morita S., Ashi J., Aoike K., Kuramoto S. (2004). Evolution of Kumano basin and sources of clastic ejecta and pore fluid in Kumano mud volcanoes, Eastern Nanaki Trough, In: Proceedings of the International Symposium on Methane Hydrates and Fluid Flow in Upper Accretionary Prisms, Engineering Geology Laboratory, Department of Civil & Earth Resources Engineering, Kyoto University, Kyoto, pp. 92–99.

Morse J.W., Wang Q., Tsio M.Y. (1997). Influence of temperature and Mg:Ca ratio on CaCO3 precipitates from seawater. Geology 25 (1), 85–87.

Morse J.W. (1994). Interactions of trace metals with authigenic sulfide minerals: Implications for their biovavailability. Mar Chem. 46, 1-6.

Mozley P.S., Burns S.J. (1993). Oxygen and carbon isotopic composition of marine carbonate concretions: an overview: Journal of Sedimentary Petrology, v. 63, p. 73–83.

Mozley P.S., Carothers W.W. (1992). Elemental and isotopic composition of siderite in the Kuparuk Formation, Alaska: Effect of microbial activity and water/sediment interaction on early pore-water chemistry: Journal of Sedimentary Petrology, v. 62 (in press).

Mozley P.S., Wersin P., (1992). Isotopic composition of siderite as an indicator of depositional environment. Geology 20, 817-820.

Muehlenbachs K., Hodges F.N. (1978). Oxygen isotope geochemistry of rocks from DSDP LEG 46.In. Reps. DSDP 46, 257-259.

Murata K.J., Friedman I., Madsen B.H. (1969).Isotopic composition of diagenetic carbonates in marine Miocene formations of California and Oregon: U.S. Geological Survey Profressional Paper, v. 614B, p. 1–24.

Murray R.W., Buchholtz ten Brink M.R., Gerlach D.C., Price Russ III G., Jones D.L. (1991). Rare earth, major, and trace elements in chert from the Franciscan Complex and Monterey Group, California: assessing sources to fine-grained marine sediments. Geochim.Cosmochim.Acta 55, 1875-1895.

Naehr T.H., Rodriguez N.M., Bohrmann G., Paull C.K., Botz R. (2000). Methane-derived authigenic carbonates associated with gas hydrate decomposition and fluid venting above the Blake Ridge diaper. In: Paull, C.K., Matsumoto, R., Wallace, P.J., Dillon W.P. (Eds.), Proc. ODP Sci. Res., vol. 164, pp. 285–300.

Nesbitt H. W., Young G. M. (1984). Prediction of some weathering trends of plutonic and volcanic rocks based on thermodynamic and kinetic considerations. Geochim. Cosmochim. Acta 48, 1523–1534.

Nesbitt H. W., Young G. M. (1996). Petrogenesis of sediments in the absence of chemical weathering: effects of abrasion and sorting on bulk composition and mineralogy. Sedimentology 43, 341–358.

Nesbitt H. W., Young G. M., McLennan S. M., Keays R. R. (1996). Effects of chemical weatheringand sorting on the petrogenesis of siliciclastic sediments, with implications for provenance studies. J. Geol. 104, 525–542.

Neubert N., Nagler T.F., Böettcher M.E. (2008). Sulfidity controls molybdenum isotope fractionation into euxinic sediments: evidence from the modern Black Sea. Geology 36, 775-778.

Neurauter T. W., Roberts H. H. (1994). Three generations of mud volcanoes on the Louisiana continental slope, Geo-Mar. Lett., 14, 120–125.

Neurauter T. W. Bryant W. R. (1990). Seismic expression of sedimentary volcanism on the continental slope, Northern Gulf of Mexico, Geo-Marine Letters, 10, 225-231.

Nicolich R. (1989). Crustal strcuture from seismic studies in the frame of the European Geotraverse (southern segment) and CROP Projects. In: The Lithosphere in Italy (Boriani A., Bonafede M., Piccardo G. B., Vai G. B., eds), Advances in Earth Science Research, Italian National Committee for the International Lithosphere Program, Atti Convegni Lincei, 80, pp. 41–61.

Nicolich R., Dal Piaz G.V. (1991). Moho isobaths. Structural Model of Italy. Scale 1: 500,000. Quaderni de La Ricerca Scientifica, 114, 3, CNR, P.F. Geodinamica.

Niemann H., Elvert M., Hovland M., Orcutt B., Judd A., Suck I., GUTT J., JOYE S., Damm E., Finster K., Boetius A. (2005). Methane emission and consumption at a North Sea gas seep (Tommeliten area). Biogeosciences. 2, 335-351.

Nozaki Y., Zhang J., Amakawa H. (1997). The fractionation between Y and Ho in the marine environment.Earth Planet. Sci. Lett. 148, 329-340.

Nothdurft L.D., Webb G.E., Kamber B.S. (2004). Rare earth element geochemistry of Late Devonian reefal carbonates, Canning Basin, Western Australia: confirmation of a seawater REE proxy in ancient limestones. Geochim.Cosmochim.Acta 68, 263-283.

Nyakairu W.A., Koeberl C. (2001). Mineralogical and chemical composition and distribution of rare earth elements in clay-rich sediments from central Uganda. Geochemical Journal, Vol. 35, pp. 13 to 28, 2001.

Olivier N., Boyet M. (2006). Rare earth and trace elements of microbialites in Upper Jurassic coral- and sponge-microbialite reefs.Chem. Geol. 230, 105-123.

Olu-Le Roy K., Sibuet M., Fiala-Médioni A., Gofas S., Salas C., Mariotti A., Foucher J.P., Woodside J. (2004). Cold seep communities in the deep eastern Mediterranean Sea: composition, symbiosis and spatial distribution on mud volcanoes. Deep-Sea Research I 51:1915-1936.

Ondréas H., Olu K., Fouquet Y., Charlou J.L., Gay A., Dennielou B., Donval J.P., Fifis A., Nadalig T., Cochonat P., Cauquil E., Bourillet J.F., Le Moigne M., Sibuet M. (2005). ROV study of a giant pockmark on the Gabon continental margin. Geo-Mar Lett 25:281-292.

Paonita A., Favara R., Nuccio P.M., Sortino F. (2002). Genesis of fumarolic emissions as inferred by isotope mass balances: CO2 and water at Vulcano Island, Italy. Geochim. Cosmochim. Acta, 66, 759-772.

Passaro S., Tamburrino S., Vallefuoco M., Tassi F., Vaselli O., Giannini L., Chiodini L., Caliro S., Sacchi M., Rizzo A.L., Ventura G. (2016). Seafloor doming driven by degassing processes unveils sprouting volcanism in coastal areas. Sci. Rep. 6, 22448; doi: 10.1038/srep22448.

Paull C.K., Chanton J.P., Neumann A.C., Coston J.A., Martens C.S. (1992). Indicators of Methane-Derived Carbonates and Chemosynthetic Organic Carbon Deposits: examples from the Florida Escarpment. Palaios. 7, 361-375.

Paull C.K., Ussler III W.S., Peltzer E.T., Brewer P.G., Keaten R., Mitts P.J., Nealon J.W., Greinert J., Herguera J., Perez M.E. (2007). Authigenic carbon entombed in methane-soaked sediments from the northeastern transform margin of the Guaymans Basin, Gulf of Calofornia. Deep-Sea Reaearch II 54, 1240-1267.

Peckmann J., Thiel V. (2004). Carbon cycling at ancient methane-seeps. Chemical Geology 205, 443-467.

Peckmann J., Reimer A., Luth U., Luth C., Hansen B.T., Heinicke C., Hoefs J., Reitner J. (2001). Methane-derived carbonates and authigenic pyrite from the northwestern Black Sea. Mar. Geol. 177, 129-150.

Petersen N.T., Smith P.L., Mortnsen J.K., Creaser R.A., Tipper H.W. (2004). Provenance of Jurassic sedimentary rocks of south-central Quesnellia, British Columbia: implications for paleogeography: Canadian Journal of Earth Sciences, v. 41, p. 103–125.

Pepe F., Sulli A., Bertotti G., Cella F. (2010). Architecture and Neogene to Recent evolution of the western Calabrian continental margin: An upper plate perspective to the Ionian subduction system, central Mediterranean. Tectonics, 29, TC3007, doi:10.1029/2009TC002599.

Pisciotto K.A., Mahoney J.J. (1981). Isotopic survey of diagenetic carbonates, in Yeats, R.S., et al., Initial reports of the Deep Sea Drilling Project, Volume 63: Washington, D.C., U.S. Government Printing Office, p. 595–609.

Plank T. (2013). The chemical composition of subducting sediments. In The Crust, Treatise on Geochemistry, vol. 4.

Plank T., Langmuir C. H. (1998). The chemical composition of subducting sediment and its consequences for the crust and mantle. Chem. Geol. 145, 325–394.

Postma D. 1982. Pyrite and siderite formation in brackish and freshwater swamp sediments. Am. J. Sci. 282:1151–1183.

Pye K., Dickson J.A.D., Schiavon N., Coleman M.L., Cox M. (1990). Formation of siderite—Mg-calcite-iron sulphide concretions in intertidal marsh and sandflat sediments, north Norfolk, England: Sedimentology, v. 37, p. 325-343.

Raccomandazione NorMal 34/91 Analisi di Materiali "Argillosi" mediante XRD. Ed. C.N.R. - I.C.R., Roma, 1991.

Reynard B., Lécuyer C., Grandjeau P. (1999). Crystal-chemical controls on rare earth element concentrations in fossil biogenic apatite and implications for paleoenvironmental reconstructions. Chem. Geol. 155, 233-242.

Ritger S., Carson B., Suess E. (1987). Methane-derived authigenic carbonates formed by subduction-induced pore-water expulsion along the Oregon/Washington margin. Geol. Soc. Am. Bull. 98, 147-156.

Robertson A. (1996). Mud volcanism on the Mediterranean Ridge: Initial results of Ocean Drilling Program Leg 160: Geology, v. 24, p. 239-242.

Roberts H.H., Aharon P. (1994). Hydrocarbon-derived carbonate buildups of the northern Gulf of Mexico continental slope: a review of submersible investigations. In: Aharon, P. (Ed.), Geology and Biology of Modern and Ancient Submarine Hydrocarbon Seeps and Vents. Geomarine Letters. Springer Verlag, pp. 135 – 148.

Roberts H.H., Aharon P., Carney R., Larkin J., Sassen R. (1990). Seafloor responses to hydrocarbon seeps, Louisiana continental slope. Geo-Marine Letters,10, 232-243.

Robin C., Colantoni P., Gennesseaux M., Rehault J.P. (1987). Vavilov seamount: a mild alkaline Quatemary volcano in the Tyrrhenian basin. Mar. Geol., 78: 125-136.

Robinson B.S., Kusakabe M. (1975). Quantitative preparation of sulfur dioxide, for 34Sp2S analyses, from sulfides by combustion with cuprous oxide. Anal. Chem., 47, 1179-81.

Roca E. (2001). The Northwest Mediterranean Basin (Valencia Trough, Gulf of Lions and Liguro-Provençal basins): structure and geodynamic evolution. In: Ziegler P.A., Cavazza W., Roberston A.H.F., Crasquin-Soleau S. (eds), PeriTethys Memoir 6: Peri-Tethyan Rift/Wrench Basins and Passive Margins. Mém. Mus. natn. Hist. nat. 186, 671-706. Paris.

Rodriguez N.M., Paull C.K., Borowski W.S. (2000). Zonation of Authigenic Carbonates within Gas Hydrate-Bearing Sedimentary Sections on the Blake Ridge : Offshore Southeastern North America. In: Paull C.K., Matsumoto R., Wallace P.J. & Dillon W.P. (eds.), Proceedings of the Ocean Drilling Program, Scientific Results, 164. College Station, TX (Ocean Drilling Program). 301-312.

Rollinson H. R. (1993). Using geochemical data: evaluation, presentation, interpretation. New York, Longman, 352p.

Rongemaille E., Bayon G., Pierre C., Bollinger C. Chu N.C., Fouquet Y., Riboulot V., Voisset M. (2011). Rare earth elements in cold seep carbonates from the Niger delta. Chem. Geol. 286, 196-206.

Rosenbaum G., Lister G.S. (2004). Formation of arcuate orogenic belts in the western
Mediterranean region. in Sussman A.J., Weil A.B., eds. Orogenic
curvature: Integrating paleomagnetic and structural analyses: Boulder, Colorado, Geological Society of America Special Paper 383, p. 41–56.

Rosenbaum G., Lister G.S., Duboz C. (2002). Reconstruction of the tectonic
evolution of the western Mediterranean since the Oligocene. In: Rosenbaum G.,
Lister G. S. (2002). Reconstruction of the evolution of the Alpine-Himalayan Orogen.
Journal of the Virtual Explorer, 8, 107 – 130.

Rovere M., Gamberi F., Mercorella A., Rashed H., Gallerani A., Leidi E., Marani M., Funari V., Pini G.A., (2014). Venting and seepage systems associated with mud volcanoes and mud diapirs in the southern Tyrrhenian Sea. Mar. Geol. 347,153-17.

Rovere M., Rashed H., Pecchioni E., Mercorella A., Ceregato A., Leidi E., Gamberi F., Vaselli O. (2015). Habitat mapping of cold seeps associated with authigenic mineralization (Paola Ridge, southern Tyrrhenian Sea): combining seafloor backscatter with biogeochemistry signals. Ital. J. Geosci. 134, 23-31.

Santo A. P., Clark A. H. (1994). Volcanological evolution of Aeolian Arc (Italy):
Inferences from 40Ar/39Ar ages of Filicudi rocks, paper presented at IAVCEI
Congress, Int. Assoc. of Volcanol. and Chem. of the Earth's Inter., Ankara.

Sartori R. (1982). Evolution of tectonic and volcanic processes in the Parece Vela interarc basin (Philippine sea). Rend. Sot. Geol. Ital.. 4: 301-304.

Sartori R. (1982). L'arco calabro-peloritano: aspetti di geologia marina. Rend. Soc. It. Min. e Petr., 38: 941-950.

Sartori R. (1990). The main results of odp leg 107 in the frame of neogene to recent geology of perityrrhenian areas, in Kastens, K. A., Mascle, J., et 1990 al Proceedings of the Ocean Drilling Program, Scientific Results, Vol. 107: College Station, TX (Ocean Drilling Program p 715-730.

Sartori R., Torelli L., Zitellini N., Carrara G., Magaldi M., Mussoni P. (2004). Crustal features along a W–E Tyrrhenian transect from Sardinia to Campania margins (central Mediterranean), Tectonophysics, 383, 171–192, doi:10.1016/j.tecto.2004. 02.008.

Sassen R., Brooks J.M., Kennicutt II M.C., MacDonald I.R. Guinasso Jr N.L. (1993). How oil seeps, discoveries relate in deepwater Gulf of Mexico. Oil and Gas Journal Week of April 19, 1–6.

Savard M.M., Beauchamp B., Veizer J. (1996). Significance of aragonite cements around Cretaceous marine methane seeps. Journal of Sedimentary Research 66 (3), 430–438.

Savini A., Malinverno E., Etiope G., Tessarolo C., Corselli C., (2009). Shallow seep-related seafloor features along the Malta plateau (Sicily channel–Mediterranean Sea): morphologies and geo-environmental control of their distribution. Marine and Petroleum Geology 26, 1831–1848.

Schulz D.H., Zabel M. (2006). Marine Geochemistry, 3-540-32143-8 Springer Berlin Heidelberg New York.

Selli R., Lucchini F., Rossi P.L., Savelli. C., Del Monte M. (1977). Dati geologici. petrochimici e radiometrici sui vulcani centro-tirrenici. G. Cieol., 42 (1): 221-246.

Serri G., Innocenti F., Manetti P. (2001). Magmatism from Mesozoic to Present: petrogenesis, time-space distribution and geodynamic implications. In: Vai G.B., Martini I.P. (Eds.), Anatomy of an Orogen: the Apennines and the adjacent Mediterranean Basins. Kluwer Academic Publishers, Dordrecht, The Netherlands, pp. 77–104.

Selli R., Lucchini F , Rossi P.L., Savelli C., del Monte M. (1977). Dati geologici, petrochimici e radiometric! sui vulcani centrotirrenici. G. Geol., 42:221-246.

Shao H., Yang S., Wang Q., Guo Y. (2015). Discriminating hydrothermal and terrigenous clays in the Okinawa Trough, East China Sea: Evidences from mineralogy and geochemistry. Chemical Geology 398, 85–96.

Shapiro L. , Brannock W. W. (1962). Rapid analysis of silicate, carbonate and phosphate rocks. U.S. Geological Survey Bullettin 1144A.

Sibuet M., Olu K. (1998). Biogeography, biodiversity and fluid dependence of deep-sea cold-seep communities at active and passive margins. Deep-Sea Research II 45, 517–567.

Somoza L., Díaz-del-Río V., León R., Ivanov M., Fernández-Puga M.C., Gardner J.M., Hernández-Molina F.J., Pinheiro L.M., Rodero J., Lobato A., Maestro A., Vázquez J.T., Medialdea T., Fernández-Salas L.M. (2003). Seabed morphology and hydrocarbon seepage in the Gulf of Cádiz mud volcano area: acoustic imagery, multibeam and ultrahigh resolution seismic data. Mar. Geol. 195, 153–176.

Spallanzani L. (1795). Viaggi alle Due Sicilie e in alcune parti dell'Appennino. Pavia

Stampfli G.M., Borel G.D. (2002). A plate tectonic model for the Paleozoic and Mesozoic constrained by dynamic plate boundaries and restored synthetic oceanic isochrons. Earth and Planetary Science Letters 196, 17–33.

Stoppani A. (1908). Il Bel Paese (reprint of 1874 edition, by A. Malladra). Cogliati: Milano.

Suess E., Bohrmann G., von Huene R., Linke P., Wallmann K., Lammers S. Sahling H. (1998). Fluid venting in the eastern Aleutian subduction zone. Journal of Geophysical Research 103, 2597–2614.

Sumner R. H., Westbrook G. K. (2001). Mud diapirism in front of the Barbados accretionary wedge: The influence of fracture zones and North America- South America plate motions, Mar. Pet. Geol., 18, 591–613.

Taylor S.R., McLennan S.M. (1985). The Continental Crust: its Composition and Evolution. Blackwell Scientific Pub, Palo Alto, CA, 328 pp.

Thiel V., Peckmann J., Richnow H.H., Luth U., Reitner J., Michaelis W. (2001). Molecular signals for anaerobic methane oxidation in Black Sea seep carbonates and microbial mat. Mar. Chem. 73:97–112.

Thyne G.D., Gwinn C.J. (1994). Evidence for paleoaquifer from early diagenetic siderite of the Cardium Formation, Alberta, Canada. J. Sediment. Res., 64:726-732.

Tinivella U., Giustiniani M. (2012). An overview of mud volcanoes associated to gas hydrate system, INTECH Open Access Publisher.

Tortorici L., Monaco C., Tansi C., Cocina O. (1995). Recent and active tectonics in the Calabrian arc (Southern Italy). Tectonophysics 234, 37–55.

Tranchina L., Basile S., Brai M., Caruso A., Cosentino C., Miccichè S. (2008). Distribution of heavy metals in marine sediments of Palermo Gulf (Sicily, Italy). Water, Air, and Soil pollution 191, 245–256.

Tribovillard N., du Châtelet E.A., Gay A., Barbecot F., Sansjofre P., Potdevin J.L. (2013). Geochemistry of cold seepage-impacted sediments: Per-ascensum or per-descensum trace metal enrichment. Chemical Geolog, 340, 1–12.

Trincardi F., Correggiari A., Field M.E., Normark W.R. (1995). Turbidite deposition from multile sources: quaternary Paola Basin (eastern Tyrrhenian Sea). Journal of Sedimentary Research, B65 469-483.

Trua T., Serri G., Rossi P. L. (2004). Coexistence of IAB-type and OIB-type magmas in the southern Tyrrhenian back-arc basin: Evidence from recent seafloor sampling and geodynamics implications, Mem. Desc. Carta Geol. d'Italia, 44, 83–96.

Unterschutz J.L.E., Creaser R.A., Erdmer P., Thompson R.I., Daughtry K.L. (2002). North American margin origin of Quesnel terrane strata in the southern Canadian Cordillera: inferences from geochemical and Nd isotopic characteristics of Triassic metasedimentary rocks: Geological Society of America, Bulletin, v. 114, p. 462–475.

Van Dijk J.P., Bello M., Brancaleoni G.P., Cantarella G., Costa V., Frixa A., Golfetto F., Merlini S., Riva M., Torricelli S., Toscano C., Zerilli A. (2000). A regional structural model for the northern sector of the Calabrian Arc (southern Italy). Tectonophysics 324, 267–320.

Vaselli O., Tassi F., Tedesco D., Poreda J.R, Caprai A. (2011). Submarine and inland gas discharges from the CampiFlegrei (southern Italy) and the Pozzuoli Bay: geochemical clues for a common hydrothermal-magmatic source. Special Volume on "Research in Shallow Marine and Fresh Water Systems", Procedia Earth Planet. Sci., 4, 57-73.

Vergnaud-Grazzini C. (1971). 18O changes in foraminiferal carbonates during the last 105 years in the Mediterranean Sea. Mar. Geol. 11, 261-282.

Vigliotti L., Langenheim V.E. (1995). When did Sardinia stop rotating? New paleomagnetic results. Terra Nova 7, 424 – 435.

Webb G.E., Kamber B.S. (2000). Rare earth elements in Holocene reefalmicrobialites: a new shallow seawater proxy. Geochim.Cosmochim.Acta 64, 1557-1565.

Whiticar M.J., (1999). Carbon and hydrogen isotope systematics of bacterial formation and oxidation of methane. Chem. Geol. 161, 291-314.

Whiticar M. J., Werner F. (1981) Pockmarks: Submarine vents of natural gas or freshwater seeps: Geo-Marine Letters, v. 1, p. 193–199.

Wittkop C., Teranes J., Lubenow B., Dean W.E. (2014). Carbon- and oxygen-stable isotopic signatures of methanogenesis, temperature, and water column stratification in Holocene siderite varves. Chem. Geol. 389, 153-166.

Wortel MJR., Spakman W. (2000). Subduction and slab detachment in the Mediterranean-Carpathian region, Science, 290:1910-1917.

Zemskaya T. I., Pogodaeva T. V., Shubenkova O. V., Chernitsina S. M., Dagurova O. P., Buryukhaev S. P. (2010). Geochemical and microbiological characteristics of sediments near the Malenky mud volcano (Lake Baikal, Russia), with evidence of Archaea intermediate between the marine anaerobic methanotrophs ANME-2 and ANME-3. Geo Mar. Lett. 30, 411–425. doi: 10.1007/s00367-010-0199-6.

Zhang J., Nozaki Y. (1996). Rare earth elements and yttrium in seawater: ICP-MS determinations in the East Caroline, Coral Sea, and South Fiji basins of the western South Pacific Ocean. Geochim.Cosmochim.Acta 60, 4631-4644.

Zhang J., Nozaki Y. (1998). Behavior of rare earth elements in seawater at the ocean margin: A study along the slopes of the Sagami and Nankai troughs near Japan. Geochim.Cosmochim.Acta 62, 1307-1317.

Zhang J., Amakawa H., Nozaki Y. (1994). The comparative behaviors of yttrium and lanthanides in seawater of the North Pacific.Geophys. Res. Lett. 21, 2677-2680.

Zhong S., Mucci A. (1995). Partitioning or rare earth elements (REEs) between calcite and seawater solutions at 25°C and 1 atm, and high dissolved REE concentrations. Geochim.Cosmochim.Acta 59, 443-453.

Zito G., Mongelli F., De Lorenzo S., Doglioni C. (2003). Heat flow and geodynamics in the Tyrrhenian Sea. Terra Nova 15, 425–432, doi: 10.1046/j.1365–3121.2003.00507.x.

Appendix (A): Major and trace elements composition of organogenic carbonate crusts from Paola Ridge.

Sample	Cal-B	Cal-C	Cal-N	Cal-H	Cal-BB	Cal-CC	Cal-AA	Cal-NN	Cal_HH
Na_2O	0.38	0.43	0.45	0.54	0.56	0.81	0.6	0.48	0.47
MgO	2.72	3.3	3	1.9	2.05	1.8	2	1.5	2.12
Al_2O_3	5.7	5.1	7.2	5.6	7.4	7.8	4.4	5.9	8.51
SiO_2	14.9	12.7	18.8	13.6	19.7	21.2	10.7	15.7	21.2
P_2O_5	0.1	0.1	0.2	0.1	0.1	0.1	0.1	0.1	0.1
K_2O	1.1	0.9	1.4	1	1.4	1.5	0.8	1.1	1.5
CaO	39.6	39.7	34.7	41.2	36.4	29.4	43.2	40.5	30.39
TiO_2	0.4	0.3	0.5	0.3	0.5	0.4	0.3	0.3	0.4
MnO	0.1	0.1	0.1	0.1	0	0.1	0	0	0
Fe_2O_3	3	3.1	4.8	2.2	3.3	3.2	2.3	2.7	3.6
L.O.I	31.16	33.88	28.16	32.86	27.19	32.36	34.4	30.6	29.34
TOT	99.16	99.61	99.31	99.4	98.6	98.67	98.8	98.88	97.63
Ba	24	355	283	216	350	384	157	270	321
Rb	39.1	39.2	41.6	39.4	46	57	23	37	43
Sr	4860	3265	3399	3952	5828	4233	5128	5968	5134
Th	6.2	5.5	6.3	6.8	4.8	7.3	4.1	4.1	5.5
U	14.4	5.3	7.3	8.3	7.8	9.1	28.5	8	7.2
Zr	72.5	81	81.5	71.9	86	112	53	83	92
Y	9.6	10.8	13.3	11.4	11	16	9	11	14
Mo	46.1	0.9	1.2	7.2	10	20	56	17	6
Cu	14.1	15.5	10.8	15.5	20	20	10	10	20
Zn	26	28	42	26	40	40	<30	<30	40
Ni	9.7	13.6	25.9	13.9	60	40	30	30	80

Appendix (B): Major and trace elements composition of siderites from Paola Ridge.

Sample	**Cal-I**	**Cal-G**	**Cal-M**	**Cal-E**	**Cal-R**	**Cal-A**	**Cal-V**	**Cal-U**	**Cal-EE**	**Cal-RR**
Na_2O	0.6	0.3	0.3	0.8	0.6	0.4	0.5	2.3	0.8	0.5
MgO	1.3	2	2.1	1.4	1	0.7	1	1.2	1.2	1.2
Al_2O_3	7.9	2.2	3.3	9.7	5.7	4.3	4	4.1	9.03	6.5
SiO_2	18.8	5.5	8.7	22.6	12.9	12.4	9.8	10.2	21.7	15.3
P_2O_5	0.2	0.4	0.5	0.3	0.3	0.3	0.1	0.1	0.2	0.2
K_2O	1	0.3	0.5	0.1	0.7	0.5	0.6	0.7	1.2	0.8
CaO	2.9	3.6	3.3	1.1	3	1.5	5.6	3.4	2.6	3.7
TiO_2	0.3	0.1	0.2	0.3	0.2	0.2	0.2	0.2	0.2	0.2
MnO	0.6	1.6	0.9	0.5	0.9	0.7	1.3	0.8	0.4	0.3
Fe_2O_3	36.8	53.3	53	37.2	47.1	44.8	48.6	48.2	36.2	46.8
L.O.I	28.8	30.4	26.9	22.7	27	33.7	27.9	26.2	25.2	23.3
TOT	99.2	99.7	99.7	96.7	99.4	99.5	99.6	97.4	98.73	98.8
Ba	71	45	83	126	179	91	72	176	112	105
Co	115.8	168.6	21.3	60.2	69.4	27.6	36	34	56	59
Rb	17.3	12.4	19.1	30.5	33.3	17.8	18	38	28	25
Sr	113.5	75.2	77	88.2	117.6	56.7	88	142	79	76
Th	2.1	1.4	2.1	3.5	4.5	2.1	2	4.7	3	3.1
U	2.5	1.3	0.5	5	9.3	4	1.2	13.5	1	2.3
V	221	96	184	144	148	168	243	157	187	103
Zr	138.5	138.9	165.6	72.3	76.9	29.8	149	88	86	60
Y	26.9	13.7	23.4	38.1	57.4	15.6	26	22	26	29
Mo	1.5	13.6	1.1	63.7	82.2	4.4	<2	45	40	38
Cu	15.2	21.8	5.5	20.8	38.3	6.8	<10	20	10	30
Pb	8.3	37.5	4.8	18.2	24.5	5.8	<5	16	17	26
Zn	105	262	49	238	350	71	140	150	200	350
Ni	77.9	138.3	18.5	29.1	29.1	11.1	70	30	50	40

Appendix (C): Major and trace elements composition of oxy-hydroxides from Paola Ridge.

Sample	Cal-F	Cal-P	Cal-T
Na_2O	0.3	0.1	7.8
MgO	1.1	1.9	1.2
Al_2O_3	9.9	16.5	9.2
SiO_2	20.3	36.1	25.1
P_2O_5	2	2.8	0.4
K_2O	1.4	2.5	2.2
CaO	0.5	1.2	0.9
TiO_2	0.4	0.8	0.6
MnO	0	0.4	0.1
Fe_2O_3	52.1	24.3	13.5
L.O.I	10.5	7.3	6.5
TOT	98.5	93.9	67.5
Ba	181	398	532
Co	5.1	13.7	21.7
Rb	46	81.1	102
Sr	116.7	231.3	266
Th	6.4	10.6	15.5
U	13.2	12.2	2.2
V	140	198	175
Zr	72.3	149.8	187.6
Y	22.7	37.3	28.2
Mo	97.1	53.5	37.6
Cu	41	32.3	25.2
Pb	57.9	74	54.7
Zn	61	53	83
Ni	11.5	17.4	33.9

Appendix (D): Major and trace elements composition of sulfides from Paola Ridge.

Sample	Cal-D	Cal-O	Cal-L	Cal-Q	Cal-S	Cal-Z	Cal-W	Cal-X
Na_2O	0.6	1.6	0.1	0.5	0.4	0.9	0.6	1.7
MgO	0.5	0.7	0.6	0.4	0.3	0.5	0.9	0.8
Al_2O_3	5.1	4.5	5.4	3.8	3.1	6.4	12.3	21.05
SiO_2	12	10.8	14.75	9.6	7.5	14.8	30.05	34.8
P_2O_5	0.1	0.1	0.2	0.04	0	0.05	0.2	0.13
K_2O	0.9	1.4	1.1	0.6	0.5	1	2.4	1.9
CaO	0.4	1.1	0.4	0.2	0.18	0.36	0.7	3.2
TiO_2	0.19	0.1	0.2	0.1	0.1	0.2	0.6	1
MnO	0.02	0.02	0.03	0.03	0.03	0.05	0.03	0.06
Fe_2O_3	30.8	29.4	10.7	28.1	31.2	26.1	13.1	10.6
S	15.3	19.4	20.3	19.2	20.3	17.07	8.8	8.6
L.O.I	33.8	30.2	45.63	37	36.2	32.1	29.1	15.44
TOT	99.71	99.32	99.41	99.57	99.81	99.53	98.78	99.28
Ba	92	202	70	41	61	92	276	273
Co	45.2	250.4	52.4	53.8	22	18	8	30
Rb	15.3	36.6	18	12	15	20	65	65
Sr	86.6	137.4	42.4	24.9	34	47	188	286
Th	2.5	4.7	2.5	1.4	1.7	2	11.1	10.5
U	9.7	1.5	3	2	0.8	1.5	12.6	11.2
V	40	26	41	35	34	38	82	136
Zr	27	33.4	35.6	18	24	29	140	187
Y	2.1	2.7	3	1.7	<2	<2	11	16
Mo	254.2	87.8	179.7	221.7	28	48	59	11
Cu	12.5	7.5	15.1	6.6	<10	<10	20	30
Pb	7	18.3	29.9	11.7	8	62	16	16
Zn	58	329	195	151	210	160	70	70
Ni	49.9	160.3	72.1	69.6	110	80	20	60

Appendix (E): Major and trace elements composition of mud samples from Paola Ridge.

Sample	L.O.I	Na_2O	MgO	Al_2O_3	SiO_2	P_2O_5	K_2O	CaO	TiO_2	MnO	Fe_2O_3
Cal-1	6.61	0.1587	1.981	20.759	52.515	0.23	3.733	1.488	1.171	0.075	7.089
Cal-2	5.79	9.0389	0.44	6.15	16.79	0.066	1.819	0.854	0.766	0.134	5.989
Cal-3	6.75	0	1.858	19.753	51.332	0.186	3.689	1.097	1.202	0.041	7.285
Cal-4	6.59	0.1997	0.899	23.134	54.468	0.245	4.119	1.867	1.258	0.03	3.591
Cal-5	6.39	4.3421	1.436	16.122	39.943	0.148	3.23	1.195	1.083	0.041	5.899
Cal-6	6.41	8.4676	0.554	8.187	21.504	0.075	2.291	0.711	0.851	0.093	5.551
Cal-7	17.15	3.0468	1.103	11.777	28.47	0.207	2.006	1.607	0.484	0.476	24.37
Cal-8	8.42	0	1.431	15.338	38.659	0.15	2.925	1.2004	0.942	0.038	6.14
Cal-9	10.78	0.334	2.144	15.201	41.026	0.171	3.279	7.682	0.853	0.13	8.016
Cal-10	10.01	0	2.284	17.736	46.795	0.168	3.34	8.823	1.02	0.114	7.037
Cal-11	6.72	6.7381	1.205	13.489	34.402	0.122	2.925	1.197	0.974	0.088	6.423
Cal-12	9.57	0	1.089	20.621	53.254	0.163	3.121	0.863	1.018	0.02	4.862
Cal-13	7.15	0	2.343	20.11	52.46	0.231	3.762	2.808	1.218	0.058	7.266
Cal-14	19.91	1.1736	0.252	10.285	31.646	0.05	3.366	0.839	0.276	0.123	12.66
Cal-15	11.21	6.9091	1.852	10.7	27.639	0.1045	2.47	5.291	0.771	0.068	6.134
Cal-16	9.59	0	2.261	18.057	44.865	0.407	3.478	5.568	1.006	0.133	11.67
Cal-17	24.18	12.185	0.71	3.009	7.734	0.057	0.896	14.053	0.288	0.031	2.39
Cal-18	10.71	0	1.104	21.332	53.865	0.174	3.311	1.118	1.083	0.031	3.639
Cal-19	6.23	6.7891	1.181	14.192	34.992	0.165	2.934	1.051	0.994	0.046	5.803
Cal-20	9.12	4.5076	0.778	15.609	35.82	0.148	2.779	1.218	1.095	0.028	3.305
Cal-21	15.95	8.2934	0.517	10.058	24.136	0.08	2.171	0.73	0.702	0.054	6.931
Cal-22	8	0	1.838	20.334	53.37	0.288	3.694	1.416	1.117	0.061	6.964
Cal-23	9.97	11.625	0.863	3.6	9.125	0.072	1.144	18.216	0.394	0.039	3.228
Cal-24	9.28	7.2181	1.286	12.754	32.839	0.1009	2.776	1.328	0.923	0.044	6.351
Cal-25	6.15	8.6107	0.884	10.206	27.343	0.094	2.54	0.981	0.879	0.086	6.348
Cal-26	6.94	7.41	1.136	12.702	32.829	0.112	2.721	0.952	0.924	0.036	6.651
Cal-27	16.97	0.1977	2.859	13.71	35.081	0.126	2.657	19.908	0.82	0.098	6.014
Cal-28	6.07	0.5748	1.218	19.685	54.736	0.3288	5.905	1.8679	0.946	0.119	5.684
Cal-29	12.77	0.3268	2.605	14.045	38.161	0.166	2.848	19.037	0.807	0.13	6.577
Cal-30	16.14	0.1675	2.52	13.971	36.086	0.1214	2.866	18.883	0.78	0.107	5.945
Cal-31	8.43	0	1.46	19.219	51.871	0.3244	3.548	1.3715	1.099	0.059	9.993
Cal-32	13.19	0.2349	2.619	16.052	41.293	0.1346	3.053	13.137	0.913	0.119	7.099

Samples	Cal-1	Cal-2	Cal-3	Cal-4	Cal-5	Cal-6	Cal-7	Cal-8	Cal-9	Cal-10	Cal-11	Cal-12	Cal-13	Cal-14	Cal-15
Ba	551	609	489	714	574	522	325	519	476	471	491	856	577	107	501
Sr	292.8	311.7	271.7	508	312.8	228	177.3	321.6	351.4	369.7	248.6	283.3	387.3	81.5	363.3
Rb	122.7	121.2	123.7	104.3	118.2	125.7	58.5	116.9	110.5	107.2	126.1	104.6	114.1	195.4	106.5
Zr	177	190.9	202.1	302.4	187.9	286.2	109.1	181.9	151.6	163.5	194.8	250.1	179.7	494.1	153.4
Co	19.5	22.3	11.6	8.9	9.3	27.4	51.5	10.8	16	13.6	24.5	11.3	13	33.2	16.5
Ga	22.6	23.3	22.9	22.3	23.2	24.7	11.3	21.7	19.6	19.6	22.9	22.6	22.2	13.8	19.3
Nb	21.3	22	23.6	46	23.1	44.3	11.1	22.1	17.8	19.3	22.1	35.9	20.9	75.8	18.7
Th	15.4	15.8	15.7	22.2	15.7	15.9	7.2	15.4	15.1	13.2	15.9	17.7	14.9	44.9	13.5
U	5.6	3.8	2.6	9.1	11.2	4.3	4.1	2.8	5	3.3	2.6	12	4.4	13.3	3.7
V	213	181	209	164	180	156	134	197	139	153	171	216	202	22	166
Mo	21.6	6.5	3.4	18.4	9.4	20.2	77.8	8.9	1	1.9	5.1	58.2	7.3	7.4	2.5
Cu	44.5	48.5	40.7	30.1	58.5	37.1	26.4	52	41.9	40.4	38.6	50	59.4	3.8	42.1
Pb	17.4	17.2	24.1	29.9	41.7	17	23.1	15.7	19.1	17.8	23.4	24	20.1	16.2	19.3
Zn	76	62	61	43	84	103	137	72	82	86	75	53	71	65	68
Ni	35.2	27.6	30.3	10.9	24	41.1	28.5	24	46.1	31.9	36.6	15.1	30.6	72.7	40.8

Samples	Cal-16	Cal-17	Cal-18	Cal-19	Cal-20	Cal-21	Cal-22	Cal-23	Cal-24	Cal-25
Ba	483	313	619	405	510	469	494	436	438	445
Sr	364.3	800.3	278.8	243.1	286.4	255.6	313.2	297.5	231.1	195.7
Rb	104.3	61.4	106.9	121.7	119.5	126.9	118.2	120.6	114.4	123.7
Zr	163.4	107.6	311	181.5	284.3	240.1	242.9	193.7	169.4	191.9
Co	16.3	7.2	6.3	11.5	7	30.5	9.3	19.8	9.2	28.6
Ga	19.2	11.4	21.2	20.6	22.9	20.6	20.4	19.7	19	19.9
Nb	21.8	11.8	39	19.2	42.1	29.8	31.2	24.2	19.7	20.5
Th	16.1	10	24.7	14.6	16.9	17.9	16	17.1	14.2	15.4
U	3.1	4.8	10.6	3.3	7.6	7.5	6.8	5.3	3	4.9
V	152	108	191	212	211	191	174	167	159	151
Mo	1.4	0.7	43.7	10.2	29.7	30.8	6.1	16.9	1	2.9
Cu	36.1	22.1	39.8	44.1	35.8	45.2	48.1	45.7	31.5	40.3
Pb	22.8	12.3	25.8	18.3	14.9	21.3	15.2	21.1	8.1	19.2
Zn	74	35	51	56	58	87	58	83	59	89
Ni	42.3	23.2	8.4	23	10	37.6	19.8	26.1	23.3	68.7

Samples	Cal-26	Cal-27	Cal-28	Cal-29	Cal-30	Cal-31	Cal-32
Ba	481	937	556	509	674	501	352
Sr	245	609	420	707	578	251	446
Rb	117.2	92	210	81	81	121	99
Zr	198	221	339	171	184	208	174
Co	10.5	8	6	8	10	13	13
Ga	19.5	15	20	14	16	21	19
Nb	22.7	24	43	16	19	20	16
Th	15.2	11.9	23.7	11.6	10	13.3	11.2
U	3.1	10.4	8.9	10.1	9.7	3	11.3
V	166	110	106	127	129	191	142
Mo	2.4	20	9	27	13	9	8
Cu	31.9	110	20	20	30	30	30
Pb	14.7	14	32	11	13	18	13
Zn	60	70	100	60	70	90	80
Ni	28.9	40	30	40	40	40	80

Conferences

Rend. Online Soc. Geol. It., Vol. 21 (2012), pp. 975-977, 2 figs.

Petrographical and mineralogical characterization of marine sediments in the mud diapir province of the Paola Basin (Southern Tyrrhenian Sea)

HEBA RASHED (*), MARZIA ROVERE (**), ELENA PECCHIONI(*), FABIANO GAMBERI (**), ORLANDO VASELLI (*,***),
GABRIELE BICOCCHI (*), FRANCO TASSI (*,***)

Key words: *Geochemistry, Mineralogy, Paola Basin, Plio-Quaternary sediments, South Tyrrhenian Sea.*

INTRODUCTION

The study area is located within the Paola Basin along the southeastern margin of the Tyrrhenian Sea. The geodynamic evolution of the Paola Basin is related to the extensional tectonics that led to the opening of the Tyrrhenian Sea. The basin is characterized by a thick Plio-Quaternary sedimentary sequence, whose origin is likely related to turbiditic currents (TRINCARDI *et alii,* 1995). The study area is bounded by a calc–alkaline volcanic complex (Alcione and Lametini) to the west, while to east is bordered by a system of normal faults that separate it from the Coastal Range in Calabria (Fig. 1). The Paola Basin hosts a 60-km-long NNW-SSE oriented prominent anticline, the Paola Ridge, interpreted to be the result of an episode of early Pleistocene compression (ARGNANI & TRINCARDI, 1988). A more recent interpretation defines the Paola Ridge as due to a mobile mud belt connected with a set of extensional faults trending NW-SE to NNW-SSE (GAMBERI & ROVERE, 2010). With the aim of proving this latter interpretation, the MVP11 oceanographic cruise was carried out in August-September 2011 on board the R/V CNR URANIA, during which very high resolution swath bathymetry and shallow seismic data were collected plus 30 gravity coring sites and 30 box-cores stations were performed in order to define the petrographical, mineralogical and geochemical composition of the cored sediments and the collected rock samples (Fig. 2).

This study is part of a PhD fellowship carried out in collaboration with the Department of Earth Sciences of Florence and the CNR-ISMAR (Institute of Marine Sciences) of Bologna (Italy) and aimed to: i) define the mineralogical and geochemical characteristics of marine sediments related to mud diapirism sampled in the study area and ii) verify the presence of gas emissions at the seafloor through the analysis of the gas-related products.

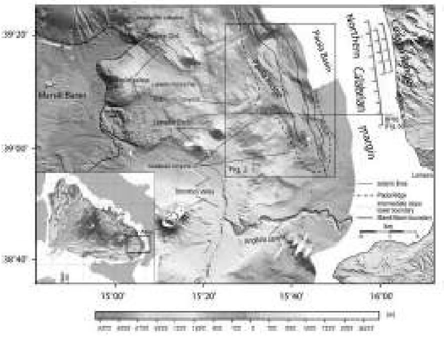

Fig. 1- Bathymetry of the southeastern Tyrrhenian Sea, Paola Basin. The study area is enclosed in the box that corresponds to the area of Fig. 2, where sampling sites are enlightened. From Gamberi & Rovere (2010).

MATERIALS AND METHODS

For this work we have analyzed different kind of samples (rocks/sediment):

a) limestone crusts cored along faults dissecting mud diapir structures; authigenic carbonates retrieved from the core catcher of stations performed over mud volcanoes and their downslope mudflows;
b) iron oxy-hydroxide crusts found in the box cores stations on top of the mud volcanoes structures, where strong gas emissions were recognized by water column multi-beam records and direct sampling;
c) flat crusts of pyrite and sulfur retrieved in the upper section of the cores and in the box cores performed on top of the mud volcanoes;
d) cohesive mud sampled along the coring sections of the most energetic mud volcanoes structures discovered in the area.

The sampling was carried out using a 1.2 t gravity coring

(*) Department of Earth Sciences – University of Florence – Via La Pira 4, 50121 Florence (Italy)

(**) CNR-ISMAR, Institute for Marine Sciences – Via P. Gobetti 101, 40129 Bologna (Italy)

(***) CNR-IGG, Institute of Geosciences and Earth Resources - Via La Pira 4, 50121 Florence (Italy).

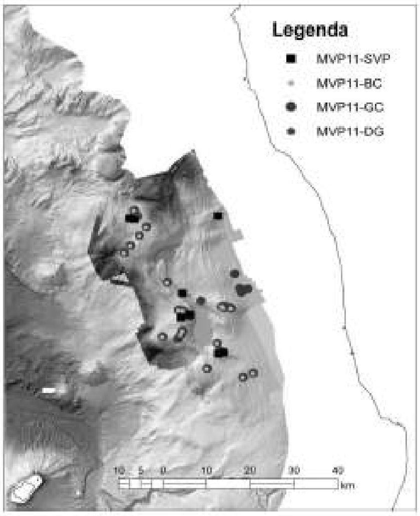

Fig. 2- High resolution swath bathymetry acquired during cruise MVP11 in the samples, MVP11-BC Box core stations, MVP11-GC gravity coring stations, MVP11-DG dredge stations.

device with a penetration length between 4 and 12 m. Box cores were collected with an oceanic box corer with a hollow metal cylinder of 50 cm in diameter and a volume capacity of 100 L. All the samples were dried (at 40 °C), grinded and grounded (with a planetary agate mill device). Both sediments and rock fragments were analyzed to determine the semi-quantitative composition of the main mineralogical phases. In the sediments the <4 μm granulometric fraction was also separated for the determination of the clay minerals content.

The mineralogical analyses were carried out by XRD with a Philips PW 1050/37 diffractometer, operating at 40 kV-20 mA, with anode a Cu, graphite monochromator at an interval 2θ of 5-70° e 2-32° (limit of detection 4%), using the X'Pert PRO Philips acquisition system. Polished thin sections of rock samples were prepared for petrographic observations by using an optical microscopy in transmitted light for the textural characterization of the samples and point out the presence of mineral index, using a microscopy ZEISS Axioskop, equipped with video camera (resolution 5 Megapixel), provided with image analysis Axiovision.

RESULTS AND DISCUSSION

The petrographic analyses by microscopy in transmitted light were only carried out on the limestone crusts, and the observations have allowed to characterize different sample types: a) fractured and porous mudstone-wackestone with the presence of pyroxenes and rare quartz and plagioclases; b) mudstone with rare presence of quartz; c) biomicrite with rare presence of quartz and medium porosity.

The preliminary mineralogical analyses on the different rock samples were used to recognize the three groups: a) carbonates mostly containing calcite, quartz, siderite, feldspars (plagioclase), and phyllosilicates and carbonates with calcite, aragonite, dolomite, phyllosilicates (muscovite and clay minerals) and pyroxene; b) sulfides mainly consisting of quartz, pyrite and/or sphalerite, marcasite and plagioclase and traces of phyllosilicates; c) iron oxy-hydroxides dominantly characterized by goethite, quartz, feldspars (plagioclase) and phyllosilicates.

The mineralogical analyses carried out on the marine sediments (cohesive mud) have indicated the presence of quartz, halite, feldspars (plagioclase and k-feldspar), muscovite and clay minerals (illite, vermiculite, chlorite, kaolinite) unless one sample where chlorite was absent; occasionally, some samples were composed by calcite and/or dolomite, siderite, hematite and pyrite.

CONCLUSIONS

The Paola Basin is a key area for better understanding the evolution of the southern part of the Tyrrhenian Sea. Regional structural studies describe the area as affected by relevant tectonic compression, but more recent high resolution investigations have revealed the presence of gas-related structures, probably activated by normal faulting. Sampling data are now available in the area. The petrographical and mineralogical data presented in this work have allowed to highlight important features that can be used to understand the geochemical processes affecting the depositional environment into which the marine sediments were deposited. In this framework, the petrographic characterization and the interpretation of the mineralogical composition will be related to the active structures (mud diapirs and mud volcanoes) recently recognized in the Paolo Basin. Furthermore, the chemical composition of the carbonate-hosting pyroxenes may shed light on their provenance studies, along with chemical and isotopic investigations in both cohesive mud sediments and pyrite and sulfur crusts that are presently in progress, the latter to be investigated in order to comprehend the effects due to the gas discharges.

REFERENCES

ARGNANI A. & TRINCARDI F. (1988) - *Paola slope basin: evidence of regional contraction on the eastern Tyrrhenian margin*. Mem. Soc. Geo. It., 44, 39-105.

GAMBERI F. & ROVERE M. (2010) - *Mud diapirs, mud volcanose and fluid flow in the rear of the Calabria Arc orogenic wedge (southeaster Tyrrenian Sea)*. Basin Res. **22**, 452-464.

TRINCARDI F., CORREGGIARI A., FIELD M.E., & NORMARK WR. (1995)- *Turbidite deposition from multiple sources: Quaternary Paola Basin (eastern Tyrrhanian Sea)*. Jour. Sediment. Res., **65**, 469-483.

Rend. Online Soc. Geol. It., Suppl. n. 2 al Vol. 35 (2015) Congresso SIMP-SGI-So.Ge.I-AIV 2015
© Società Geologica Italiana, Roma 2015

Geochemical and mineraloical characterization of marine sediments in the mud diapir province of the Paola basin (Southern Tyrrhenian Sea)

Rashed H.*[1], Rovere M.[2], Pecchioni E.[1], Gamberi F.[2] & Vaselli O.[1-3]

1. Dipartimento di Scienze della Terra, Università di Firenze. 2. Istituto di Scienze Marine (ISMAR), CNR, Bologna.
3. Istituto di Geoscienze e Georisorse, CNR, Firenze.

Corresponding email: hibarashed86@hotmail.com

Keywords: Geochemistry, mineralogy, Paola Basin.

The study area is located along the Paola Ridge, a NNW-SSE 60-km-long anticline that confines the Paola Basin westward (north-western Calabrian margin), in the south-eastern Tyrrhenian Sea. The Paola Ridge has recently been interpreted as due to a mobile mud belt (comprised of D1, D2, D3 diapirs and MMV, RMV mud volcanoes) connected with a set of extensional NW-SE to NNW-SSE trending faults (Gamberi & Rovere, 2010). In August-September 2011 the MVP11 oceanographic cruise was carried on board the R/V CNR Urania. During the cruise, multi-beam bathymetric data, Chirp profiles, gravity coring and box cores, were acquired to define the sedimentological, petrographical, mineralogical and geochemical features of the marine sediments. In this work a detailed mineralogical and geochemical investigation of sediments collected from cores and box cores along the specific structures of the Paola Ridge is reported. The studied samples include: limestone crusts, carbonates of tubular form, iron oxy-hydroxide crusts, pyrite and sulfur crusts and cohesive muds. Each sample was characterized and analyzed by means of optical petrography, XRD, SEM-EDS, XRF, ICP-AES and ICP-MS. Selected samples were chosen for carbon, oxygen and sulfur isotopic analyses. The petrographical, mineralogical, chemical and isotopic data, obtained from the cored sediments and the rock samples, allowed to define the depths of the biogeochemical zones and the geochemical processes affecting the depositional environment into which the marine sediments were deposited (Rovere et al., 2015). Organogenic carbonate crusts consist of calcite, aragonite and dolomite, few phyllosilicates, feldspars and pyroxenes, and associated with macro fauna bivalves that are symbionts of sulfur oxidizing bacteria and usually live in extreme environments, as cold seeps (Rovere et al., 2015). Stable isotopes (C and O) on the organogenic carbonates are depleted in $\delta^{13}C$ and slightly enriched in $\delta^{18}O$. Tubular authigenic carbonates contain siderite, quartz and few phyllosilicates. Stable isotopes (C and O) on the siderite are enriched in both heavy carbon and oxygen isotopes. Iron oxy- hydroxide crusts are comprised of goethite. Pyrite and sulfur crusts have pyrite and/or sphalerite, quartz and few feldspars. Cohesive muds showed a quartz, halite, feldspars, muscovite and clay minerals (illite, vermiculite, chlorite, kaolinite) and in some sample calcite or dolomite, siderite, hematite and pyrite.

Gamberi F. & Rovere M. 2010. Mud diapirs, mud volcanose and fluid flow in the rear of the Calabria Arc orogenic wedge (southeaster Tyrrhenian Sea). Basin Res., 22, 452-464.

Rovere M., Rashed H., Pecchioni E., Mercorella A., Ceregato A., Leidi E., Gamberi F. & Vaselli O. 2015. Habitat mapping of cold seeps associated with authigenic mineralization (Paola Ridge, southern Tyrrhenian): combining seafloor backscatter with biogeochemistry signals. Ital. J. Geosci., 134, 23-31.

Venting and seepage in the Paola Basin (SE Tyrrhenian Sea) investigated

Marzia Rovere, Fabiano Gamberi, Lucilla Capotondi, Alessandro Ceregato, Elisa Leidi, Michael Marani, Alessandra Mercorella, Luigi Vigliotti (*) Heba Rashed, Orlando Vaselli, Elena Pecchioni, Luciano Giannini, Franco Tassi (**, ***) Fabrizio Zgur, Lorenzo Facchin, Lorenzo Sormani, Gianpaolo Visnovic (****) Fulvio Franchi (*****) Valerio Funari (******) & Matthias Zabel (°)

(*) Istituto di Scienze Marine, Consiglio Nazionale delle Ricerche, Bologna, Italy
(**) Dipartimento di Scienze della Terra, Università di Firenze, Italy
(***)Istituto di Geoscienze e Georisorse, Consiglio Nazionale delle Ricerche, Firenze, Italy
(****) Osservatorio Geofisico Sperimentale, Sgonico, Trieste, Italy
(*****) Botswana International University of Science and Technology, Palapye, Botswana
(******) Dipartimento di Scienze Ambientali, Geologiche e Biolo, Università di Bologna, Italy
(°) Center for Marine Environmental Studies, Bremen University, Germany

Key words: Chemosymbiontic macro fauna, Cold seeps, Critical raw materials, Foraminifera, M reflector, Magnetic susceptibility, Multibeam bathymetry and seafloor backscatter, Multichannel seismics, Pockmark, Pore water, Radiorcarbon dating, REE, Siderite, Stable isotopes.

Cold seeps were first identified between 700 and 900 m water depth along the Paola Ridge (NW Calabrian margin, southeastern Tyrrhenian Sea), with the aid of full-ocean depth multibeam and backscatter data acquired in the '90s. Here seepage is presente alongside 2 mud volcanoes (RMV and R1MV) and 3 mud diapirs (D1, D2, D3) characterized by the presence of pockmarks on top of them.

Higher resolution acquisition of bathymetry, seafloor backscatter and seismic data plus seafloor sampling were carried out in 2011. The data lead to the discovery of active gas venting at the seafloor and precipitation of oxy-hydroxides, sulfides and siderites, these latter characterized by heavy oxygen and carbon isotopic composition, in the sub-seafloor of the mud volcanoes. Stable isotopes (C, O, S) and REE composition, together with pore water content and XRF core-scanning data are under investigation for tracing fluid migration and early diagenesis of sea bottom sediment.

Authigenic calcite and aragonite, associated with dead chemosymbiontic shelly macrofauna, were discovered near the seabed on the pockmarks-punctuated mud diapirs. The carbonates retrieved from the diapirs' sub-seafloor showed an isotopic signature compatible with formation during sulfate-dependent microbially-mediated anaerobic oxidation of methane.

The down-core trend of abundance, radiocarbon dating and isotopic characteristics of both chemosymbiontic clam beds (*Lucinoma kazani* and *Acharax* sp.), benthic and planktonic foraminifera (*Uvigerina peregrina* and *Globigerina bulloides*), authigenic aragonites and the magnetic susceptibility showed that the diapirs have remained geochemically optimal habitats over a period of more than 40, 000 years BP. Episodes of enhanced methane flux have been identified and happened near globally recognized abrupt climate oscillations: the beginning of the Dansgaard/Oeschger cycle 10 (at 41 ka) and during the early part of cycle 8 (at 37.5 ka), the beginning of the Bølling interstadial (at 13.5 ka) of the Bølling-Ållerød cycle (14.6-12.9 ka), at the Younger Dryas-Preboreal transition (~11.6 ka). The youngest radiocarbon dated bivalves have lived just before the Little Ice Age (cal AD ~ 1400).

Articles

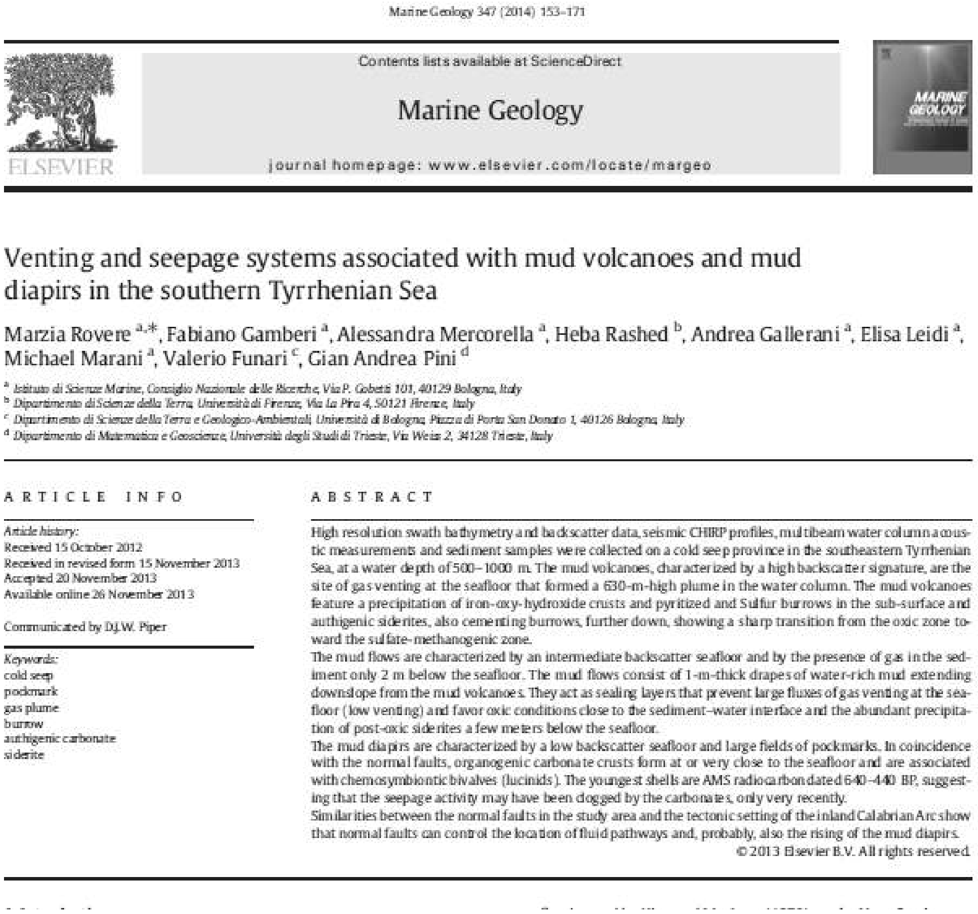

Marine Geology 347 (2014) 153–171

Contents lists available at ScienceDirect

Marine Geology

journal homepage: www.elsevier.com/locate/margeo

Venting and seepage systems associated with mud volcanoes and mud diapirs in the southern Tyrrhenian Sea

Marzia Rovere [a,*], Fabiano Gamberi [a], Alessandra Mercorella [a], Heba Rashed [b], Andrea Gallerani [a], Elisa Leidi [a], Michael Marani [a], Valerio Funari [c], Gian Andrea Pini [d]

[a] *Istituto di Scienze Marine, Consiglio Nazionale delle Ricerche, Via P. Gobetti 101, 40129 Bologna, Italy*
[b] *Dipartimento di Scienze della Terra, Università di Firenze, Via La Pira 4, 50121 Firenze, Italy*
[c] *Dipartimento di Scienze della Terra e Geologico-Ambientali, Università di Bologna, Piazza di Porta San Donato 1, 40126 Bologna, Italy*
[d] *Dipartimento di Matematica e Geoscienze, Università degli Studi di Trieste, Via Weiss 2, 34128 Trieste, Italy*

ARTICLE INFO

Article history:
Received 15 October 2012
Received in revised form 15 November 2013
Accepted 20 November 2013
Available online 26 November 2013

Communicated by D.J.W. Piper

Keywords:
cold seep
pockmark
gas plume
burrow
authigenic carbonate
siderite

ABSTRACT

High resolution swath bathymetry and backscatter data, seismic CHIRP profiles, multibeam water column acoustic measurements and sediment samples were collected on a cold seep province in the southeastern Tyrrhenian Sea, at a water depth of 500–1000 m. The mud volcanoes, characterized by a high backscatter signature, are the site of gas venting at the seafloor that formed a 630-m-high plume in the water column. The mud volcanoes feature a precipitation of iron-oxy-hydroxide crusts and pyritized and Sulfur burrows in the sub-surface and authigenic siderites, also cementing burrows, further down, showing a sharp transition from the oxic zone toward the sulfate-methanogenic zone.

The mud flows are characterized by an intermediate backscatter seafloor and by the presence of gas in the sediment only 2 m below the seafloor. The mud flows consist of 1-m-thick drapes of water-rich mud extending downslope from the mud volcanoes. They act as sealing layers that prevent large fluxes of gas venting at the seafloor (low venting) and favor oxic conditions close to the sediment–water interface and the abundant precipitation of post-oxic siderites a few meters below the seafloor.

The mud diapirs are characterized by a low backscatter seafloor and large fields of pockmarks. In coincidence with the normal faults, organogenic carbonate crusts form at or very close to the seafloor and are associated with chemosymbiontic bivalves (lucinids). The youngest shells are AMS radiocarbon dated 640–440 BP, suggesting that the seepage activity may have been clogged by the carbonates, only very recently.

Similarities between the normal faults in the study area and the tectonic setting of the inland Calabrian Arc show that normal faults can control the location of fluid pathways and, probably, also the rising of the mud diapirs.

Ital. J. Geosci., Vol. 134, No. 1 (2015), pp. 23-31, 7 figs., 1 tab. (doi: 10.3301/IJG.2014.15)
© *Società Geologica Italiana, Roma 2015*

Habitat mapping of cold seeps associated with authigenic mineralization (Paola Ridge, southern Tyrrhenian Sea): combining seafloor backscatter with biogeochemistry signals

MARZIA ROVERE (*), HEBA RASHED (**), ELENA PECCHIONI (**), ALESSANDRA MERCORELLA (*),
ALESSANDRO CEREGATO (*), ELISA LEIDI (*), FABIANO GAMBERI (*) & ORLANDO VASELLI (**), (***)

ABSTRACT

Mineralogical, petrographic and stable isotope analyses were carried out on sediment and rock samples collected from a deep-sea cold seep province in the Paola Ridge (southeastern Tyrrhenian Sea). The results, coupled with the interpretation of the seafloor backscatter, constrained both the biogeochemical zonation and the spatial distribution of the cold seep habitats in the area. These have proved to change in depth in a range of few meters and laterally within narrow zones. The mud volcanoes, characterized by a high backscatter signature, are the site of vigorous gas venting and, in the subsurface, show a rapid transition from the oxic sea water interface toward the methane-sulfate transition zone in the sediments. Intermediate backscatter typifies areas where free venting is hampered by the presence of mudflows at the seafloor. These conditions favor: *i*) the oxidation of sulfides near the seafloor, *ii*) the precipitation of siderites a few meters below the seafloor and *iii*) the formation of sulfides deeper in the sub-seafloor. Faults are likely candidates to act as conduits for sulfates and metal oxides that juxtapose different redox environments. Siderites precipitated in the fast and low venting sites showed enrichment in $\delta^{13}C$ and $\delta^{18}O$, which are compatible with their precipitation in the methanogenic zone. The heavy-oxygen isotopic compositions of the siderites are possibly related to the dissociation of gas hydrates, which have not been mapped so far by seismic data in the study area. Mud diapirism is characterized by low backscatter seafloor, large fields of pockmarks and is dissected by normal faults. In coincidence with the normal faults, authigenic calcites and aragonites are present at or very close to the seafloor. They have the typical isotopic signature indicating formation during sulfate-dependent microbially-mediated anaerobic oxidation of methane. They are associated with *Lucinoma borealis*, the youngest being dated 640-440 BP. This suggests that the seepage activity in the mud diapirs was likely clogged by either carbonates or activity of the faults only very recently.

KEY WORDS: *Pockmark, siderite,* Lucinoma borealis, *stable isotopes, Tyrrhenian Sea.*

INTRODUCTION

Cold seeps are seafloor expressions of focused fluid flow in the marine environment (JUDD & HOVLAND, 2007). Fluid flow includes a large range of geological features such as pockmarks, mud volcanoes and diapirs and they are found on several continental margins worldwide. Cold seeps represent hotspots for increased biological activity, where chemosynthetic communities inhabit. Bio-mediated reactions, such as methan oxidation and sulfate reduction (BOETIUS *et alii*, 2000), increase carbonate alkalinity in the form of dissolved inorganic carbon, which can lead to the precipitation of isotopically depleted carbonates in the sulfate reduction zone and at the sulfate/methane transition zone (RITGER *et alii*, 1987; PAULL *et alii*, 1992; BOHRMANN *et alii*, 1998; ALOISI *et alii*, 2000; NIEMANN *et alii*, 2005; CAMPBELL *et alii*, 2010; BAYON *et alii*, 2013). Deeper in the sub-seafloor, >10 m below the seafloor (BERNER, 1981), always in sulfate-depleted sediments (BOROWSKI *et alii*, 1999; D'HONDT *et alii*, 2002; LELOUP *et alii*, 2007) carbonates, especially siderites, can precipitate through methanogenesis and/or gas hydrates formation/decomposition (MATSUMOTO, 1989; COLEMAN, 1993). Siderites, precipitated in association of methane production, have different isotopic signatures compared to other carbonate mineral phases, such as dolomite and aragonite, and are ^{13}C and ^{18}O enriched (MATSUMOTO, 1989; RODRIGUEZ *et alii*, 2000). The precipitation of authigenic carbonates, associated with the seepage of methane-rich fluids through pockmarks, is a process occurring at several continental margins (HOVLAND *et alii*, 2012). Carbonate crusts related to fluid-rich structures have been also recently reported in the Central Mediterranean area, i.e. the Adriatic Sea (CAPOZZI *et alii*, 2012), the carbonate platform of the Malta plateau (CANGEMI *et alii*, 2010) and the Strait of Sicily (TAVIANI *et alii*, 2013). New high resolution seafloor mapping and backscatter images, seismic profiles, multibeam water column acoustics and sediment samplings have revealed that cold seeps, characterized by the deposition of carbonates and chemosymbiotic fauna assemblages, are also present in the Paola Ridge, southern Tyrrhenian Sea, at 500-1000 m water depth (ROVERE *et alii*, 2014). When the fluid flow is vigorous, it usually produces mud volcanoes (TALUKDER, 2012). In the study area, mud volcanoes are associated with gas plumes in the water column and precipitation of siderite in the sub-seafloor. Conversely, when the flux is very low or even absent, authigenic carbonates are formed near the seabed (TALUKDER, 2012). In the study area the carbonates are associated with chemosymbiotic fauna on pockmarks-punctuated mud diapirs (ROVERE *et alii*, 2014). This paper briefly outlines the preliminary results of the mineralogical, geochemical and isotopic analyses performed on the authi-

---

(*) Istituto di Scienze Marine, Consiglio Nazionale delle Ricerche, Via P. Gobetti, 101 - 40129 Bologna, Italy.
(**) Dipartimento di Scienze della Terra, Università di Firenze, Via La Pira, 4 - 50121 Firenze, Italy.
(***) Istituto di Geoscienze e Georisorse, Consiglio Nazionale delle Ricerche, Via La Pira, 4 - 50121 Firenze, Italy.
Corresponding author: Marzia Rovere m.rovere@ismar.cnr.it, Istituto di Scienze Marine Via P. Gobetti, 101 - 40129 Bologna, Italy. Fax +39 051 6398940, Telephone +39 051 6398861.